FIRST DIRECT MEASUREMENT OF THE ENERGY SPECTRA OF INDIVIDUAL AUGER CASCADE STEPS IN SOLID MnO, Ag AND Pd

by

RAJALAKSHMI SUNDARAMOORTHY

Presented to the Faculty of the Graduate School of

The University of Texas at Arlington in Partial Fulfillment

of the Requirements

for the Degree of

DOCTOR OF PHILOSOPHY

THE UNIVERSITY OF TEXAS AT ARLINGTON

May 2007

ACKNOWLEDGEMENTS

I would like to take this moment to reflect on the past three and a half years after my M.S. Thesis and gratefully acknowledge people whose help guidance and support has been instrumental in the successful completion of my graduate studies.

First I would like to express my sincere gratitude and respect towards my research and thesis advisor, Prof. Dr. Alex Weiss. He gave me the great opportunity to perform this experiment at Brookhaven National Laboratory amidst an atmosphere of great scientists and research scholars. This experience honed my perspective of approach towards both theory and experiment. He has been constant source of encouragement and motivation throughout my research program. The intuition knowledge and the extensive knowledge of Dr.Weiss has always impressed me. He has used these tools to come up with great ideas and solutions for both theoretical and experimental problems we faced in the course of our experiment. The wisdom that Dr.Weiss possesses can be best described by the words of the famous Tamil poet Thiruvalluvar,

"Impressing with clear exposition of thoughts and comprehending

Subtle senses, is the quintessence of wisdom"- (Kural-424).

Indeed, I am indebted to our collaborator Dr. Steve Hulbert of the National Synchrotron Light Source (NSLS) at BNL who has helped me with my research. I have been amazed by the way, in which he is able to tackle all our problems simultaneously with inexplicable speed. His vast experience and his thorough knowledge proved to be instrumental in overcoming the hurdles, which I encountered during my research at

BNL. Amidst his busy schedule as the Section head for Beam line support (now head of the mechanical and beam line departments) which by itself was a huge task, he used to come directly to U16B to fix any and all problems. He has also been instrumental in helping me prepare for almost all the talks on my research that I have presented. I also wish to thank Dr Bob Bartynski of Rutgers University for his support and encouragement.

I wish to thank our Physics Department Chairman, Dr Horwitz for his constant encouragement, moral support. I sincerely thank Dr. Sharma for helping me by extending his suggestions and also thank him for accepting to serve on the defense committee. My sincere gratitude also extends to Dr. Koymen, whose warm suggestions have thrown more light on the important aspects that I need to concentrate upon during my research and I also thank him for accepting to serve on the defense committee. I thank Dr. Fry for the constant encouragement and support he extended while he was our chairman. This support relieved me of my tensions and allowed me to focus my thoughts on the research. I also thank him for agreeing to be on the panel of defense Committee members. I also wish to thank Dr. Fazleev for accepting to be on the panel of defense committee and I am grateful for his constant encouragement and support throughout my research.

I wish to extend my sincere thanks to all our office staff Margie Jackymack, Amy Osborn, Jean Hanlon, Fran Smith, Victor Reece, Lab coordinator Doug Coyne at UTA and Gary Nintzel and Barry Karlin of BNL for extending their technical help at times when I needed them the most. I wish to thank Dr. Daniel Fischer, spokes person for the X24A beam line for giving us the beamtime during summer 2004 to take the coincidence data for Ag discussed in Chapter 4. I also would like to thank Dr. Dario Arena for his help. I would also extend my sincere thanks to Dr. Asok Ray, and Dr.

Qiming Zhang, Dr. Musielak, Dr. Kaushik De, Dr. Jay Yu, Dr. Nilakshi, Dr. Rubins for their contribution towards my successful completion of my degree. I would also like to thank all my friends of both UTA and BNL for extending their help during my studies and research.

Finally I would like to express my deep gratitude and heartfelt thanks to my parents who have been role models in developing a strong will to face any hardships. Their constant encouragement and motivation from my early days of schooling proved to be most instrumental in the successful path of my academic career. Their advice and moral support kept my spirits always on the high end, whenever I felt their absence. My sincere thanks are due to my sister for her love, affection and support. I am happy and fortunate enough to have my father along with me when I am presenting my dissertation defense, and my graduation. As the sayings in Thirukkural written by a famous poet Thiruvalluvar goes

"The mother, hearing her son's/daughter's merit
Delights more than when she begot." (Kural-69)

My father is so happy to participate in all the events.

I had requested that Dr Weiss to give me a research topic, which has never been done before so that I can work on something new, keeping in mind the hardships that might come on its way. It so happened that this experiment along with the new theoretical model developed to explain it turned out to be of great interest. Words just cannot explain my sincere thanks towards Dr.Weiss. I am fortunate to have him as my research advisor and mentor.

April 20, 2007

ABSTRACT

FIRST DIRECT MEASUREMENT OF THE ENERGY SPECTRA OF INDIVIDUAL AUGER CASCADE STEPS IN SOLID MnO, Ag AND Pd

Publication No. _____

RAJALAKSHMI SUNDARAMOORTHY, PhD.

The University of Texas at Arlington, 2007

Supervising Professor: ALEXANDER HERMAN WEISS

We present the first direct measurements of energy spectra of electrons emitted in the later steps of the Auger cascade processes in solids. Measurements were carried out for the L→MV→VVV and L→MM→MVV→VVVV Auger cascades in MnO and L→MM→MVV, M→NV→VVV Auger cascades in Ag and M→NV→VVV Auger cascade for Pd. The spectra associated with the later steps in the cascade were separated from overlapping spectral contribution from other decay processes by acquiring the cascade induced spectra in time coincidence with Auger electrons emitted in the prior cascade step. The Auger spectra associated with the decay of core holes created via, Auger Cascade processes are significantly wider than spectra associated with Auger decays in directly following the photo-ionization of the core hole. A new

theoretical model was developed to allow for the inclusion of processes in which holes generated in the valence band in a prior cascade step change to a different energy in the valence band during the next cascade step. A comparison of the measured spectra with model calculation enabled an estimation of the valence-valence, core-core, and core-valence correlation energies. The success of the model in accounting for the increased width observed in the spectra of Auger electrons emitted in the later steps of the Auger cascade provides strong evidence that valence holes left from the previous cascade step participate in the subsequent Auger transitions in the case of transitions involving the outer cores.

TABLE OF CONTENTS

LIST OF ILLUSTRATIONS

CHAPTER 1

AUGER-AUGER COINCIDENCE SPECTROSCOPY

1.1 Motivation

In this dissertation, I present the results of the first measurement of Auger spectra resulting exclusively from the second and third stages of the Auger cascade processes in a solid. The spectrum of individual cascade steps was separated from overlapping spectral components by using a new type of coincidence spectroscopy: Auger-Auger Coincidence Spectroscopy (AACS).

The Auger cascade process may be described as follows. Atoms that are highly excited due to the presence of a hole in an inner shell often relax via an Auger transition [1-3] in which a less tightly bound electron fills the inner-shell hole and the excess energy is carried off by yet another electron which exits the atom. This auto-ionizing process results in a final state with two holes. If one or more of these holes is in an inner shell, then the initial Auger transition can be followed by one or more additional Auger transitions [4]. This sequence of transitions [5-7] is termed an "Auger Cascade Process."

X-Ray photoelectron spectroscopy (XPS) and Auger electron spectroscopy (AES) are two widely studied surface science techniques. The analysis of the spectra obtained using these methods contain information about the sample under investigation

including the local density of states at the surface, charge transfer effects, chemical bonding, atomic charge and post collision interaction effects[8-13]. Unfortunately these spectra include a large background which obscure some of the valuable information. Many numerical techniques have been developed to remove the background. These techniques are model dependent and may involve considerable loss of information. Coincidence techniques have been shown to be capable of extracting the information from the large background. In addition, using coincidence techniques, it is possible to uniquely correlate a de-excitation channel with a given excitation channel immediately preceding it. The pairs of excitation events which are of common interests are Photo-electron and Auger electron pair [14-20], electron–ion pairs[21], electron-electron pairs[22-23], photoelectron-fluorescence photon pairs to mention a few. To excite these events, photon sources like Al Kα, Mg Kα lines having enough energy to excite deep core levels were conventionally used. With the advent of tunable sources like the synchrotron storage rings with its continuous spectral distribution from infra-red to ultra violet and X-ray regimes has allowed selective probing of the required energy levels of interest.

Of the coincidence pairs discussed above, Auger-Auger coincidence has until now only been studied in gasses - not in solids. Further literature search on the Auger-cascade measurements lead us to studies relating to the excitations above and below a particular core's ionization threshold energy to show the contribution of an extra hole to the whole system. The presence of an extra hole in the core level significantly alters the line shape (due to the formation of multiplets), valence band contribution, core hole and

valence hole interactions thereby altering the correlation energies and ultimately the Auger spectrum shifts either to the low energy side or to the high energy side based on the strength of the correlation energies of the holes different levels. The presence of the hole in the core level significantly alters the line shape of the valence band spectrum.

The spectra of Auger cascades have been a subject of interest for quite some time due to the insight such spectra provide into many hole processes. AACS provides a unique way not only to study the correlation energies of the electrons formed during the process but also allows us to study multi-hole dynamics during an Auger decay process.

This dissertation is organized as follows. The remaining of chapter 1 discusses the direct and cascade induced Auger process. Chapter 2 describes the experimental set up used to perform the measurement at the NSLS. It explains in detail about the beam line configuration, the detailed circuitry, analyzer used, its operation, counting electronics, timing electronics and the experimental procedure. Chapter 3 describes the photoemission spectra of MnO and the results obtained using the direct coincidence of the Mn M-core with the M→VV Auger electrons also included in this chapter are the results obtained using the Auger-Auger coincidence of the subsequent Auger transitions involved in the cascade process and a comparison of the direct coincidence Auger spectra and the cascade coincidence Auger spectra provided unanticipated discovery: The broadening, an extension to the higher energy of the spectra associated with the filling of outer cores in the presence of previously created valence holes. These results can be successfully modeled using the full participation of the valence band hole

transitions in which the initial valence holes(s) are filled during the transition results in a effective rearrangement of the final state valence band holes. The new spectral features observed for the first time, (e.g.) the increase in the spectral weight on the high energy side using AACS are discussed in chapter 3, together with their theoretical ramifications. Chapter 4 provides a detailed account of the photoemission spectra of Ag. It provides a discussion about the high energy Auger-Auger and Auger–photoelectron coincidence spectrum obtained at X-24A and the low energy Auger-Auger coincidence spectra obtained at U-16B. Chapter 5 provides a detailed account of the photoemission spectra of Pd, discusses about the low energy Auger-Auger and Auger–photoelectron coincidence spectrum obtained at U-16B during the last run at NSLS. Chapter 6 explains in detail about the theoretical model proposed to explain the full participation of valence holes during the Auger-Auger coincidence and the failure of the "Two step model". Chapter 7 discusses possible future work and also discusses the potential applications of the release of energy in biological cells in the form of coulomb explosion to kill the diseased cells when nanoparticles of the right size are implanted in the cell and summarizes the results obtained. The Appendix A included at the end describes the acronyms used, the Appendix B describes the background subtraction, the Appendix C describes the convolution program and correlation program developed to do the convolutions and correlations of the valence band density of states and the Appendix D describes the estimation of the correlation energies-U_{dd}, U_{pd} and U_{pp}.

1.2 Direct Auger transitions

When an atom in a sample is excited by photons of energy hν, it may knock out a photoelectron from a core level with binding energy E_C. ($BindingEnergy_{core} < h\nu$). Subsequently the atom is in the excited state having a hole in the core level. The excited atom may relax by filling the core hole by an electron from the valence band. The difference in the binding energy between the core hole and the valence band hole may be released by either of the processes: X-ray emission or Auger electron emission. For core holes with binding energies <2keV, the preferred way of de-excitation is Auger emission. For higher binding energies X-ray emission becomes the predominant mechanism.

The direct Auger decay process is described [24-28] using an energy level diagram as shown in Fig. 1.1. The process of emission of an electron from the valence band immediately following a photoemission process is described as CVV Auger decay or the Direct Auger decay, where E_C is defined as the binding energy of the core hole and E_{V1} and E_{V2} is the binding energy of the valence hole created in the process. The kinetic energy of the outgoing Auger electron is given by the following equation;

$$KE_{CVV\ Auger\ electron} = E_C - E_{V1} - E_{V2} - \phi_A \qquad (1)$$

where ϕ_A is the work function of the electron energy analyzer. The final state of the direct Auger process has two holes in the valence band.

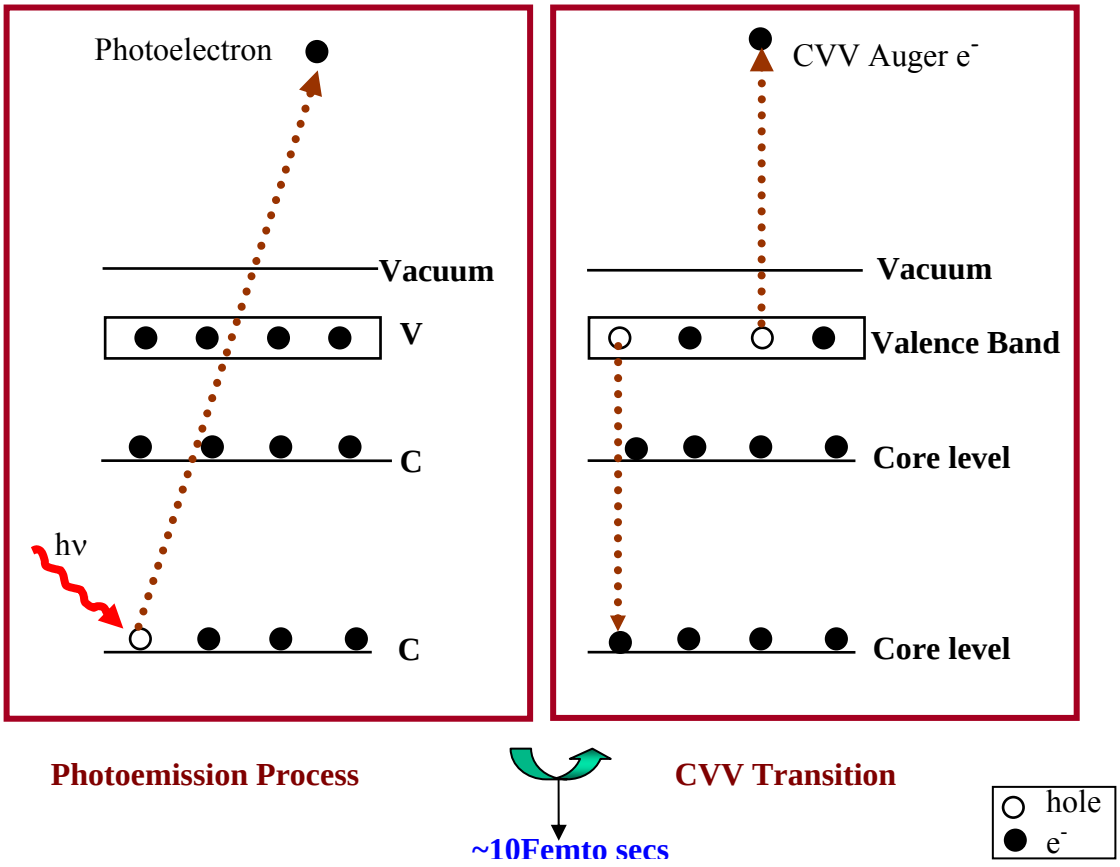

Fig. 1.1 The direct Auger decay process

An electron which is emitted from the sample needs some energy to leave the sample into the vacuum. This energy is referred to as the work function of the sample(ϕ_s). The analyzer is also made up of a metal; it has its own work function (ϕ_A). Therefore when the electron leaves the sample and enters the analyzer there is a difference in the work function which is shown in Fig. 1.2 (ϕ_s-ϕ_A). So only those electrons which have enough energy to over come the difference in the work function can reach the analyzer and will be detected. Photons which hit the sample excite photoelectrons, Auger electrons and

in that process create secondary electrons (photoelectrons and auger electrons on the way out knock out other electrons which creates a cascade of electrons known as secondary electrons). A cartoon of the photoelectron spectrum with the secondary electrons are shown in Fig. 1.2.

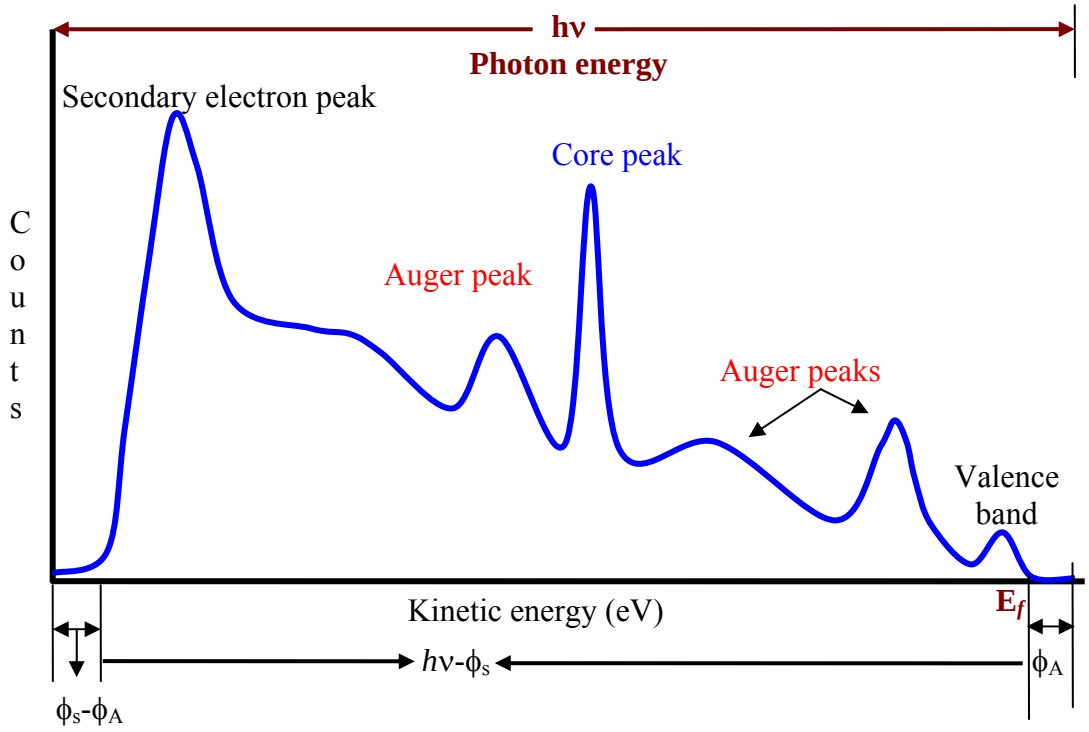

Fig. 1.2 The cartoon of the kinetic energy spectra of a photo excited sample

In this cartoon it is assumed that $\phi_s>\phi_A$. The minimum energy of the electrons entering the analyzer is the one which has $0+(\phi_s-\phi_A)$ and the maximum energy of the electrons entering the analyzer will be $(h\nu-\phi_s)+(\phi_s-\phi_A)=h\nu-\phi_A$. So the difference between the

measured Fermi level and the photon energy hν will give the work function of the analyzer (ϕ_A)[29].

Let us examine the extreme cases of the kinetic energy (KE) of the electron emitted in the final step of the Auger process. The KE of the Auger electron will be maximum when both the electrons (for simplicity consider E_f =Vacuum=0) come from the top of the valence band (i.e.)

$$KE_{Auger}\,(max) = E_C - \phi_A \qquad \ldots (2)$$

On the other hand, the kinetic energy of the Auger electron will be minimum when both electrons come from the bottom of the valence band. If the valence band has an energy width W, then the kinetic energy of the Auger electron will be

$$KE_{Auger}\,(min) = E_C - 2W - \phi_A \qquad \ldots(3)$$

Thus the energy spectra of the CVV Auger line will have a FWFM (Full width full maximum) to be given by the difference in the maximum and minimum KE of the Auger electron.

$$\Delta KE_{Auger} = KE_{Auger}\,(max) - KE_A\,(min) = 2W \qquad \ldots(4)$$

The above equation is valid only when the effect of hole-hole interaction in the valence band is considered to be negligible. The hole-hole interaction energy is called the correlation energy (U) [30-41]. When the valence band width is large compared to the coulomb repulsion then we can assume that the correlation energy is negligible. Usually the CVV Auger spectrum having two holes in the final state is modeled using the self convolution of the density of states under the assumption stated above. Thus the Auger spectrum becomes more complicated when more than 2 holes are found in

the final state of the cascade process. Usually depending upon which shell of the atom is excited often the final state of the cascade process ends up having 3 or 4 or multiple holes in the final state. However, this complication opens up an opportunity. As the CVV Auger process is intimately connected with the electrons in the valence band, the AES can be used as a probe of the valence levels that are localized in the vicinity of the core hole.

1.3 Notation used

In order to characterize the cascade transitions, we analyze the process in terms of a series of individual steps, each of which results in the emission of an Auger electron and is labeled by its initial and final hole state. Each symbol consists of a letter that specifies the principal quantum number with an optional subscript that denotes the spin-orbit splitting of the principal atomic levels. For example, the direct MVV transition (Fig. 1.2) is denoted $M_{2,3}$→VV, the Auger cascade chains associated with L→MV decay (Fig. 1.3) is written as $L_{2,3}$→$M_{2,3}$V(initial hole state), $M_{2,3}$V→VVV(final hole state), and the cascade associated with L→MM decay (Fig. 1.4), encompassing decays of both of the M holes, is written as $L_{2,3}$→$M_{2,3}M_{2,3}$ (initial), $M_{2,3}M_{2,3}$ →$M_{2,3}$VV(intermediate) and $M_{2,3}$VV→VVVV(final hole states). Thus, $L_{2,3}$→$M_{2,3}M_{2,3}$ refers to an Auger process in which an initial core hole in the 2*p* level is filled by an electron from the 3d level and results in the ejection of electron from the 3d level. In the transitions involving valence electrons, V is used to indicate a final state hole in the valence level with out differentiating the spin and orbital content of the electrons in the valence band. Therefore, an $M_{2,3}$→VV Auger process denotes a transition where an

initial core hole in an $M_{2,3}$ level is filled by unspecified electron from the valence band while a second valence band electron caries away the excess energy. Our notation also assumes that the valence hole(s) created in the prior cascade step does not get filled at the time of subsequent Auger decay.

1.4 Auger cascade transitions

When the initial hole created by photo excitation is in a deeper level, the excited atom can relax itself by series of Auger decays. This multiple subsequent decay process is termed Auger cascade decay. These Auger decay channels have multiple holes in the intermediate and final states.

1.4.1 Auger cascade decay process [L→MV→MVV]

The Auger cascade process [L→MV→MVV] is schematically explained by means of an energy level diagram in Fig. 1.3. In this Auger cascade process, the atom is excited with higher photon energy ~740eV (Binding energy of Mn L_2 is 649.9eV) [X-ray data booklet] so as to excite the deeper core such as the L shell. As a result of the photoemission process, the atom is left behind with a hole in the L-core. The atom relaxes by dropping an electron from a loosely bound core level (M); and excess energy is carried away by an Auger electron from the valence band (this is one way; another possibility is explained in Fig. 1.4[42-46]. This transition named as the L→MV has one hole in the core level (M) and one hole in the valence band. This step is the intermediate step in the Auger cascade process.

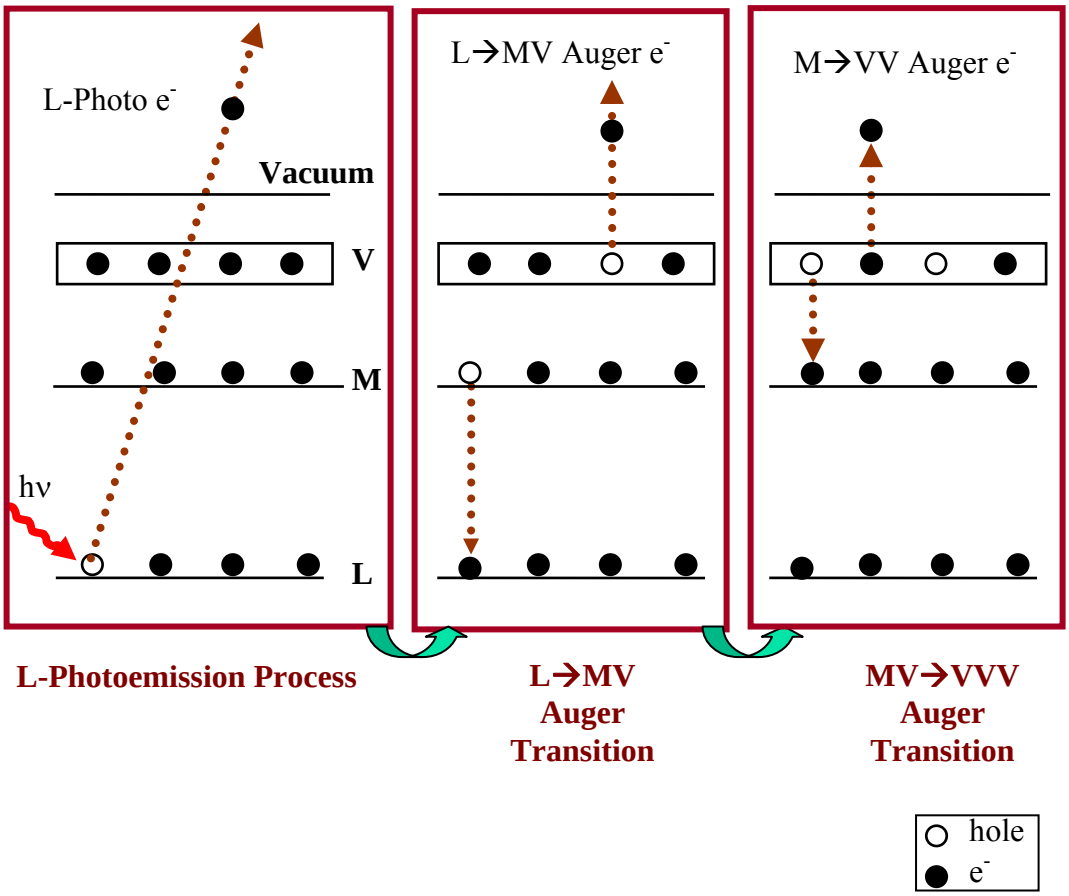

Fig. 1.3 One of the sequence of Auger decays if the hole is in a core level (L). The transitions are L-photoemission process followed by $L_{2,3} \rightarrow M_{2,3}V$ (initial hole state), $M_{2,3}V \rightarrow VVV$(final hole state)

The energy of Auger electron, which is detected at the electron energy analyzer emitted in the intermediate step is given by, is given by:

$$KE_{(L \rightarrow MV\ Auger\ e^-)} = E_L - E_M - E_{V1} - \phi_A \qquad (5)$$

Now, the hole in the core level (M) gets filled up by an electron from the valence band and yet another Auger electron leaves the atom (to bring the atom to its ground state) from the valence band to conserve energy. This transition named as the MV→VVV Auger decay which has three holes in the valence band. This is the final state of the Auger cascade process which has three holes in the valence band. The kinetic energy of the Auger electron, which is detected at the electron energy analyzer emitted in the final step of this Auger cascade process, is given by:

$$KE_{(MV \rightarrow VVV\ Auger\ e^-)} = E_M - E_{V1} - E_{V2} - \phi_A \qquad (6)$$

In the above expression, E_M is the binding energy of the core electron in the M level, E_{V1} and E_{V2} are the binding energies of the valence electrons involved in the Auger transition and ϕ_A is the work function of the electron energy analyzer. In eqn (5) and eqn (6), all energies are assumed to be positive and all energies are referenced to the Fermi level (E_f) of the solid.

1.4.2 Auger cascade decay process [L→MM→MVV→VVVV]

In an Auger Cascade process, shown schematically in the following Fig. 1.4, when the hole is created in the L shell due to the photoemission process, the ionic system relaxes when an electron from the M shell drops down to fill the core hole created in the L shell. A second electron referred to as an Auger electron, is then ejected from the M shell of the solid to conserve energy (as opposed to the electron coming out of the VB in the L→MV process described earlier). Now, the atom is left with 2 holes in the M shell. Two subsequent cascade processes occur. In the first

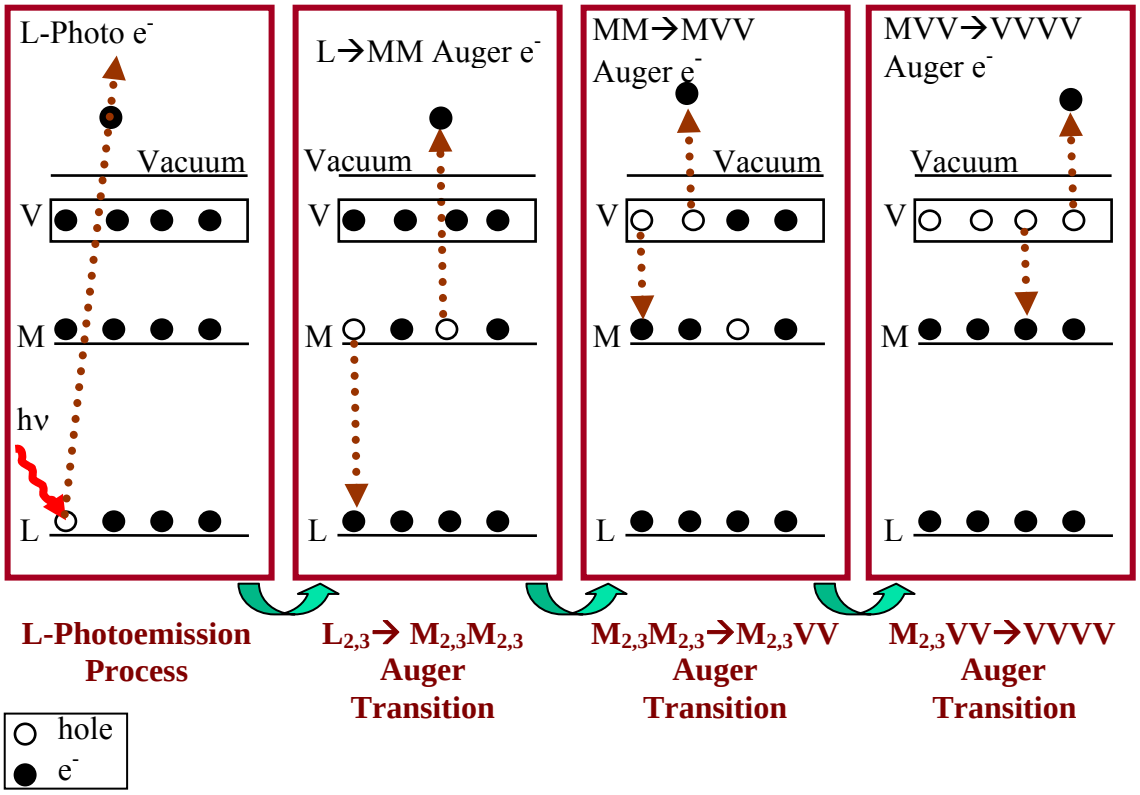

Fig. 1.4 One of the sequence of Auger decays if the hole is in a core level (L). The transitions are L-photoemission process followed by $L_{2,3} \rightarrow M_{2,3}M_{2,3}$ Auger decay $M_{2,3}M_{2,3} \rightarrow M_{2,3}VV$ Auger decay, $M_{2,3}VV \rightarrow VVVV$ Auger decay

process, an electron from the valence band drops down to fill one of the holes in the M level, while an Auger electron leaves the valence band in order to conserve energy, while the other M core hole acts as a spectator. This transition is termed as MM→MVV. This transition has 2 valence holes with one hole in the M level as the

spectator. Now, in the second process, an electron from the valence band fills the spectator hole in the M level, while another Auger electron leaves the atom from the valence band to conserve energy. Thus the atom is left behind with four holes in the valence band in final state. This transition is MVV→VVVV.

1.5 Sample description

The surfaces chosen for the AACS studies reported in this dissertation were MnO single crystal, Ag (100) sample and a thick film of Pd grown on Ag. The reasons for the choice of the samples are enumerated below.

MnO sample was a good choice for the multiple AACS study because there are three Auger peaks associated with an initial hole in the L shell: L→MV, L→MM and L→VV. These three Auger lines there are well separated in kinetic energy of the outgoing electron, which permits measurement of their corresponding coincidence spectra without spectral overlap. In addition previous APECS results were analyzed for comparison. We could excite to L Level with our beam line [maximum photon energy 800eV] (e.g. Cu would be difficult with our beam line since E_B (L_2 = 952eV). The presence of strong L→MV and L→MM Auger peaks allowed us to solve the difference between three hole final state in the L→MV→VVV process and the two-hole (plus one spectator and four hole final states in MM→MVV and MVV→VVVV processes.

Previous studies [47] were performed in which the Ag and Pd were excited above and below the L_3 threshold to see the effect of multiple holes in the intermediate state on the final state spectra of any particular Auger decay process. These studies

were not able to separate out the contributions of individual Auger cascades to the final state. So to find out the individual contribution of each and every Auger decay channel to the final state, we had to do Auger-Auger coincidence studies.

CHAPTER 2

COINCIDENCE SPECTROSCOPY INSTRUMENTATION

Core level spectroscopy was first performed using conventional x-ray tubes [48]. These sources provide useful flux in the hard x-ray region (2-100keV) but little in the soft x-ray region (0.5-2keV). With the advent of synchrotron radiation sources [49-52], high-flux sources of soft X-rays with tunable photon energy became available making it possible to achieve improved signal to noise ratios and higher energy resolution. Coincidence experiments initially were performed using conventional x-ray sources. The availability of synchrotron sources has made these experiments more practical due to the significant reduction in time needed to collect data and the possibility of the photoemission final state energies for achieving optimal surface sensitivities by minimizing escape depths. All experiments reported in this dissertation were carried out at beam line U16B, X24A and U4A of the National Synchrotron Light Source (NSLS), Brookhaven National Lab (BNL), NewYork. Auger and Photoelectron coincidence measurements [53, 54] provide a great deal of information on the energetics, line shapes [55,56], electronic structure of atoms [57,58], molecules and solids.

2.1 NSLS storage ring

The NSLS is a Department of Energy (DOE) funded research facility dedicated to producing intense UV and X-Ray light. The NSLS operates two electron storage rings shown in Fig. 2.1, which provide intense focused light spanning the electromagnetic spectrum from infrared through x-ray energies. The electrons are injected into the NSLS storage rings from a 750MeV booster synchrotron fed by a 120MeV LINAC. The NSLS injector linear accelerator, or LINAC consists of several parts that generate, accelerate and shape the electron beam for injection into the booster synchrotron and then into the NSLS storage rings. LINAC consists of the electron gun and low energy beam transport system (LEBT) accelerating cavities, the RF system and the beam transport system [59]. Bunches of electrons are generated using an electron gun. By applying suitable voltages the electrons can be bunched together. The bunched electrons are then transported to the booster ring using the low energy beam transport system which also prepares the beam for efficient injection and capture in the LINAC. This beam is accelerated by a LINAC to energy of about 120MeV. The radiofrequency fields (2856MHz) provide the voltage which accelerates the electrons from 100KeV to 116MeV. This beam has to be focused and guided so that most of the electrons are captured, so as to reduce the radiation caused by the rejected electrons. Quadrupoles help to focus the electrons both in the horizontal and vertical direction and the dipole magnets help to bend the beam around the corners. After the beam is shaped by the quadrupoles to fit the booster both vertically and horizontally, the beam is injected

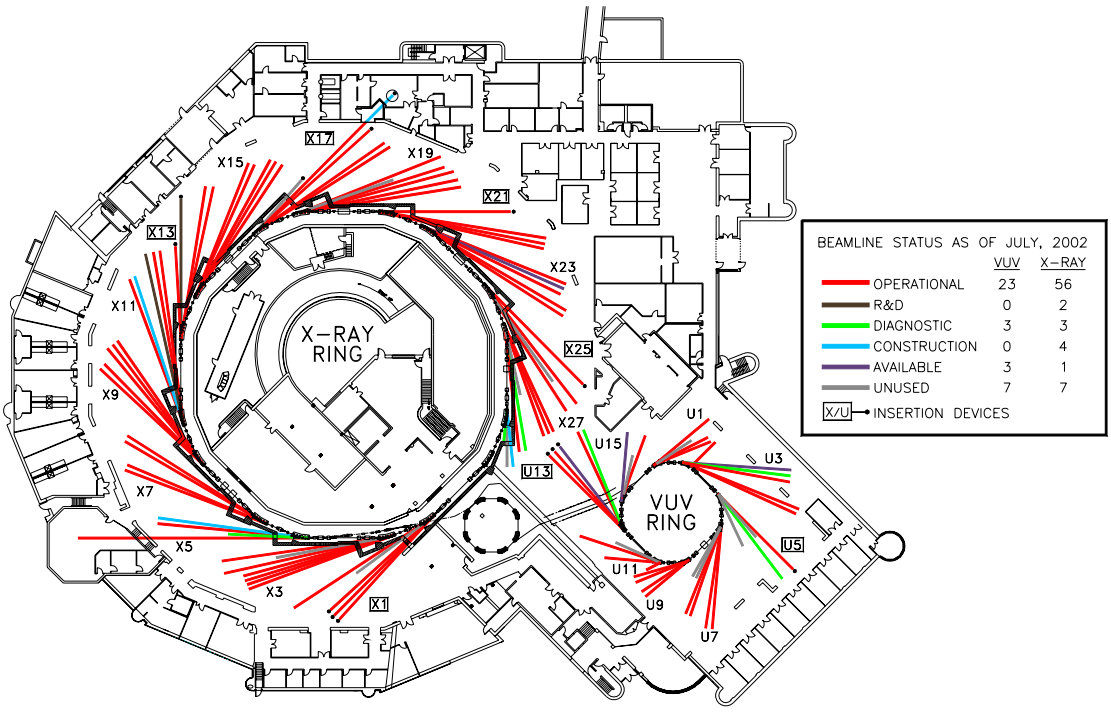

Fig. 2.1 National Synchrotron Light Source: Floor plan
of the X-ray ring and the VUV ring

into the booster ring and a RF accelerating cavity boosts the electron energy to 750MeV. When the maximum energy is reached then it is fed into either the X-Ray or VUV ring. In the first case the electron bunches are shunted by magnets through a storage line into the VUV storage ring [60], where up to 9 electron bunches orbit the ring at the energies of 800MeV. As soon as the VUV ring is filled to a desired operating current, the injection system is turned off. The stored electron bunches are forced into a closed orbit around the ring by eight dipole bending magnets. At each bend the circulating electrons lose energy in the form of synchrotron light. Energy is put back into the circulating electrons by means of radio frequency cavities (52.89MHz) in the ring. Photon shutters may be opened at the two beam ports on each bend and the synchrotron light, predominantly in the VUV region, is allowed down through the beam lines to the research end stations.

The X-Ray storage ring [61] is filled in a similar fashion. Electron bunches are once again injected into the LINAC and accelerated in the booster ring to 750MeV. Up to 30 bunches of electrons orbiting with 750MeV fill the X-Ray storage ring. Once the X-Ray ring is filled to the desired operating current the radio frequency cavity is used to increase and maintain ring energy of 2.8GeV. In the X-Ray ring, sixteen bending magnets force the electron in a closed orbit. Photon shutters may be opened at the two beam ports on each bend and the synchrotron light, predominantly in the X-Ray region, is allowed down through the beam lines to the research end stations.

2.2 NSLS beamlines

The Auger-Auger coincidence experiment and Auger photoelectron coincidence experiments were performed at beamlines U16B and X24A at the National Synchrotron Light Source (NSLS) at Brookhaven National Laboratory. The VUV storage ring [62] at the NSLS operates at a primary energy of 800MeV with a maximum beam current of ~1000mA. The ring operates with 9 "buckets" out of which 7 consecutive "buckets" are filled with electrons, while the last two are left empty. When these bunches of electrons revolve around the ring, at each bend they produce intense electromagnetic radiation in the form of light pulse, which is incident upon the sample. The orbital period of the electrons around the storage ring is 170 ns, which gives a bunch-to-bunch separation time of ~19.2ns. There are 16 beamlines in the UV ring. The X-ray storage ring at the NSLS operates at a primary energy of 2.8GeV with a maximum beam current of ~300mA. The ring operates with 30 "buckets" out of which 25 consecutive "buckets" are filled with electrons. The life time of the beam is ~20hours. The electron orbital period around the ring is about 567.2ns. This gives a bunch to bunch separation of about ~18.9ns. There are 61 beamlines in the X-ray ring.

2.2.1 U16B Beamline and ERG monochromator

The beam line consists of a series of optical elements, which directs the beam to the ERG monochromator designed by F.C.Brown and S.L.Hulbert.[63,64] All scan motions are controlled by computer which selects particular range of photon energies, which is directed onto the sample in the sample chamber. The layout of the beam line is described in detail in the following paragraph.

The beamline U16B shown in Fig. 2.2 consists of horizontal collection and focusing mirror M_0, the ERG monochromator, a refocusing mirror M_3 and the sample chamber. The ERG monochromator focuses and disperses the radiation in a vertical plane. It has mirrors M_1, M_2, and gratings G_1 and G_2 as its components. M_1 is a gold coated 30 cm long bent elliptical mirror located a fixed distance (52cm) from the entrance slit S_1. The slit focuses the synchrotron light as a horizontal line. A demagnification takes place with a ratio of 7 to 1. M_2S_1 is a Codling mirror/slit combination [65]. The incoming radiation is steered onto one of the gold coated gratings G_1, G_2 or G_3 of 2m, 3.7m or 5m radius of curvature, respectively which are ruled at 1200 lines per mm. The widths of the entrance slit S_1 and exit slit S_2 are variable in order to allow adjustment of the monochromator resolution. The scanning of the monochromator is accomplished by Rowland circle geometry which is related to the Vodar-type geometry [66] for the gratings. The Rowland circles rotate about S_2 to produce a fixed exit beam direction. The gratings are mounted on arms S_1G. The entire arm is pivoted about S_1 and this combination with mirror M_1 translates parallel to the incoming beam. A linear air bearing referenced to a ground granite slab provides a smooth, accurate, straight-line motion of the M_1-S_1-G assembly. The two grating arms and Codling mirror/slit assembly rotate on three pairs of precision ball bearings. The absolute positions of the optical elements, the angular rotations of the grating arms, the tilt of the Codling mirror and the linear motion of the air bearing are effected by four stepping motors equipped with optical shaft encoders along with mechanical limit switches. A Newport ESP7000 Universal High-Performance Motion Controller/Driver

coordinates the stepping motor-driven movements and allows continuous scanning of the wavelength of the monochromated light. The task of coordinating monochromator movements with the reading and recording of input data channels in, is provided by the software program 'Un' which was installed in the U16B computer [67]. The 2m grating was used to obtain high statistics valence band spectra, while the 3.7m grating was used in the photon energy range of 450eV to 750eV to obtain all the photoemission and the coincidence spectra acquired.

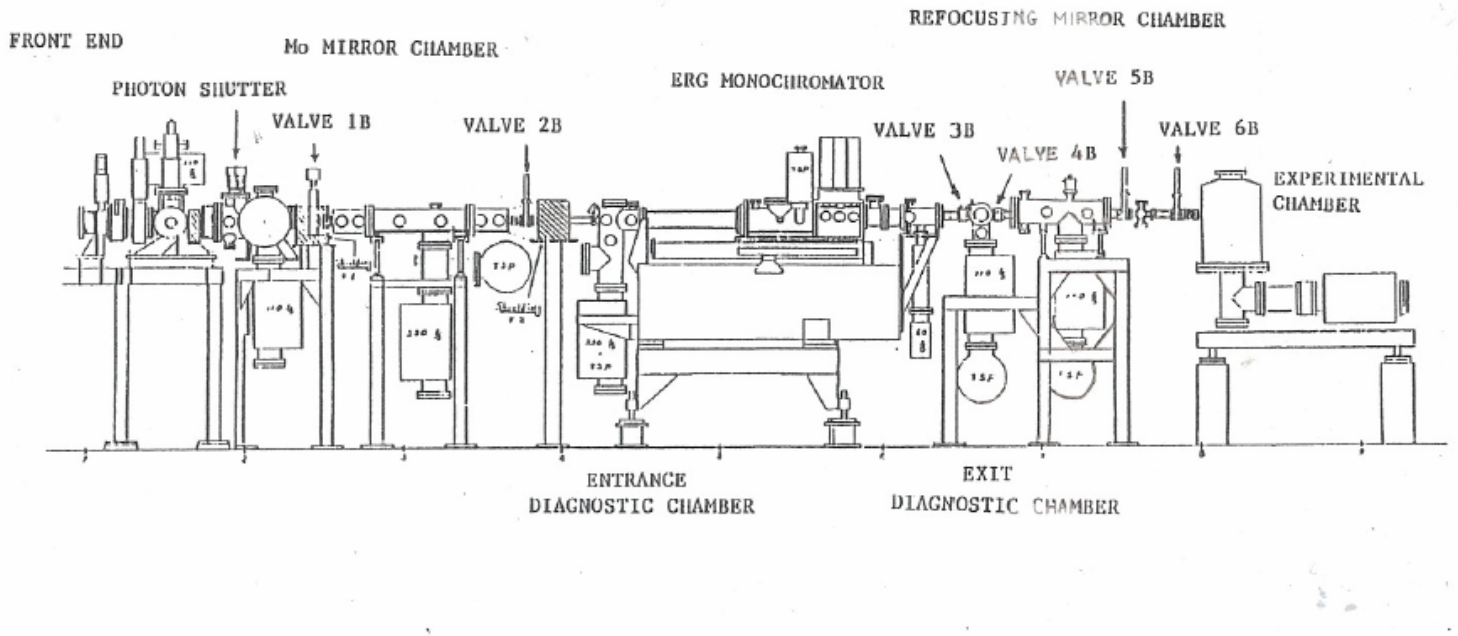

Fig.2.2 The beam line configuration at NSLS, U16B at BNL

Vacuum pumping for the beam line is provided by an ion pump and a Ti sublimator combination. In order to minimize carbon contamination of the optical elements, the key pumping design feature of the ERG is good differential pumping between upstream and downstream of the ERG itself, providing a great vacuum upstream even if the pressure is relatively poor downstream, or, thought of another way, it provides very good "insulation" of the ring from a vacuum accident in the endstation [68]. A pressure in the low 10^{-10} Torr range can be achieved and is necessary so that the beamline can be opened to the ring vacuum to allow the passage of the SR. As shown in Fig. 2.2, the monochromator can be isolated from the rest of the beam line by gate valves. Valves 1B and 2B isolates the M_0 mirror chamber, while the monochromator is located between valves 2B and 3B, and the refocusing mirror is between valves 4B and 5B and the experimental chamber is isolated from the refocusing mirror by valve 6B. The mirror M_3 is gold coated diamond turned ellipsoidal mirror [69]. It refocuses the monochromatic beam from the exit slit at the center of the photoemission chamber with 1:1 demagnification. Valves 5B and 6B are closed, whenever we are introducing gas inside the chamber, or evaporating and depositing metals on the substrate, to make sure that the elevated chamber pressure is isolated from the beamline and the ring. There are interlock valves and safety shutters which act as safety measures to protect the ring vacuum. Using angle-integrated electron energy analyzers focused on a single small spot on the sample, photoemission, Auger-photoelectron and Auger–Auger coincidence experiments can be performed in the chamber.

2.3 Introduction

Photoelectron and Auger Electron Spectroscopy are powerful techniques for studying the electronic structure of solids. Auger spectra reveal chemically specific information about valance band electronic structure and about the coupling of the core hole to other electron levels. The two spectroscopies are closely related, as core holes with binding energy less than ~1keV produced by photoemission nearly always decay by subsequent Auger electron emission. Lifetimes of Auger decay are of the order of 10^{-15} seconds, while typical laboratory timing resolution for electronic events is of the order of 10^{-9} sec. Thus, a photoelectron and its corresponding Auger electron may be considered to be emitted simultaneously given the resolution time of the detectors. The technique of AACS uses this fact to identify subsequent pairs of Auger electrons. Two electron analyzers are used. Both are Auger electron analyzers. One of them is tuned to energy to detect the low energy Auger electron. Another one is tuned to energy to detect the higher energy Auger electrons in the appropriate Auger spectrum. The detection of electrons in both analyzers within in the experimental time resolution is interpreted to mean that both electrons came from the same excitation decay event, from the same atom. The experiment can be run in either of the two modes, which we term as "forward" and "reverse" scans. In the forward scan mode, one of the analyzers is fixed at the peak of one of the Auger electron emitted in the high-energy range and the other analyzer is scanned through the low energy Auger peak. In the reverse scan mode, the low energy Auger peak is fixed and the other analyzer is scanned through the

Auger electron emitted with high kinetic energy. An ordinary Auger spectrum, called the singles spectrum, is acquired along with the coincidence spectrum.

2.4 Overview of the experiment

Synchrotron radiation from the NSLS storage ring is monochromated by the ERG monochromator which selects out the appropriate photon energy used to illuminate the sample in the UHV chamber. The photons from the monochromator excite the photoelectrons and Auger electrons along with secondary electrons from the sample. Two cylindrical mirror analyzers (CMA's) are used to capture the electrons from the sample. One CMA is maintained at a fixed kinetic energy corresponding to an Auger electron peak or a photoelectron peak, while the second CMA is scanned over an energy range which includes the peak of the energy distribution of the Auger electrons that are subsequently emitted from the sample after the initial/intermediate Auger or photoelectron decay. Since both the electrons are emitted within 10femtoseconds, which is very less than the timing resolution of the CMA's, both events may be considered simultaneous events.

The output of each CMA is directed to an amplifier and a discriminator. The amplified and discriminated signal from one CMA is used as the start signal of a time-to-amplitude converter (TAC). The signal from the second CMA is also amplified, discriminated and fed through the delay circuit to bring the data into the positive time regime, and this is used as a stop signal to the TAC. The TAC outputs a signal whose amplitude is proportional to the time interval between the start and the stop pulse; this

signal having a particular height is recorded as a histogram in the MCA as pulses having a particular height binned in the corresponding timing channel.

2.5 Experimental set up at the beamline-U16B

The experimental set up [70,71]consists of a source-SR, the vacuum chamber, pumps to maintain vacuum, standard surface science instrumentation such as electron gun, evaporator, sample manipulator, leak valve, the analyzers and the electronics.

2.5.1 Vacuum equipments

The transition from the atmospheric pressure to the bottom of the UHV range (~1*10 $^{-12}$ Torr) is a dynamic range of almost 10^{15} and well beyond the capabilities of any single pump. To get to any pressure below 10^{-4} Torr requires more than one pump. So a combination of a series of pumps is used to get the desired pressure.

The Turbo Pfeiffer TPU-050(50- L/S) is backed up by Varian SD-90, a rotary vane mechanical pump. Once the pressure reaches 10^{-6} then, the Ion pump Perkin Elmer Model # 2070122 (120 L/S) brings the pressure to $9*10^{-11}$ Torr.

2.5.2 UHV chamber

A picture of the experimental set up along with the UHV chamber at beamline U16B is shown in Fig. 2.3. The main chamber is a standard ion and turbo-molecular-pumped stainless steel ultra-high vacuum chamber. It achieves vacuum ~10^{-10} Torr after overnight bake outs. It has 2 eight-inch ports oriented at 145° from one another in a plane 10° below horizontal to accommodate the two electron energy analyzers. It is also equipped with a sputter ion gun, as well as Argon gas line and Oxygen gas lines to introduce the gas into the chamber when needed. The SR enters the chamber

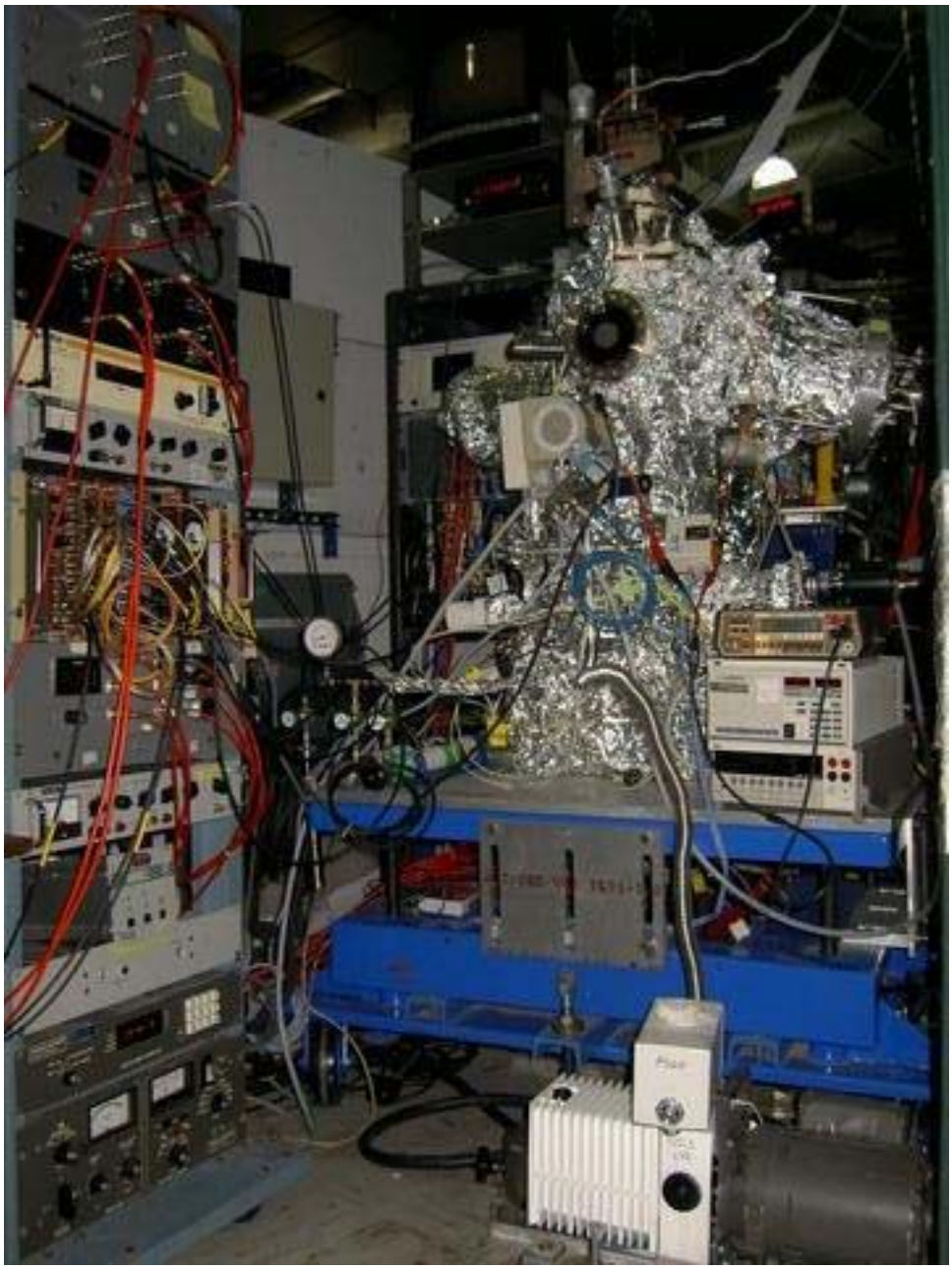

Fig. 2.3 APECS/AACS experimental setup at beam line U16B NSLS, BNL

horizontally midway between the analyzers and typically normal to the sample surface. When taking data, it is important that the sample, the SR, and the image positions of both analyzers must coincide.

The sample is mounted on a sample manipulator which has 4 degrees of freedom to move (x, y, z, and θ) and the chamber is on adjustable kinematic mounts which allow the sample, the light and the stationary analyzer focal point image to be made to coincide. The second analyzer has its own manipulator. Accurate alignment is critical, as the degree to which the two analyzers image the same volume directly determines the maximum achievable effective count rate.

The energy resolution of the analyzers depends on the size of their apertures, which can be adjusted either to the large or the small setting by the turn of a knob. For the small (large) aperture setting the analyzer energy resolution is 0.6% (1.6%) of the pass energy. In the coincidence measurements, we utilized large apertures, while for taking high statistics photoemission spectrum we maintained small apertures with less pass energy of the order of few tens of volts.

Fig. 2.4 describes the experimental set up using a block diagram and a detailed wiring of the electronics of the whole set up is shown in Fig. 2.5. The schematic diagram can be divided into 4 main components. 1) The U16B computer and the CAMAC crate and the counting electronics 2) The CMA controller, CMA's and its associated power supplies 3) Coincidence electronics and the 4) Timing electronics.

Explanation of each of the components on an individual basis is essential to get a complete understanding of all the modules in the experimental set up. Individual components are described in more detail below.

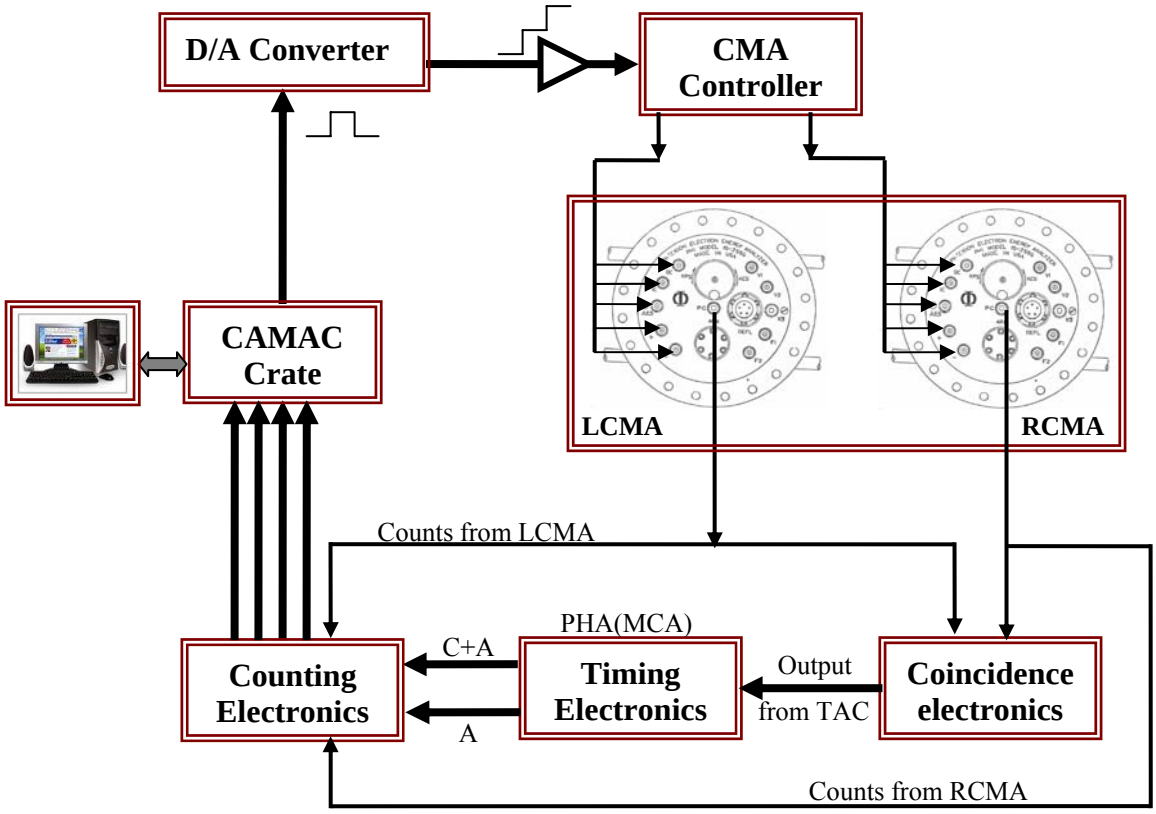

Fig. 2.4 Block diagram of the experimental setup

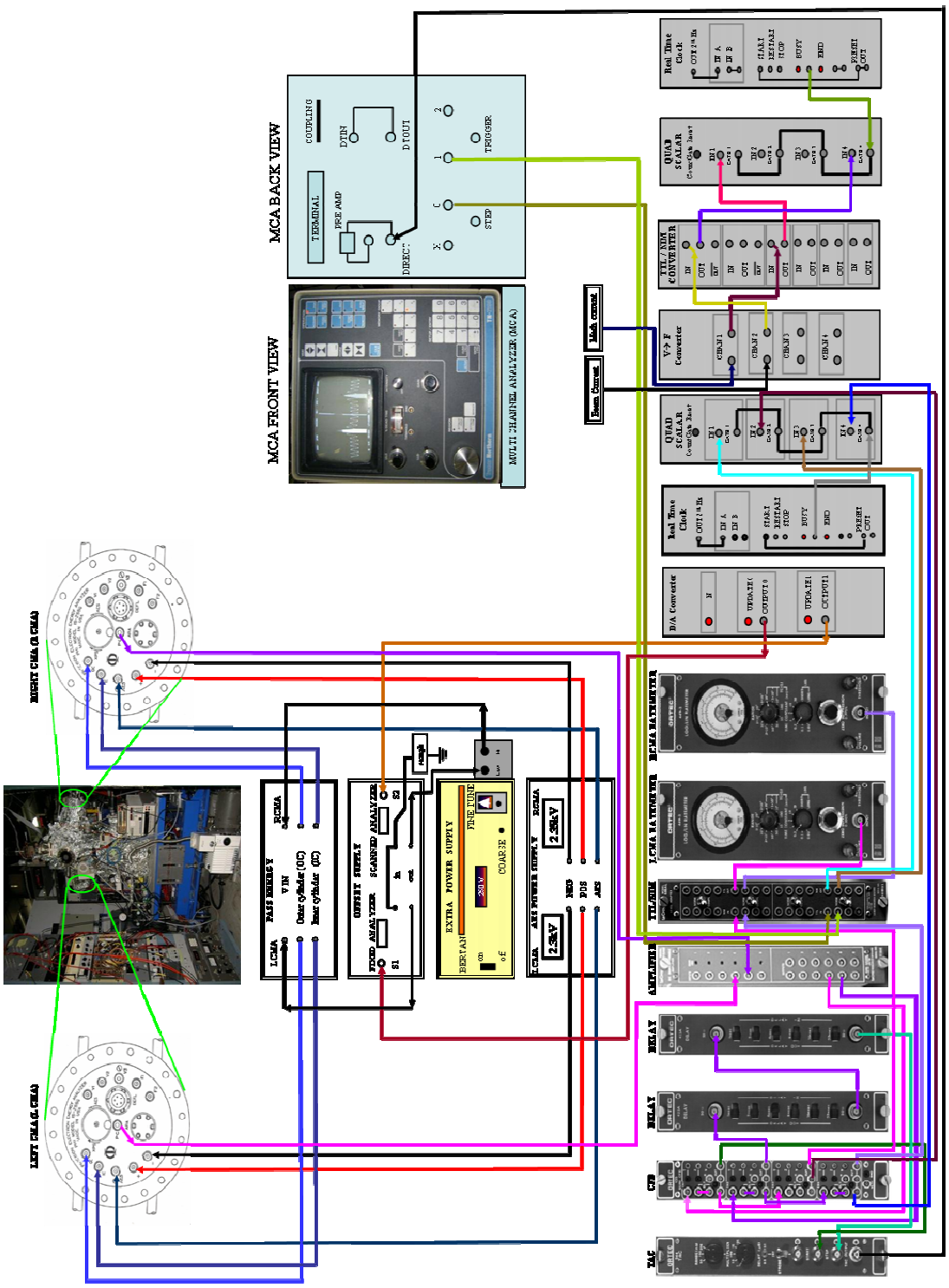

Fig. 2.5 Circuit diagram of the experimental setup

2.6 The U16B computer and the CAMAC crate components

The heart of the U16B control electronics is the CAMAC crate (Kinetic Systems model 1502 CAMAC Crate). It acts as an interface between the U16B computer and the electronics. The U16B computer is a LINUX based system, which not only talks to the CAMAC Crate, but also to the ERG Monochromator controller to set the ERG to the desired photon energy by moving the three motors.

CAMAC CRATE**:** Kinetic systems model 1502, the CAMAC crate houses two QUAD Counting Scalers, two Real time clocks, a D/A converter, NIM to TTL converter and a V-F converter. A detailed inspection of each of the modules follows.

D/A Converter**:** The computer sends commands to the D/A converter in the CAMAC crate to set the voltages on the panel named "OFFSET SUPPLY" which is the power supply for the fixed and the scanned analyzer. The D/A converter converts the 16-bit digital input number to an analog ramp signal. The analog ramp voltage is amplified and fed to a visual display unit for us to see where the starting voltages are set on the analyzers. The fixed analyzer is set to a voltage which is either the centroid of the peak of interest (or $2p_{3/2}$ or the $3p_{5/2}$ in case we have a spin orbit coupling term). The scanned analyzer is set to scan the Auger peak of interest of a given energy range which is the final state of the cascade process.

DSP RTC018 Real-Time Clock: For timing purposes, the crystal oscillator output (2^{18}Hz = $(4\mu s)^{-1}$) is connected to input A. The *preset out* output is connected to *start*. Since we are using the DSP QS-450 scaler, the *busy* output is connected to the *gate* input on the scaler module. The signals to be counted are fed into any of the four scaler

inputs. The Real-time clock accepts the dwell time specified by "TSTP" command from the computer and then it generates a precise gate signal equivalent to (1/ 2^{18} * dwelltime) s, which is used to define the counting interval of the QS-450.

Quad V-F converter**:** The Quad V-F converter (Model SLS-60.440) [72] has 4 channels comprised of 4 inputs and 4 outputs. The inputs receive voltage signals and convert them into pulse train signals with a frequency linearly proportional to the input voltage The output signals are fed into the TTL-NIM converter, which is then connected to a QUAD SCALER (Right). The Quad scalar is a Digital Signal processing Unit (DSP-QS-450-4 Channel Counter) [74]. It has 4 inputs and 4 gates coupled together. Only 2 are used. The beam current signal, which comes from a solenoid pickup in the VUV storage ring, is converted to a voltage (1V corresponds to 100mA beam current) and delivered to the beamlines. The beam current is ~1000mA at the beginning of a fill and ~400mA at the end of a fill which lasts for ~5 hrs. The voltage signal is fed to the 1st channel of the V/F converter which generates a TTL signal with frequency proportional to the beam current. The photocurrent signal generated at a metal mesh located downstream of the U16B ERG exit slit is used to monitor the beam line photon flux. This mesh current is measured by a Keithley 6485 picoammeter [73] which provides the required amplification. A proportional voltage output signal from the picoammeter is fed to the 2nd channel of the V-F converter

TTL to NIM converter**:** As the Quad Scalars which are the counting devices accepts only NIM logic signals, all the signals such as the mesh current, beam current, and (true + accidental) coincidence and accidental coincidence signals from the PHA and the

photoemission counts from each of the CMA's, which are all TTL signals, must be converted to the corresponding NIM signal levels. To accomplish this we have the TTL to NIM converter.

QUAD SCALER (Left)**:** The Quad scalar is a Digital Signal processing Unit (DSP-QS-450-4 Channel Counter) [74]. It has 4 inputs and 4 gates coupled together. The input to the gate is received from the real-time clock (DSP RTC018) which acts as a clocking timer to start and stop the counting process. The counting starts from the point when the gate receives the signal from the real time clock and then counts until a point when the clock pulse goes to zero. Thus the counts are registered for every point on the energy scale. Since the Quad scaler has no software to control the gates, all four gate input signals have been tied, using hardware cables to the real time clock. It accepts two inputs (photoemission counts) from the CFD's and 2 inputs (coincidence counts) from the MCA .

COUNTING ELECTRONICS**:** The signals from the CMA's (left, LCMA and right, RCMA) are amplified, discriminated, and converted to NIM signals and fed to the counters (QUAD SCALER) which are provided with gate signals for counting from the Real time clock. Similarly the Coincidence counts and Accidental counts from the PHA are converted to NIM signals and then fed into the Quad Scaler, gated by the same precise gate signal from the RTC018. The mesh current and the beam current are fed to another Quad scaler which in turn has another real time clock to gate the pulse counting. The detailed wiring schematic of the counting electronics is shown in Fig. 2.6.

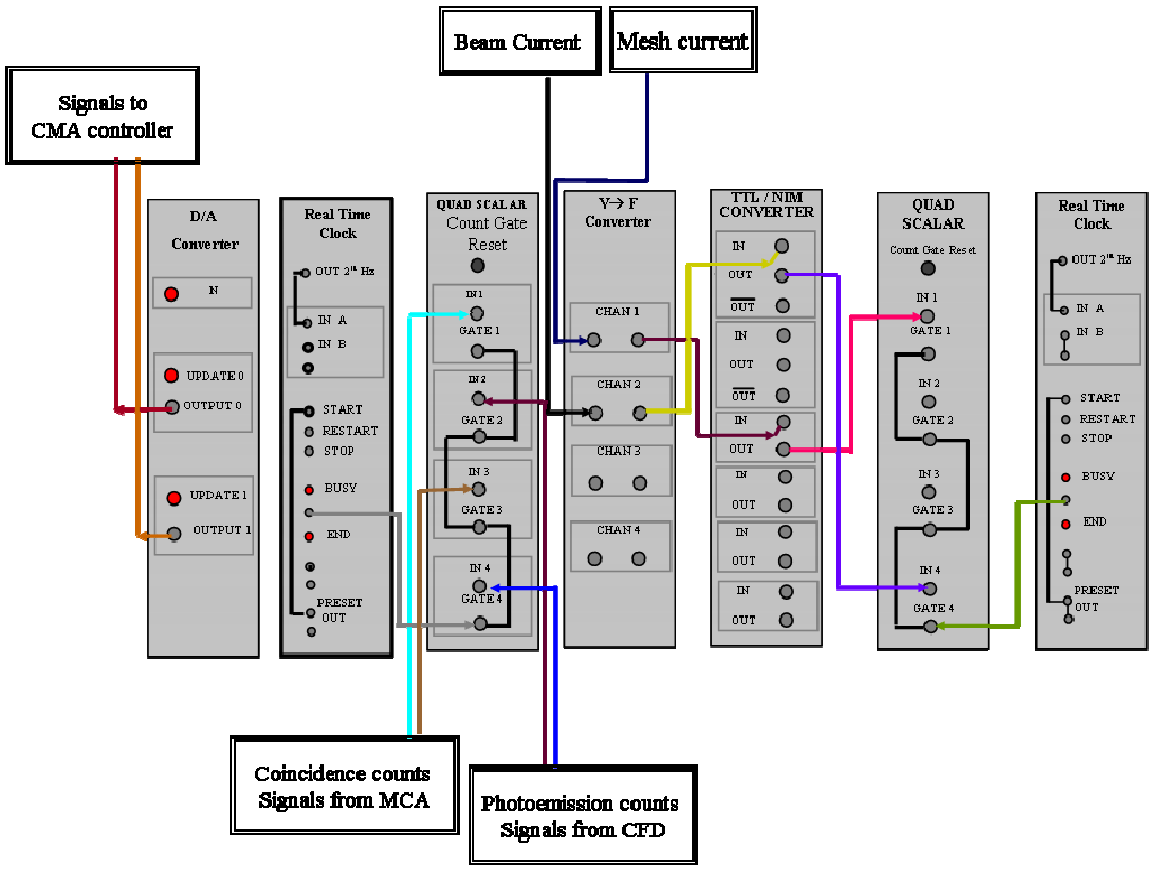

Fig. 2.6 Detailed wiring diagram of the counting electronics

2.7 CMA controller (associated power supplies) and CMA

2.7.1 CMA controller and its power supplies

The block diagram of the power supply unit to set the voltages on the IC and OC of the CMA's is given in Fig. 2.7.

OFFSET SUPPLY**:** This unit is a precision power supply with output (0-500V DC) linearly proportional to the 0-10V DC input from the CAMAC D/A module. It consist of two programmable power supplies which are used to set the retarding voltage of the CMA's that select the energy of the electrons which pass through the CMA. Front panel meters indicate the voltages at which the Right CMA (RCMA) and the Left CMA (LCMA) are set, often called the V_{ramp}

EXTRA POWER SUPPLY**:** The computer controlled power supply for the CMA can only output enough voltage to scan up to 500eV. But practically, upon which core is being excited in any given metal, the kinetic energies of interest may range above 1KeV. The energy range > 500eV is accessed by adding one or two more power supplies The Fig. 2.8 shows the detailed circuitry of the power supplies used in setting up the voltages on the CMA's and the IC and OC of the CMA.

AES POWER SUPPLY**:** The voltages to the channeltron were set at ~2.3kV and ~2.36kV for the LCMA and RCMA respectively. The AES lead is connected to the AES connectors of the CMA's which acts as the collector bias. AES power supply is shown in Fig. 2.5.

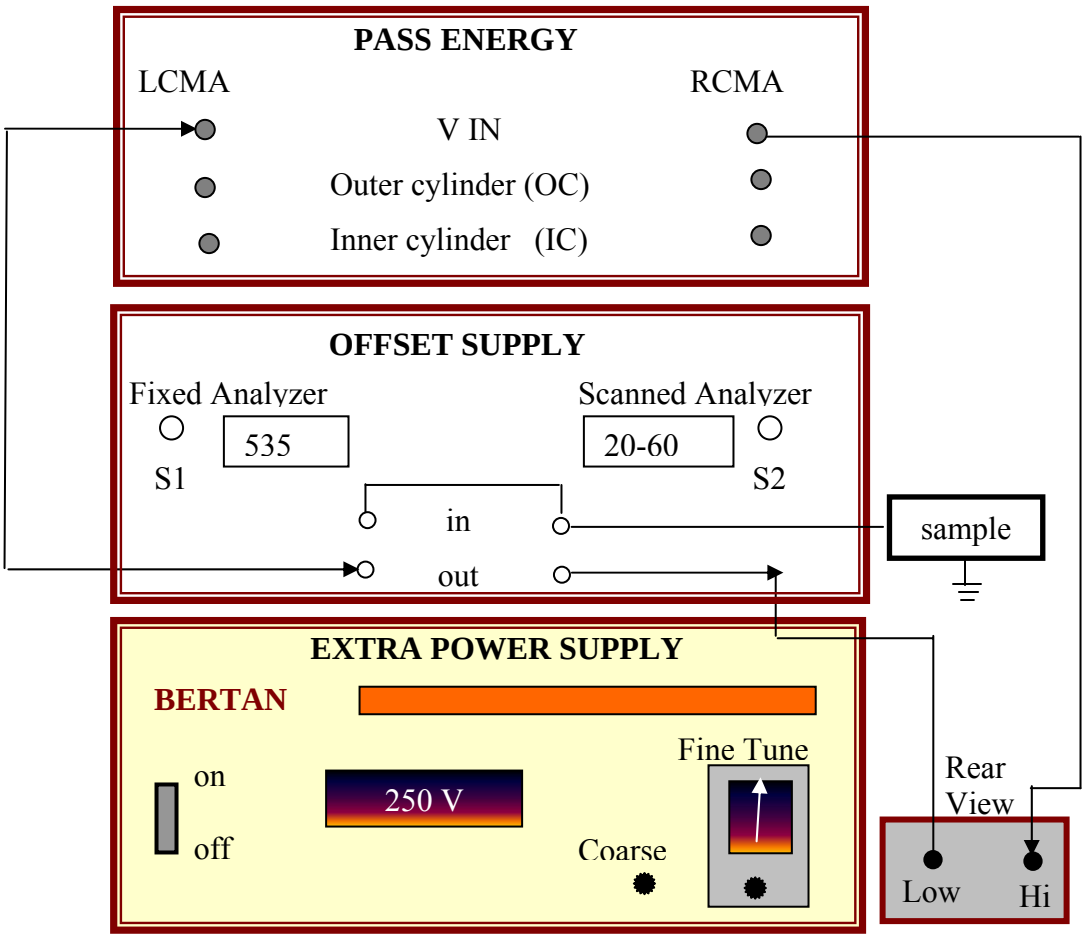

Fig. 2.7 Block diagram of power supply unit to set the voltages on the IC and OC of the CMA's

PASS ENERGY: The circuit diagram which gives the voltages for setting the pass energy on the IC and OC is given in Fig. 2.8. The CMA's IC and OC are set in such a

way that the electrons having the KE equivalent to the pass energy alone can reach the channeltron. V_{ramp} is always negative.

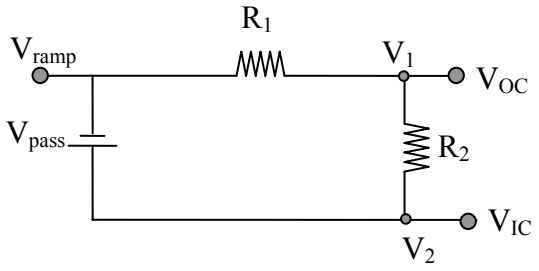

Fig. 2.8 Circuit diagram for the pass energy

$$V_1 = V_{OC} = V_{ramp} + \left(\frac{R_1}{R_1 + R_2} \right) V_{pass} \quad (1)$$

$$V_2 = V_{IC} = V_{ramp} + V_{pass} \quad (2)$$

Always inner cylinder(IC) more positive than outer cylinder (OC).

2.7.2 Cylindrical Mirror Analyzer (CMA)

Two double-pass cylindrical mirror electron energy analyzers (PHI Model 15-255G)[76], are installed in the two 8-inch ports oriented at 145° from one another in a plane 10° below the horizontal on the chamber. The CMAs consist of two concentric cylindrical metal cylinders termed the inner and outer cylinders respectively. The inner cylinder is equipped with grid covered apertures to allow electrons into and out of the region between the cylinders.

Each CMA consists of the following: 1) Channeltron, 2) Analyzer, 3) Variable Aperture, 4) Retardation Grid, 5) Internal electron gun, and 6) Deflection Plates. The aperture control and the flange-mounted terminals on the PHI model 15-255G Precision electron energy analyzer are shown in Fig. 2.9. The internal apertures may be switched from small to large apertures, by rotating the knob on the back of the flange of the CMA. The control should operate freely within its range and stop abruptly at either end. The flange to specimen distance is important for accurately measuring the kinetic energy of the electrons ejected from the specimen. The flange to specimen distance for the model that we are using is 27.94cm. Since we use photons from the NSLS storage ring, the internal electron gun is not used. The spectrometer used in the AACS experiment was previously designed by Jensen *et al.*.

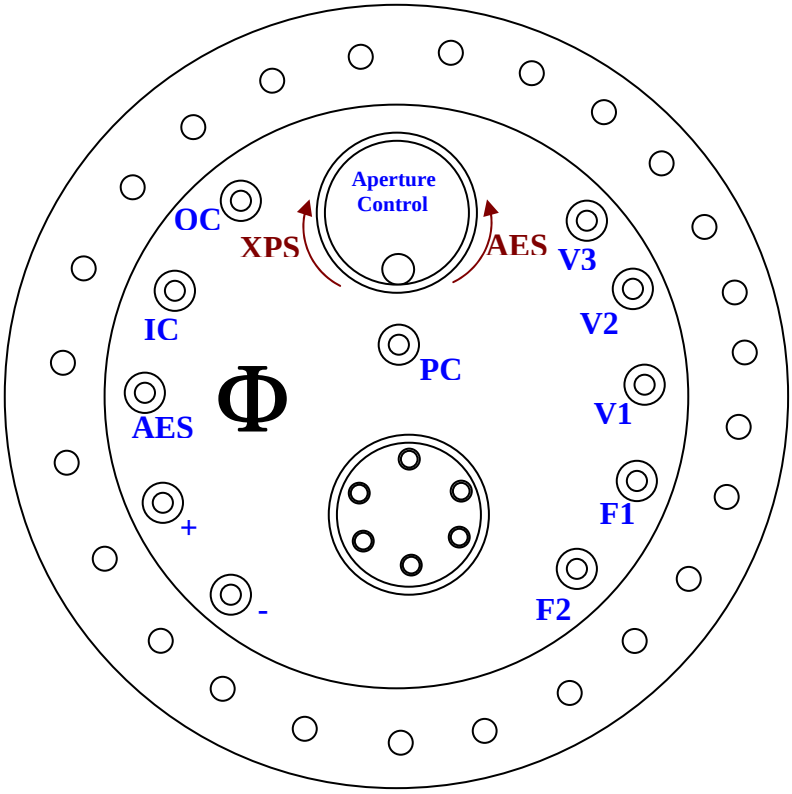

Fig. 2.9 The aperture control and the flange-mounted terminals on the PHI model 15-255G Precision electron energy analyzer

2.7.3 Working of the CMA

When the photons hit the sample, (which is grounded), electrons of different kinetic energies are knocked out. The electrons are emitted into all possible angles. The CMA's access only those electrons emitted at an angle of 48° ± 5°. The outer

cylinder is biased negatively with respect to the inner cylinder resulting in a radial electric field between the two cylinders. Electrons emerging from the sample enter the gap between the two cylinders which deflect the electrons towards the axis of the cylinder. If the electrons are traveling too fast then they will impinge on the outer cylinder, while electrons traveling too slowly will hit the inner cylinder. Hence only the electrons of a specific energy (dictated by the voltage difference between the CMA's IC (Inner Cylinder) and OC (Outer Cylinder)), called the pass energy, succeed in getting past the cylinders and into the detector. The "double pass" design incorporates a second stage of filtering, intended to reduce the spurious background signal due to secondary electrons generated within the analyzer. Negative voltage is applied to the outer cylinder to repel electrons through openings in the side of the inner cylinder forcing these electrons through the openings in the inner cylinder so that they can enter the electron multiplier. The channeltron electron multiplier amplifies (gain ~10^6 to 10^7) the electron signal to generate a measurable signal on the collector plate. To preserve the channeltron, it is important that the channeltron output current be kept below 0.1 μA. The deflection of electrons by the Outer Cylinder is dependent on both the kinetic energy of the electrons and the repelling voltage applied between the Outer cylinder and the Inner cylinder. The inner cylinder is set to attract the electrons; therefore always the OC is more negative than the IC. The greater the applied voltage, the greater the resulting electron repulsion from the OC and the great the attraction to the IC. Inside, the IC has slits to let the electrons pass through. Thus the kinetic energy of electrons passing through the analyzer can be controlled by the voltage applied to the Inner

Cylinder (IC) and Outer Cylinder (OC). Only if the kinetic energy of the emitted electrons is equal to the pass energy can those electrons reach the channeltron. The relationship of the energy of electrons selected to pass through the analyzer (pass energy-PE) and the voltage applied to terminals is $E_{pass} \sim 1.7(V_{IC}-V_{OC})$, where E_{pass} is in electron volts (eV) and $V_{cylinder}$ is in volts (V).

The hemispherical retarding grids and two cylindrical mirror analyzers help us to achieve the required energy resolution. When a larger aperture is used, a better signal-to-noise ratio can be obtained with a corresponding loss in energy resolution. Correspondingly, when a smaller aperture is used, the energy resolution is improved at the expense of the signal-to-noise ratio. The aperture diameter affects energy resolution and luminosity (the product of transmission and imaged specimen area).

2.7.4 CMA modes

This model has both retarding and non-retarding operation. We use the retarding mode. In this mode the electrons enter the two stage (double-pass) cylindrical mirror analyzer with their initial kinetic energy either accelerated or decelerated to obtain fixed pass energy. The acceleration or deceleration is achieved by the retarding grid which is connected to the OC of the CMA. The other retarding grid is connected to electrical ground which is the shield of the CMA. The energy resolution of velocity analyzers is defined as $\Delta E/PE$. With this definition, the energy resolution varies when operating in a retarding mode; and for the double-pass cylindrical mirror analyzer with a source point, $\Delta E/PE$ is about 06% for the small aperture and 1.6% for the large aperture.

2.7.5 Application of the CMA's in the coincidence measurements

For example, consider the L→MV→MVV transition. Let the LCMA be fixed at the centroid of the L→MV Peak which is around 575eV while the RCMA is scanned for the low energy Auger electrons (20-60eV). Let the pass energy of the fixed LCMA be set at 300eV and the pass energy for the scanned RCMA be set at 80eV. So the electrons having the KE of 300eV±2.4eV (1.6%(PE)=1.6%(300)=4.8) will alone pass through the slits between IC and OC to reach the channeltron. While for the RCMA the electrons having the KE of 80±0.24eV (0.6%(PE)=1.6%(80)=0.48) will alone reach the channeltron. But when the SR light impinges on the sample, electrons of different energies are knocked out of the sample.

LCMA: Consider the Fig. 2.10 which shows the configuration of the voltages applied on the IC and OC of a cylindrical mirror analyzer which has huge pass energy. The signal sent by the D/A converter from the computer is 325eV is fed to a floating power supply (negative polarity) where it picks up extra voltage of -250V which is (-325eV-250eV= -575eV; V_{extra}= -250eV) then applied to the V_{IC} through the V_{pass} which adds +300V. Now the voltage that the IC sees is (-575+300= -275eV). Now according to the ratio given in equation 1, the OC sees a voltage 176.47= (-275-OC). Therefore OC= -130V. So now if an LMV electron of KE= 575eV is knocked out of the sample, it passes through the first grid and sees a -130V and gets decelerated and when it reaches the IC it picks up -275V and now it has an energy 300V which is exactly the pass energy of the CMA. So this electron which satisfies the condition of having its KE=Pass energy will reach the channeltron.

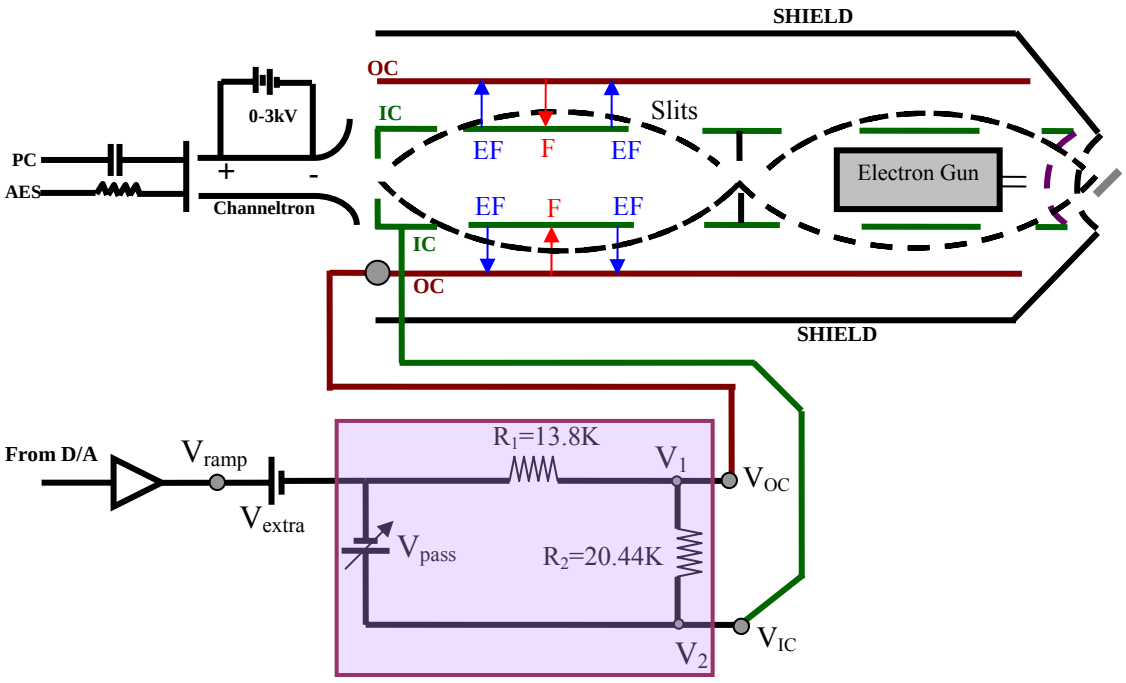

Fig. 2.10 Configuration of the voltages applied on the IC and OC of a cylindrical mirror analyzer which has pass energy (eV_{pass})

RCMA: The Fig. 2.10 shows the configuration of the voltages applied on the IC and OC of a cylindrical mirror analyzer which has low pass energy with V_{extra}=0V. The signal sent by the D/A converter is in the range of 20eV to 60eV. For example consider the energy of the electron to be 35eV. The pass energy set for the RCMA is 80eV. So the voltage on the inner cylinder is (-35+80=45V). Now the voltage on the outer cylinder is -3eV. Now when an MVV electron is knocked out of the sample as a result of the

cascade processes, it comes with a kinetic energy of 35eV. The OC is more negative than the IC. So the Electric Field (EF) points from IC to OC which in turn creates a force which bends the incoming electron inside the cylinder between IC and OC. Now when the electron sees 45eV it picks up energy and now it has 80V which is equivalent to the pass energy. So this electron will reach the channeltron.

2.8 Coincidence electronics

The main components of the coincidence electronics are presented schematically in Fig. 2.11. The output of each CMA is directed to an amplifier and a discriminator. The amplified and discriminated signal from one CMA is used as the start signal of a time-to-amplitude converter (TAC). The signal from the second CMA is also amplified, discriminated and fed through the delay circuit to bring the data into the positive time regime, and this is used as a stop signal to the TAC. The TAC outputs a signal whose amplitude is proportional to the time interval between the start and the stop pulse; this signal having a particular height is recorded as a histogram in the MCA as pulses having a particular height binned in the corresponding timing channel.

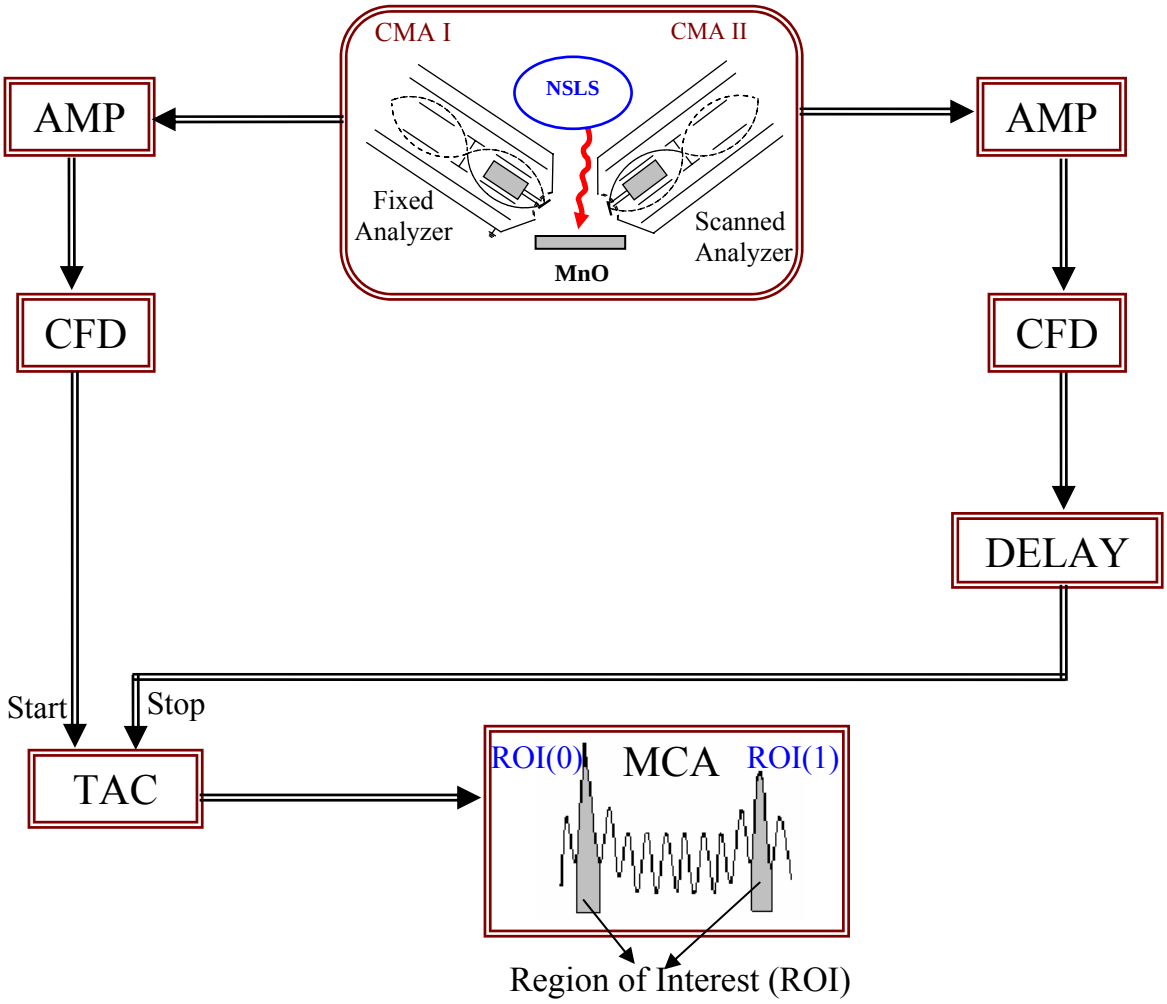

Fig. 2.11 Schematic diagram of coincidence electronics

Fig. 2.12 is a schematic illustration of the energy ranges used in the coincidence measurement of the MV→VVV and the M→VV Auger spectra. To measure the direct decay of the M→VV Auger spectra, (i.e.) M-Photoelectron in coincidence with the

corresponding low energy M→VV Auger electron, the RCMA is fixed at the peak of the M core(green peak) and the LCMA is scanned for its contribution to the M→VV peak within the energy range of 20eV to 60eV. Only the electrons created as a result of the M-Photoelectron emission will be seen in coincidence and counted as valid coincident events. So all the M→VV electrons which was preceded by the M-photoelectron emission give rise to the M→VV coincident spectra shown in green. Similarly, to measure the cascade decay of the MV→VVV Auger spectra, (i.e.) L→MV Auger electron in coincidence with the corresponding low energy MV→VVV Auger electron, the RCMA is fixed at the peak of the L→MV Auger electron peak (red peak) at around 575eV and the LCMA is scanned for its contribution to the MV→VVV peak within the energy range of 20eV to 60eV. Only the MV→VVV electrons created as a result of L→MV Auger electron emission will be seen in coincidence and counted as valid coincident events.

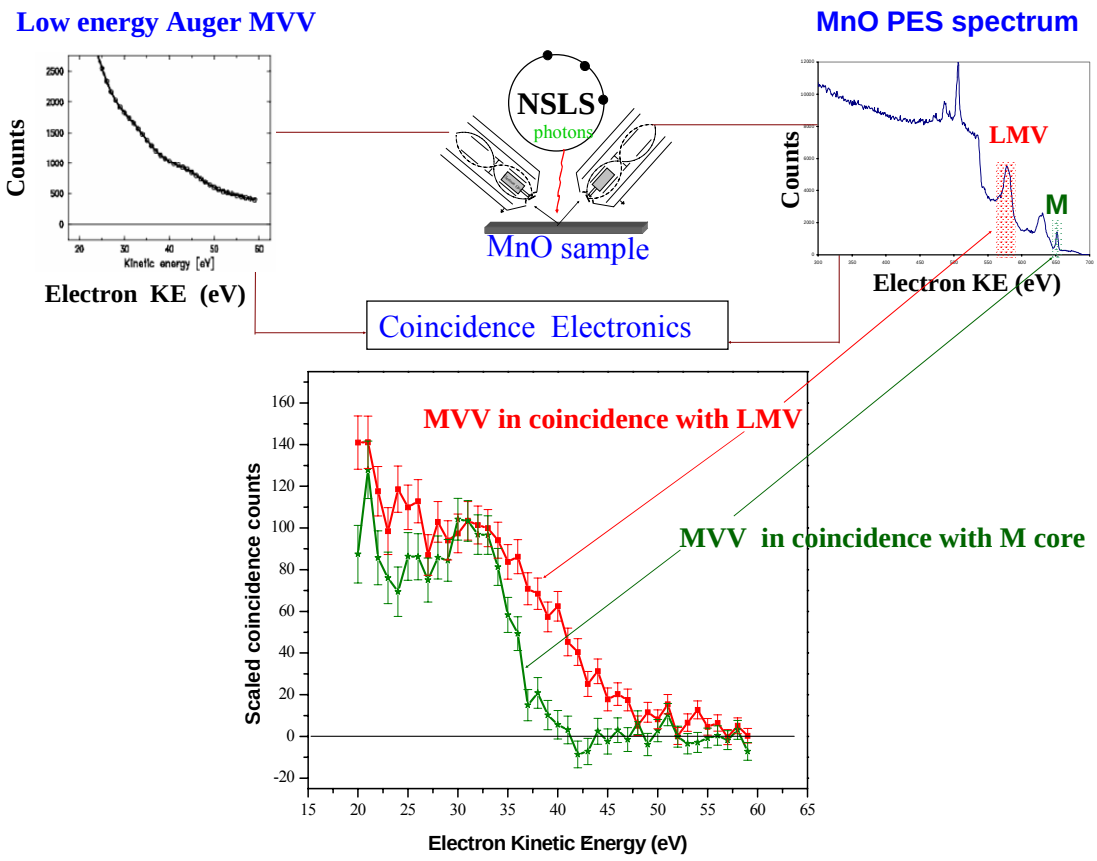

Fig. 2.12 Schematic illustrating the energy ranges used in measuring the low energy M→VV Auger spectra in coincidence with high energy Augers (for AACS- red) or cores (for APECS-green)

NIM ELECTRONICS**:** The detailed wiring diagramof the coincidence electronics at U16B is shown in Fig.2.13. The solid line signifies 50Ω coaxial cables. Individual components are described in detail below.

AMPLIFIER: The Model 612AM is a 6-channel NIM standard module, optimized for the amplification of fast photomultiplier-type signals. Each of the 6 channels of the Model 612AM, uses two internal amplifiers to achieve a variable gain up to 40X

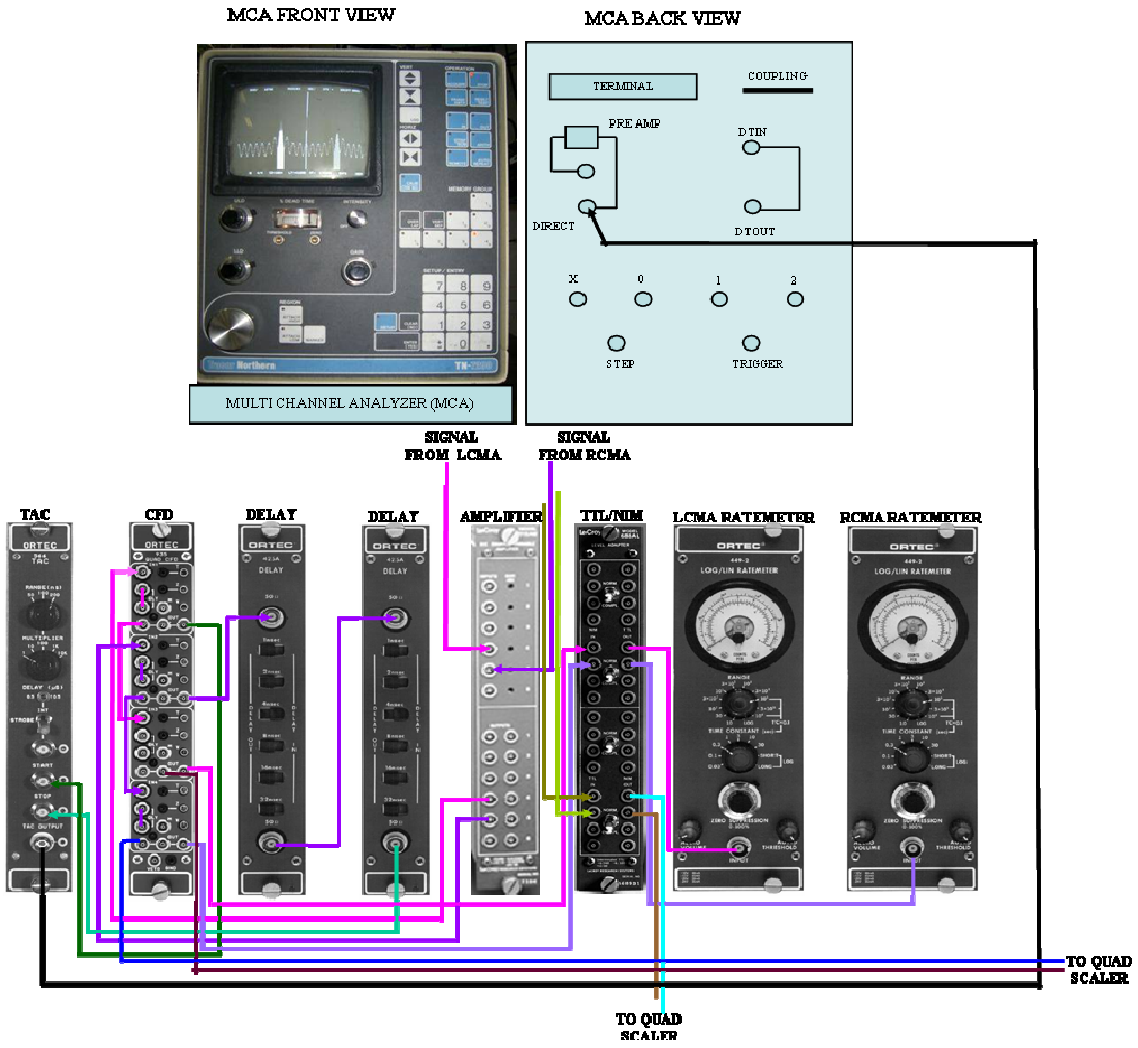

Fig. 2.13 Detailed circuitry of coincidence electronics at U16B

CONSTANT FRACTION DISCRIMINATOR (CFD): The CFD is used to discriminate against noise pulses by setting a lower level below which pulses are rejected. The constant fraction provides a way of minimizing timing "walk" due to pulse height variations. The CFD's job is to get the timing right – assume that there are a range of pulse heights, e.g. from a channeltron, but they all have nearly the same risetime (this is typical of a channeltron circuit) – a standard discriminator will "fire" at a specific voltage, which will be a varying fraction of the signal height for signals of varying height – so if they have the same risetime, the output pulses will come at different times relative, say, to the peak of the pulse, or the baseline – this time jitter is called "walk' – by firing at constant fraction, pulses of the same risetime will produce output pulses at the same time, independent of pulse height.

DELAY: The Delay Unit used here is ORTEC Model 425A Nanosecond delay unit. It provides a calibrated delay for any type of signal in 1ns in steps of 0 to 63 ns. Longer delays can be obtained by cascading several Model425A's. We require a delay of 90>Delay>500ns. We accomplish this by cascading two of the Model425A's in series. The effective delay time introduced is 126ns and on top of this delay it also includes the intrinsic delay incorporated in the cable itself (which will be of the order of 1ns/foot of cable). This unit does not require any power.

TAC :(Time to Amplitude Converter): The ORTEC Model 566 Time-to-Amplitude Converter (TAC) measures the time interval between pulses to its start and stop inputs and generates an analog output pulse proportional to the measured time. The TAC output is connected to the DC-coupled input of a multi channel analyzer. The output

from the TAC is a pulse of height proportional to the time difference between the START and the STOP pulses. The output of the CMA which collects the high energy electrons is delayed by 123ns and the intrinsic delay introduced by the cable is connected to the STOP input of the TAC and the output of the CMA which collects the low energy electrons is the START input of the TAC. A signal due to the arrival of an Auger electron and a photoelectron or another Auger electron will result in a START and STOP pulse to the TAC. Let us consider an example of the L→MM Auger decay. Then the LCMA is fixed at energy of 535eV—so it will be triggered when an L→MM auger electron hits the channeltron. The corresponding decay has 2 M→VV Auger electrons within a span of 10fs and 30fs respectively in the RCMA which will be the STOP pulse for the TAC. Then the START and STOP pulses arrive simultaneously. Since the L→MM auger electron has high KE it arrives first (say at t=0) while the M→VV Auger electron arrives at a negative time. So to push the M→VV electrons to a positive time we need to introduce a delay. So we can use the pulses due to M→VV electrons as the START pulse and the pulses due to the L→MM electrons delayed by the 123ns as the STOP pulse. The TAC gives an output pulse whose height is proportional to the time between the START and the STOP pulse. The range of the TAC is 500ns corresponds to full pulse width of 8V.

PHA:(Pulse Height Analyzer): The PHA is TRACOR NORTHERN TN7200. The number of channels in the MCA is 1024. The PHA displays the spectra of the counts in the form of a histogram as a function of time. The input to the PHA is from the TAC. The output pulse of the TAC corresponds to a range of 0-10V. The total number of

channels 1024 is divided equally among 500ns which is the input range of TN7200. Now the incoming TAC pulse in volts is converted to time ~500ns and then the time is converted into counting pulses of a particular height (based on the capacitors charging time) and based on the voltage of the pulse the counts are put in a particular channel. There are 9 memory locations which can be used when needed. The button called "ACCQUIRE" is activated when the regions of interest are set.

REGION OF INTERST**:** We have to select two regions of interest called ROI 0 and ROI 1. Region of Interest 0 (ROI 0) corresponds to counts coming from both true and the accidental coincidences. Region of Interest 1 (ROI 1) corresponds to counts from accidental events alone.

To set the ROI's **:** In order to set the ROI's, first open up the slits to get a high count rate. Then activate the "acquire" button, and select a memory group. Erase any previous data obtained in that memory location by pressing "ERASE" button. After good signal has been saved until a point where you can define the channels in each ROI's (by using the rotating knob cursor), which should be even/odd and equal in both REGIONS(~52/55 channels), reduce the slits to the original settings and then change over to a different memory location and start taking data. The ROI's once fixed is the same for all the memory groups. Check the T/A counts.

The TAC's output is a pulse of the order of 0-10V corresponding to 500ns of the MCA. But when the MCA spectrum saved shows that there are 20.7periods each of which is 1/52.887MHz long = 18.9ns. Thus, the total range of the MCA spectrum is

~400ns (391ns rounded). Therefore the actual range recorded by the MCA corresponds to 400ns as opposed to 500ns.

RATEMETER: It is an analog device which gives the number of counts that are coming from the channeltron. There are a few reasons why we use the rate meter. Primarily it is used to monitor the counts while aligning the sample with respect to the beam and the overlap cross sectional area of the two CMA's. Also it is used to find out the approximate value of the counts in the fixed spectrum on the fly. Alignment of the two spectrometers is critical, as the degree to which the two analyzers image the same volume directly determines the maximum achievable effective count rate. So the ratemeter is used to align the two analyzers to get maximum efficiency.

2.9 Timing electronics

Fig. 2.14 shows the timing spectrum recorded by the MCA. The data are reflective of the timing structure of the synchrotron bunches. There are two peaks which are significantly taller than the rest of the peaks. These peaks corresponds to events in which both the pulses are detected by the CMA's at the same time ±15ns correspond to electrons ,resulting from photons from the same synchrotron bunch. This peak is the "coincidence" peak(C). The second large peak corresponds to electrons detected in CMA as the result of the bunch after it travels 170ns once around the ring . This corresponds to the detection of electrons resulting from two different photon pulses. This peak is the "accidents" peak (A). The resulting spectrum is as a result of the timing structure created by the 7 filled buckets out of the 9 buckets in the storage ring. This main peak which is labeled $\Delta t=0s$ is the coincidence peak which contains

contributions from both true and accidental coincidences. Δt is defined as the time between the emission of electrons into one CMA and the emission of electrons into other CMA. Its width is broadened by three factors a) the timing resolution of the CMAs; b) a small contribution (~ 1 ns) from the width of the electron bunches in the storage ring, and c) some timing contributions from the electronic modules. The other peak, labeled at Δt=170ns highlighted in the Fig. 2.16, is the accidental peak, which occurs 170 ns after the coincidence peak. 170 ns correspond to the orbital period of the electrons in the storage ring. This accidental peak does not contain any true coincidence events. There are nine peaks between the coincidence peak at Δt=0ns time and the accidents peak at Δt=170 ns. These peaks have a different intensity when compared with the coincidence and the accidental peak. A detailed analysis show that the accidental intensity distribution follows a cyclical pattern (starting at the main coincidence peak) of 7/9, 6/9, 5/9, 5/9, 5/9, 5/9, 5/9, 5/9, 6/9, 7/9 and so forth as shown in Fig. 2.15.

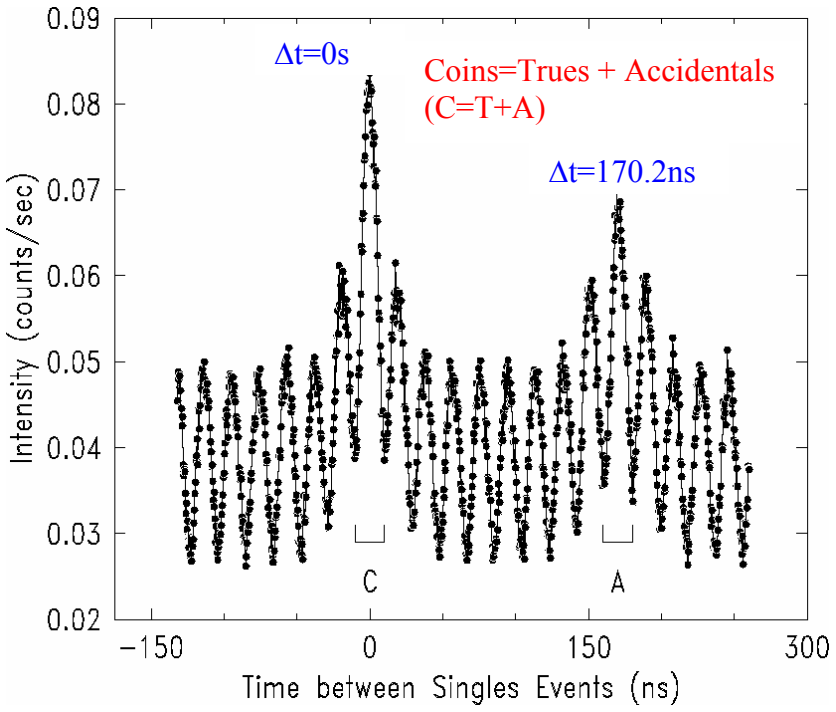

Fig. 2.14 Timing spectra of the synchrotron bunch from the storage ring in the MCA

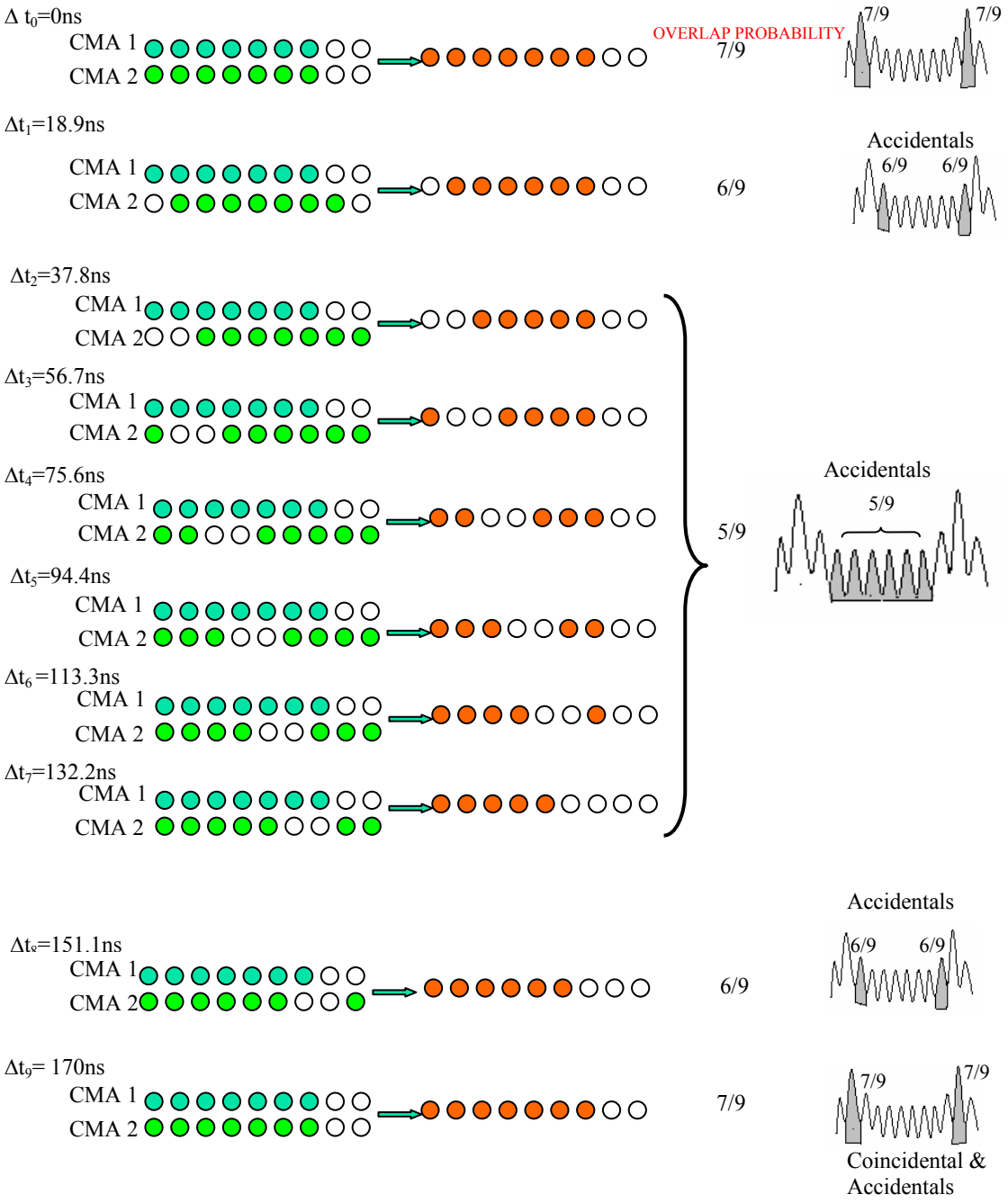

Fig. 2.15 Overlap of the empty bunches with the filled ones

2.9.1 Explanation of the Coincident and Accidental events based on the Synchrotron timing structure

The first bunch impinges on the sample and creates cascade of electrons. Let us consider one event say MV→VVV Auger cascade.(termed as LMV for simplicity) Let the CMA1 be set so that it receives the HE LMV Auger electron while the CMA2 is set to scan for the LE M→VV Auger electron.(termed as MVV here) So as the first bunch excites the sample, it not only excites one atom but also since the SR light illuminates ~1mm width of the sample it excites many other atoms which also creates LMV cascade. For simplicity, let us consider 2 atoms and extend the same argument to more than 2 atoms. When atom1 is excited it knocks off LMV1 and MVV1. When atom2 is excited it knocks off LMV2 and MVV2. (Remember LMV's come at 575eV, and MVV's comes at 32eV). Now let us see what happens when bunch1 (The electrons excited by bunch1, bunch2… bunch9 are indicated as subscripts) impinges on the sample. It excites both atom1 and atom2. Now true coincidences are the ones which came from the same atom. So when CMA1 captures $LMV1_1$ and CMA2 captures $MVV1_1$, it is a true coincident event. But when CMA1 captures $LMV1_1$ and CMA2 captures $MVV2_1$, i.e. CMA's capturing electrons excited from different atoms, even though the electrons energy are the ones which match the pass energy, these are accidental coincidences as it did not come from the same atom. But these events also lie in the same ROI 0(corresponding to $\Delta t=0$) as the true coincidences. As second possibility for the accidental coincidence is described here: It happens when the second electron bunch comes along 19.2ns after the first one hit the sample ($\Delta t=19.2$ns). At this time CMA1 sees $LMV1_2$ and CMA2 sees $MVV1_1$. This sequence is illustrated in the 2nd

set of cartoon in Fig. 2.21. Here the CMA1 sees the events from 1st electron bunch while the CMA2 sees no electrons, as there are no atoms excited by the empty bunch to create coincident events. In the same way, there are two other times when there no coincident events created. One when CMA1 sees electrons excited by the 8th bunch (none- as 8th bunch is an empty bunch) and the CMA2 sees the electrons excited by the 7th filled bunch and CMA1 sees electrons excited by 9th empty bunch, while CMA2 sees electrons excited by the 8th empty bunch. In all the above cases, there are no true coincident events created. There are 6 possibilities when there are accidental events created. The overlap probability of the filled bunches with the empty ones are given by 6/9 which occurs twice. In the same way the overlap probability of the filled bunches with the empty ones when there is only 5 times accidental events are created is given by 5/9 which occurs 6 times. Thus the events which fall in coincidence but from different bunch are termed accidental coincidence. The electron bunches follow a shift register pattern where the coincident events does not occur in synchronization. Those events are also termed as accidental coincidences. Since there are 7 out of 9 filled bunches the probability of having accidental coincidences shift happening 5 times in different combinations is illustrated in the Fig. 2.17. So there are 5 peaks having the intensity 5/9 intensity, 2 peaks having the intensity 6/9 and after 170ns 7/9 ways to achieve accidental coincidences. The accidental rate can be shown to be proportional to the product of the instantaneous counting rates in each CMA and the effective resolving time of the coincidence system. Conservation of the number of ways accidental coincidences can occur indicates that the average accidental rate should be the same for

the $\Delta t=0$ and $\Delta t=170$ns peaks. Thus the coincident events which comprises of both the trues and the accidentals and the pure accidental events are found taking advantage of the synchrotron bunch structure.

The CMAs and timing electronics allow for the simultaneous acquisition of four spectra, referred to as the singles from the two CMA's, coincidence and accidental spectra. The singles spectrum is directly obtained from the two CMAs after amplification. The singles spectrum is the wide range photoelectron spectrum obtained shown in Fig. 2.1 of the second chapter. The coincident events and the accidental events are obtained form the MCA corresponding to $\Delta t=0$s and $\Delta t=170$ns. Since the accidental counts are proportional to the product of the count rates of the two analyzers, we would expect that if one analyzer is set at a fixed energy the accidental counts are exactly similar to the singles spectrum. Therefore the high statistics singles spectrum is scaled to match the sum of the accidental spectrum and then used to subtract from the coincident counts to obtain the true counts. The time taken to obtain the spectrum is long enough to ignore the statistical noise in the singles spectrum. Thus the uncertainty in value of the accidental rate at each energy is determined by the total sum of all the coincidence counts in the spectrum. This process reduces the uncertainty in the value of the accidental rate by a factor of $(1/\sqrt{N})$ where N is the number of data points in the scans as compared to subtracting the accidental rate measured at an individual energy.

In designing an Auger electron spectrometer, one's overall goals are to generate high-energy resolution data with good statistics in as short a time as possible for a coincidence experiment. Increasing the incident flux leads to only marginal reduction

in the time required to accumulate a desired level of statistically significant data. The fact that one is no longer able to make up for lost counts with more light makes the apparatus design much more critical than in the case of non-coincidence experiments. The results are discussed in the next chapter.

CHAPTER 3

EXPERIMENTAL DATA AND ANALYSIS OF MnO

Our goal is to study the correlation between subsequently emitted Auger electrons of a solid target after photo-excitation. Such a process occurs when the final state of the Auger decay of a core level contains at least one other (shallower) core hole which itself subsequently Auger decays.

3.1 Experimental considerations

The MnO (TMO) sample [77-81] used in our AACS experiment is a single crystal specimen of ~ 5mm by 5mm area and about 3mm thick. The MnO sample was a good choice to report the first solid-state Auger- Auger Coincidence Spectroscopy studies as there are three Auger peaks associated with an initial hole in the L shell: L→MV, L→MM and L→VV and are well separated in kinetic energy of the outgoing electron. This permitted measurement of their corresponding coincidence spectra without spectral overlap and allowed us to separate out the contributions of the initial holes created in the system by the L→MV and L→MM Auger transitions.

The MnO surface was prepared by cycles of sputtering with Ar^+ bombardment at 900K (630°C) for 2 min by radiative heating from filament (filament current 5.4A) and subsequent annealing [82] until no contamination could be detected by UPS. After cleaning the sample, a wide range energy photoelectron spectrum was acquired at

incident photon energy of 660eV, 690eV and 740eV. This spectrum contains photoelectron, both core and valence, and Auger electron (Mn $L_{2,3}M_{2,3}M_{2,3}$, $L_{2,3}M_{2,3}V$, $L_{2,3}VV$, and $M_{2,3}VV$(Lower figure) and O KVV) peaks as depicted in the Fig. 3.1. At low kinetic energies, the MVV Auger peak is seen as a tiny bump around 32eV which is buried deep under the spectrum dominated by the rising (as the KE decreases) background of secondary electrons which are inelastically scattered as shown in Fig. 3.2. The comparison of the photoelectron spectrum (at low electron kinetic energies) shown in Fig. 3.3 clearly shows the shift in the Mn 3p core level peak as a function of incident photon energy. The comparison of the photoelectron spectrum (at high electron kinetic energies) shown in Fig. 3.4 shows that the Auger peaks are independent of the incident photon energy, (i.e.) the various Auger peaks of Mn and the Oxygen Auger peak remains fixed but the Mn $M_{2,3}$ core peak shifts with respect to the photon energy. Fig. 3.5 shows a comparison of photoelectron spectrum of MnO acquired at the threshold of Mn L_{II} shell and a spectrum obtained at photon energy well above threshold. It illustrates the increase in the intensity of LXX Augers when the atom is excited at the Mn L_2 threshold while the intensity of the Oxygen Auger is considerably decreased.

3.1.1 AACS experiment

All AACS measurements were carried out at beamline at U16B at the National Synchrotron Light Source at Brookhaven National Lab. Coincidence measurements were acquired with the specialized spectrometer described in the previous chapter. Briefly, the device consists of two cylindrical mirror analyzers (CMAs) [83], associated

computer controlled power supplies together with timing electronics is used to detect the time interval between the detection of electrons in the two CMAs. Three spectra were simultaneously acquired in order to produce a true coincidence spectrum: a singles spectrum, a total coincidence spectrum(C+A), and an accidental coincidence spectrum (A). Subtracting the appropriate accidental contribution from the total coincidence spectrum generated the true coincidence spectrum (C) [84-88].

In the coincidence measurements, the CMA, which scanned through the spectrum of interest, was operated with large apertures (1.6% of the PE) with a pass energy of 80eV. The CMA which is fixed at the particular peak of interest was also operated with large apertures (1.6% of the PE). The PE was usually set to be of the order of a few hundred eV. The increased acceptance of the CMA's was necessary in order to maintain the true coincidence rate at an acceptable level. Otherwise, while the true to accident ratio at the lower count rate would be quite high, the acquisition rate for true coincidences would drop to unreasonably low levels.

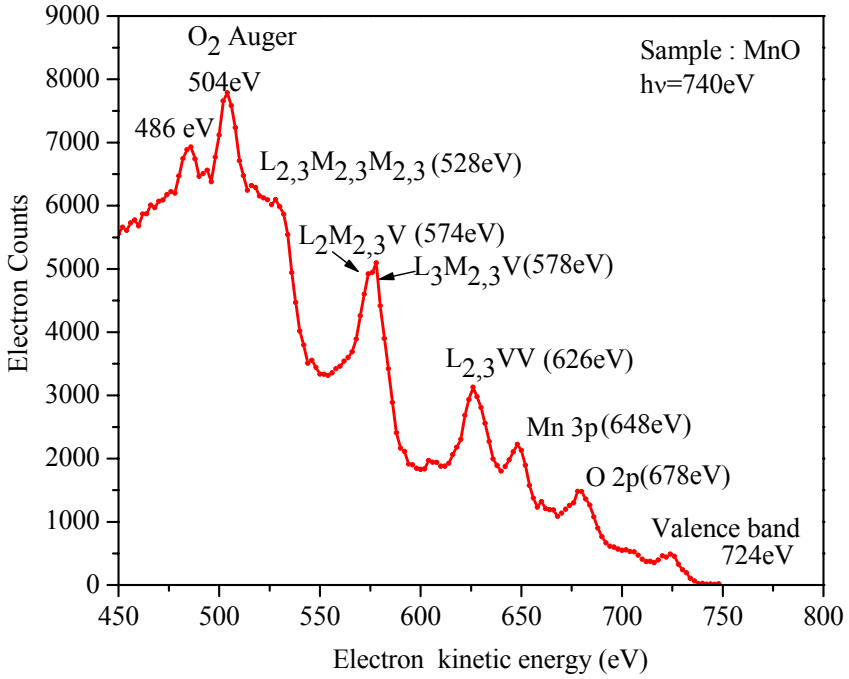

Fig. 3.1 A wide range energy photoelectron spectrum acquired at incident photon energy of 740eV

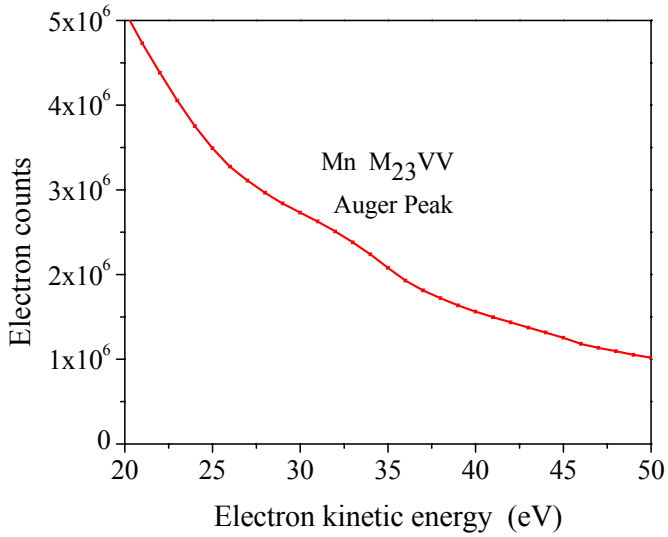

Fig. 3.2 Photoelectron spectrum of MnO acquired at incident photon energy of 740eV

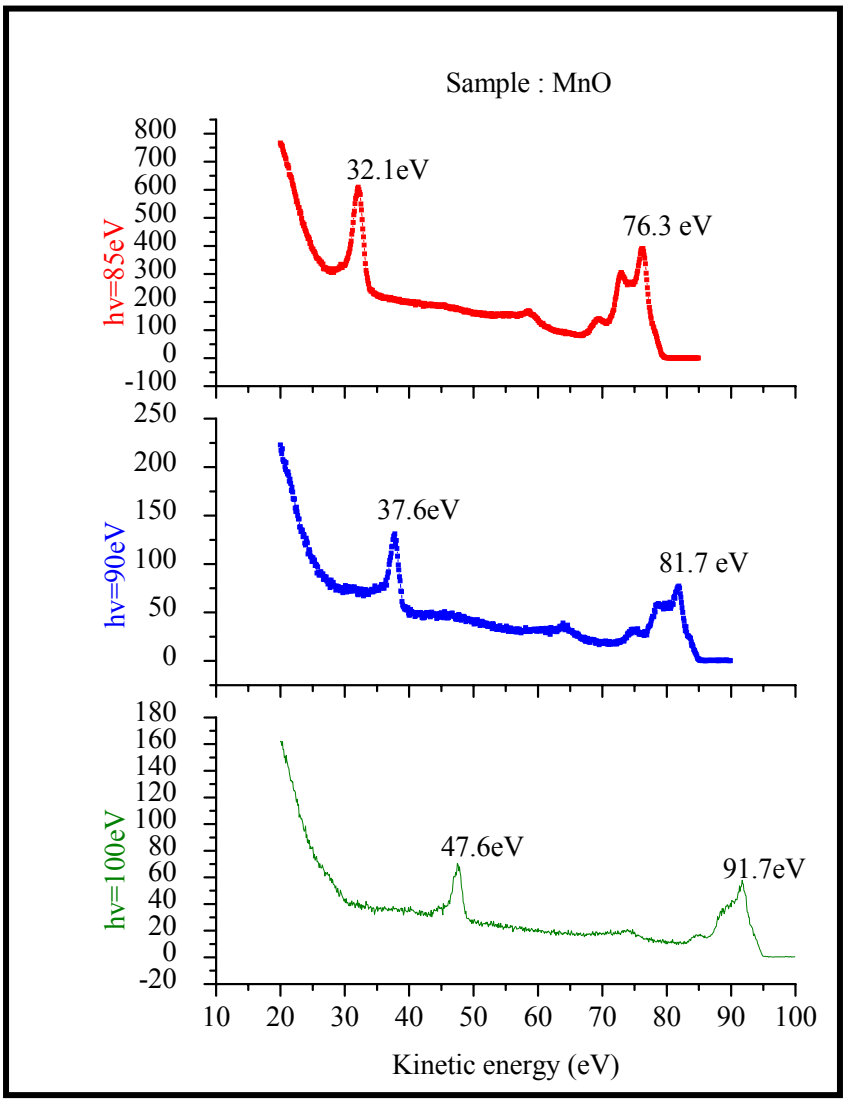

Fig. 3.3 Comparison of photoelectron spectrum of MnO acquired at different incident photon energies to illustrate the Mn 3p core level shift with respect to the incident photon energy

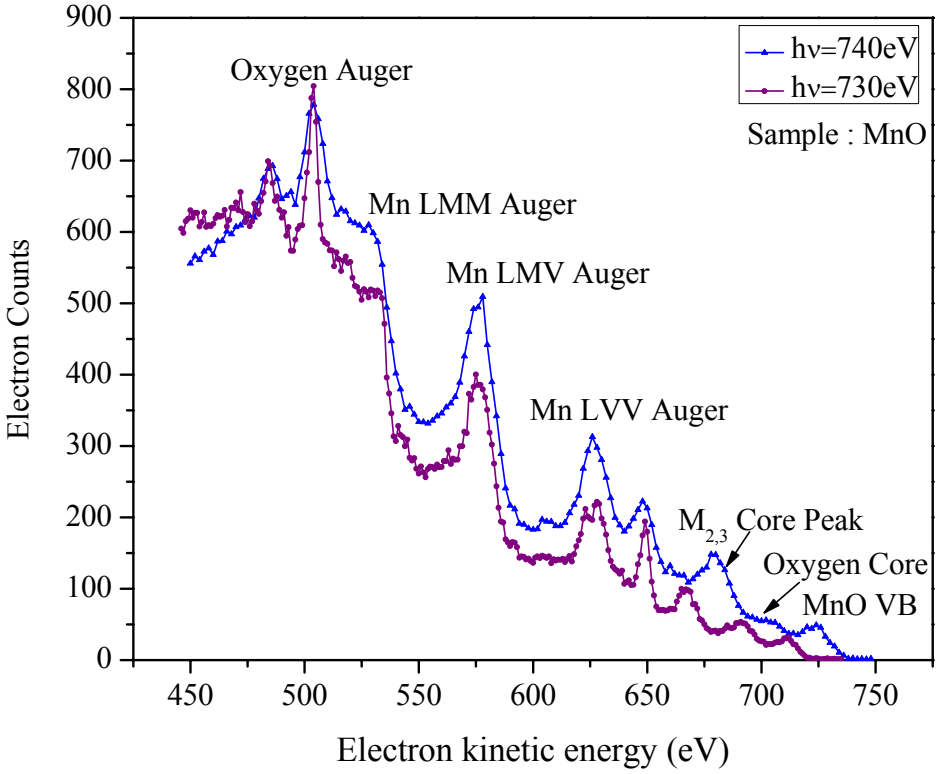

Fig. 3.4 A comparison of high kinetic energy photoelectron spectrum of MnO acquired at different incident photon energies to illustrate the fixed position of the Auger peaks and shifted core level peaks with respect to the incident photon energy

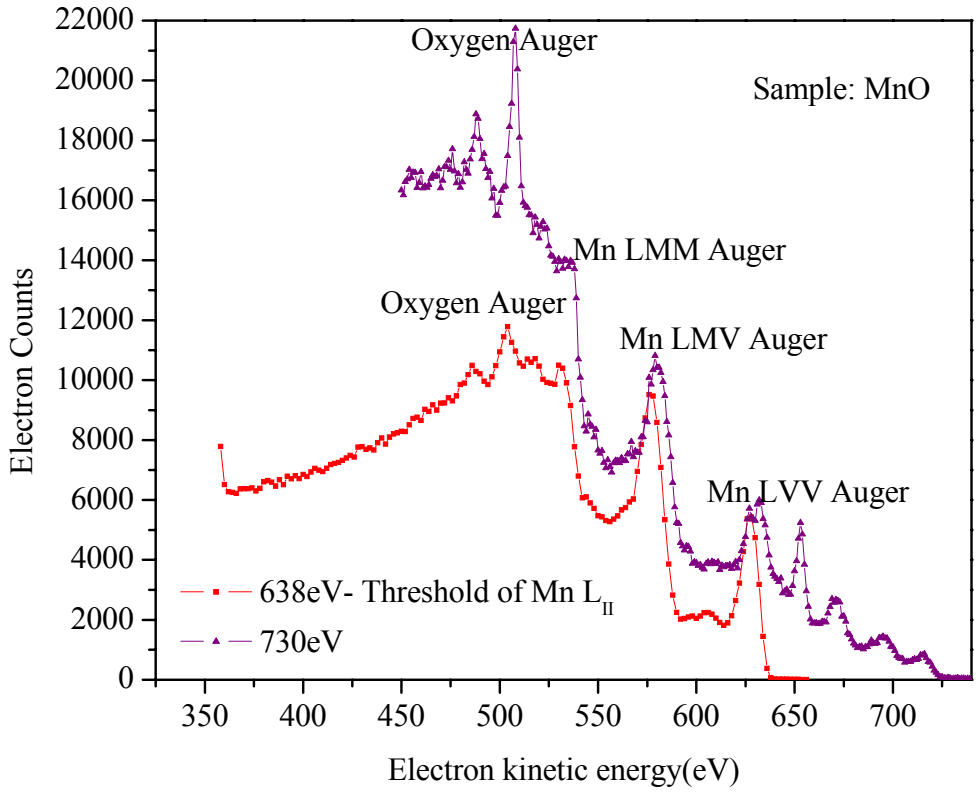

Fig. 3.5 A comparison of photoelectron spectrum of MnO acquired at the threshold of the Mn L_{II} and at a photon energy well above threshold. Note the increase in the intensity of Mn LXX Augers at the Mn L_{II} threshold relative to the Oxygen Auger

3.2 The spectra of the $M_{2,3}$→VV Auger electrons taken in time coincidence with the $L_{2,3}$→XX Auger electrons or the photoelectrons

3.2.1 Measurement of the spectra of electrons from $M_{2,3}$→VV Augers in time coincidence with electrons from $L_{2,3}$→$M_{2,3}$V peak

In an Auger process, shown schematically in the Fig.1.3, the ionic system relaxes when an electron from the M level fills the core hole created in the L shell during the photo-excitation process. The $L_{2,3}$→$M_{2,3}$V Auger electron, leaves the solid in the subsequent decay process. In the decay of the remaining M core hole, (i.e) $M_{2,3}$ V→VVV, the two electronic levels involved in the de-excitation of the initial $M_{2,3}$ core hole are in the valence band of the solid and so the $M_{2,3}$V→VVV Auger final state contains three holes in the valence band.

To measure the individual contributions from subsequent steps of the decay process, the photon energy was first selected to be 740eV which is ~90eV more than enough energy to knock out the electron from the L_{II} shell, which has a binding energy of 649.9eV. The spectrum in Fig. 3.6 shows a coincidence peak between the Mn $L_{2,3}$→$M_{2,3}$V and $M_{2,3}$ →VV Auger Spectra. The left-hand CMA was fixed at the $L_{2,3}$ →$M_{2,3}$V Auger Peak at 575.5eV and the right hand CMA was scanned for the $M_{2,3}$ →VV Auger peak between 20 and 60eV. In the light of the long collection time required for acquiring the coincidence data, partial results were saved every ~30min (40 sweeps) so that we do not lose all the data collected in case of an equipment failure. The total spectra were obtained by summing all the partial results. The intensities (or counts) of all spectra in these figures are referenced to the same zero. In the coincidence Auger spectra, the blue curve in each spectrum is the corresponding singles spectrum

that was obtained at the same time as the coincidence spectrum which has been scaled. The red line with dots and error bars represents the experimental data. The purpose of the scaling is twofold, one is to provide an estimate of the inelastic background which is not removed by coincidence and two, to illustrate that the contribution of the coincidence which peaks right above $M_{2,3}VV$ singles. The coincidence data has been scaled to the incoming photon flux. Several important observations are immediately apparent. Firstly, the background of in elastically scattered electrons at high kinetic energies, i.e. above the range of allowed Auger electron energies, is eliminated from the coincidence spectrum. Second, the individual contributions from the steps following the Auger cascade can be obtained through Auger-Auger coincidence. Third, is enhanced surface sensitivity.

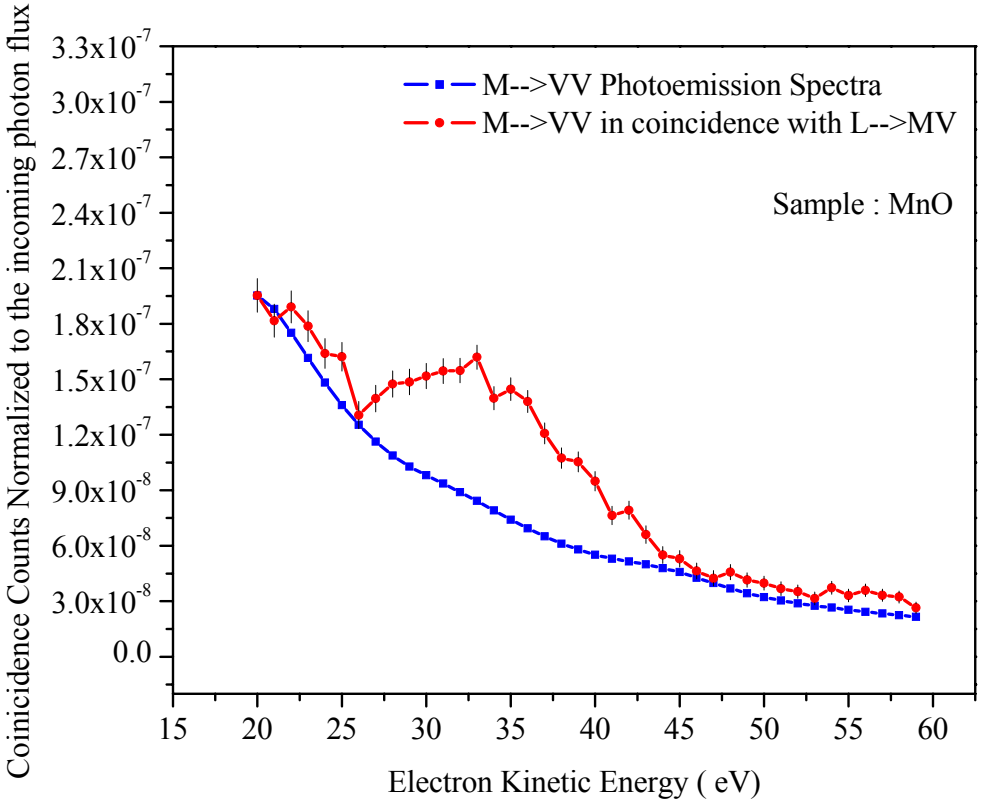

Fig. 3.6 Spectra of Mn $M_{2,3}$→VV Augers measured in time coincidence with the detection of electrons at 575.5eV (the peak of the Mn $L_{2,3}$→$M_{2,3}$V Auger transition) at a photon energy of 740eV

3.2.2 Measurement of the spectra of electrons from [$M_{2,3}M_{2,3}$→ $M_{2,3}VV$ and $M_{2,3}VV$→$VVVV$] Augers in time coincidence with electrons from $L_{2,3}$→$M_{2,3}M_{2,3}$ peak

In an Auger process, shown schematically in the following Fig.1.4, a hole created in the L shell due to the photoemission process, is filled from an electron in the M shell. An Auger electron is then ejected from the M shell of the solid to conserve energy, leaving the atom with 2 holes in the M shell. Two subsequent cascade steps occur. In the first cascade step, $M_{2,3}$ $M_{2,3}$→ $M_{2,3}VV$ there are two holes in the valence band and one hole in the M level. In the second cascade step, the atom has four holes in the valence band in the final state. This transition is labeled as $M_{2,3}VV$ → VVVV.

To measure the individual contributions from subsequent steps of the decay process, the MnO sample was excited at 740eV. The spectrum in Fig.3.7 shows coincidence peak between the $L_{2,3}$ → $M_{2,3}M_{2,3}$ and $M_{2,3}$ →VV Auger Spectra. The left-hand CMA was fixed at the $L_{2,3}$ →$M_{2,3}M_{2,3}$ Auger Peak 532eV and the right hand CMA was scanned for the $M_{2,3}$ $M_{2,3}$→$M_{2,3}VV$ and $M_{2,3}VV$→VVVV Auger peak between 20 and 60eV.

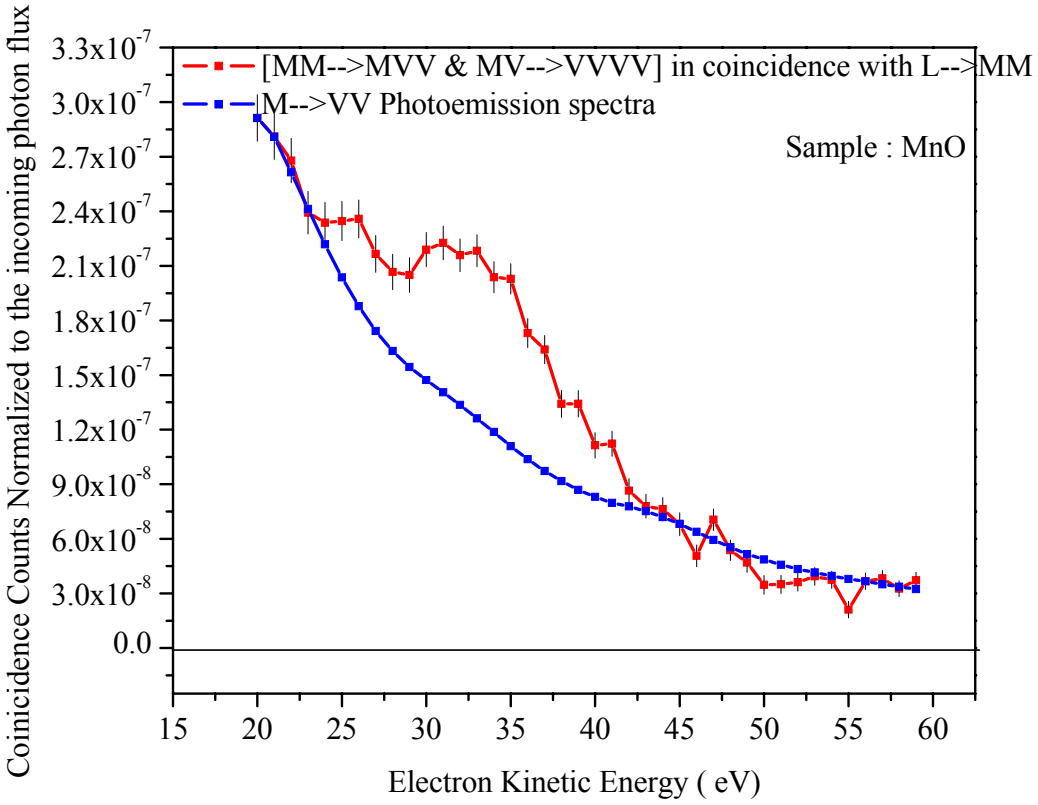

Fig. 3.7 Spectra of Mn $M_{2,3}M_{2,3}$→$M_{2,3}VV$ and $M_{2,3}VV$→VVVV Augers measured in time coincidence with the detection of electrons at 535 eV (the peak of the Mn $L_{2,3}$→$M_{2,3}M_{2,3}$ Auger transition) at a photon energy of 740eV

3.2.3 Measurement of the spectra of electrons from $M_{2,3}$→VV Augers in time coincidence with electrons from $L_{2,3}$→VV peak

It is known from the wide range singles spectrum that the $L_{2,3}$→VV Auger spectrum has a peak at 626eV. In a similar way as we did for the previous $L_{2,3}$ →$M_{2,3}$V and $L_{2,3}$ → $M_{2,3}M_{2,3}$ scans, in the $L_{2,3}$ →VV process, the spectrum in Fig. 3.8 shows no coincidence peak between the $L_{2,3}$ → VV and $M_{2,3}$ →VV Auger Spectra. The Left-hand CMA was fixed at the $L_{2,3}$→VV Auger Peak 626eV and the right hand CMA was scanned for the $M_{2,3}$→VV Auger peak between 20 and 60eV. It can be clearly seen from the spectrum that there are many fewer coincidence counts as expected since there is no participation of $M_{2,3}$ electrons in the process of filling the hole created by the emission of $L_{2,3}$ photoelectron. Upon further thought, it was realized that at the photon energy used the 2p(L_2) photoemission peak was at an energy of ~78eV, consequently there were true coincidences between the inelastic tail of the 2p photoemission peak. This undesired background (present also in the MV→VVV and MM→MVV, MVV→VVVV spectra) was eliminated by moving the photon energy to 660eV to move the 2p photoelectron peak down to ~10.eV so that its inelastic tail were below the spectra of interest.

Fig. 3.9 shows the comparison of the coincidence spectra obtained at photon energy of 740eV, which is well above the threshold of Mn-L_2 level. It is clear that these spectra contains a background which are true coincidences from the tail of the $2p_{1/2}$ and $2p_{3/2}$ photoelectrons with the $L_{2,3}$→$M_{2,3}$V, $L_{2,3}$ →$M_{2,3}M_{2,3}$ and $L_{2,3}$ →VV Auger peaks.

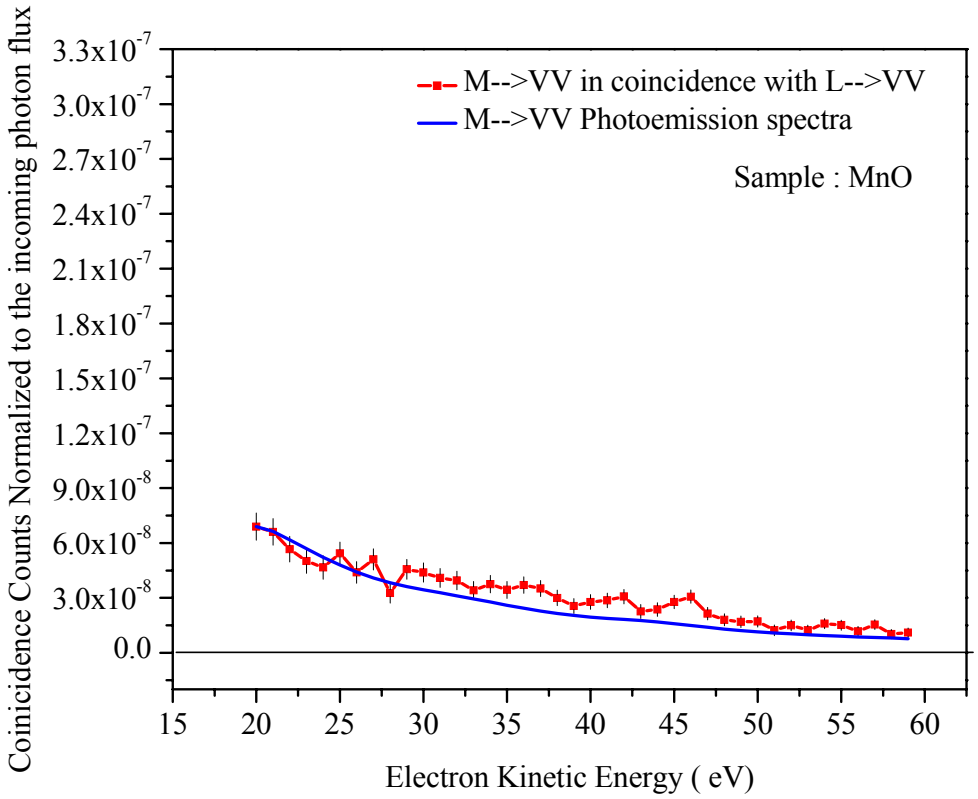

Fig. 3.8 Spectra of Mn $M_{2,3}$→VV Augers measured in time coincidence with the detection of electrons at 626eV (the peak of the Mn $L_{2,3}$→VV Auger transition) at a photon energy of 740eV

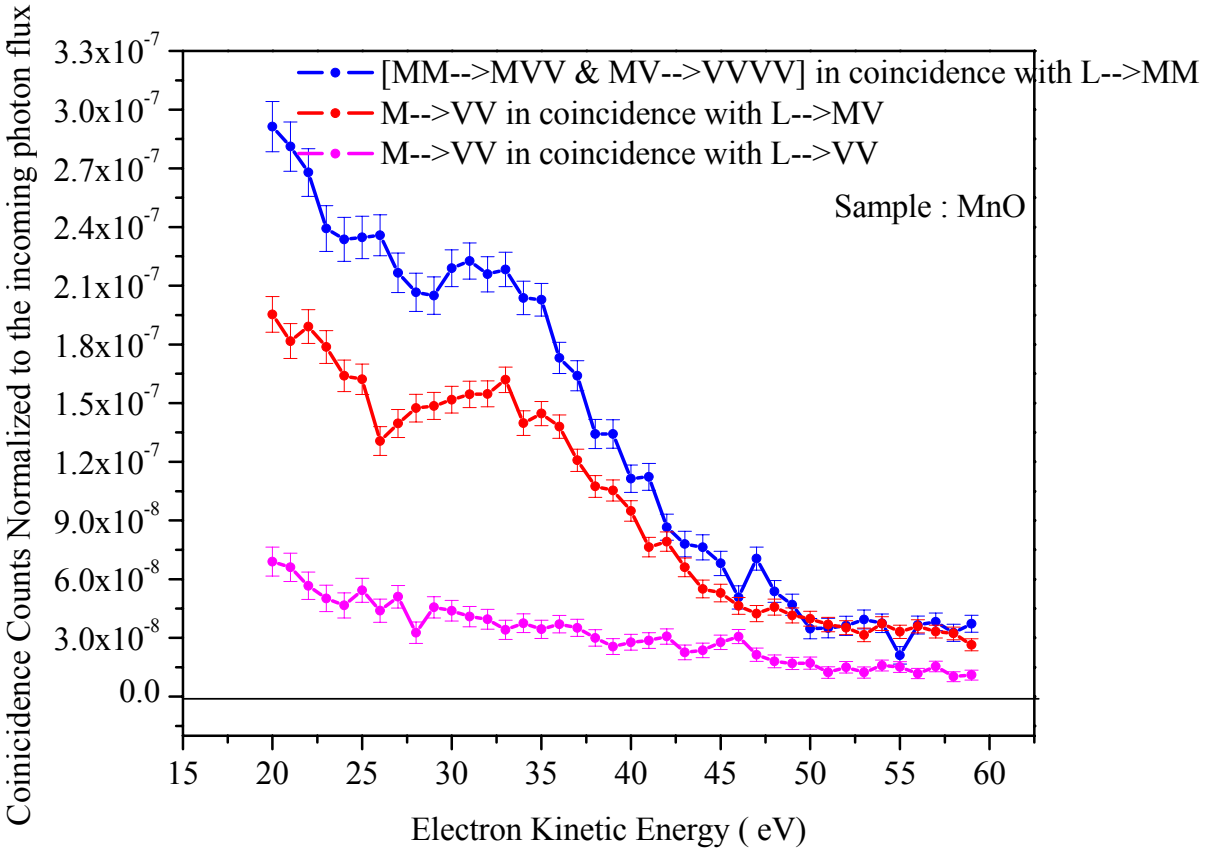

Fig. 3.9 Comparison of the spectra of Mn $M_{2,3}$→VV Augers from MnO measured in time coincidence with the electrons from the peak of Mn $L_{2,3}$→$M_{2,3}$V Auger, Mn $L_{2,3}$→$M_{2,3}M_{2,3}$ Auger, and Mn $L_{2,3}$→VV Auger transitions at photon energy of 740eV

3.3 The spectra of the electrons emitted from $L_{2,3}$→MM, $L_{2,3}$→MV, and $L_{2,3}$ →VV Auger transitions detected in time coincidence with the electrons emitted from the $M_{2,3}$→VV Auger peak

In the so called "Reverse Scan" we keep one analyzer at peak fixed at 33eV the approximate peak of electrons emitted in the M→VV, MV→VVV, MM→MVV, MVV→VVVV transitions. The "scanned" analyzer was set at a pass energy of 80eV and the "fixed" analyzer was fixed at a pass energy of 300eV we scanned for the

1) The range 557eV to 600eV was scanned to include the peak of $L_{2,3}$ →$M_{2,3}$V whose centre lies at 575.5eV. 2) The energy range 500eV to 557eV was scanned to include the peak of $L_{2,3}$→ $M_{2,3}M_{2,3}$ whose centre lies at 532eV. 3) The energy range 600eV to 643eV was scanned to include the peak of $L_{2,3}$→VV whose centre lies at 626eV. The coincidence spectrum for $L_{2,3}$ →$M_{2,3}$V, $L_{2,3}$ →$M_{2,3}M_{2,3}$ and $L_{2,3}$ →VV are shown in the Fig. 3.10, Fig. 3.11, Fig. 3.12 respectively.

Two observations are made. One, the substantial fraction of the inelastic tail observed in the singles spectrum (blue) is eliminated in the coincidence spectrum. Two, we were able to see the coincidence spectrum for $L_{2,3}$→$M_{2,3}$V and the $L_{2,3}$→$M_{2,3}M_{2,3}$ peaks in coincidence with the $M_{2,3}$VV Auger peaks exactly at the place where the singles are observed. Even though the Oxygen Auger(504eV) lies in the scanned range of the $L_{2,3}$ →$M_{2,3}M_{2,3}$ spectra, it does not appear in the coincidence spectra, as the Oxygen Auger does not contribute to the $M_{2,3}$→VV Augers. Since there should be no coincidence between the $L_{2,3}$ →VV and the $M_{2,3}$→VV peaks (as there is no $M_{2,3}$ holes created in the $L_{2,3}$→VV transition), this spectrum also shows almost no coincidence counts as may be seen in the Fig. 3.12. Except for the existence of low-energy tail in

both the coincidence and singles spectra, which can be eliminated considerably by exciting MnO at the $L_{2,3}$ Threshold, this "Reverse Scan" provides a stringent test for the Auger–Auger coincidence in solids.

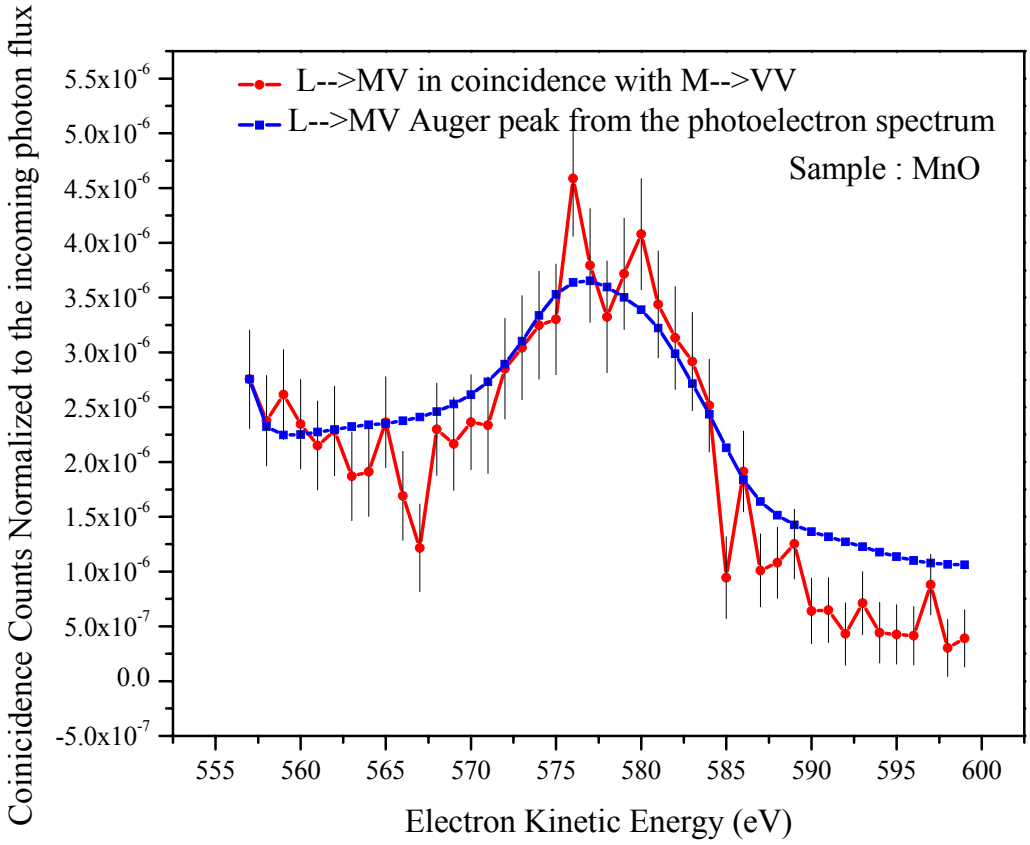

Fig. 3.10 Spectra of electrons emitted in the range of the Mn $L_{2,3}$→$M_{2,3}$V Auger transition (557-600eV) measured in time coincidence with the electrons emitted at 33eV (peak of the Mn $M_{2,3}$→VV Auger transition)

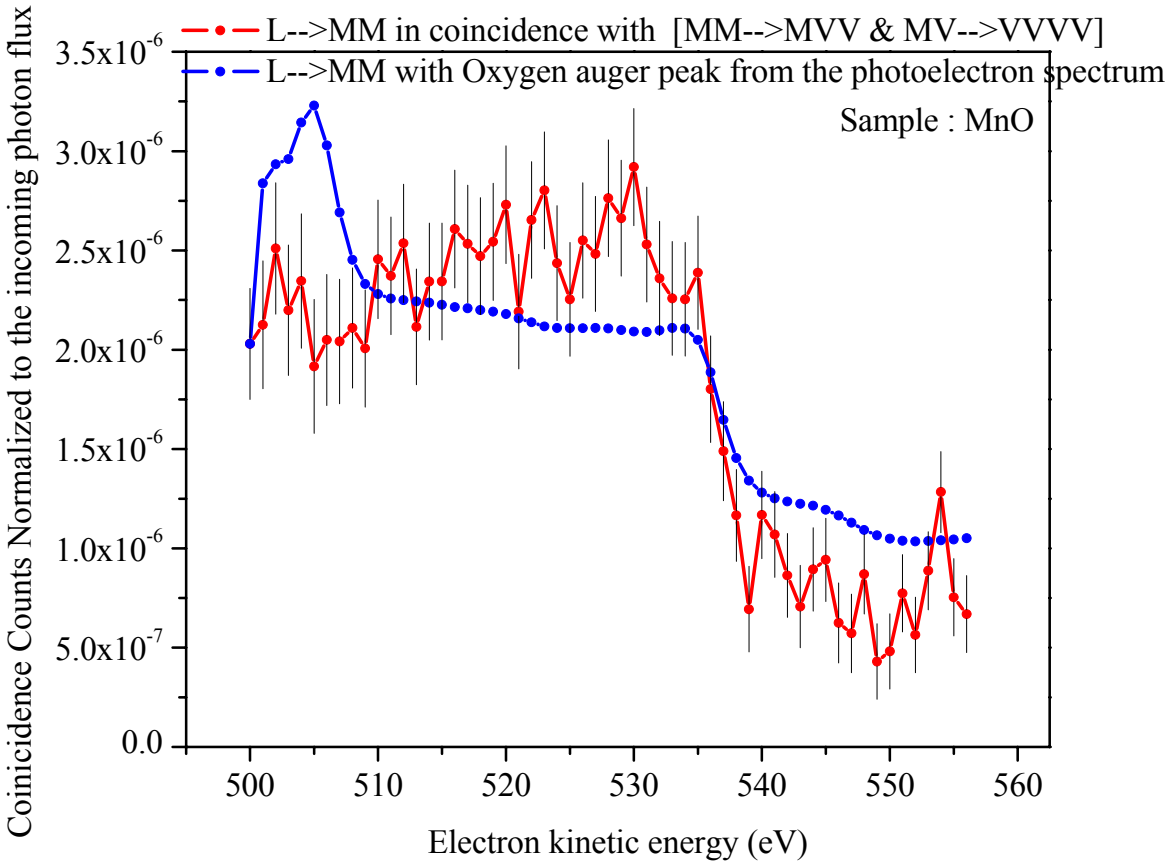

Fig. 3.11 Spectra of electrons emitted in the range of the Mn $L_{2,3}$→$M_{2,3}M_{2,3}$ Auger transition (495eV-560eV) measured in time coincidence with the electrons emitted at 33eV (peak of the Mn $M_{2,3}$→VV Auger transition)

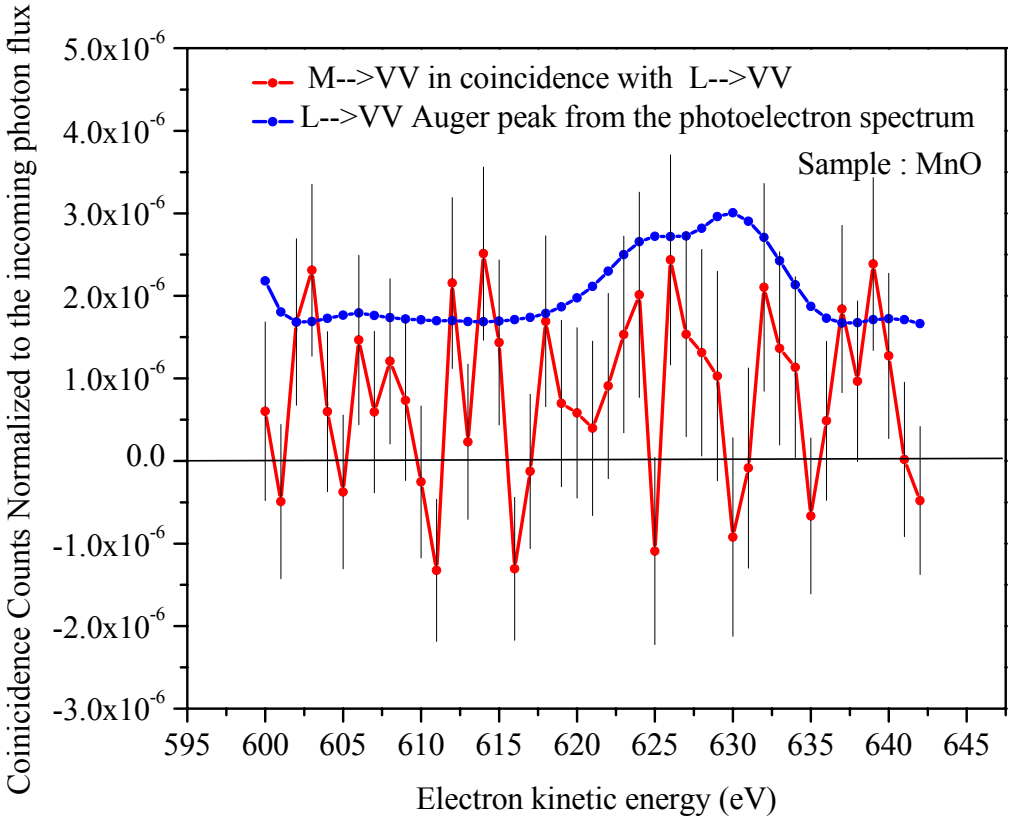

Fig. 3.12 Spectra of electrons emitted in the energy range of the Mn $L_{2,3}$→VV Augers transition measured in time-coincidence with electrons emitted at 33eV (the peak of the Mn M→VV Auger transition)

3.4 Coincidence spectra obtained at the photon energy just above the Mn L_2 threshold (660eV)

The coincidence spectrum obtained at a photon energy of 740eV shown in Fig.3.9 which is well above the threshold of Mn-L_2 level, contains a background which are true coincidences from the tail of the $2p_{1/2}$ and $2p_{3/2}$ photoelectrons with the $L_{2,3} \rightarrow M_{2,3}V$, $L_{2,3} \rightarrow M_{2,3}M_{2,3}$ and $L_{2,3} \rightarrow VV$ Auger Peaks. In order to eliminate the background, we repeated the coincidence measurement at a photon energy 10eV above the $L_{2,3}$ threshold energy in hope of eliminating most of the background, which results from the coincidence of $2p_{1/2}$ and $2p_{3/2}$ photoelectron with the $L_{2,3} \rightarrow M_{2,3}V$, $L_{2,3} \rightarrow M_{2,3}M_{2,3}$ and $L_{2,3} \rightarrow VV$ Auger Peaks. The results showed that it was indeed possible to eliminate the unwanted background due to the inelastic tail of the 2p photoemission peak. Fig. 3.13 shows the comparison between the wide range singles Auger spectra at 740eV and the threshold energy 660eV. Fig. 3.14 shows a comparison of the low energy range singles spectra obtained at 740eV and the threshold energy 660eV and Fig. 3.15 shows the comparison between the residual part of the low energy range singles spectra obtained from 740eV and the threshold energy 660eV. Clearly we can see in both Fig. 3.14 and Fig. 3.15 that an extra bump is observed at 44eV and also the photoelectron peak around 80eV observed in the 740eV spectrum is completely removed in 660eV spectrum.

In pursuit of identifying the extra bump at 44eV, we had to go to very low photon energies, available at U4A beamline and took a series of low energy MnO photo electron spectra. Since MnO is a wide band gap semiconductor, the effects of creating multiple holes in the process of exciting Augers from the sample, will charge the

sample and to avoid that the MnO was doped with Li[89-92]. So we went close to the threshold of Li to find out whether we can see Li in the photoelectron spectra. But we were not able to see the Li peak as shown in the Fig. 3.16. So the peak at 44eV is still not identified. We note that this peak was not observed in either the APECS or the AACS spectra indicating that it is not associated with either the cascade or the direct Auger processes involving the filling of MnO $M_{2,3}$ holes. Fig. 3.17, Fig. 3.18, Fig. 3.19 shows the energy spectra of electrons in the range from 20 to 60eV taken in coincidence with the $L_{2,3}\rightarrow M_{2,3}M_{2,3}$, $L_{2,3}\rightarrow M_{2,3}V$, $L_{2,3}\rightarrow VV$ Auger transitions respectively. The spectral contribution of the second step of the $L_{2,3}\rightarrow M_{2,3}V$, $M_{2,3}V\rightarrow VVV$ cascade was measured by setting the fixed CMA's at 578eV (nominal), corresponding to the $L_{2,3}\rightarrow M_{2,3}V$ Auger peak, and scanning the other CMA from 20eV to 60eV. Similarly, to separate out the low energy spectral contributions of the three step cascade: $L_{2,3}\rightarrow M_{2,3}M_{2,3}$ followed by: $M_{2,3}M_{2,3}\rightarrow M_{2,3}VV$ followed by: $M_{2,3}VV\rightarrow VVVV$ the fixed CMA's was set at 535 eV (nominal), corresponding to the $L_{2,3}\rightarrow M_{2,3}M_{2,3}$ Auger peak, and the other CMA was again scanned from 20eV to 60eV.

Note that the spectra taken in coincidence with the $L_{2,3}\rightarrow VV$ Auger transition is essentially zero - consistent with the fact that no hole is created in the M level in this transition and that therefore no true coincidence is expected. This spectra provides a measure of the effectiveness of the coincidence technique in separating out different spectral contributions and indicates that the accidental and other backgrounds are less than ~5% of the coincidence signal for the spectra taken in coincidences taken with the $L_{2,3}\rightarrow M_{2,3}M_{2,3}$, $L_{2,3}\rightarrow M_{2,3}V$, $L_{2,3}\rightarrow VV$ Auger transitions.

Fig.3.20 shows the comparison of the energy spectra of electrons in the range from 20 to 60eV taken in coincidence with the $L_{2,3}\rightarrow M_{2,3}M_{2,3}$, $L_{2,3}\rightarrow M_{2,3}V$, $L_{2,3}\rightarrow VV$ Auger transitions. Note that the intensity of the AACS spectra taken in coincidence with the $L_{2,3}\rightarrow M_{2,3}M_{2,3}$ transition is roughly twice that of the AACS spectra taken in coincidence with the $L_{2,3}\rightarrow M_{2,3}V$ transition. This 2:1 ratio is to be expected since there are two $M_{2,3}VV$ Auger decays ($M_{2,3}M_{2,3}\rightarrow M_{2,3}VV$, $M_{2,3}VV\rightarrow VVVV$) in the Auger cascade chain initiated by the $L_{2,3}\rightarrow M_{2,3}M_{2,3}$ transition and only one decay ($M_{2,3}V\rightarrow VVV$) following the $L_{2,3}\rightarrow M_{2,3}V$ transition.

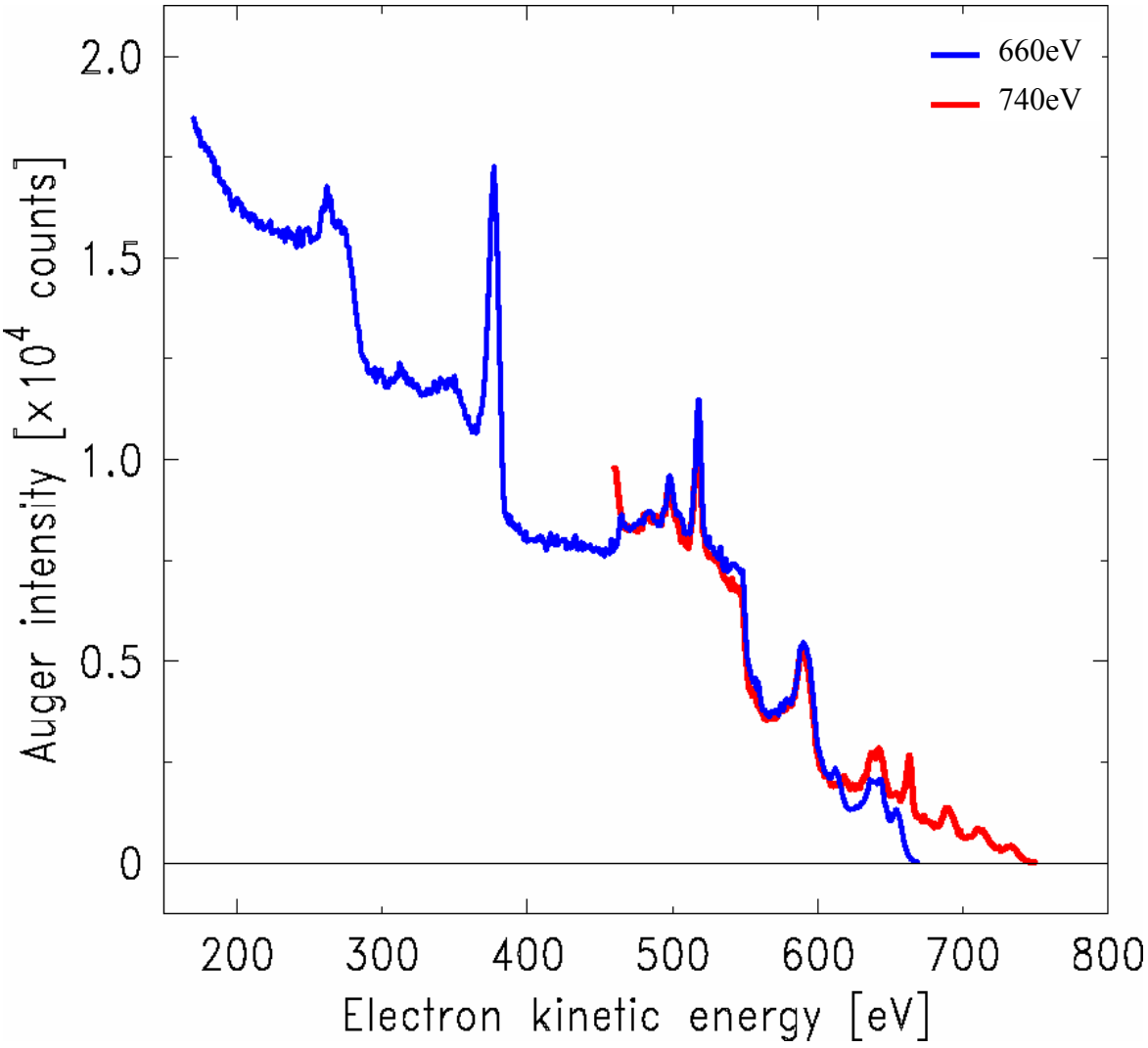

Fig. 3.13 Comparison between the wide range photoemission Auger spectra obtained at a photon energy of 740eV (red) and at the photon energy of 660eV (blue) (~10eV above the Mn $L_{2,3}$ threshold)

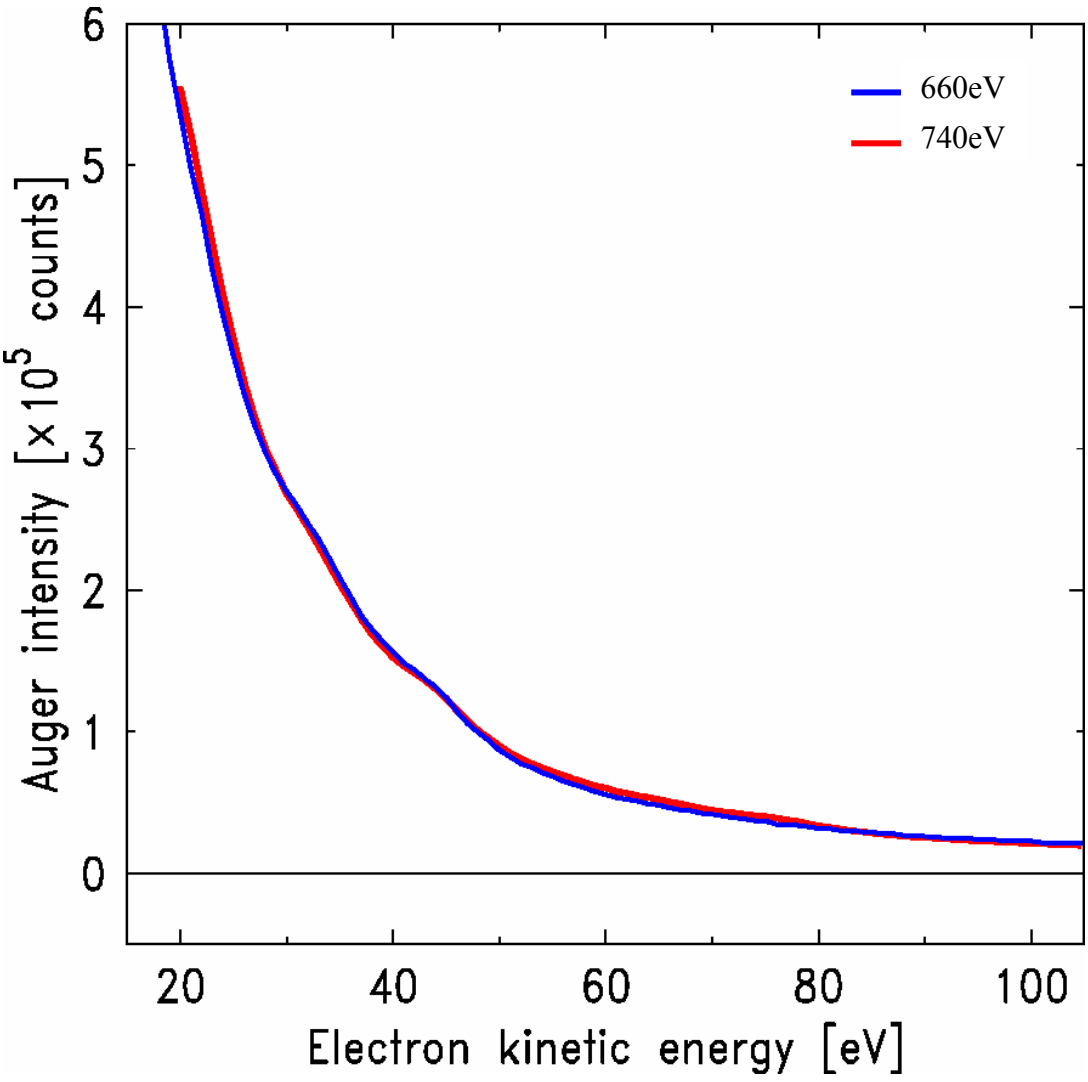

Fig. 3.14 Comparison between the low energy range photoemission spectra of MnO obtained at a photon energy of 740eV (red) and at ~ 660eV (blue) (photon energy which is 10eV above the threshold energy of Mn $L_{2,3}$)

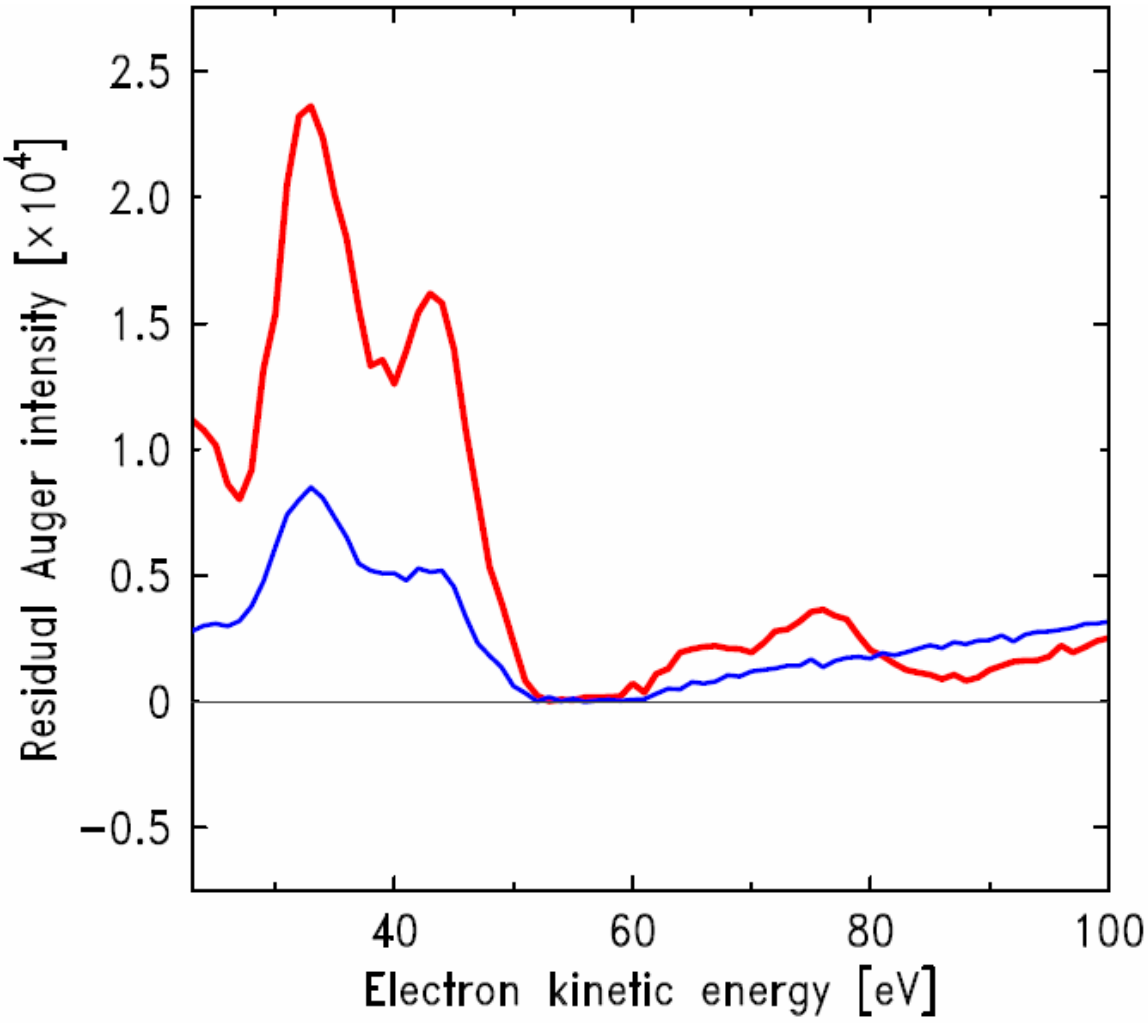

Fig. 3.15 Comparison between the residual parts of the low energy range photoemission spectra of MnO obtained at a photon energy of 740eV and at ~ 660eV (photon energy which is 10eV above the threshold energy of Mn $L_{2,3}$)

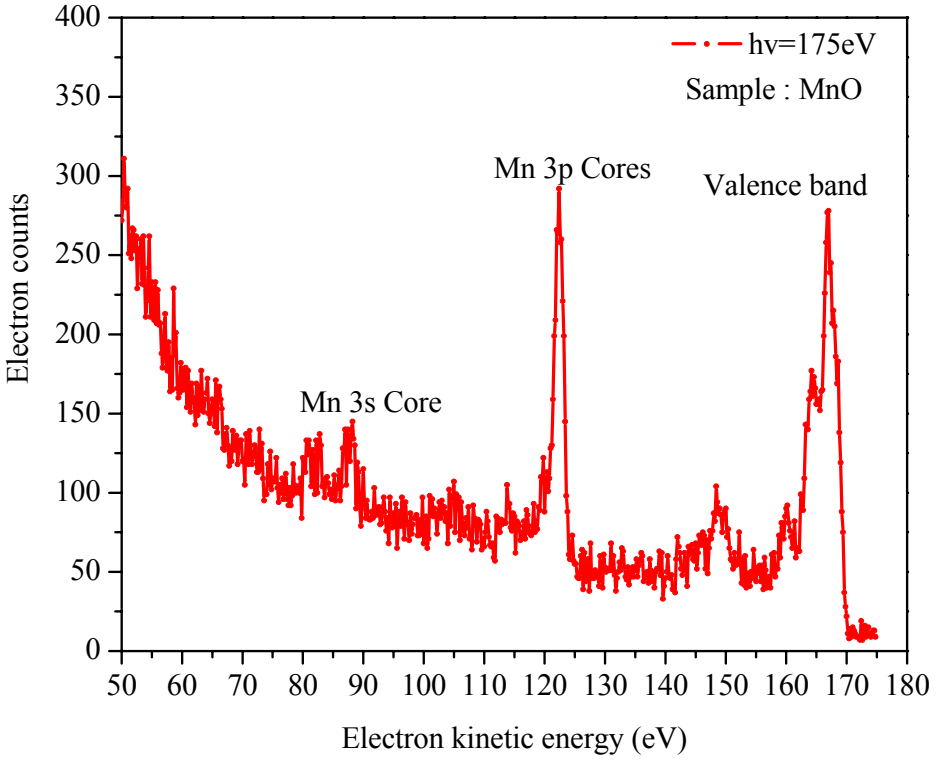

Fig. 3.16 In search of Li –Photoemission spectra of MnO excited at a photon energy of 175eV

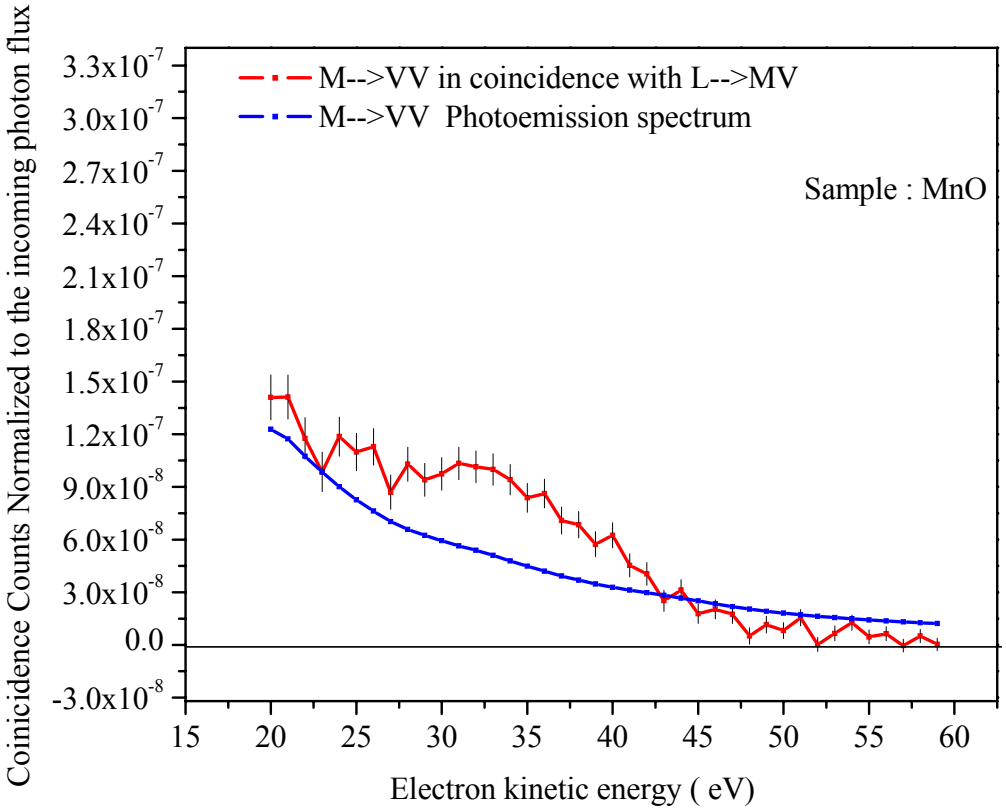

Fig. 3.17 Spectra of Mn $M_{2,3}$→VV Augers measured in time coincidence with the detection of electrons at 575.5eV (the peak of the Mn $L_{2,3}$→$M_{2,3}$V Auger transition) at a photon energy of 660eV

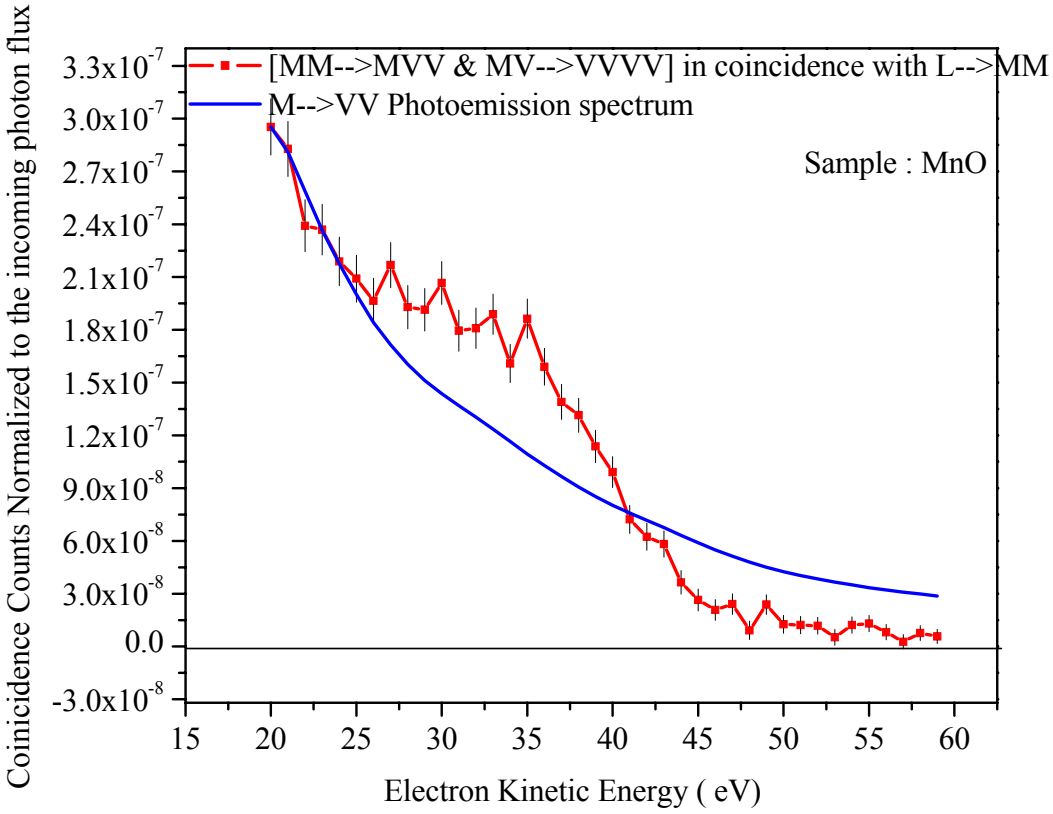

Fig. 3.18 Spectra of Mn $M_{2,3}M_{2,3}$→$M_{2,3}VV$ and $M_{2,3}VV$→VVVV Augers measured in time coincidence with the detection of electrons at 535eV (the peak of the Mn $L_{2,3}$→$M_{2,3}M_{2,3}$ Auger transition) at a photon energy of 660eV

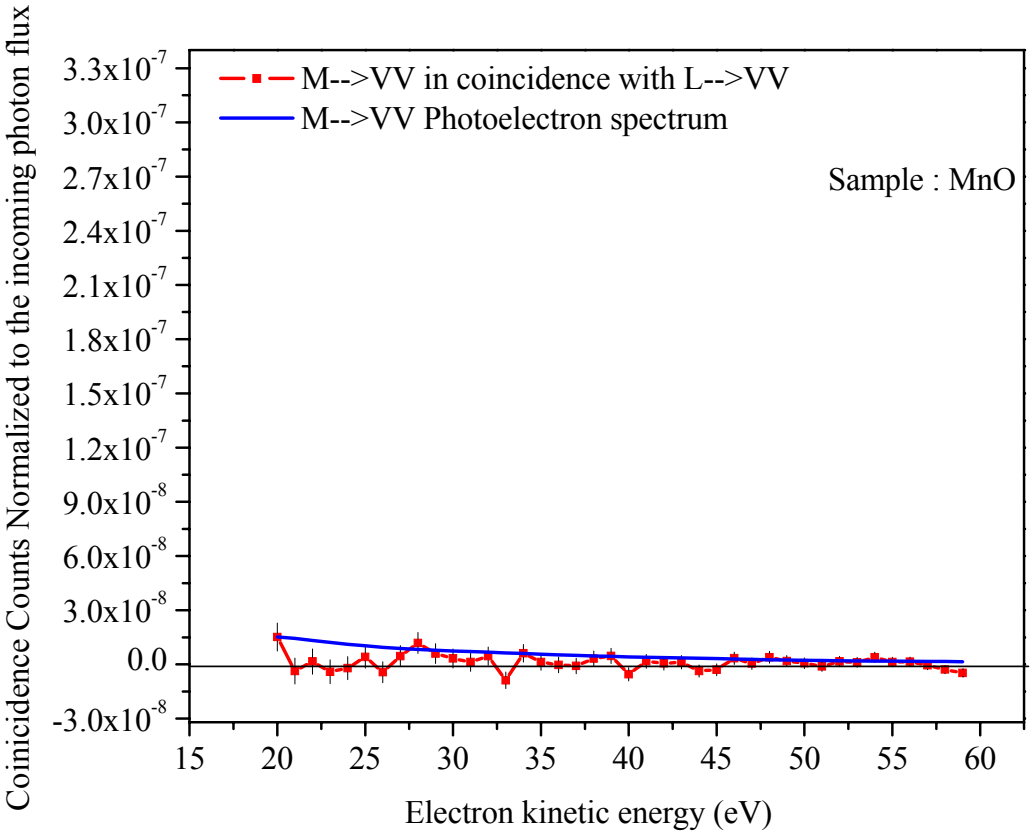

Fig. 3.19 Spectra of Mn $M_{2,3}$→VV Augers measured in time coincidence with the detection of electrons at 626eV (the peak of the $L_{2,3}$→VV Auger transition) at a photon energy of 660eV

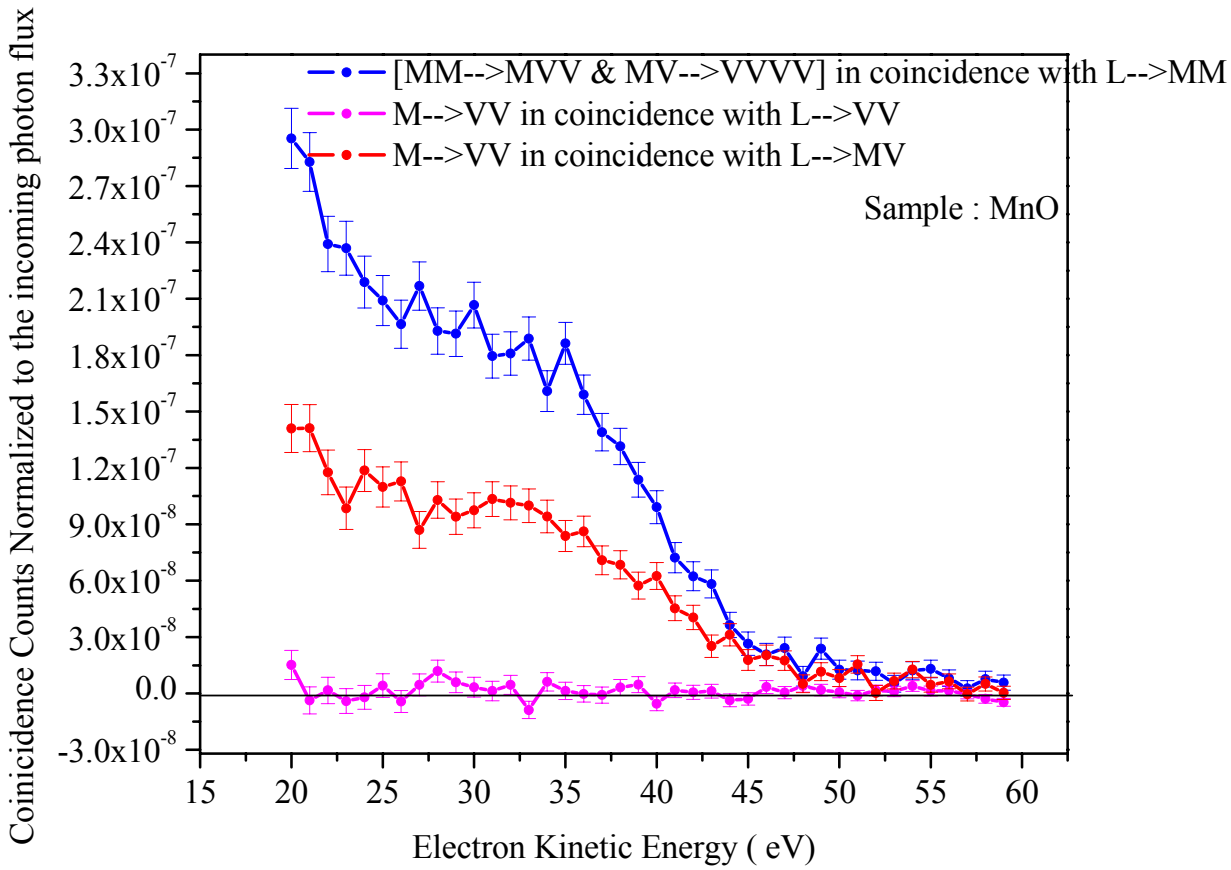

Fig. 3.20 Comparison of the spectra of Mn $M_{2,3}$→VV Augers from MnO measured in time coincidence with the electrons from the peak of $L_{2,3}$→$M_{2,3}$V Auger, $L_{2,3}$→$M_{2,3}M_{2,3}$ Auger, and $L_{2,3}$ →VV Auger transitions at photon energy of 660eV

3.5 Comparison of the Auger-Auger coincidence spectrum obtained at hν=660eV with the M-photoelectron coincidence spectrum obtained at hν= 620eV

Fig.3.21 shows the APECS spectrum which was taken with photon energy (620eV) below the L_2–threshold of Mn to eliminate background contributions from excitation of the L-level. The APECS spectrum was obtained by setting the fixed CMA at 560eV and scanning the other CMA from 20eV to 60eV. The scanned ($M_{2,3}$→VV) and fixed analyzers (M-Core) were set at constant pass energies of 80eV and 310eV, respectively, resulting in an energy resolution of 1.3eV, and 4.96eV, respectively. Again the APECS spectrum demonstrates the significant reduction of secondary electron background relative to the primary emission; this permits the insight into the competition between the intrinsic and the extrinsic secondary electron backgrounds.

Fig.3.22 shows a comparison between the AACS spectrum taken in coincidence with the $L_{2,3}\rightarrow M_{2,3}M_{2,3}$ transition (corresponding to the sum of the spectra of the $M_{2,3}M_{2,3}\rightarrow M_{2,3}VV$, $M_{2,3}VV\rightarrow VVVV$ transitions) with an APECS spectrum measured in coincidence with photoelectrons from the 3p ($M_{2,3}$) level. This comparison reveals that while both AACS and APECS show a peak at ~32 eV, the AACS spectrum is much broader than the APECS data and shows spectral contributions that extend up ~5 eV higher in energy. Both the spectra exhibits significant inelastic background at the low energy side which will be removed by using Shirley background subtraction [93] and the further analysis of these spectra in comparison with the convolutions and correlations of the VB-DOS is discussed in the 6th chapter [94-98].

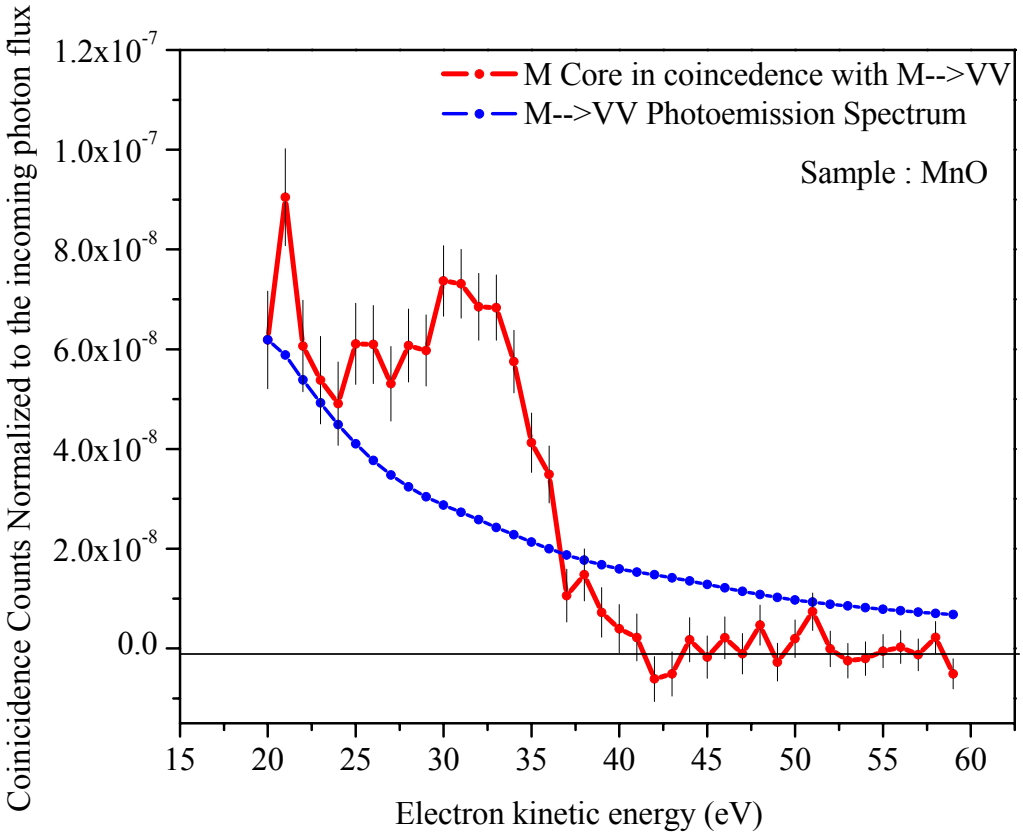

Fig. 3.21 Spectra of Mn $M_{2,3}$→VV Augers measured in time coincidence with the detection of electrons at 560eV (Mn $M_{2,3}$ photoemission peak) at a photon energy of 620eV

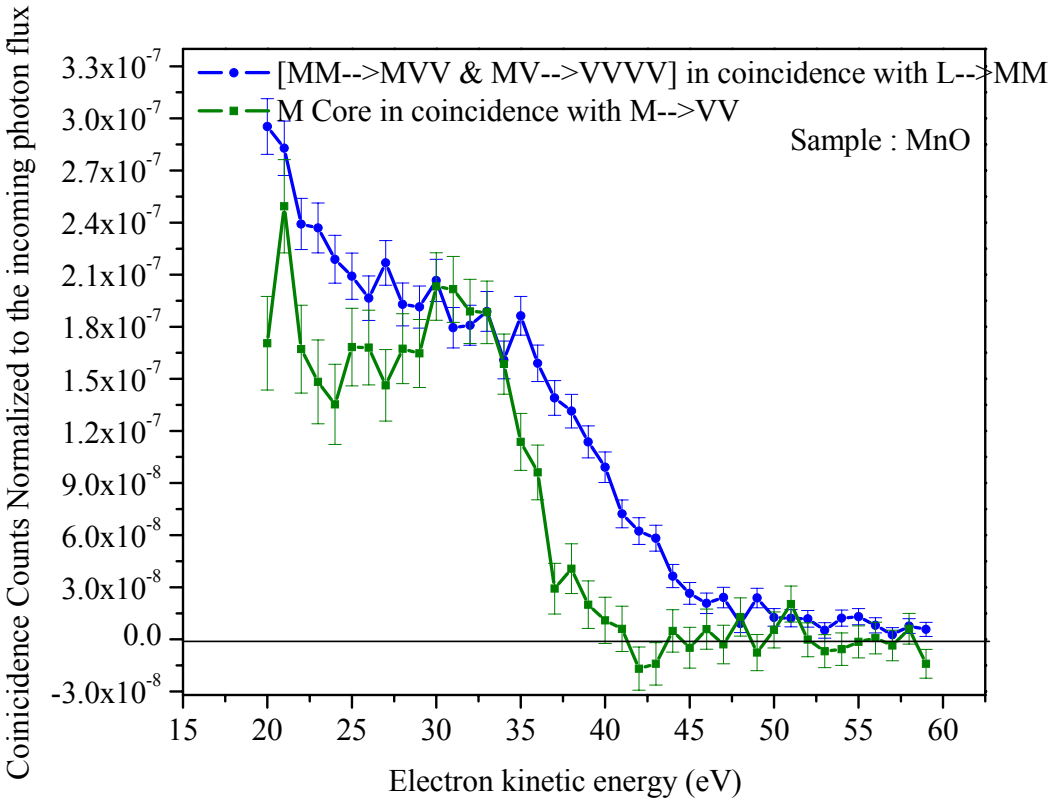

Fig. 3.22 Comparison of the spectra of Mn $M_{2,3}$→VV Augers from MnO measured in time coincidence with the electrons at 535eV (the peak of $L_{2,3}$→$M_{2,3}M_{2,3}$ transition) with the spectra of Mn $M_{2,3}$→VV Augers measured in time coincidence with the detection of electrons at 560eV (Mn $M_{2,3}$ Photoemission peak) at a photon energy of 620eV

.

CHAPTER 4

AACS AND APECS MEASUREMENT OF Ag

4.1 Ag Photoelectron spectrum

The Fig. 4.1 presents the wide range photoelectron spectrum of Ag (100) crystal excited by photons of energy 465eV taken at the U16B beam line. All the important features of the spectrum labeled on the figure are shown here below.

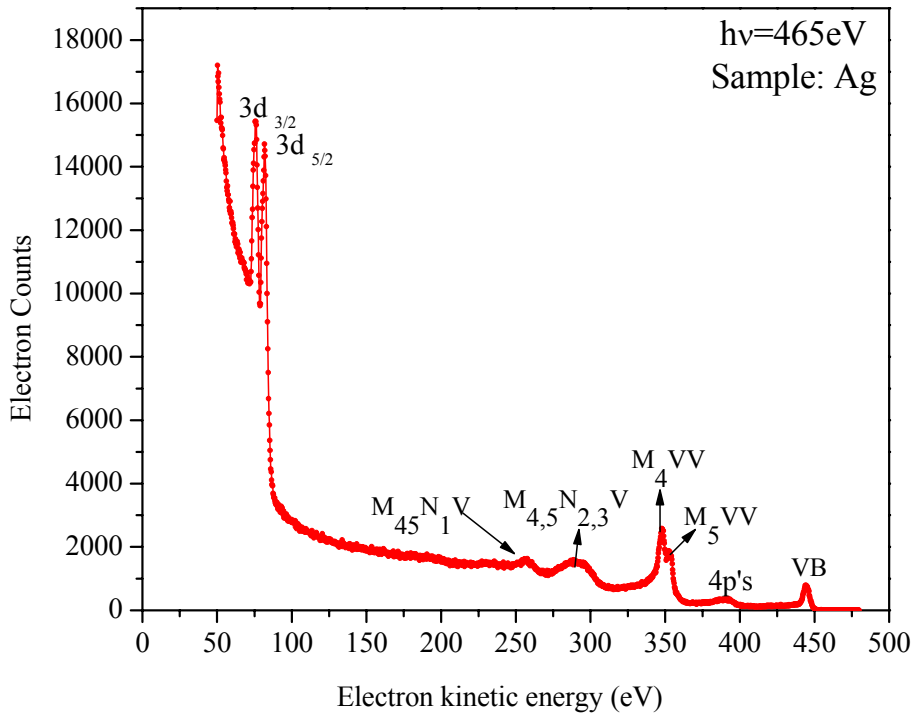

Fig. 4.1 Wide range photoelectron spectrum of Ag (100) obtained at hν=465eV

There are two M shell core peaks M_4 and M_5 prominent at ~75eV and ~81eV, and the two overlapping N core peaks N_4 and N_5 at ~370eV. These cores, when excited undergo direct Auger decay process where the final state of the decay transition is the $M_{4,5} \rightarrow VV$ Auger peaks at ~350eV. If the same $M_{4,5}$ core undergoes cascade decay, then the energy of the intermediate step decay into $M_{4,5} \rightarrow N_{2,3}V$ and $M_{4,5} \rightarrow N_1V$ Augers is around 250 to 300eV while these $M \rightarrow NV$ Augers further decay into 3 hole final state which is the NVV peak at ~35eV. The $N \rightarrow VV$ Peak is buried under a large secondary electron background [99].

Fig.4.2 shows the photoemission spectra of $L_{2,3} \rightarrow MM$ Auger electrons of Ag(100) taken at X-24A beam line at a photon energy of 3600eV.

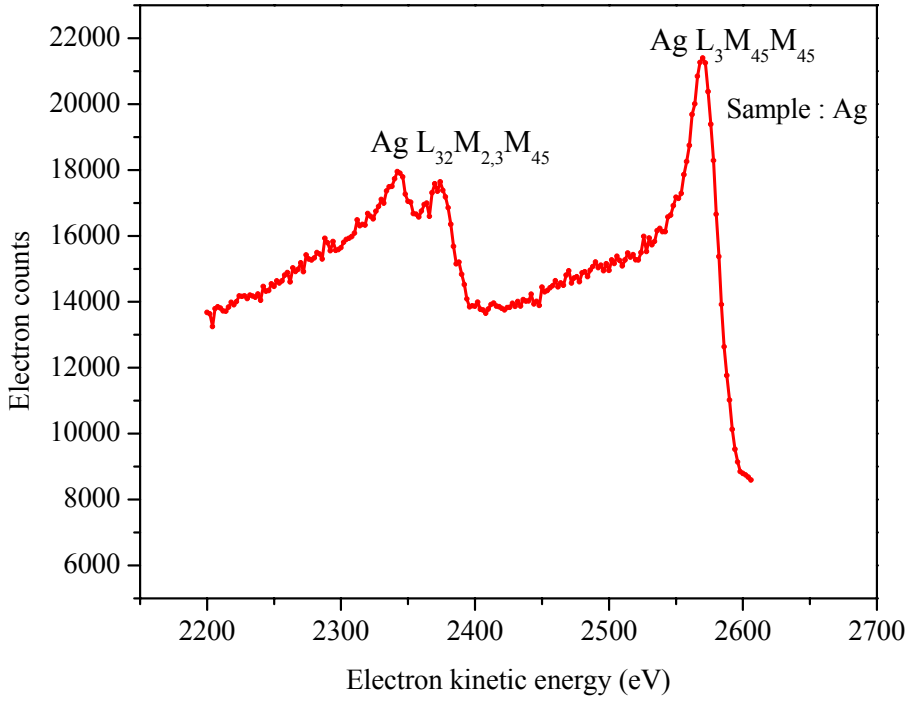

Fig. 4.2 Photoelectron spectrum of Ag (100) obtained at photon energy 3600eV

4.2 Complete screening and Quasi-atomic Ag M→VV Auger line shapes

The spectra of the multi hole final states of an Auger cascade processes provides information on screening mechanisms in the system being studied as well as the correlation of the valence holes[100,101] formed. The CVV spectrum of Ag[102] has a quasi-atomic nature as was explained by Cini and Sawatzky [103,104] based on the effective coulomb interaction (U) and the width of the valence band (W). When U >>W then the spectrum behaves quasi-atomically in nature which tells us that it has both atomic multiplet features and also band like features. When W>>U, the spectrum is

dominated by the band-like features, and when W~U, the spectrum is mostly band like and does not contain atomic-like features.

When a core hole is formed by a photoemission process, it decays into a final state where there are 2 holes in the valence band. According to the Quasi atomic model, this core hole which is formed is seen as an additional proton by the d-band electrons. These valence d electrons screen the core hole until the valence band becomes completely filled. This screening process has direct effect on the Lang-Williams Auger parameter (U) [105-109]. So in order to study the effect of the core hole on the line shape of the valence band Kleiman [110-113] compared the spectra of Ag obtained above and below the L-threshold. The MVV spectra obtained by Kleiman have been digitized and reproduced in the Fig.4.3. The blue curve is the MVV spectrum of Ag obtained by the direct excitation of an M level electron at a photon energy of 3335eV, while the red curve is the MVV spectrum obtained by exciting the L-core hole at a photon energy of 3364eV (The L_3 binding energy of Ag is at 3351eV).

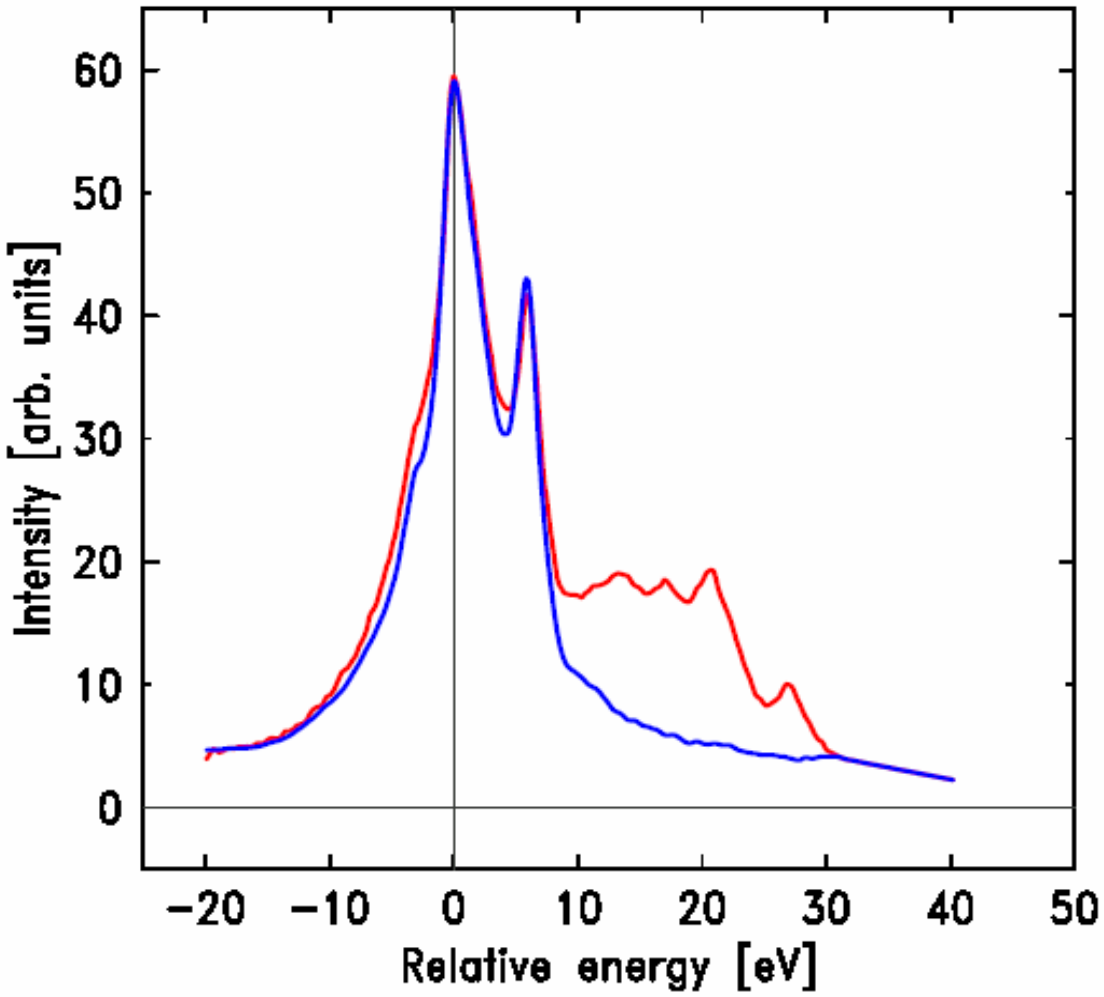

Fig. 4.3 Comparison of Ag MVV Auger spectra obtained above and below the ionization energy of Ag L_3 level

Upon ionizing the L_3 shell of Ag, there is a noticeable extra structure observed on the high-energy side (10-40eV) of the MVV spectrum. This is attributed to interaction between the two holes present in the final state of the L→MM transition.

The low energy portion of these MVV spectra is quasi-atomic in nature, and its shape is not altered as the exciting photon energy goes from below to above the ionization energy of the Ag L_3 level.

In the above experiment, by exciting the atom above and below the ionization level of L_3, Kleiman's group was able to assess the contribution of all the intermediate state holes formed in the Auger cascade, including those associated with both possible cascade decay chains L→MM→MVV→VVVV and L→MV→VVV. They were not able to identify the contributions of the individual cascades. By using Auger-Auger coincidence techniques, we were able to measure the contributions of each of the two cascade chains to the Ag M→VV spectrum. In order to obtain the Ag M→VV Auger spectra associated with the excitation of the L_3 level we needed photons with energy more than 3351eV, the binding energy of the L_3 level. As the VUV ring would not be able to go up to such high photon energies, we had to move our coincidence chamber to the X-Ray ring which is capable of providing hard X-ray photons.

4.3 Comparison of the spectra of M→VV Augers measured in time coincidence with the detection of electrons at 2550eV (the peak of Ag L→MM Auger transition) AACS and Spectra of M→VV Augers measured in time coincidence with the detection of electrons at 100eV (the peak of Ag $2p_{3/2}$) APECS

The UHV chamber along with the NIM electronics, counting electronics, and the PHA was moved over to the X24A beamline. The chamber was aligned so as to focus the SR beam onto a small spot on the sample seen by the two CMA's by carefully monitoring the counts in both the CMA's using two ratemeters. Fig. 4.4 shows the

M→VV auger spectra of Ag obtained in coincidence with L photo-electron peak(APECS-green) and M→VV Auger spectra obtained in coincidence with L→MM Auger Peak (AACS- red).

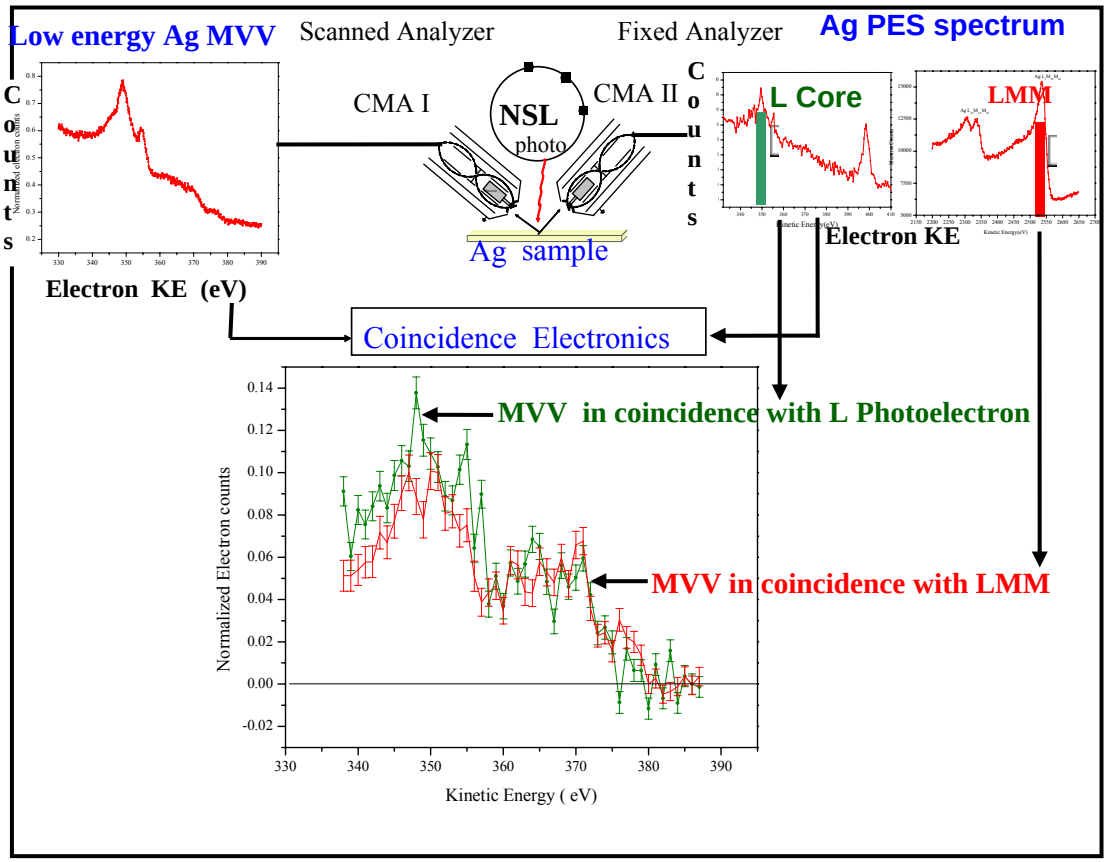

Fig. 4.4 Schematic illustrating the energy ranges used in measuring the M→VV Auger spectra in time coincidence with high energy Augers emitted in L→MM Auger transition (AACS- red) or L photoelectron (for APECS-green)

In response to initial problems with the thermal drift in the monochromator, a feed back control circuit was established on to the monochromator crystal by Dr Lonny Berman. The program followed a coarse feed back to find the maximum of the given photon energy range and then fine tuned the result, then used the second mirror tilt (SMT) which was the mirror feed back signal along with a curve fitting program. A log file was created to monitor the time evolution of the mesh current, motor position,and fixed analyzer counts which could help in our data analysis later. All these were incorporated in the "optimize macro" which takes care of the beam reaching the sample.

Fig. 4.5 shows the photoelectron spectrum of Ag $2p_{3/2}$ and the M→VV Auger peak obtained at hν=3960eV. The Ag $2p_{3/2}$ peak is at 398eV while the M→VV peak is at 348eV. Since the photoelectron peak lies at a higher energy than the M→VV Auger peak, the secondary electrons from the photoelectron peak create a background under the MVV peak. This contribution will be measured while taking APECS (MVV-Ag $2p_{3/2}$). It was deemed important to move the photoelectron peak to lower energy than the MVV peak in order to avoid the background which might be coincident with the MVV peak. Thus the photon energy was lowered to 3470eV which shifted the Ag $2p_{3/2}$ photoelectron peak to ~100eV below the M→VV to avoid the background created by the secondaries of the L-Photoelectron as shown in Fig.4.6. Fig. 4.7 shows the high energy L_3→$M_{4,5}M_{4,5}$ Auger peak[4-11] obtained at a photon energy of 3470eV. The high statistics photoelectron spectrum of Ag $M_{4,5}$→VV Auger peak measured at a photon energy of 3470eV is shown in Fig. 4.8.

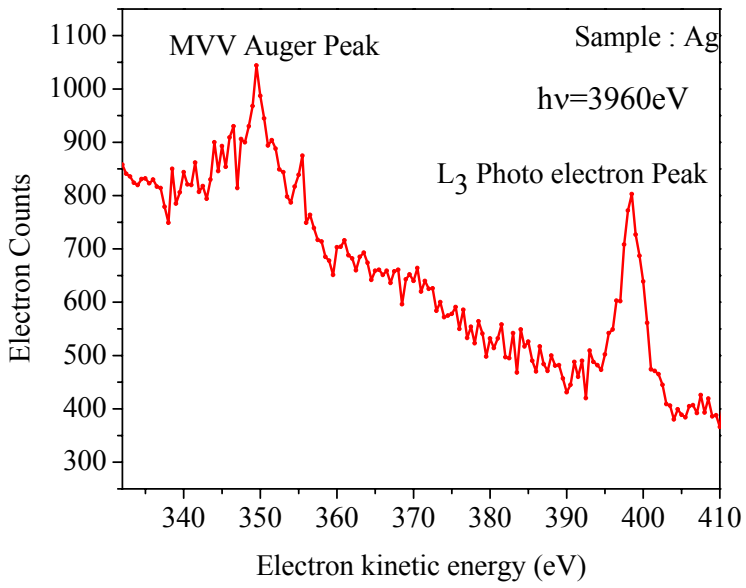

Fig. 4.5 Photoemission spectra of Ag obtained at hν=3960eV

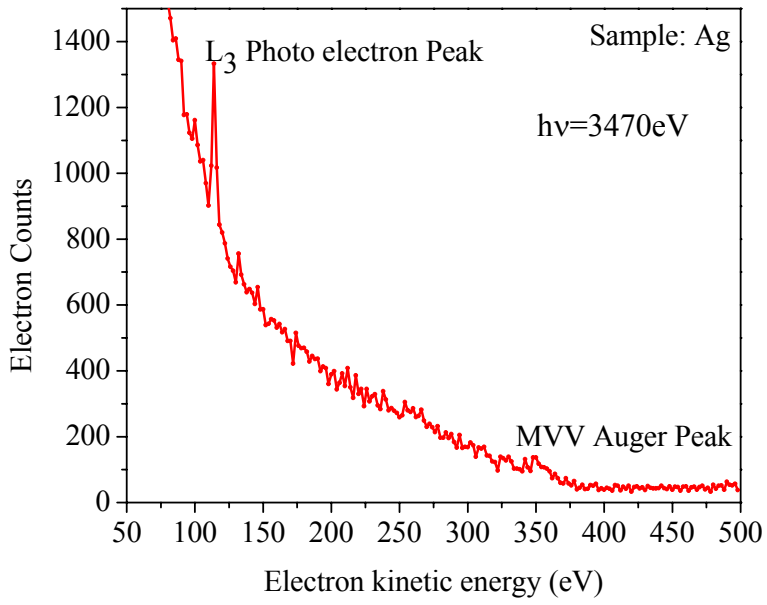

Fig. 4.6 Photoemission spectra of Ag obtained at hν=3470eV. Note that Ag $2p_{3/2}$ shifted to an energy below the M→VV Auger peak to avoid background (from Ag $2p_{3/2}$ to M→VV)

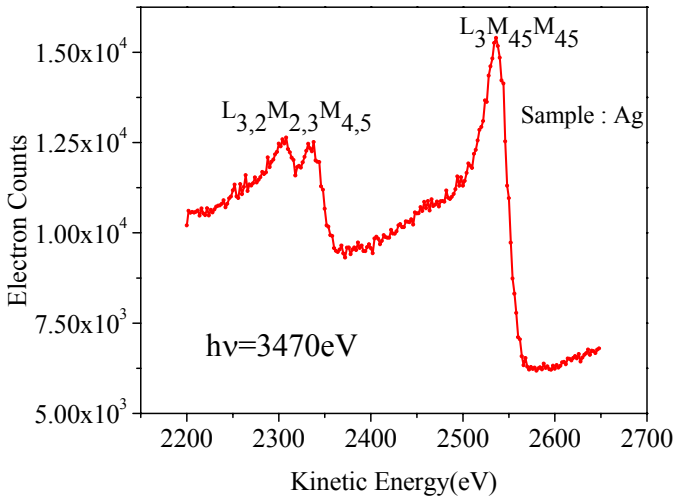

Fig. 4.7 Ag $L_3 \rightarrow M_{4,5}M_{4,5}$ peak measured at photon energy 3470eV

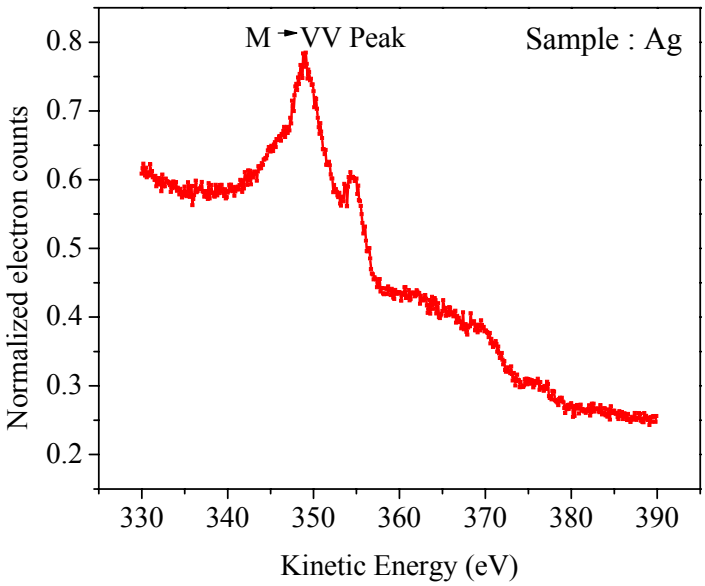

Fig. 4.8 Photoemission spectrum of Ag $M_{4,5} \rightarrow$ VV Auger peak taken at hν=3470eV

with L→ MM Auger peak (Auger cascade decay) with the Ag M→VV spectrum (green) taken in coincidence with Ag2$p_{3/2}$ photoelectron peak. Both spectra were taken at hν =3470eV. Some of the important observations on analyzing the spectra shown in Analyzing the Fig. 4.9 and comparing it with the spectra obtained by Kleiman's group (Refer Fig.4.3)[114] by exciting above and below the L_3 threshold are discussed below.

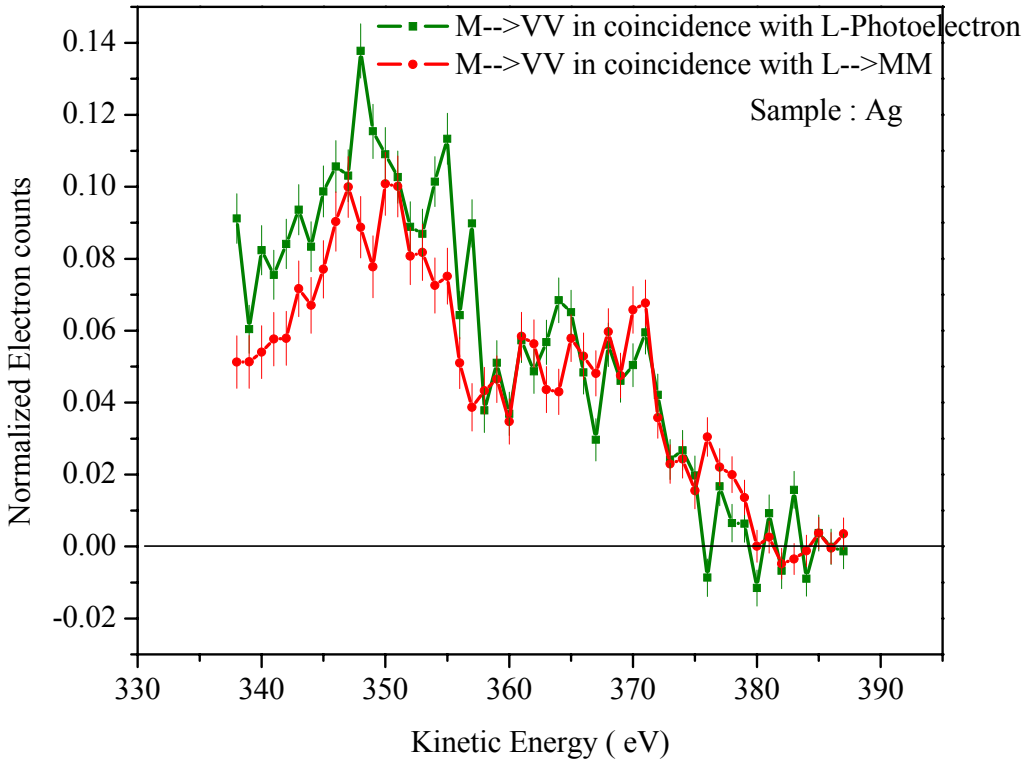

Fig. 4.9 Comparison of Ag $M_{4,5}$→VV Augers measured in time coincidence with the electrons at 2550eV (The peak of L→MM transition)[Auger-Auger cascade decay in red] with the spectra of Ag $M_{4,5}$→VV Augers measured in time coincidence with the detection of electrons at 100eV(Ag 2$p_{3/2}$ photoelectron peak)(direct Auger decay in green) both taken at photon energy of 3470eV

The Ag M→VV spectrum obtained in coincidence with L→MM Auger peak (Auger cascade decay) contains contribution of the Auger cascade initiated by the L-photoelectron emission where the initial state has two M holes and the final state has one hole in the M shell and 2 holes in the valence band. The spectrum obtained is shown in red. The spectrum obtained when M→VV spectrum is in coincidence with the Ag 2p3/2 photoelectron peak is shown in green. Both spectra are normalized to the incoming photon flux. This coincidence spectrum contains contributions from L→MV→MVV, L→MM→MVV and also contributions from M→VV. In both cases, the shape of the spectrum is the same; on the high energy side it contains the atomic like contribution, which is same as the extra structure shown in Fig. 4.3 when Ag is excited above the L level. The two spectra are normalized to the area under the atomic-like peaks on the high energy side (360-380eV) which shows that there is more intensity in the low energy portion (340-360eV) of the APECS spectrum than the AACS spectrum. The peak found between 340eV to 360eV exhibits quasi-atomic nature as found in Kleiman's data. We note that it was not possible to measure the coincidence between M→VV peak with the L→MV peak due to arcing inside the CMA's when we tried to increase the V_{ret} to the -1350V in order to detect the L→MV peak which was at ~2970.eV.

The comparison of the AACS and APECS data obtained at X-24A shows that the spectra have similar features. Both the coincidence spectra maintain the shape of the singles MVV spectrum shown in Fig. 4.8. The normal MVV region (340eV to 360eV) in both AACS and APECS has quasi-atomic nature. As the spectator M hole created is

strongly bound to the nucleus, the valence holes sees the spectator M hole as an extra proton, which results in the multiplet splitting. This is consistent with the Kleiman's data. But Kleiman explains that we should be able to see only the multiplet feature, when we subtract the normal region of the spectrum, taken above and below the L ionization level, but we still see considerable intensity in the normal region, which does not go to zero. So we went to lower photon energies to determine the contribution of the low energy cascades to the MVV Auger peak, particularly those involving the M-level. The similarity in the line shape of the L→MM→MVV→VVVV and L→MV→MVV raises a question whether there is one hole or two holes in the intermediate state [115-119]. As we could selectively probe individual subsequent transitions in an Auger cascade process using Auger-Auger coincidence, we wanted to see whether the full participation of the valence band holes occurs in metals as it does in MnO, which is a wide band gap semiconductor.[120-125]

4.4 Comparison of the low energy (20-60eV) M→VV Auger spectrum measured in time coincidence with 2p3/2 photoelectrons and Ag $3d_{5/2}$ photoelectrons (APECS)

To check the overall performance of our coincidence set up we took a test spectrum of M→VV data in coincidence with 3d cores, which turns out to be the simplest of all the available combination pairs of the coincidence data that can be obtained. The photon energy used to excite the Ag sample was 465eV which was sufficient enough to excite both M_4, M_5 and the N shells. Due to the thermal drift in the monochromator there was a drift in the peak position of the cores excited. The peak

position was redetermined every 40 sweeps using routine “fit”. These fitting parameters are stored in a separate folder so as to check for any abnormalities.

One of the CMA’s with pass energy of 90eV was fixed at the M_5 peak ($3d5_{/2}$ peak) while the other CMA with pass energy of 80eV was scanned for the M→VV augers from 340eV to 380eV arising from the transition initiated by exciting the $3d_{5/2}$. The count rate of the fixed analyzer was 3510 Hz. Since this was only a test, we just ran 3 sets of scan containing 155 sweeps to find out that our coincidence set up was working as expected. Fig. 4.10 shows the comparison of M→VV taken in coincidence with $3d_{5/2}$ core and the MVV spectrum taken in coincidence with L→MVV. Since the M→VV spectrum is a very low statistics spectrum, the error bars where huge, this completely obscured the data and therefore for clarity did not include the error bars. As we see from the comparison, the M ($3d_{5/2}$) in coincidence with the M→VV lies in the low energy side of the M→VV spectrum obtained in coincidence with the $2p_{3/2}$ which is again a clear test that the contribution is mainly from the $3d_{5/2}$.

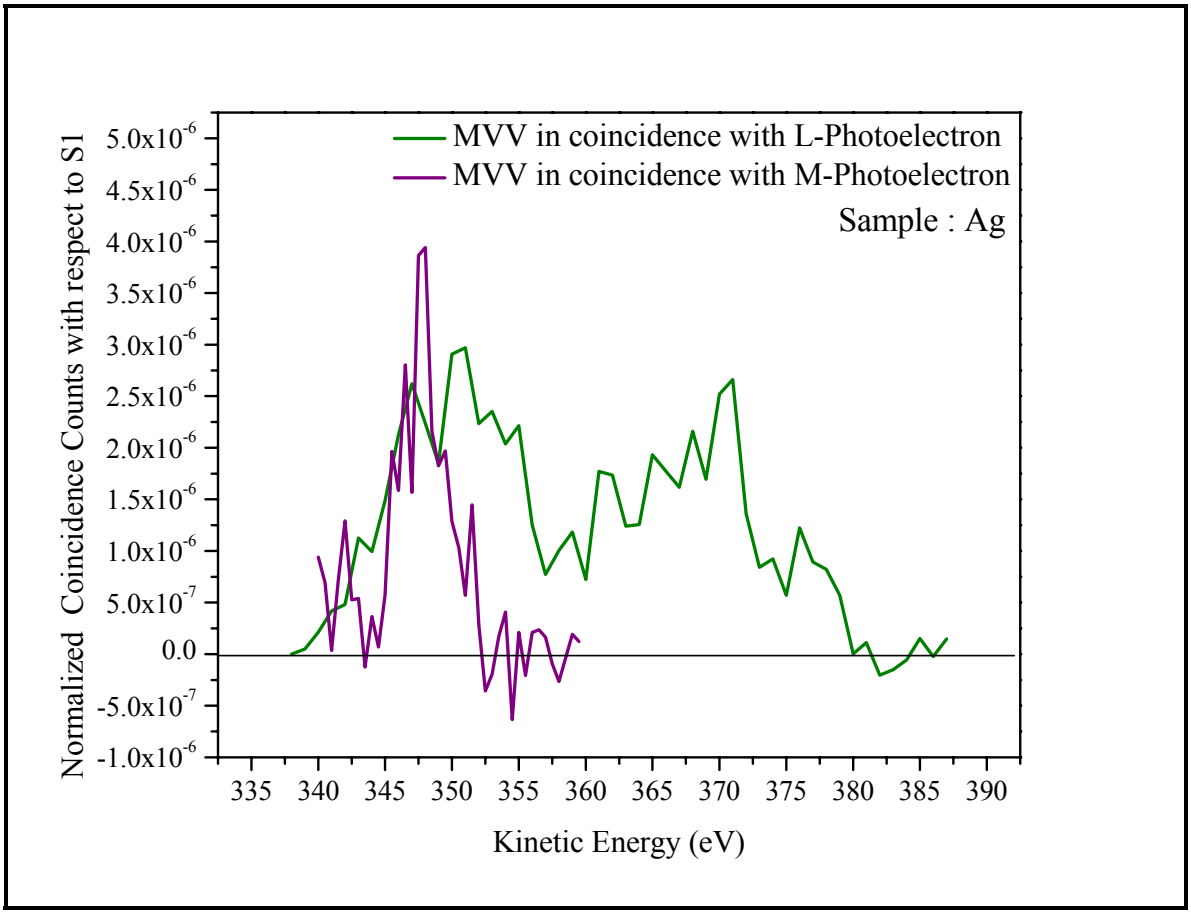

Fig. 4.10 Comparison of the spectra of Ag $M_{4,5}$→VV Augers measured in time coincidence with the detection of electrons at 100eV(Ag $2p_{3/2}$ photoelectron peak)(direct Auger decay in green) taken at photon energy of 3470eV with the spectra of Ag $M_{4,5}$→VV Augers measured in time coincidence with the detection of electrons at 100eV (Ag $3d_{5/2}$ photoelectron peak) (direct Auger decay in purple) taken at a photon energy of 465eV

4.5 Ag $M_{4,5}$→$N_{2,3}$V→VVV Auger cascade decay

This Auger cascade is initiated by M-photoemission. It has one hole in the N level and one hole in the valence band in the intermediate state and the atom relaxes to a final state which has 3 holes in the valence band.

4.5.1 Spectra of NV→VVV Augers taken in time coincidence with the electrons emitted at (299eV) peak of M→NV transition

To obtain the Auger-Auger coincidence spectrum of the NV→VVV transition, one of the CMA's with pass energy of 450eV was fixed at the peak M→NV Auger peak at 299eV while the other CMA with pass energy of 80eV was scanned for the NV→VVV Augers from 20eV to 60eV. The average count rate of the fixed analyzer was ~1568 Hz. Fig. 4.11 shows the pass energy distribution of the fixed analyzer around the $M_{4,5}N_{4,5}$V peak of the photoemission spectrum of M→NV Augers. The centre line shows that the CMA is fixed at 299eV, and the lines on either side of the centre line indicates the pass energy width (1.6% of PE) which allows electrons from the range 295.4eV to 302.6eV to be considered as the ones coming from the peak for valid coincident events. Fig. 4.12 shows the AACS spectrum where the NV→VVV Augers were measured in coincidence with the M→NV Augers.

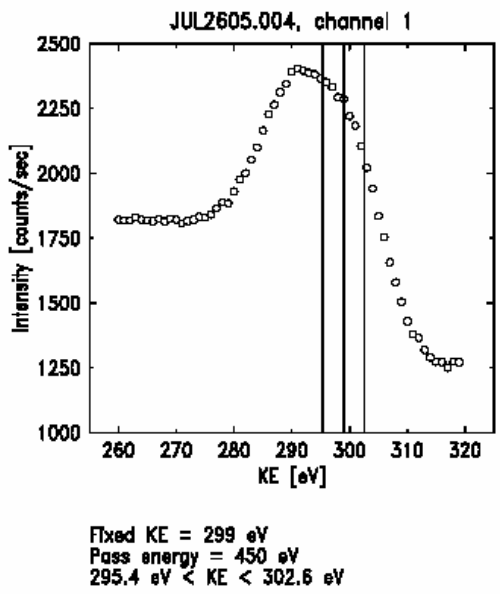

Fig. 4.11 Photoemission spectrum of M→NV Augers of Ag measured at hν=465eV

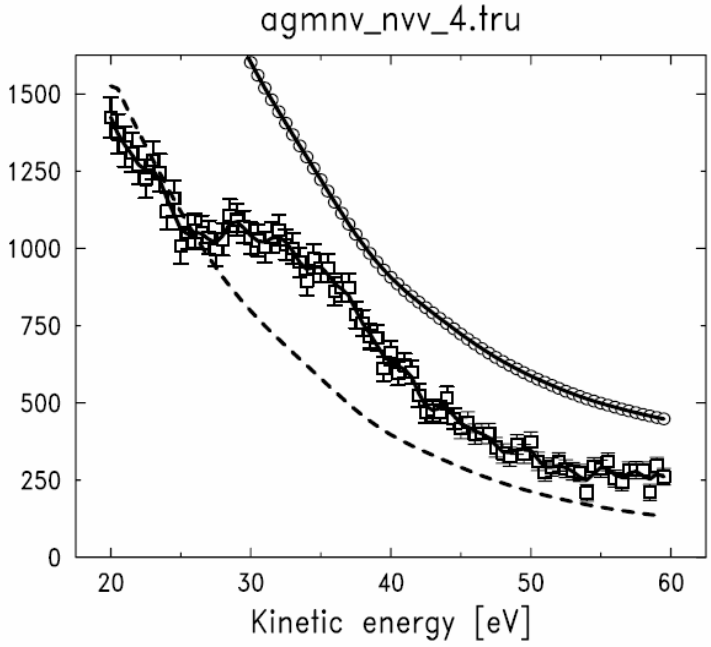

Fig. 4.12 The spectra of electrons emitted in the range of 20-60eV Ag $N_{4,5}$V→VVV Augers measured in time coincidence with the electrons at 299eV (The peak of M→ NV transition)[Auger-Auger cascade decay]

Fig 4.13 shows the photoemission spectrum of Ag from 50eV to 500eV where M→NV Augers are at ~299eV, the M→VV Augers are at 348eV and the N cores are at 380eV. The M cores at ~75eV and ~81eV can give rise to a contribution to N→VV peak when the M hole decays into N→VV Auger electrons. This could have been avoided if the M-cores could have been moved below the energy range of N→VV as we did for the MnO (refer section-3.4).On the other hand, M→VV Augers does not contribute to the N→VV Auger spectra as MVV is the final state of M core hole decay. To avoid the background from the N cores at 370eV to M→NV Augers one of the analyzers was fixed at energy 324eV with pass energy of 450eV which allowed the fixed energy to vary from 320.4eV to 327.6eV between the N cores and the M→NV Augers and the other analyzer was scanned from 20eV to 60eV for the N→VV Augers.

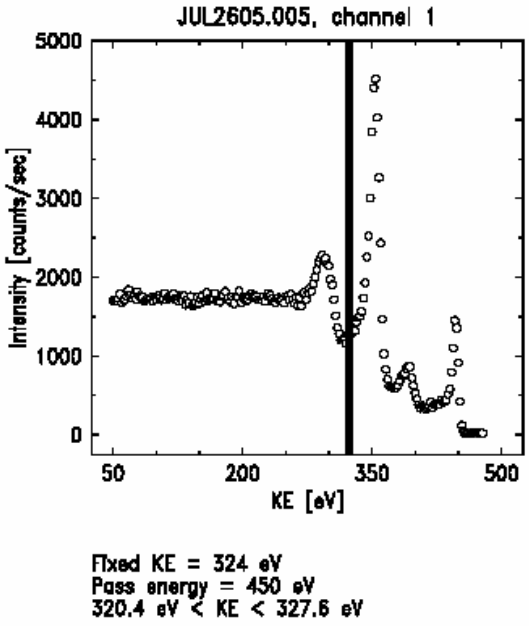

Fig. 4.13 Photoemission spectrum of Ag measured at hν=465eV showing M→NV Augers (270eV), M→VV Augers (350eV), 4p cores (380eV) and valence band (448eV)

Fig. 4.14 shows the background of Ag NV→VVV coincidence spectrum from the N– cores. Fig. 4.15 shows the spectrum of electrons emitted in the range of 20-60eV in coincidence with electrons emitted at ~325eV in the tail of M→NV Auger peak and the normalized spectrum of the NV→VVV coincidence with respect to the sum of S1 counts. This normalized background is subtracted from the coincidence and is shown in Fig. 4.16. Still there is the inelastic background which was not eliminated by the coincidence. This has to be removed to obtain the real coincident spectrum. So a Shirley background subtraction was performed and the resultant area normalized NV→VVV coincidence spectrum is shown in Fig. 4.17.

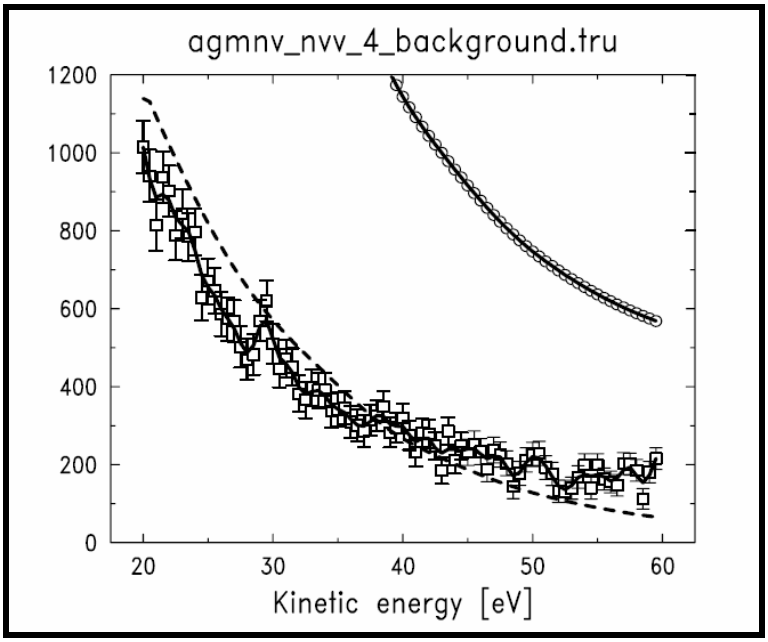

Fig. 4.14 Spectra of electrons emitted in the range of 20-60eV in time coincidence with electrons emitted (at 324eV) in the tail of the M→NV Auger spectrum

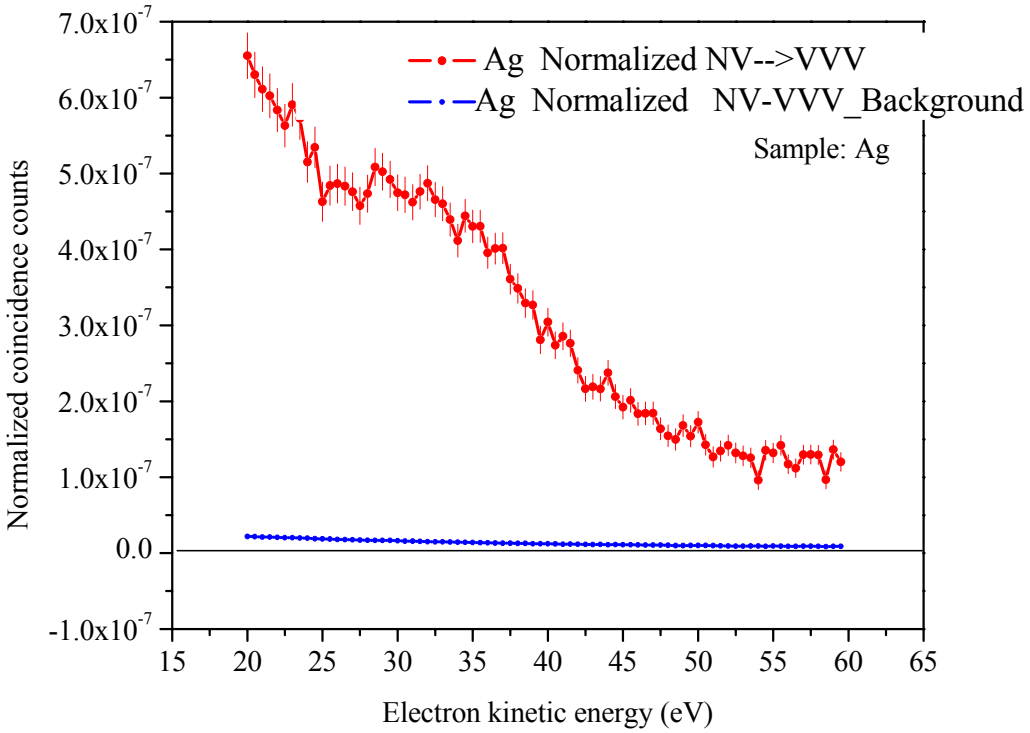

Fig. 4.15 Ag NV→VVV spectrum of electrons in time coincidence with M→NV Auger electrons (red) and electrons emitted in the range of 20-60eV in time coincidence with electrons emitted at ~324eV in the tail of M→NV Auger peak (blue)

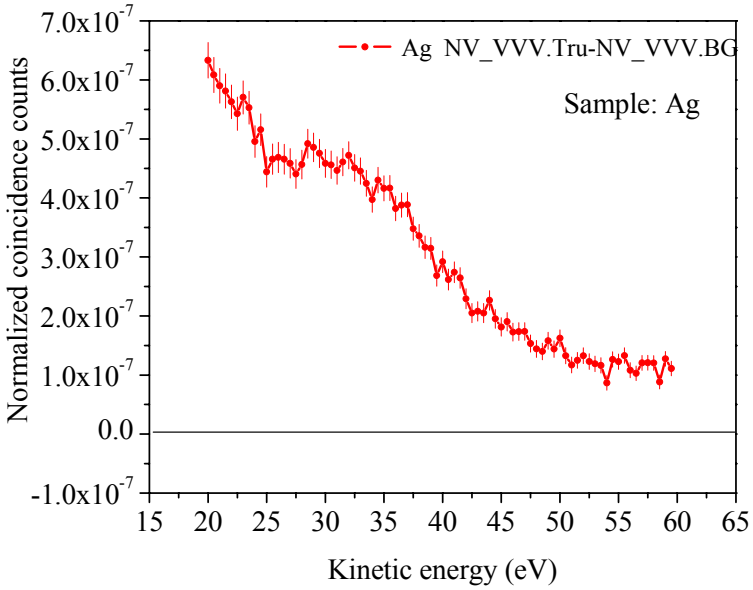

Fig. 4.16 Ag NV→VVV coincidence spectrum after the subtraction of the background to the Auger peak from the 4p cores

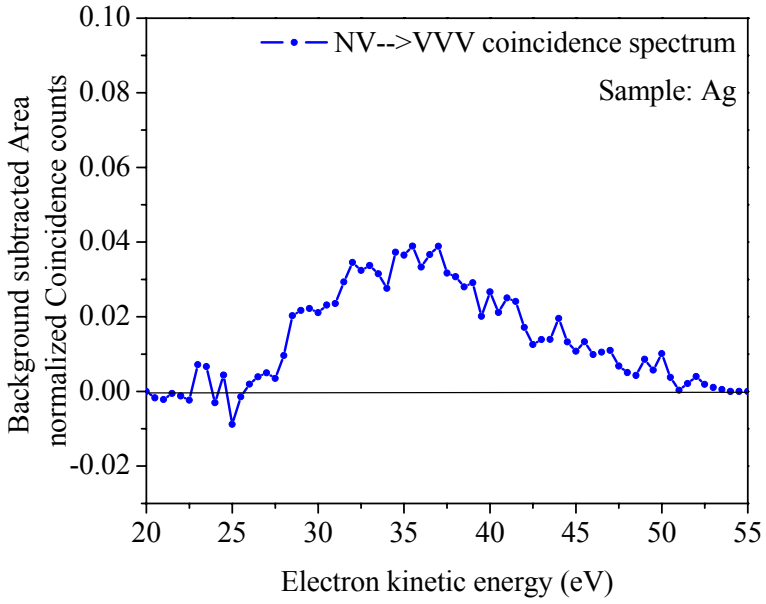

Fig. 4.17 The spectra of Ag NV→VVV Augers emitted in the energy range 20-60eV in time coincidence with the electrons emitted at 299eV (the peak of M→NV transition) after Shirley background subtraction

4.6 Ag $N_{2,3}$→VV Auger spectrum measured in coincidence with the electrons from 4p photoemission peak- Direct Auger decay

The Ag 4p cores have a binding energy of 63.7eV and 58.3eV. When we excite the sample with photon energy 465eV, the 4p photoemission peak at ~392eV.

4.6.1 Ag $N_{2,3}$→VV spectrum measured in coincidence with the electrons emitted at (397eV) 4p photoemission peak

To obtain the spectrum of the electrons emitted from the N→VV transition in coincidence with the electrons emitted from the 4p3/2 photoemission peak, one of the CMA's with pass energy of 300eV was fixed at the 4p3/2 core peak at 397eV while the other CMA with pass energy of 80eV was scanned for the N→VV augers from 25eV to 60eV. The average count rate of the fixed analyzer was ~792.9Hz. Fig. 4.18 shows the pass energy distribution of the fixed analyzer around the 4p3/2 of the photoemission spectrum of N cores. The centre line shows that the CMA is fixed 397eV, and the lines on either side of the centre line indicates the pass energy width (1.6% of PE) which allows electrons from the range 394.6eV to 399.4eV to be considered as the ones coming from the peak for valid coincident events. Fig. 4.19 shows the coincidence spectrum of the N→VV Augers measured in coincidence with the 4p cores. Fig. 4.20 shows a Shirley background subtracted area normalized coincidence spectrum of N→VV coincidence spectrum.

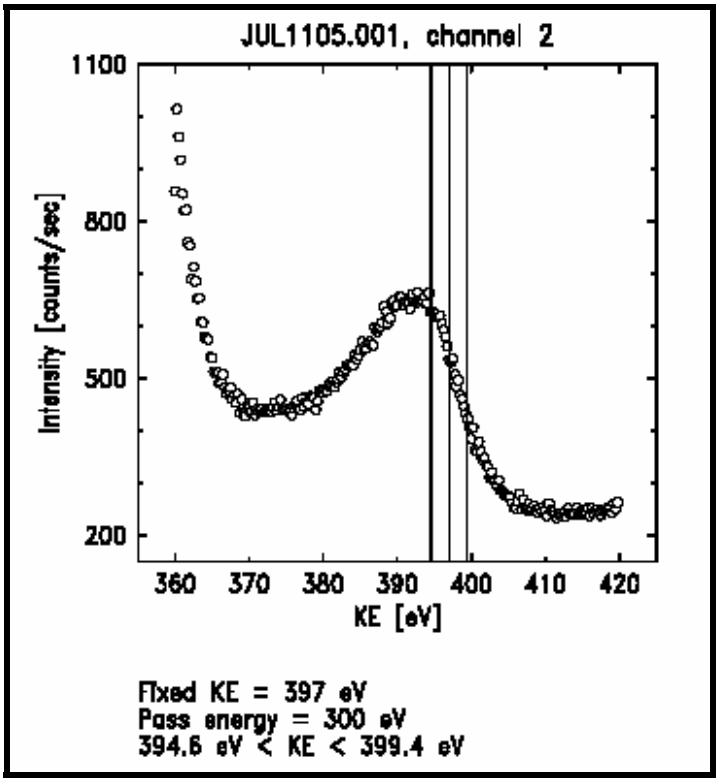

Fig. 4.18 Ag $4p_{3/2}$ photoemission peak showing the pass band selected at hν=465eV

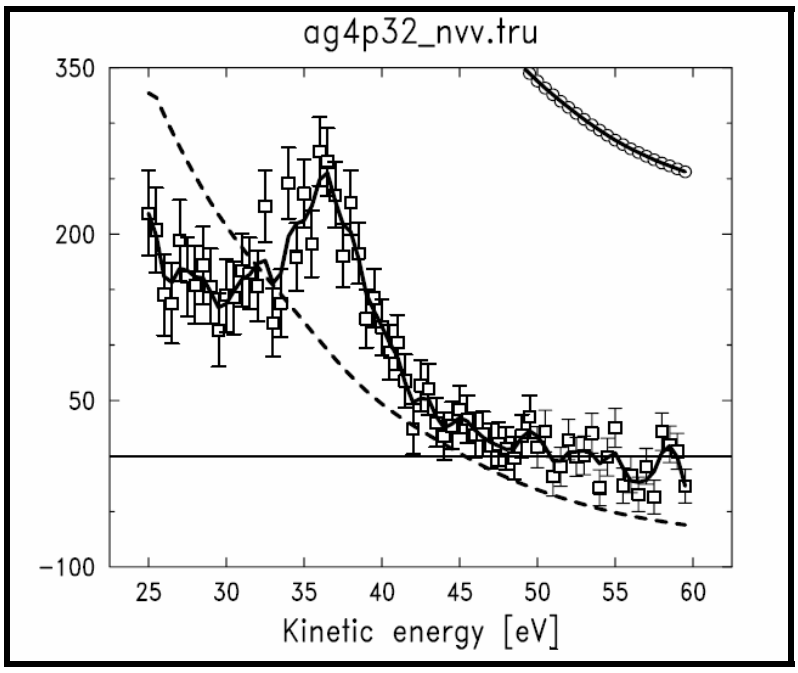

Fig. 4.19 Ag $N_{4,5}$→VV Augers measured in time coincidence with the electrons at 397eV (The N-photoelectron peak)[APECS]

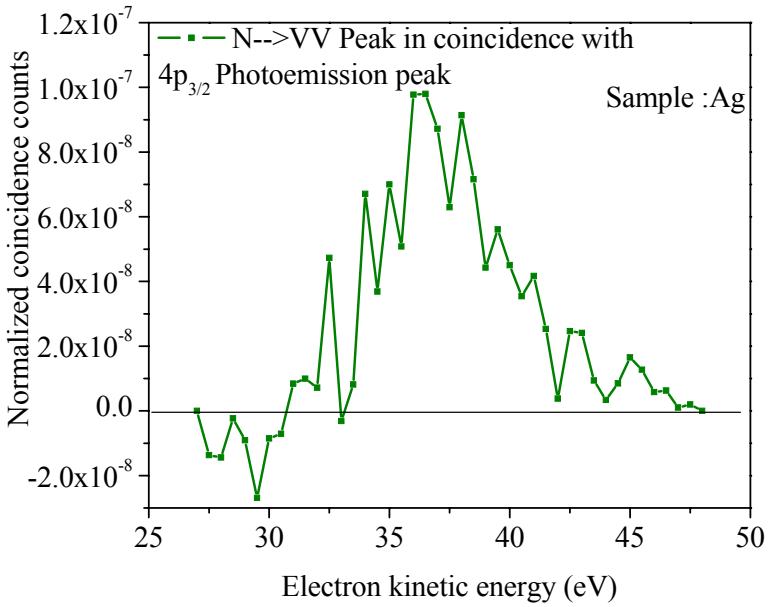

Fig. 4.20 Ag N→VV Augers measured in time coincidence with the $4p_{3/2}$ photoemission peak after subtraction of the background

Fig. 4.21 shows the comparison of the background subtracted area normalized AACS spectrum taken in coincidence with M→NV transition with an APECS spectrum measured in coincidence with photoelectrons from the $4p_{3/2}$ orbital.

This comparison reveals that while both cascade induced decay and direct decay show a peak at ~37eV, the spectrum measured following the Auger decay is much broader than the spectrum measured following the direct decay and shows spectral contributions that extend up ~5eV higher in energy. Shirley background subtraction has been performed to remove the inelastic background representing the experimental data.

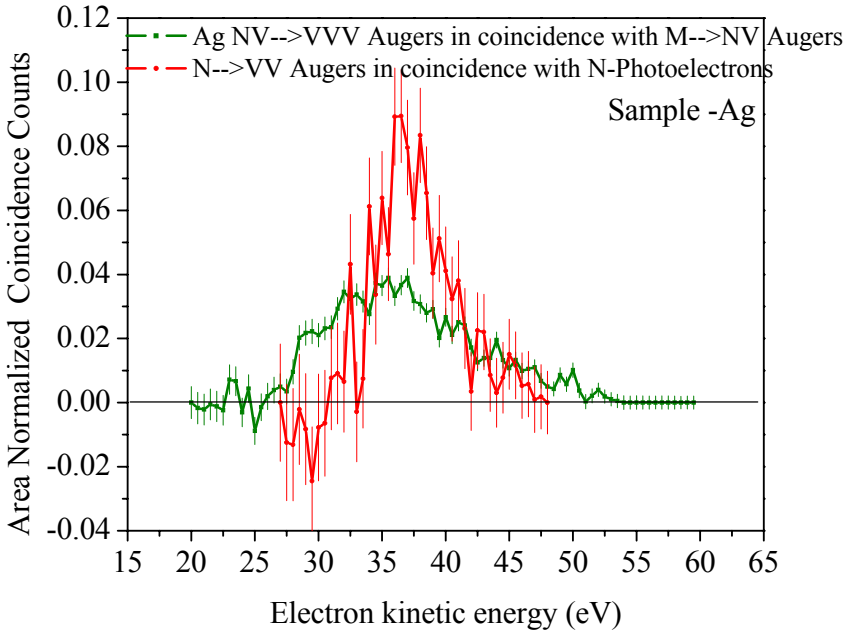

Fig. 4.21 Comparison of the spectra of Ag $N_{4,5}V$→VVV Augers measured in time coincidence with the electrons at 299eV (the peak of M→NV transition) (AACS-green) with the spectra of Ag $N_{4,5}$→VV Augers measured in time coincidence with the detection of electrons at 397eV (Ag $N_{4,5}$ photo-emission peak) (APECS-red) at a photon energy of 465eV

We posit that the significant broadening of the Auger–Auger coincidence spectra may be accounted for in terms of the participation of valence holes remaining from previous steps in the cascade. Model calculations are presented in chapter 6 for Ag that account for both the width and centroid of the individual spectra and from which the core-core (CC), core-valence (CV) and valence-valence (VV) correlation energies in the many-hole states are estimated.

CHAPTER 5

AACS AND APECS MEASUREMENT OF Pd

5.1 Pd Photoelectron spectrum

The Fig. 5.1 presents the wide range photoelectron spectrum of Pd deposited on Ag excited by photons of energy 465eV taken at the U16B beam line. All the important features of the spectrum labeled on the figure are shown here below.

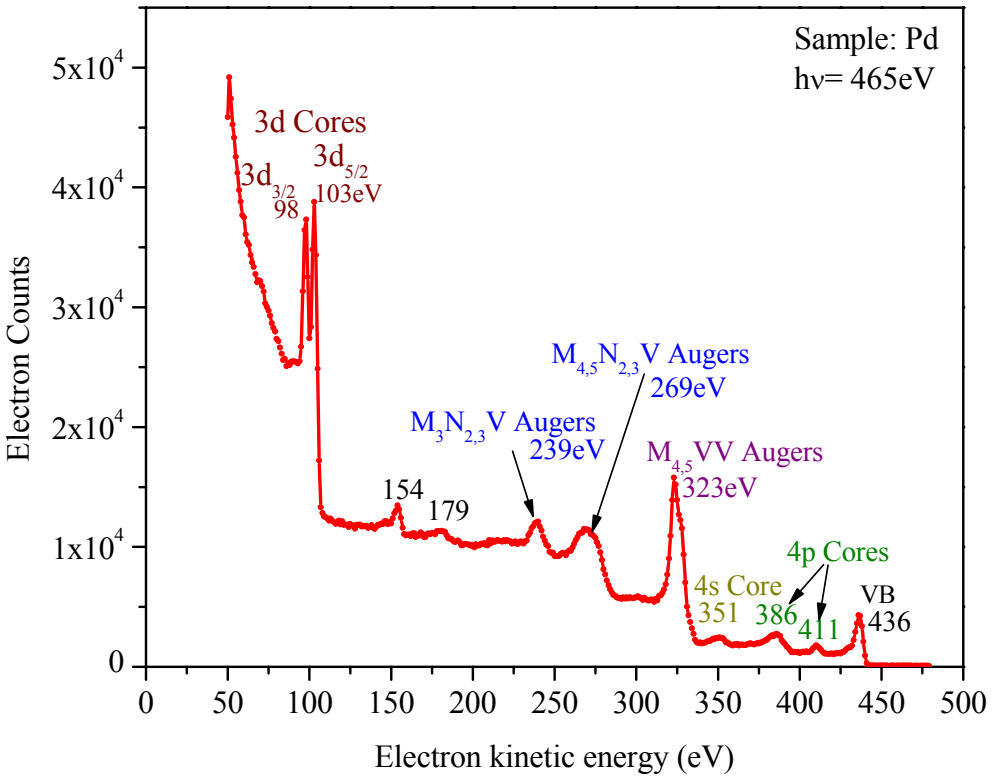

Fig. 5.1 Wide range photoelectron spectrum of Pd obtained at hν=465eV

There are two M shell core peaks M_4 and M_5 prominent at 98eV and 103eV respectively, and the two overlapping N core peaks N_4 and N_5 at ~386eV. These cores, when excited undergo direct Auger decay process where the final state of the decay transition is the $M_{4,5}$→VV Auger peaks at ~323eV. If the same $M_{4,5}$ core undergoes cascade decay, the intermediate step is $M_{4,5}$→N_1V Augers and $M_{4,5}$→$N_{2,3}$V Augers around 265 to 272eV respectively, while these N_1V and $N_{2,3}$V Augers further decay into 3 hole final state which is due to $N_{2,3}$V→VVV transition at ~35eV. The three hole final state ($N_{2,3}$V→VVV) is buried under a large secondary electron background which is not visible in the photoelectron spectrum.

5.2 Complete screening and Quasiatomic Pd M→VV Auger line shapes

A few interesting observations of the Pd MVV spectrum obtained by Kleimans group are discussed here. The binding energy of Pd L_3 is at 3173eV. Upon ionizing the L_3 shell of Pd at a photon energy of 3197eV, which is below the threshold of L_3, there is a noticeable extra structure observed on the high-energy side of the 10-40eV MVV spectrum. This is attributed to the extra M hole present during the MM→MVV transition. The MVV spectra on the low energy side shows bandlike nature, and its shape is does not appear to be altered by the fact that the Pd is excited above and below the ionization energy of the L_3 level. [110,126,127]

By exciting the atom above and below the ionization level of L_3, Kleiman's group endeavored to find the overall contribution of the intermediate holes formed in the Auger cascade which not only includes L→MM→MVV→VVVV. However their

spectra also include the contribution of the MV→VVV. They were not able to separate the contributions of the individual cascades.

5.3 Comparison of the low energy (20-60eV) M→VV Auger spectrum measured in time coincidence Pd $3d_{5/2}$ photoelectrons

The photon energy used to excite the Pd sample was 465eV which was sufficient enough to excite both M_4, M_5 and the N orbitals. Due to the thermal drift in the monochromator, there was drift in the peak position of the cores excited. The peak position was redetermined every 40 sweeps using routine "fit". These fitting parameters are stored in a separate folder so as to check for any abnormalities.

Fig. 5.2 shows the Pd $3p_{5/2}$ photoemission spectrum. In order to obtain the spectra of Pd M→VV spectrum in coincidence with the $3p_{5/2}$ photoelectrons, one of the CMA's with pass energy of 90eV was fixed at the M_5 peak ($3d5_{/2}$ peak ~ 102eV) while the other CMA with pass energy of 80eV was scanned for the MVV augers from 315eV to 340eV arising from the transition initiated by exciting the $3d_{5/2}$. Fig. 5.3 shows the M→VV Augers of Pd (red), Constant Background subtracted (Blue) and Shirley background subtracted M→VV (green). Fig. 5.4 shows the Shirley background subtracted M→VV Spectrum obtained in coincidence with the Pd M-cores.

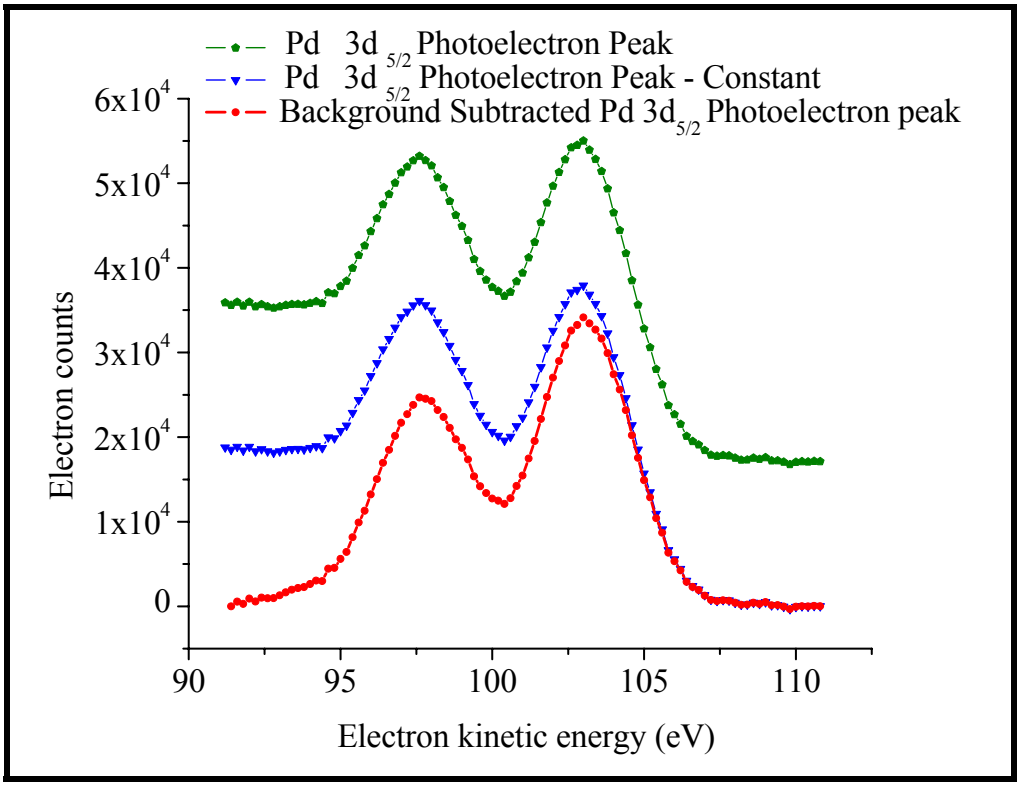

Fig. 5.2 Photoemission spectra of Pd $3d_{5/2}$ electrons (green), a constant background subtracted from the photoemission spectra of Pd $3d_{5/2}$ electrons (blue) with a shirley background subtraction (red)

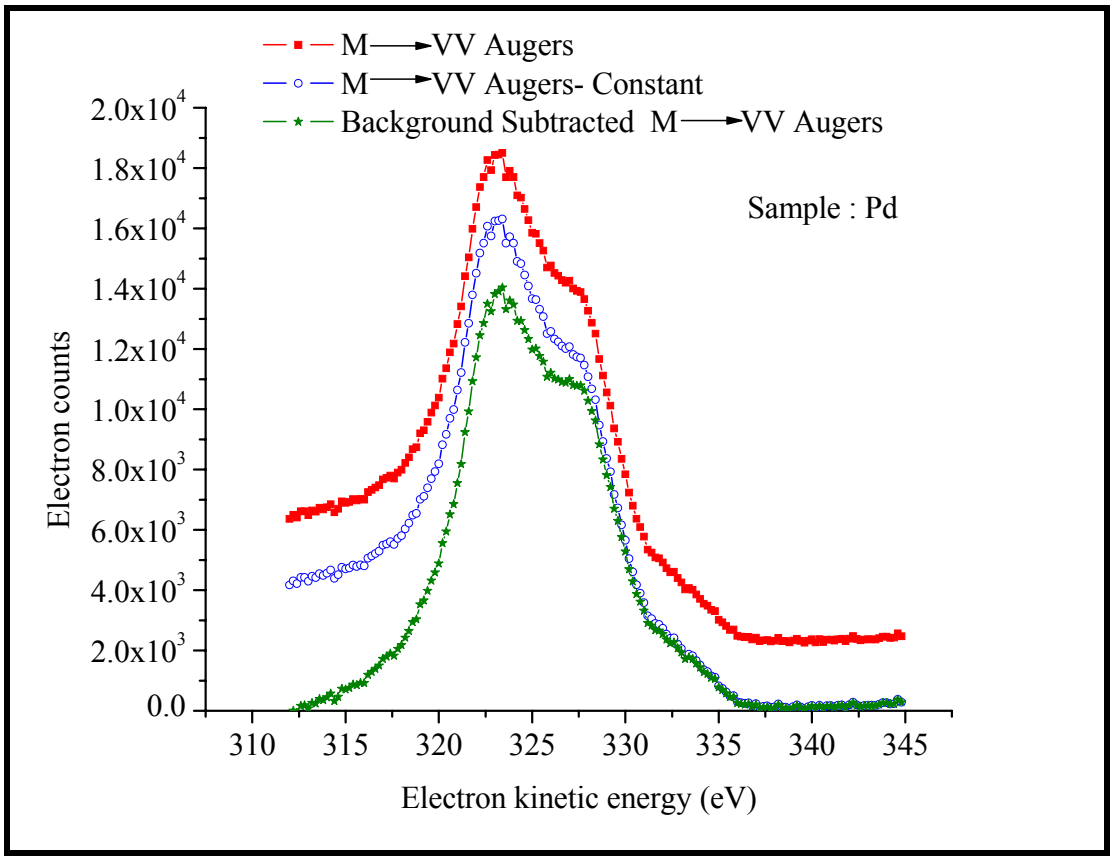

Fig. 5.3 Spectra of electrons emitted from Pd M→VV transition at a photon energy of 465eV (red). Spectra shown here are a constant background subtracted from the Pd M→VV Augers shown in blue, and these spectra are compared to the spectrum of M→VV with a Shirley background subtracted shown in green

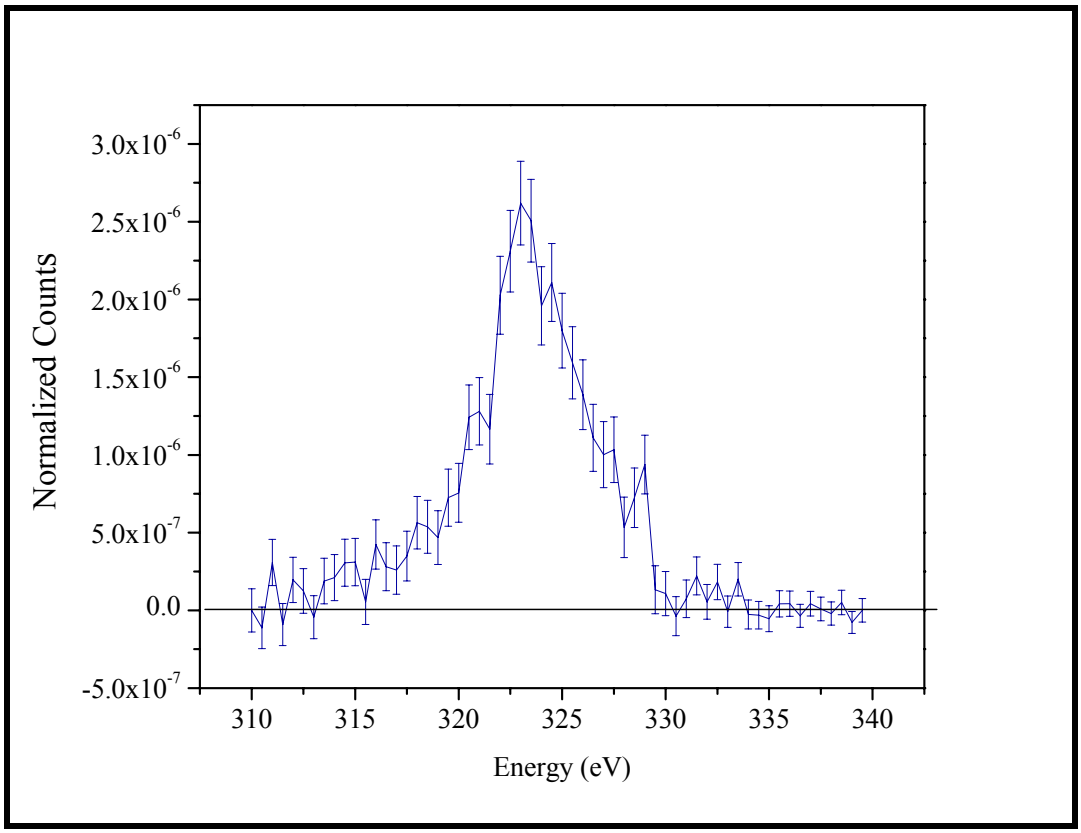

Fig. 5.4 Spectra of the electrons emitted from M→VV Auger transition measured at a photon energy of 465eV in time coincidence with the electrons emitted at 104eV (peak of the Pd 3d photoelectrons)

5.4 Low energy Pd $M_{4,5}$→ $N_{2,3}$V→VVV Auger cascade decay

This Auger cascade decay is initiated by the ionization of the M-level. It has one hole in the N level and one hole in the valence band in the intermediate state and the atom relaxes to a final state which has 3 holes in the valence band.

To obtain the Auger- Auger coincidence spectrum of the NV→VVV transition,

the LCMA with pass energy of 300eV was fixed at M→NV Auger peak at 279eV while the RCMA with pass energy of 80eV was scanned for the NV→VVV Augers from 20eV to 60eV. Fig. 5.5 shows the M→NV Augers as obtained at a photon energy of 465eV shown in blue. The spectrum with constant background subtracted is shown in red and with a Shirley background subtracted in blue. These spectra are compared with a Shirley background subtracted $M_{4,5}$→NV spectrum. The M→NV Augers at ~299eV are immediately followed by the N cores. To avoid the background from the N cores to M→NV Augers one of the analyzers was fixed at energy 300eV with pass energy of 400eV which allowed the fixed energy to vary from 398eV to 402eV between the N cores and the M→NV Augers and the other analyzer was scanned from 20eV to 60eV for the N→VV Augers at 80eV pass energy.

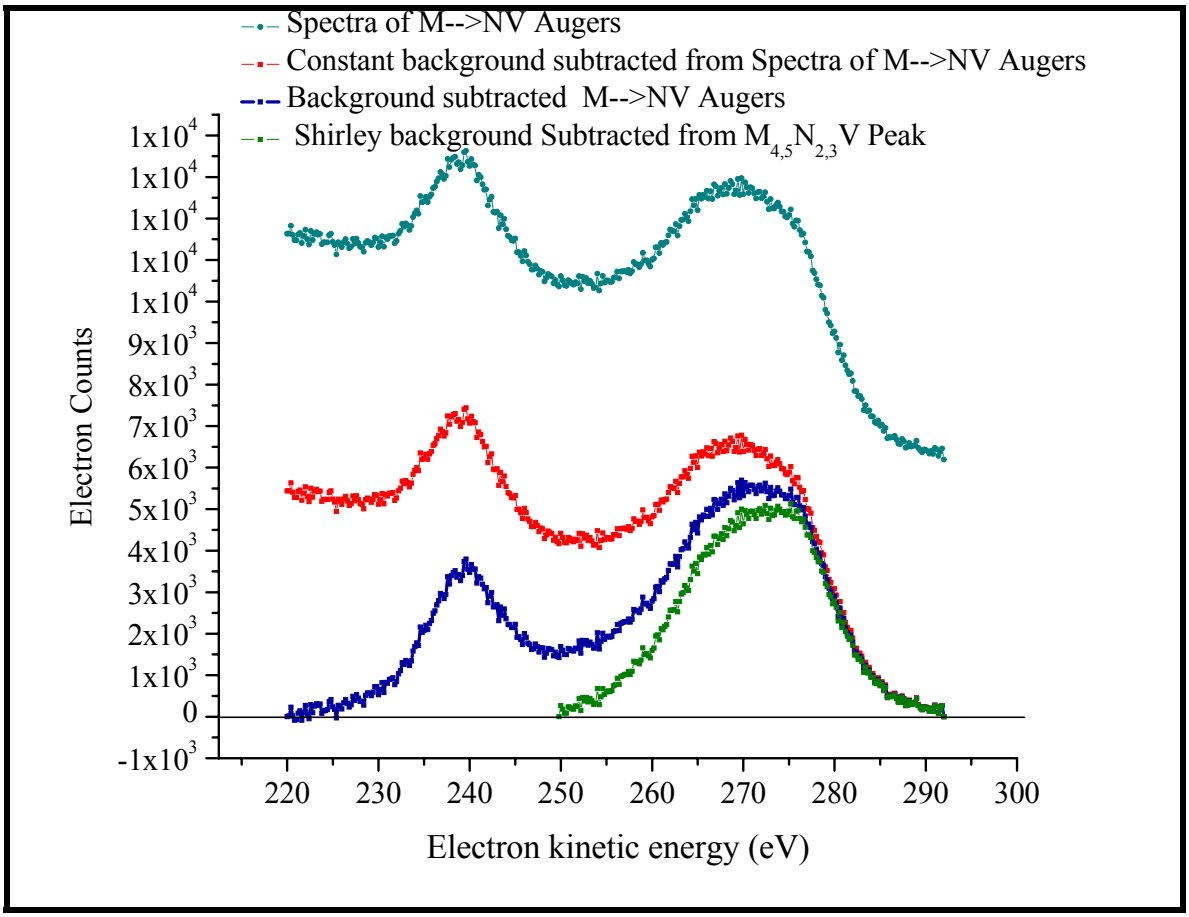

Fig. 5.5 Spectra of the electrons emitted from Pd M→NV Auger transition measured at a photon energy of 465eV. The spectrum are shown with a constant background subtracted (red), and Shirley background subtracted (blue) .These are compared to the spectrum of $M_{4,5}$→NV transition with a Shirley background subtracted

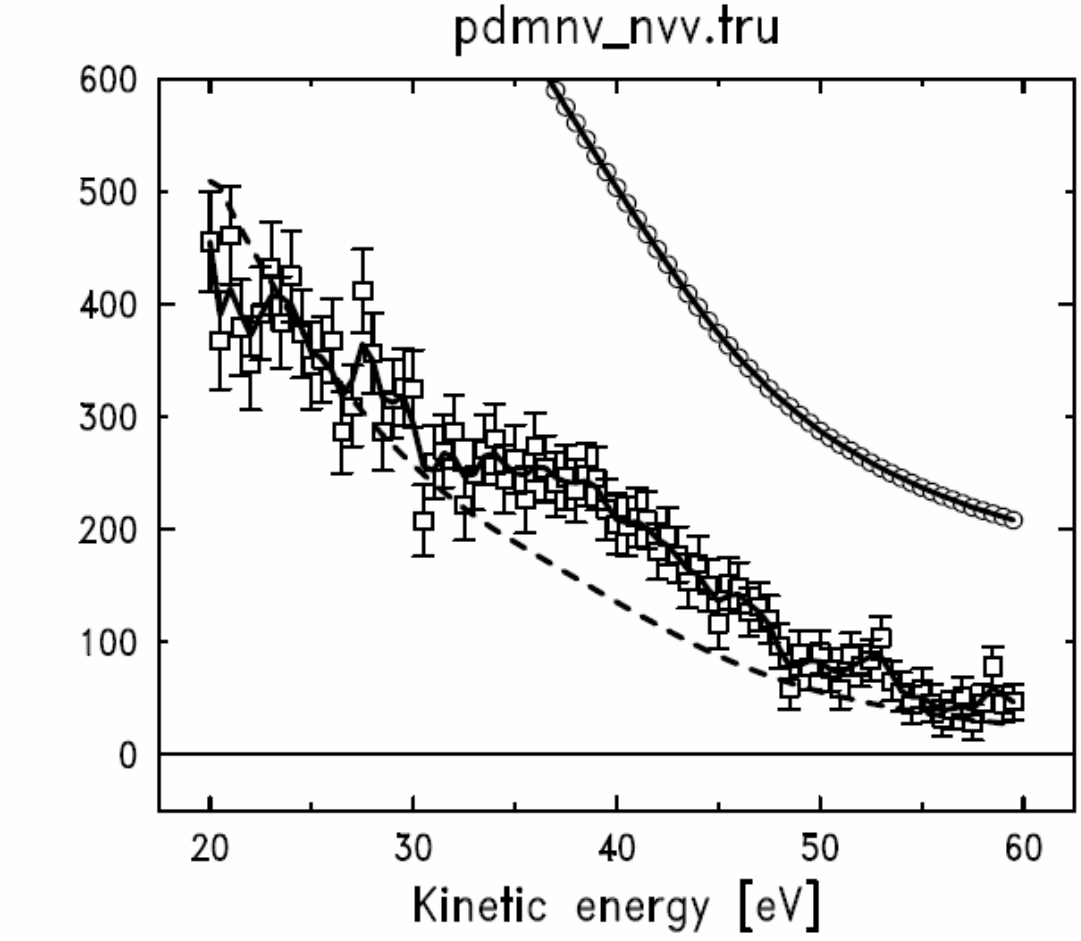

Fig. 5.6 The spectra of Pd $N_{4,5}V \rightarrow VVV$ Augers measured in time coincidence with the electrons emitted at 279eV (the peak of M→NV transition) taken at a photon energy of 465eV [Auger-Auger cascade decay]

Fig. 5.7 shows the background obtained from the N-cores which are in true coincidence with the NV→VVV spectrum. Fig. 5.8 shows the background (green) from the N cores to the NV→VVV spectrum, Pd NV→VVV coincidence spectrum (red) normalized to sum of S1, and Normalized background subtracted from Pd NV→VVV coincidence

spectrum(blue). Still there is the inelastic background which was not eliminated by the coincidence. This has to be removed to obtain the real coincident spectrum. So a Shirley background subtraction was performed and the resultant area normalized NV-VVV coincidence spectrum is shown in Fig. 5.9.

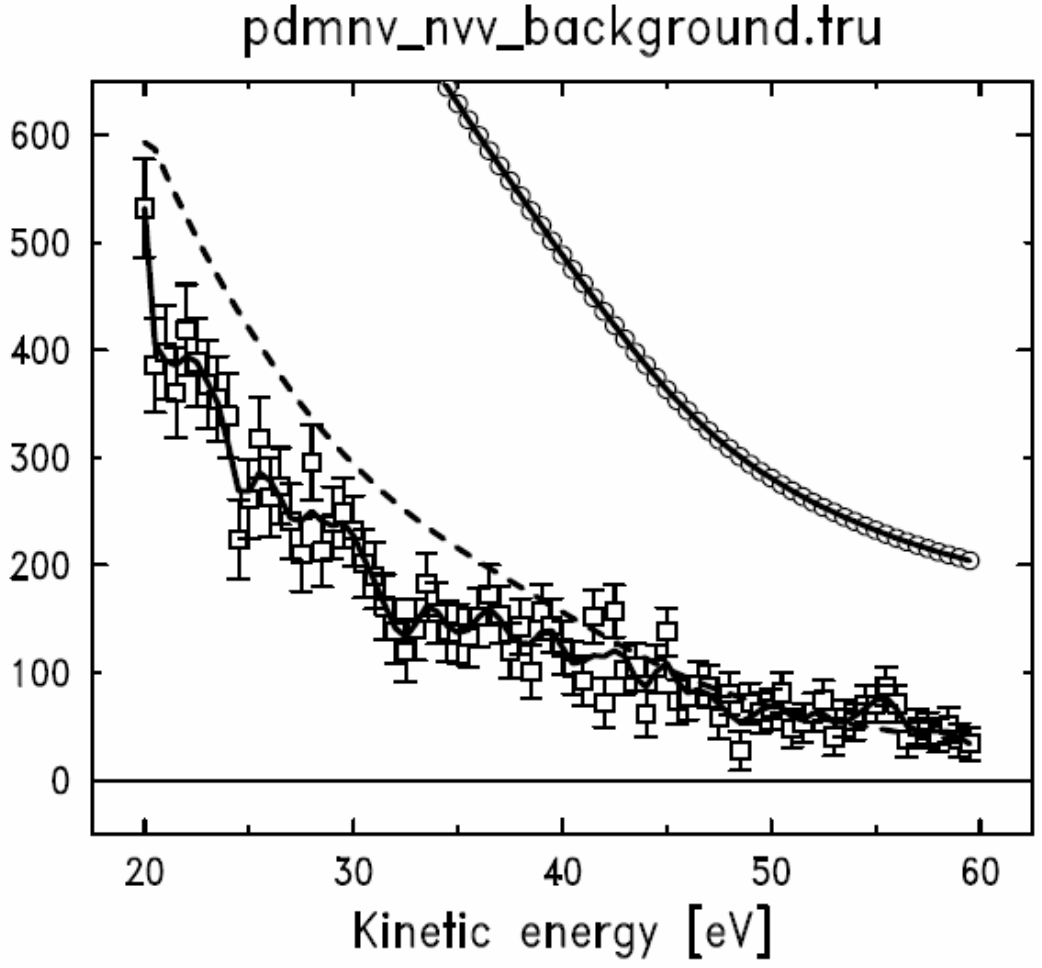

Fig. 5.7 Spectra of electrons emitted in the range of 20-60eV in time coincidence with electrons emitted (at 300eV) in the tail of the M→NV Auger spectrum

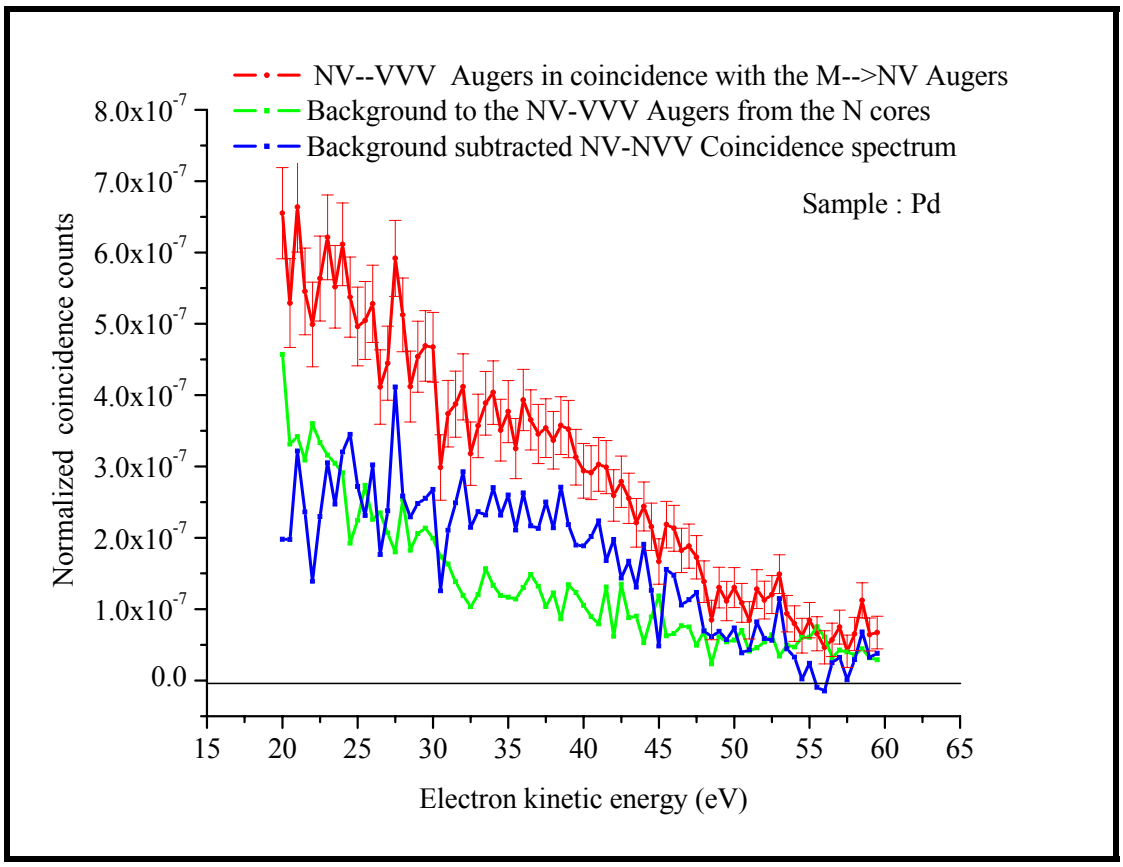

Fig. 5.8 Pd NV→VVV spectrum of electrons in time coincidence with M→NV Auger electrons (red) and electrons emitted in the range of 20-60eV in time coincidence with electrons emitted at ~300eV in the tail of M→NV Auger peak (green). Spectra of Ag NV→VVV coincidence spectrum after the subtraction of the measured background to the NV→VVV Auger peak from the 4p cores

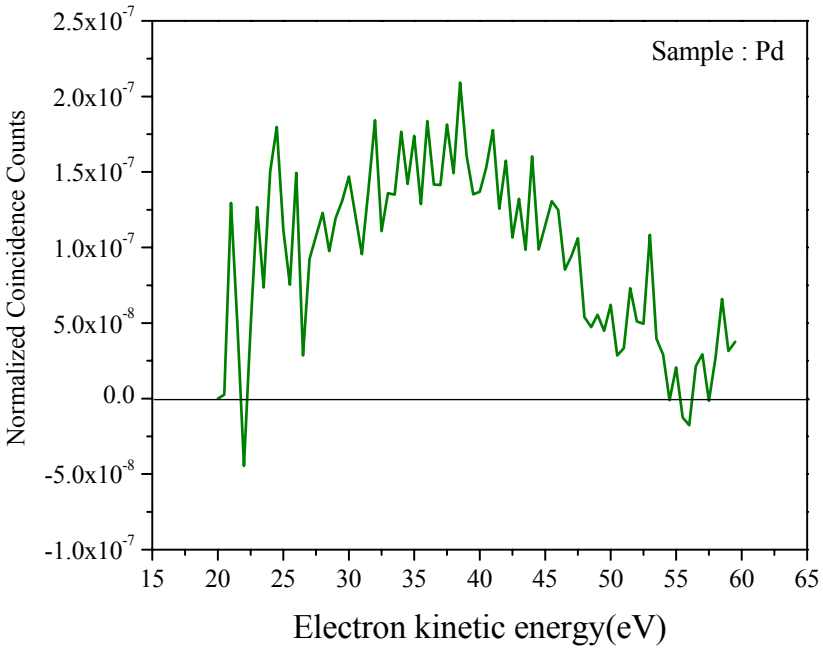

Fig. 5.9 The spectra of Pd NV→VVV Augers emitted in the energy range 20-60eV in time coincidence with the electrons emitted at 279eV (the peak of M→NV transition) after Shirley background subtraction

5.5 The spectra of $N_{2,3}$→VV Augers taken in time coincidence with the electrons at (386eV) the peak of 4p photoelectrons

The 4p cores have a binding energy of 55.7eV and 50.9eV. When we excite the sample with photon energy 465eV, the 4p cores peak at ~386eV To obtain the N→VV Auger-Auger coincidence spectrum of the N→VV transition, one of the CMA's with pass energy of 300eV was fixed at the 4p3/2 core peak at 397eV while the other CMA with pass energy of 80eV was scanned for the N→VV augers from 25eV to 60eV. Fig. 5.10 shows the coincidence spectrum of electron emitted in the range of N→VV

Augers. Fig. 5.11 shows the same spectra with a Shirley background subtracted and area normalized N→VV coincidence spectrum [128-130].

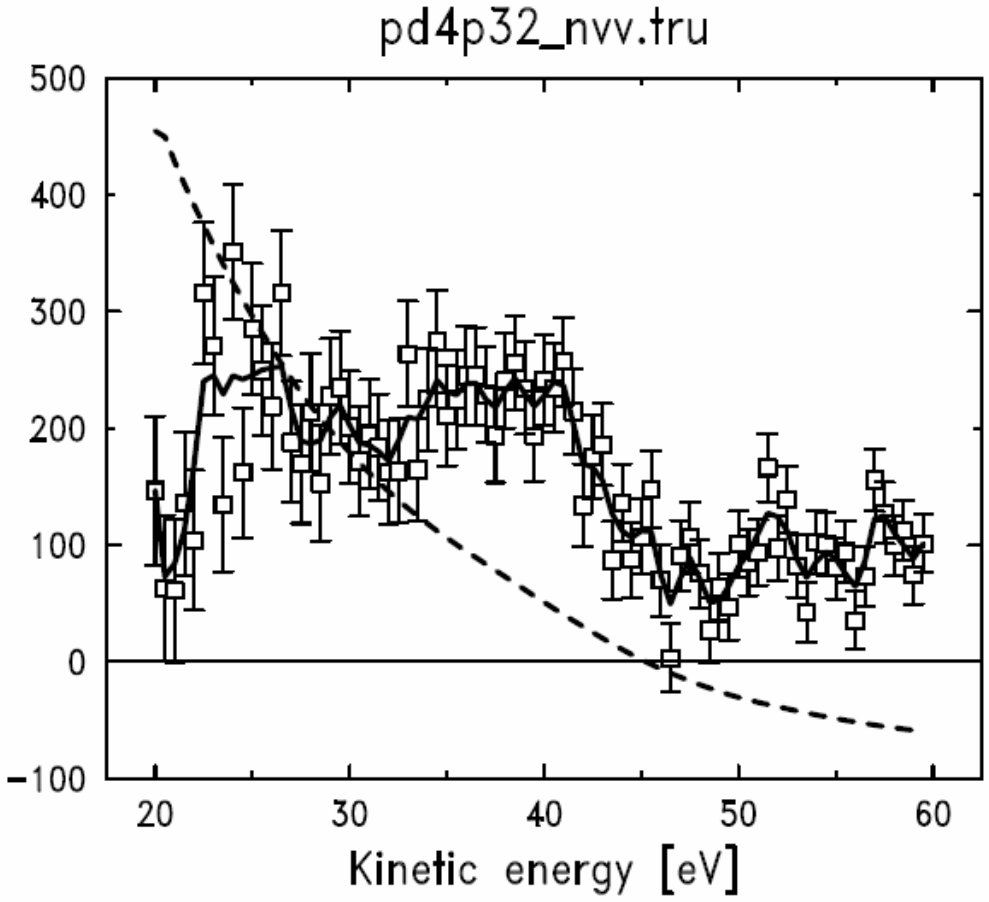

Fig. 5.10 The spectra of Pd $N_{2,3}$→VV Augers measured in time coincidence with the electrons emitted at 411eV (The $4p_{3/2}$ photoelectron peak) [APECS]

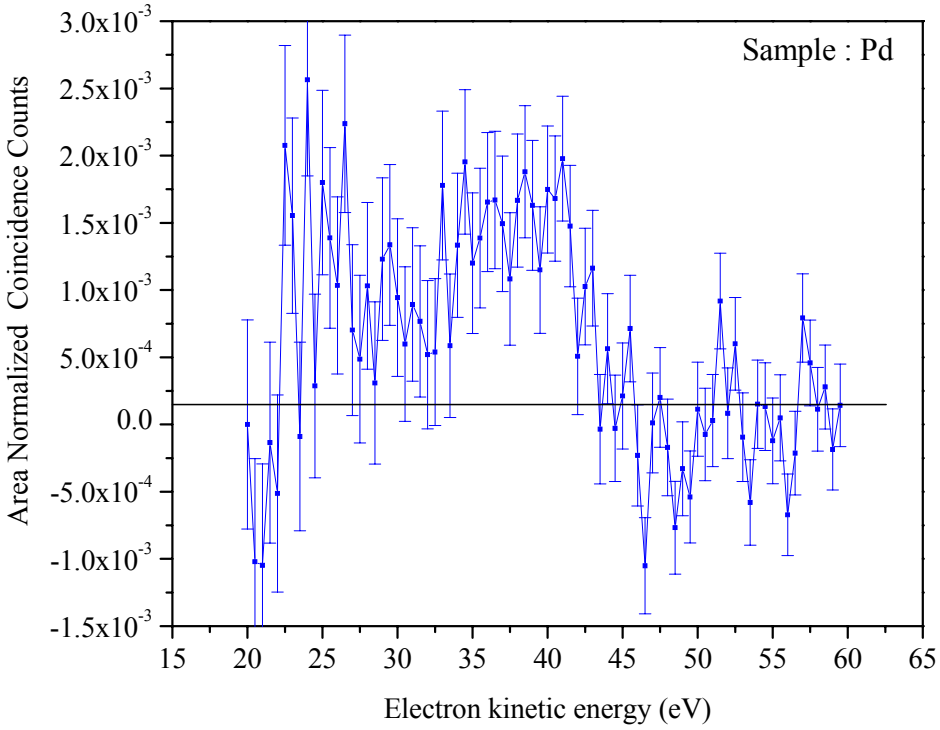

Fig. 5.11 Pd N→VV Augers measured in time coincidence with the $4p_{3/2}$ photoemission peak after subtraction of the background

The comparison of the AACS and the APECS spectra shows that the AACS spectra is significantly wider than the APECS spectra and, this can be explained only if the valence holes present in the initial state changes energy during the Auger transition NV→VVV. As there are no holes in the initial state of the direct decay process the width of the APECS spectrum is narrow as compared to the width obtained by the AACS. A theoretical model based on this assumption is developed in the next chapter fits the experimental data lending strong support to this hypothesis. The correlation energies (U's) obtained for the Pd are as follows: U_{dd}=3eV and U_{pd}=4.5eV and the BE of the 4p3/2 is taken to be 54.0eV.

CHAPTER 6

THEORETICAL MODEL OF THE AACS SPECTRA

6.1 Cascade phenomenon

In chapter 3, Fig. 3.22 shows a comparison between the AACS spectrum taken in coincidence with the $L_{2,3}\rightarrow M_{2,3}M_{2,3}$ transition (corresponding to the sum of the spectra of the $M_{2,3}M_{2,3}\rightarrow M_{2,3}VV$, $M_{2,3}VV\rightarrow VVVV$ transitions) with an APECS spectrum measured in coincidence with photoelectrons from the 3p ($M_{2,3}$) level. This comparison reveals that while both cascade induced decay and direct decay show a peak at ~32 eV, the spectrum measured following the Auger decay is much broader than the spectrum measured following the direct decay and shows spectral contributions that extend up ~5 eV higher in energy. Both the spectra exhibit significant inelastic background at the low energy side. We posit that the significant broadening of the Auger–Auger coincidence spectra may be accounted for in terms of the participation of valence holes remaining from previous steps in the cascade. Model calculations are presented that account for both the width and centroid of the individual spectra and from which the core-core (CC), core-valence (CV) and valence-valence (VV) correlation energies in the many-hole states are estimated. The calculations indicate that rearrangement of participator valence holes in the transition can lead to energy gains as large as the width of the valence band.[131-133] Such energy gains are larger

than previously observed from shake-up contributions to direct Auger transitions and constitute a maximal violation of the two step model in which it is assumed that the core hole states are fully relaxed by the time of the Auger transition[134-136].

The decay schemes for the cascade Auger channels of interest previously described in chapter 3 along with the illustration of the rearrangement of the participator holes are shown in Fig.6.1. The transitions are labeled in terms of the holes in the initial and final states with the assumption that the valence holes created in previous decay steps remain unfilled at the time of subsequent decays. The upper pathway of Fig. 6.1 show a L→MM cascade chain in which a L_{23} core hole results in the emission of an Auger electron at 535eV and leaves the ion with two holes in the M_{23} level. These holes subsequently decay via sequential transitions A ($M_{23}M_{23}$→M_{23}VV) and B (M_{23}VV→VVVV), both of which result in the emission of Auger electrons in the same range of kinetic energies (20 - 60eV) as the direct M_{23}→VV Auger transition. The lower pathway of Fig. 6.1, illustrates a L→MV cascade in which a L_{23} hole decays by ejecting an Auger electron at 578eV and leaves the ion with one hole in the valence band and one in the M_{23} level. This intermediate state decays via transition C (M_{23}V→VVV) in which an Auger electron is emitted in the same KE range as processes A and B.

A conventional, non-coincidence (also called singles) photoemission spectrum was acquired along with the coincidence data discussed in detail in earlier chapter Fig. 3.1 shows an energy spectrum of electrons emitted from the MnO surface as a result of irradiation with 740eV photons. The three features at 535 eV (Mn LMM), 578 eV (Mn

LMV), and 631eV (Mn LVV), correspond to the Mn LMM, LMV and LVV Auger transitions, respectively. The Fig 3.2 shows a broad peak near 33eV which contains contributions from the direct M→VV transition resulting from photo-ionization of the $M_{2,3}$ level, as well as electrons emitted in transitions A, B, and C, of the cascade processes shown in Fig. 6.1. Fig. 3.20 shows a comparison of the energy spectra of electrons in the range from 20 to 60eV taken in coincidence with the electrons from $L_{2,3}\rightarrow M_{2,3}M_{2,3}$ (A & B), $L_{2,3}\rightarrow M_{2,3}V$ (C), $L_{2,3}\rightarrow VV$ Auger transitions measured at photon energy of 660eV . The data shown in figures will be compared with the theoretical model.

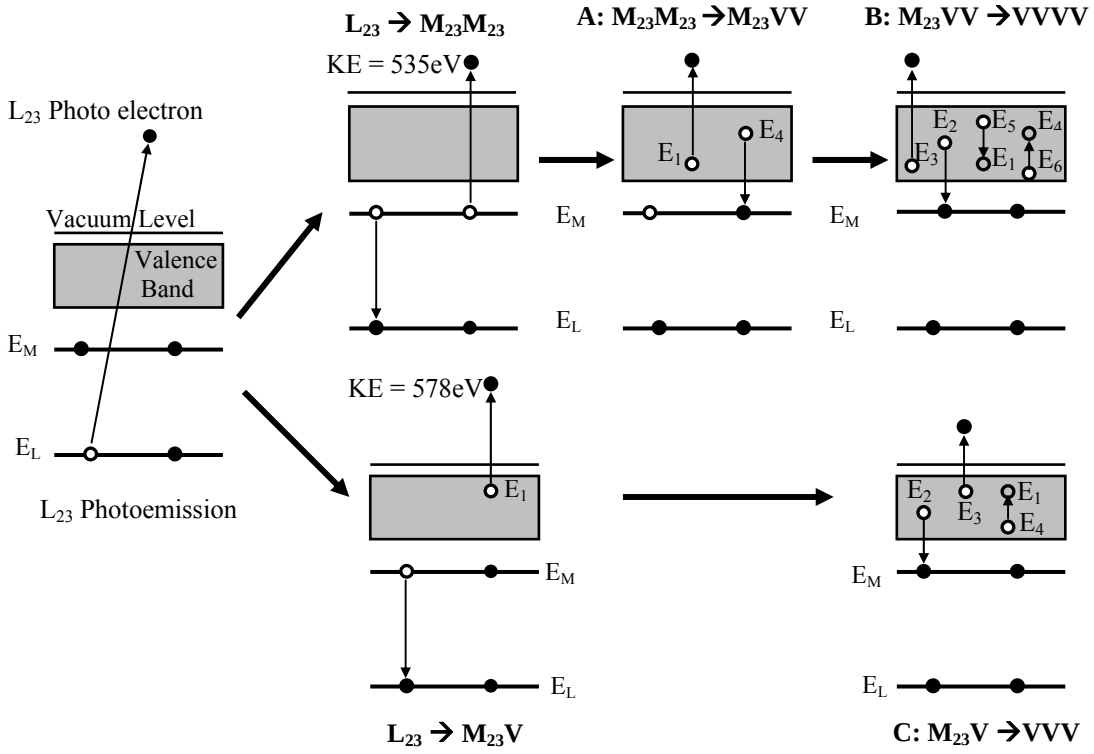

Fig. 6.1 The decay schemes for the cascade Auger channels of $L_{2,3}$ photoemission

6.2 Heuristic model to explain the energy gain on the high energy side of the Auger-Auger cascade spectra

Here we present a heuristic model to explain the extra spectral weight at higher energy and the increase in energy widths of the spectra corresponding to the $M_{2,3}V \rightarrow VVV$ transition and the $M_{2,3}M_{2,3} \rightarrow M_{2,3}VV$, and $M_{2,3}VV \rightarrow VVVV$ transitions as compared to the direct $M_{2,3} \rightarrow VV$ transition. In this model we posit that the additional energy stems from the rearrangement of "not so innocent" by-stander hole(s) in the valence band. Let us consider the extreme cases when Auger electrons have the highest and lowest kinetic energies.

6.2.1 The direct M-excitation: $M_{2,3} \rightarrow VV$ transition

First, consider the $M_{2,3} \rightarrow VV$ process following the direct excitation of an M-hole with no "spectator" holes in the valence band. This is the direct excitation of the M-hole (APECS). The energy of the initial state is given by $E_i = E_M$ and the energy of the final state is given by $E_f = E_{KE\ MVVAuger} + V_1 + V_2 + U_{12}$ where M and V_i are the energies of the core hole and valence holes respectively, U_{ij} is the energy of hole-hole repulsion, and E_{KE} is the kinetic energy of the Auger electron. Equating E_f and E_i, and taking V_t and V_b, to be the top and bottom of the valence band, since the binding energies of the core levels are with respect to the top of the valence band, it may be seen from Fig. 6.2(a) and 6.2(b), that the highest and lowest energy Auger electrons are emitted with kinetic energies: (where $W = V_b - V_t$ is the valence band width.)

$$E_{kMax} = E_M - 2V_t - U_{dd} - \phi \quad (1)$$

and $$E_{KMin} = E_M - 2V_b - U_{dd} - \phi \quad .. \ (2)$$

respectively, where U_{dd} is the correlation energy between the two holes in the valence band .

In this case the full width of the Auger peak is given by:

$$FWFM\ (M\rightarrow VV) = E_{kMax} - E_{kMin}$$

$$= (E_M - 2V_t - U_{dd} - \phi) - (E_M - 2V_b - U_{dd} - \phi)$$

$$= 2(V_b - V_t) = 2W \qquad (3)$$

6.2.2 Modeling of the spectra of the $L_{2,3}\rightarrow M_{2,3}V$ Auger cascade step

Fig 6.3(a) and 6.3(b) shows a schematic of two possible valence hole rearrangements during the $M_{2,3}V\rightarrow VVV$ transition (following after a $L_{2,3}\rightarrow M_{2,3}V$ transition). The transition leading to the highest energy Auger electron (shown Fig. 6.3(a)) has one hole in the $M_{2,3}$ level and one hole at the bottom of the valence band and the final state has three holes at the top of the valence band. This transition results in an Auger electron of kinetic energy:

$$E_{kMax} = (E_M + V_b + U_{pd}) - (3V_t + 3U_{dd} + \phi)$$

$$E_{kMax} = E_M - 3V_t + V_b + U_{pd} - 3U_{dd} - \phi \qquad (4)$$

The lowest energy Auger electron results from a transition (shown in Fig. 6.3 (b)) in which the initial state has one hole in the M level and one at the top of the valence band and the final state has three holes at the bottom of the valence band resulting in a kinetic energy,

$$E_{KMin} = (E_M + V_t + U_{pd}) - (3V_b + 3U_{dd} + \phi)$$

$$E_{KMin} = E_M + V_t + U_{pd} - 3V_b - 3U_{dd} - \phi \qquad (5)$$

where U_{pd} accounts for repulsion between core and valence holes .

The full width of the Auger peak can be estimated from the difference between the most energetic and least energetic Auger electron:

FWFM ($M_{2,3}V \rightarrow VVV$)

$$= E_{kMax} - E_{KMin}$$

$$= (E_M - 3V_t + V_b + U_{pd} - 3U_{dd} - \phi) - (E_M + V_t + U_{pd} - 3V_b - 3U_{dd} - \phi)$$

$$= 4(V_b - V_t) = 4W \quad (6)$$

Comparing equations (4) and (5) it may be seen that an "extra" energy of W is made available to the highest kinetic Auger electron during the $M_{2,3}V \rightarrow VVV$ transition when an electron at the top of the valence band fills the initial hole in the bottom of the valance band. In addition, a comparison of equations (3) and (6), shows that the FWFM increases from 2W for the direct $M \rightarrow VV$ transition to 4W for the $M_{2,3}V \rightarrow VVV$ transition.

6.2.3 Modeling of the spectra of the $M_{2,3}M_{2,3} \rightarrow VVVV$ Auger cascade step

In a similar way, let us examine the highest and lowest energy Auger electrons emitted by the $M_{2,3}$ $M_{2,3} \rightarrow M_{2,3}VV \rightarrow VVVV$ transitions in $M_{2,3}$ $M_{2,3} \rightarrow VVVV$ Auger cascade.

6.2.3.1 Modeling of the $M_{2,3}M_{2,3} \rightarrow M_{2,3}VV$ transition

Fig. 6.4(a) and 6.4(b) shows a schematic of two possible valence hole rearrangements during the $M_{2,3}M_{2,3} \rightarrow M_{2,3}VV$ transition.

$$E_{KMax} = 2E_M + U_{pp} - E_M - 2V_t - U_{dd} - 2U_{pd} - \phi \quad (7)$$

and $$E_{KMin} = 2E_M + U_{pp} - 2V_b - U_{dd} - 2U_{pd} - \phi \quad (8)$$

where U_{pp} is the correlation energies for two holes in the core level and the U_{pd} is the correlation energy between the hole in the core level and the hole in the valence band. Thus we have

$$E_{KMax} - E_{KMin} = (2E_M+U_{pp}- E_M -2V_t–U_{dd}-2U_{pd}-\phi)-(2E_M+U_{pp}+ E_M -2V_b- U_{dd} -2U_{pd}-\phi)$$

$$E_{KMax} - E_{KMin} = 2 (V_b – V_t) = 2W \quad (9)$$

This width resembles the $M_{2,3} \rightarrow VV$ model, since there are no holes in the initial state.

6.2.3.2 Modeling of the $M_{2,3}VV \rightarrow VVVV$ transition

Fig. 6.5(a) and 6.5(b) shows a schematic of two possible valence hole rearrangements during the $M_{2,3}VV \rightarrow VVVV$ transition giving rise to highest and lowest kinetic energies.

$$E_{KMax} = E_M +2V_b +2U_{pd} +U_{dd}-4V_t -6U_{dd} -\phi = E_M +2V_b - 4V_t +2U_{pd}-5U_{dd} -\phi \quad (10)$$

$$E_{KMin} = E_M +2V_t +2U_{pd} +U_{dd} - 4V_b -6U_{dd} -\phi = E_M +2V_t +2U_{pd} - 4V_b -5U_{dd} -\phi \quad (11)$$

$$E_{KMax} - E_{KMin} = (E_M +2V_b - 4V_t +2U_{pd}-5U_{dd} -\phi) - (E_M +2V_t +2U_{pd} - 4V_b -5U_{dd} -\phi)$$

$$E_{KMax} - E_{KMin} = 6(V_b – V_t) = 6W \quad (12)$$

For the transition $M_{2,3}VV \rightarrow VVVV$, we have two holes in the valence band and one hole in the $M_{2,3}$ -level. So the presence of the two holes in the initial state gives the extra width to the Auger-Auger coincidence spectrum which is attributed to the rearrangement of “not so innocent” by-stander hole(s) in the valence band or the “participator holes” in the valence band.

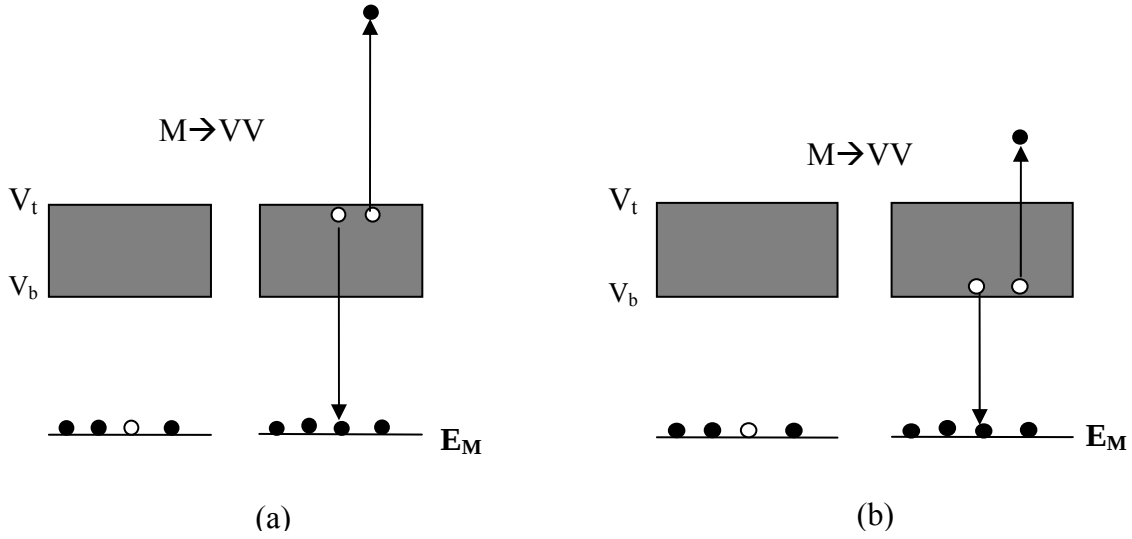

Fig. 6.2 Kinetic energy of the outgoing M→VV Auger electron
(a)highest (b)lowest

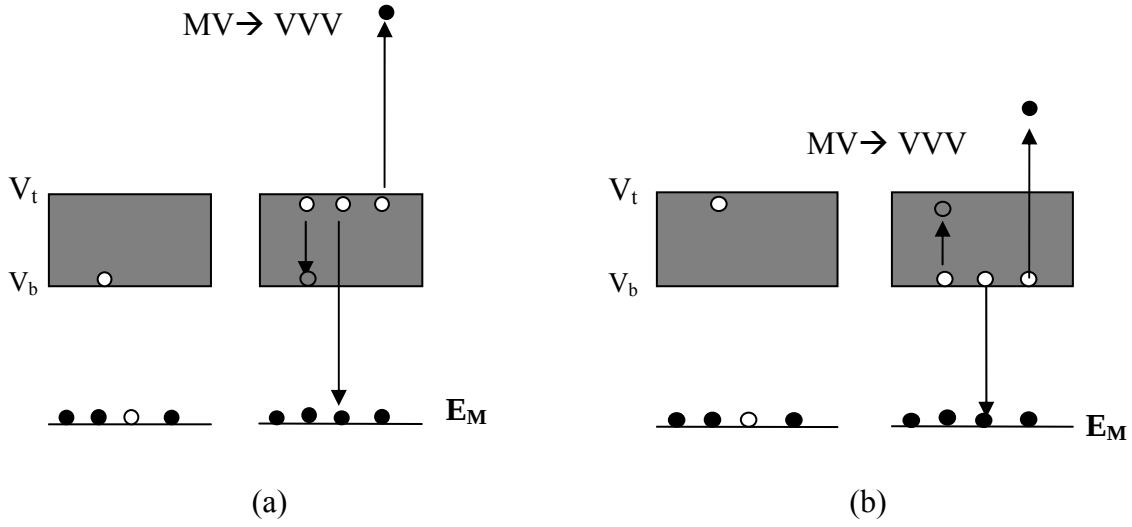

Fig. 6.3 Kinetic energy of the outgoing MV→VVV Auger electron
(a)highest (b)lowest

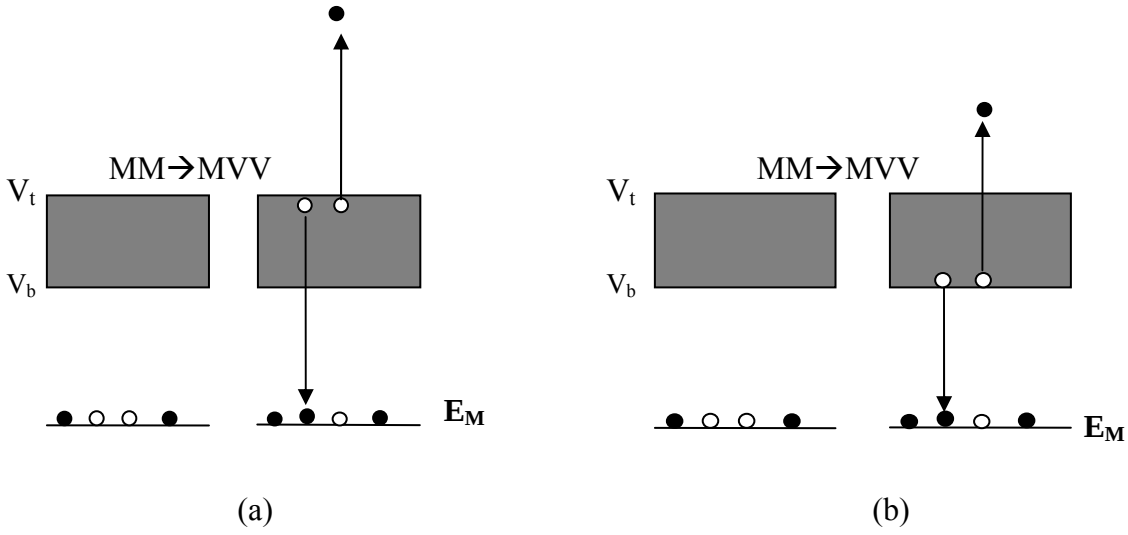

Fig. 6.4 Kinetic energy of the outgoing MM→MVV Auger electron
(a)highest (b)lowest

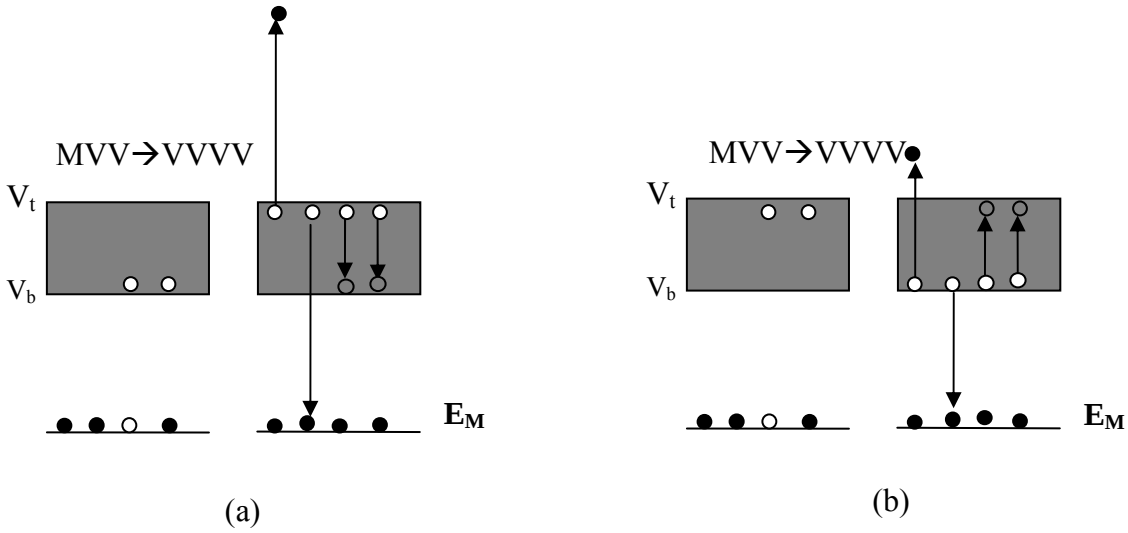

Fig. 6.5 Kinetic energy of the outgoing MVV→VVVV Auger electron
(a)highest (b)lowest

6.3 Detailed model of the later steps in the Auger cascade processes in solids

The influence of participator hole dynamics on the peak energy and width of the cascade Auger spectra can be estimated using a more detailed model that accounts for the possible rearrangements of holes within the valance band. The line shapes of the transitions are found from multiple-integrations over products of the valence band densities of states (VBDOS) and an energy conserving delta function. Constants U_{dd}, U_{pd} and U_{pp}, are used to describe the CC, CV and VV correlation energies between the holes respectively. These correlation energies, valence band hole energies (i.e.) E_1, E_2 and the spectrometer work function (ϕ) are taken into account in the energy conserving delta function.

In the case of the direct $M_{2,3}$→VV Auger transition this model yields the result that the Auger spectrum is proportional to a shifted self convolution of the DOS, a function well known to be appropriate for modeling band like Auger transitions.

Applying conservation of energy for this case, after setting

Energy (Initial state) = Energy (Final state):

$E_M = E_1 + E_2 + U_{dd} + KE_{MVVAuger} + \phi$ where E_M, E_1 and E_2 are the energies of the two holes created in the valence band, U_{dd} is the correlation energy between those holes, defining $U_1 = U_{dd} + \phi$, and rearranging the terms we have

$KE_{MVVAuger} = E_M - E_1 - E_2 - U_1$

Thus the energy conserving delta function may be expressed as

$\delta(KE_{MVVAuger} + E_1 + E_2 - E_M + U_1)$,

$$N(KE_{MVVAuger}) = \int_{-\infty}^{\infty}\int_{-\infty}^{\infty} \rho(E_1)\rho(E_2)\delta(KE_{MVVAuger} + E_1 + E_2 - E_M + U_1)dE_1 dE_2 \quad (13)$$

Integrating with respect to E_2, we have (Solving for $E_2 = E_M - E_1 - U_1 - KE_{MVVAuger}$)

$$N_{MVVAuger}(KE) = \int_{-\infty}^{\infty} \rho(E_1)\rho(E_M - E_1 - U_1 - KE_{MVVAuger})]dE_1 \quad (14)$$

Thus we may write:

$$N_{MVV\ Auger}(KE) \propto \rho * \rho(KE_{MVVAuger} - E_M + U_1) \quad (15)$$

where $\rho(E)$ represents the VBDOS, $U_1 \equiv U_{dd} + \phi$ and the symbol * is the convolution operator.

The photoemission spectrum of MnO in Fig. 6.6 shows the Mn 3p core and the valence band taken at photon energy 200eV. The interpolated valence band on MnO is shown in Fig. 6.7. The self convoluted VBDOS compared with the APECS spectrum obtained at 620eV photon energy is shown in Fig. 6.8.

In contrast, for the transitions in the Auger cascade processes, the model predicts that the cascade induced transitions will be significantly wider. For example, for the $M_{2,3}V \rightarrow VVV$ transition (transition C in Fig. 6.1) the line shape is found by integrating over the product of the VBDOS's of the initial valence hole and the three final state valence holes which can explained using the calculation shown here.

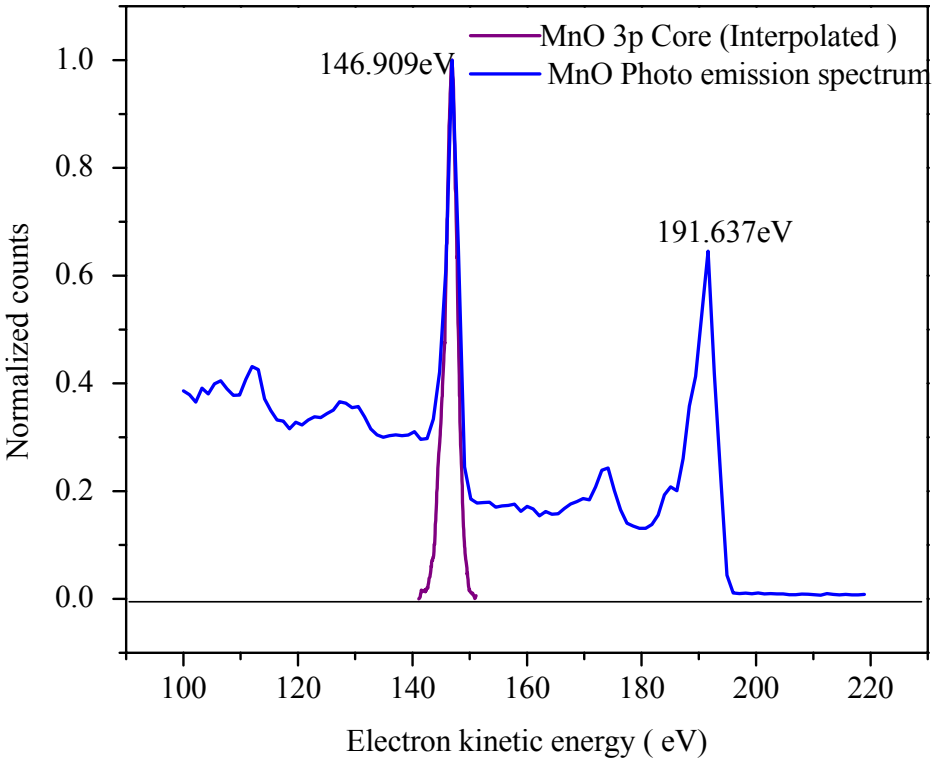

Fig. 6.6 Photoemission spectrum of MnO taken at a photon energy of 200eV. The purple spectrum shows the interpolated Mn 3p core

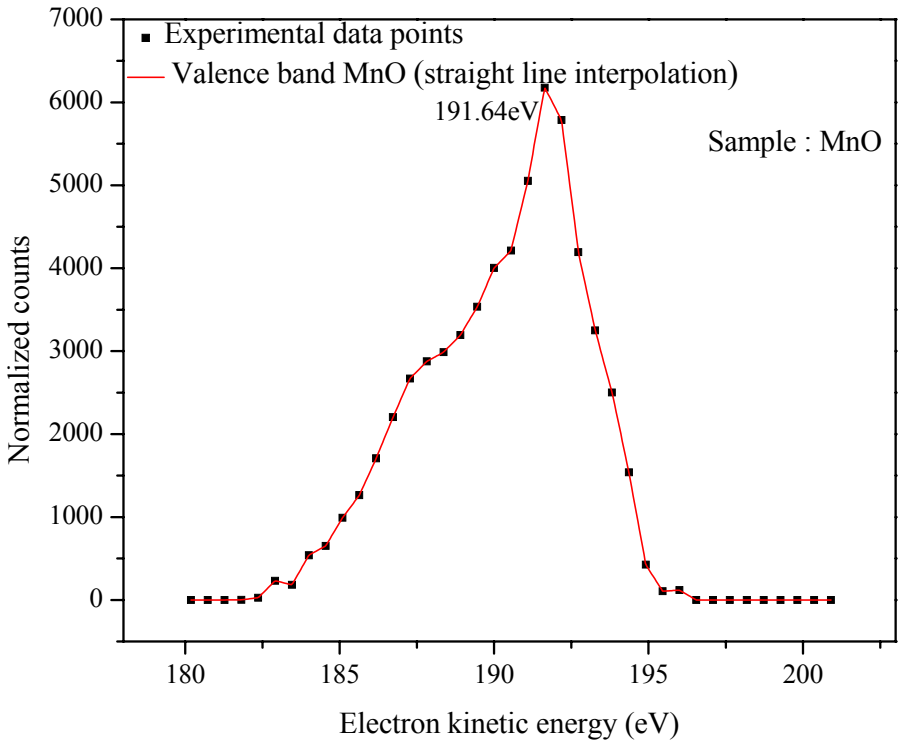

Fig. 6.7 Photoemission spectrum from valence band of MnO measured with a photon energy of 740eV

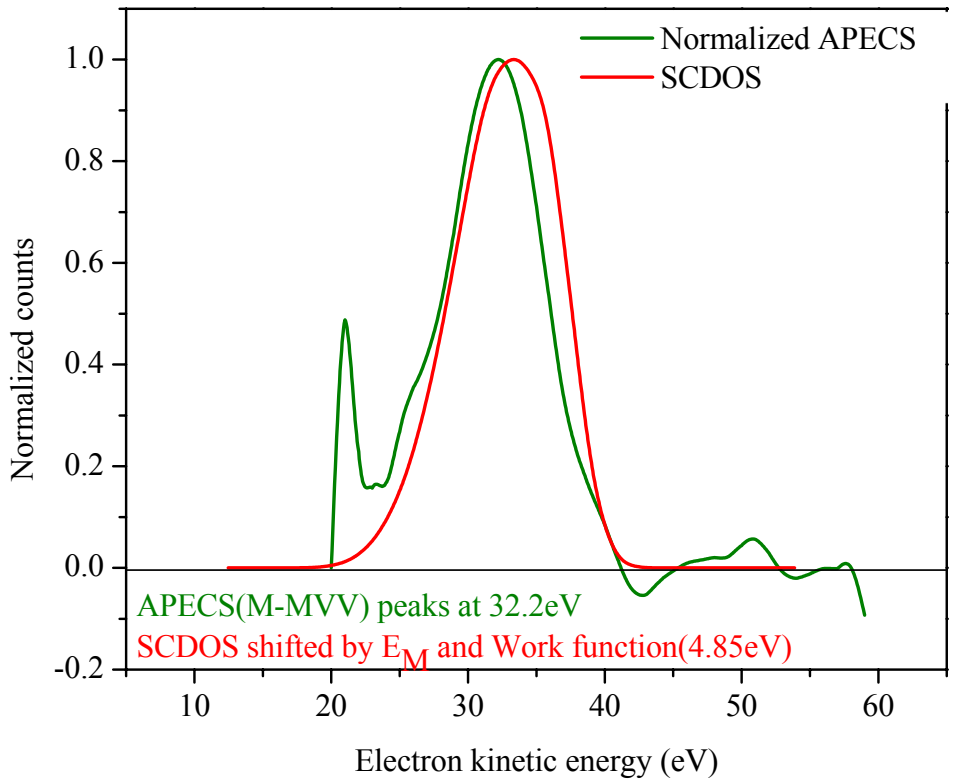

Fig. 6.8 Comparison of the APECS spectrum of M→VV transition with the self convolution of the valence band density of states (SCDOS) shifted by the binding energy of Mn $M_{2,3}$ and the work function

6.3.1 Modeling of the spectrum of the $M_{2,3}V \rightarrow VVV$ Auger transition

In the $L_{2,3} \rightarrow M_{2,3}V \rightarrow VVV$ Auger cascade the $L_{2,3} \rightarrow M_{2,3}V$ transition shown in the lower pathway of Fig. 6.1, results in a final state with one hole in the $M_{2,3}$ level and one hole in the valence band. In the $L_{2,3} \rightarrow M_{2,3}V \rightarrow VVV$ Auger cascade the $M_{2,3}V$ intermediate step relaxes by filling the $M_{2,3}$ hole with another valence electron, leaving a final state with three holes in the valence band.

Let the binding energy of the valence electrons be E_1, E_2, E_3, E_4 respectively. The electrons can rearrange themselves within the valence band, so the electron having the binding energy E_1 in the initial state may not have the same binding energy in the final state; instead it has a different binding energy E_2. Integrate over all possible combinations of initial and final state configurations to obtain the KE of the outgoing Auger electron.

Applying conservation of energy for this case we have: after setting

Energy (Initial state) = Energy (Final state)

$E_M + E_1 + U_{pd} = E_2 + E_3 + E_4 + 3U_{dd} + KE_{LMVAuger} + \phi$ and defining $U_1 = 3U_{dd} - U_{pd} + \phi$

Rearranging the terms we have the energy conserving delta function to be

$\delta(KE_{LMVAuger} - E_M - E_1 + E_2 + E_3 + E_4 + U_1)$,

$$N(KE_{LMVAuger}) \propto \int_{-\infty}^{\infty}\int_{-\infty}^{\infty}\int_{-\infty}^{\infty}\int_{-\infty}^{\infty} \rho(E_1)\rho(E_2)\rho(E_3)\rho(E_4)\delta(KE_{LMVAuger} + E_4 + E_3 + E_2 - E_1 - E_M + U_1)dE_1 dE_2 dE_3 dE_4 \quad (16)$$

Integrating with respect to E_4, we have (Solving for $E_4 = E_M + E_1 - E_2 - E_3 - KE_{LMVAuger} - U_1$)

$$N(KE_{LMVAuger}) \propto \int_{-\infty}^{\infty}\int_{-\infty}^{\infty}\int_{-\infty}^{\infty} \rho(E_1)\rho(E_2)\rho(E_3)[\rho(E_M + E_1 - E_2 - E_3 - KE_{LMVAuger} - U_1)]dE_1 dE_2 dE_3$$

Rearranging the terms so that we can integrate with respect to E_3

$$N(KE_{LMVAuger}) \propto \int_{-\infty}^{\infty}\int_{-\infty}^{\infty}\int_{-\infty}^{\infty} \rho(E_1)\rho(E_2)[\rho(E_3)\rho(E_M + E_1 - E_2 - KE_{LMVAuger} - U_1 - E_3)dE_3]dE_1 dE_2$$

now define $U_2 = E_M+E_1-E_2-KE_{LMVAuger}-U_1$

$$N(KE_{LMVAuger}) \propto \int_{-\infty}^{\infty}\int_{-\infty}^{\infty} \rho(E_1)\rho(E_2)\int_{-\infty}^{\infty}[\rho(E_3)\rho(U_2 - E_3)dE_3]dE_1 dE_2 \qquad (17)$$

The integration with respect to E_3 is identical to a convolution of two functions which is defined as $f * g = \int_0^{\tau} f(\tau)g(t-\tau)d\tau$.

So the above equation becomes

$$N(KE_{LMVAuger}) \propto \int_{-\infty}^{\infty}\int_{-\infty}^{\infty} \rho(E_1)\rho(E_2)(\rho * \rho)(U_2)dE_1 dE_2$$

Substituting back the value of U_2 we have

$$N(KE_{LMVAuger}) \propto \int_{-\infty}^{\infty}\int_{-\infty}^{\infty} \rho(E_1)\rho(E_2)(\rho * \rho)(E_M + E_1 - E_2 - KE_{LMVAuger} - U_1)dE_1 dE_2$$

now define $U_3 = E_M+ E_1-KE_{LMV\ Auger} -U_1$ and rearranging the terms so that we can integrate with respect to E_2

$$N(KE_{LMVAuger}) \propto \int_{-\infty}^{\infty} \rho(E_1)[\rho(E_2)(\rho * \rho)(U_3 - E_2)dE_2]dE_1 \qquad (18)$$

Again, the above expression integrated with respect to E_2 is nothing but a convolution of two functions ρ and (ρ∗ρ) .So the above equation becomes

$$N(KE_{LMVAuger}) \propto \int_{-\infty}^{\infty} \rho(E_1)[\rho * (\rho * \rho)](U_3)dE_1 \tag{19}$$

Substituting for U_3 we have

$$N(KE_{LMVAuger}) \propto \int_{-\infty}^{\infty} \rho(E_1)[\rho * (\rho * \rho)](E_M - \mathrm{KE}_{\mathrm{LMV\ AUGER}} - \mathrm{U}_1 + E_1)dE_1 \tag{20}$$

This integral can be put in the form of a correlation integral

$$f \otimes g = \int_{-\infty}^{\infty} f(x)g(x+u)dx \tag{21}$$

By substituting $.x' = x + u$ the correlation operator may be written as:

$$f \otimes g = \int_{-\infty}^{\infty} f(x'-u)g(x')dx' \tag{22}$$

Integrating Eqn.(20)with respect to E_1 and setting E_M-KE-U_1 = U, the integral becomes:

$$N(KE_{LMVAuger}) \propto \int_{-\infty}^{\infty} \rho(E_1)[\rho * (\rho * \rho)](U + E_1)dE_1 \tag{23}$$

$$N(KE_{LMVAuger}) \propto \int_{-\infty}^{\infty} \rho(E_1 - U)[\rho * (\rho * \rho)](E_1)dE_1 \tag{24}$$

Writing this integral as a correlation operator yields:

$$N(KE_{LMVAuger}) \propto \rho \otimes \rho * (\rho * \rho)(E_M - KE_{LMVAuger} + 3U_{dd} - U_{pd} + \phi) \tag{25}$$

Fig. 6.9 shows the $M_{2,3}V \rightarrow M_{2,3}VV$ Auger-Auger coincidence data compared with the spectrum obtained using the participator hole model for $M_{2,3}V \rightarrow M_{2,3}VV$ transition (Red curve).

6.3.2 Modeling of the spectra of [$M_{2,3}M_{2,3}$→$M_{2,3}$VV and $M_{2,3}$VV→VVVV] Auger cascade steps

Following the $L_{2,3}$-photoemission process, in the $L_{2,3}$→ $M_{2,3}M_{2,3}$ transition shown in the upper pathway of Fig. 6.1, the intermediate state is left with two holes by the $M_{2,3}$ level. In the cascade process to follow, the atom relaxes by filling one of the $M_{2,3}$ holes with a valence electron. The difference in energy is carried away by an Auger electron from the valence band. The state with one hole left behind in the $M_{2,3}$ level and two holes in the valence band serves as the initial state for the next step in the cascade process. The atom relaxes by filling the hole left behind in the $M_{2,3}$ shell with an electron from the valence band, while the excess energy is carried away by yet another Auger electron from the valence band. Thus the final state in the $L_{2,3}$→$M_{2,3}M_{2,3}$→ $M_{2,3}$VV→VVVV has four valence band holes in the final state.

Let the binding energy of the valence electrons be E_1, E_2, E_3, E_4, E_5, E_6 as shown in the Fig. 6.1. Again, allowing the electrons to rearrange themselves within the valence band, the electron having the binding energy E_1 in the initial state does not have the same binding energy in the final state; instead it has a different binding energy E_2. As before, integrate over all possible valence band initial and final state combinations.

Applying conservation of energy for the transition $L_{2,3}$→$M_{2,3}M_{2,3}$ we have: after setting Energy (Initial state) = Energy (Final state)

$$2E_M + U_{pp} = E_M + E_1 + E_2 + 2U_{pd} + U_{dd} + KE_{Auger} + \phi$$

$$KE_{Auger} + E_1 + E_2 - E_M + 2U_{pd} + U_{dd} - U_{pp} + \phi = 0$$

$$Let.....U_1 = 2U_{pd} + U_{dd} - U_{pp} + \phi$$

Rearranging the terms we have the energy conserving delta function to be

$\delta(KE_{Auger} + E_1 + E_2 - E_M + U_1)$,

$$N_A(KE) \propto \int_{-\infty}^{\infty}\int_{-\infty}^{\infty} \rho(E_1)\rho(E_2)\delta(KE + E_1 + E_2 - E_M + U_1)dE_1 dE_2 \tag{26}$$

Integrating with respect to E_2, we have

$$N_A(KE) \propto \int_{-\infty}^{\infty} \rho(E_1)\rho(E_M - U_1 - KE - E_1)dE_1 \tag{27}$$

This integral is a convolution integral

$$\int_{-\infty}^{\infty} \rho(E_1)\rho(E_M - U_1 - KE - E_1)dE_1 \equiv \rho * \rho(KE - E_M + U_1) \tag{28}$$

Thus $N_A(KE) \propto \rho * \rho(KE - E_M + U_1)$ (29)

Now applying conservation of energy for the transition $M_{2,3}VV \rightarrow VVVV$ we have :

after setting Energy (Initial state) = Energy (Final state)

For the transition $MVV \rightarrow VVVV$ we have

$$E_M + E_1 + E_2 + 2U_{pd} + U_{dd} = E_3 + E_4 + E_5 + E_6 + 6U_{dd} + KE_{Auger} + \phi$$
$$KE_{Auger} + E_3 + E_4 + E_5 + E_6 + 5U_{dd} + \phi - 2U_{pd} - E_M - E_1 - E_2 = 0$$
$$Let.....U_2 = 5U_{dd} - 2U_{pd} + \phi$$

Rearranging the terms we have the energy conserving delta function to be

$\delta(KE_{Auger} + E_3 + E_4 + E_5 + E_6 - E_M - E_1 - E_2 + U_2)$

$$N_B(KE) \propto \int_{-\infty}^{\infty}\int_{-\infty}^{\infty}\int_{-\infty}^{\infty}\int_{-\infty}^{\infty}\int_{-\infty}^{\infty}\int_{-\infty}^{\infty} \rho(E_1)\rho(E_2)\rho(E_3)\rho(E_4)\rho(E_5)\rho(E_6)$$

$$\times \delta(KE + E_6 + E_5 + E_4 + E_3 - E_2 - E_1 - E_M + U_2)dE_1 dE_2 dE_3 dE_4 dE_5 dE_6 \tag{30}$$

$$N_B(KE) \propto \int_{-\infty}^{\infty}\int_{-\infty}^{\infty}\int_{-\infty}^{\infty}\int_{-\infty}^{\infty}\int_{-\infty}^{\infty} \rho(E_1)\rho(E_2)\rho(E_3)\rho(E_4)$$

$$\times [\rho(E_5)\rho(E_M + E_1 + E_2 - E_3 - E_4 - E_5 - U_2 - KE_{LMMAuger})dE_5]dE_1 dE_2 dE_3 dE_4$$

Rearranging the terms by defining $U_3 = E_M + E_1 + E_2 - E_3 - E_4 - U_2 - KE_{LMMAuger}$,

$$N_B(KE) \propto \int_{-\infty}^{\infty}\int_{-\infty}^{\infty}\int_{-\infty}^{\infty}\int_{-\infty}^{\infty}\int_{-\infty}^{\infty} \rho(E_1)\rho(E_2)\rho(E_3)\rho(E_4)$$

$$\times [\rho(E_5)\rho(U_3 - E_5)dE_5]dE_1 dE_2 dE_3 dE_4 \tag{31}$$

Integrating with respect to E_5, we have,

$$N_B(KE) \propto \int_{-\infty}^{\infty}\int_{-\infty}^{\infty}\int_{-\infty}^{\infty}\int_{-\infty}^{\infty} \rho(E_1)\rho(E_2)\rho(E_3)\rho(E_4)[\rho * \rho(U_3)]dE_1 dE_2 dE_3 dE_4$$

Substituting back the value of U_3

$$N_B(KE) \propto \int_{-\infty}^{\infty}\int_{-\infty}^{\infty}\int_{-\infty}^{\infty}\int_{-\infty}^{\infty} \rho(E_1)\rho(E_2)\rho(E_3)$$

$$\times \rho(E_4)[\rho * \rho(E_M + E_1 + E_2 - E_3 - E_4 - U_2 - KE_{LMMAuger})]dE_1 dE_2 dE_3 dE_4$$

Rearranging the terms by defining $U_4 = E_M + E_1 + E_2 - E_3 - U_2 - KE_{LMMAuger}$,

$$N_B(KE) \propto \int_{-\infty}^{\infty}\int_{-\infty}^{\infty}\int_{-\infty}^{\infty}\int_{-\infty}^{\infty} \rho(E_1)\rho(E_2)\rho(E_3)\{\rho(E_4)[\rho * \rho(U_4 - E_4)]dE_4\}dE_1dE_2dE_3$$

$$N_B(KE) \propto \int_{-\infty}^{\infty}\int_{-\infty}^{\infty}\int_{-\infty}^{\infty} \rho(E_1)\rho(E_2)\rho(E_3)[\rho * \rho * \rho(U_4)]dE_1dE_2dE_3 \qquad (32)$$

Substituting back the value of U_4

$$N_B(KE) \propto \int_{-\infty}^{\infty}\int_{-\infty}^{\infty}\int_{-\infty}^{\infty} \rho(E_1)\rho(E_2)\rho(E_3)$$

$$\times \rho * \rho * \rho(E_M + E_1 + E_2 - E_3 - U_2 - KE_{LMMAuger})dE_1dE_2dE_3$$

Rearranging the terms by defining $U_5 = E_M + E_1 + E_2 - U_2 - KE_{LMMAuger}$

$$N_B(KE) \propto \int_{-\infty}^{\infty}\int_{-\infty}^{\infty}\int_{-\infty}^{\infty} \rho(E_1)\rho(E_2)\rho(E_3)\{\rho * \rho * \rho(U_5 - E_3)dE_3\}dE_1dE_2$$

$$N_B(KE) \propto \int_{-\infty}^{\infty}\int_{-\infty}^{\infty} \rho(E_1)\rho(E_2)\rho * \rho * \rho * \rho(U_5)]dE_1dE_2 \qquad (33)$$

Substituting back the value of U_5

$$N_B(KE) \propto \int_{-\infty}^{\infty}\int_{-\infty}^{\infty} \rho(E_1)\rho(E_2)[\rho * \rho * \rho * \rho(E_M + E_1 + E_2 - U_2 - KE_{LMMAuger})]dE_1dE_2$$

Rearranging the terms by defining $U_6 = E_M + E_1 - U_2 - KE_{LMMAuger}$,

$$N_B(KE) \propto \int_{-\infty}^{\infty}\int_{-\infty}^{\infty} \rho(E_1)\{\rho(E_2)[\rho * \rho * \rho * \rho(U_6 + E_2)]dE_2\}dE_1 \qquad (34)$$

This integral within the curly brackets may be written as a correlation integral

$$N_B(KE) \propto \int_{-\infty}^{\infty} \rho(E_1)[\rho \otimes \rho * \rho * \rho * \rho(U_6)]dE_1 \quad (35)$$

Substituting back the value of U_6

$$N_B(KE) \propto \int_{-\infty}^{\infty} \rho(E_1)[\rho \otimes \rho * \rho * \rho * \rho(E_M + E_1 - U_2 - KE_{LMMAuger})]dE_1$$

Rearranging the terms by defining $U_7 = E_M - U_2 - KE_{LMMAuger}$,

$$N_B(KE) \propto \int_{-\infty}^{\infty} \rho(E_1)[\rho \otimes \rho * \rho * \rho * \rho(U_7 + E_1)]dE_1 \quad (36)$$

Again the integral is of the form of a correlation integral, on substituting the value of U_7, the integral becomes,

$$N_B(KE) \propto \rho \otimes \rho \otimes \rho * \rho * \rho * \rho(KE - E_M + U_2) \quad (37)$$

where, $U_2 \equiv 5U_{dd}\text{-}2U_{pd} + \phi$, and $\otimes$ and $*$ are the correlation and convolution operators respectively. Fig. 6.10 shows the $M_{2,3}M_{2,3}$ -VVVV AACS data (Red dots with error bars) compared with the spectrum obtained using the "Full Participation" model for $M_{2,3}M_{2,3}$ -VVVV transition (Blue curve).

6.4 Failure of the "TWO-STEP MODEL"

The increased energy width of the Auger transitions that follow prior L→MM or L→MV decays strongly suggests the involvement of valence hole(s) created in the prior cascade step. This necessitates that these holes were not filled at the time of the subsequent Auger decay in contradiction to the assumptions of the two-step model [6-13] in which it is assumed that the screening time is short compared to the core-hole life time and that consequently the Auger decay process is independent of the details of the creation of the core hole filled during the decay. The shifts observed in our measurements are higher than seen previously in near threshold excitation and indicate a maximal violation of the two step model of Auger emission following core hole creation through Auger cascade processes in solids.

6.4.1 $3p_{3/2}$ initiated $M_{2,3}$→VV direct Auger decay

The width of the $M_{2,3}$→VV coincidence spectra (resulting after the direct $M_{2,3}$ Excitation) is not affected because there is no hole in the initial state to start with.

In contrast to the above, we have a valence hole in the intermediate state in the $L_{2,3}$→$M_{2,3}$V→VVV and multiple valence holes in the intermediate state of the $L_{2,3}$→$M_{2,3}M_{2,3}$→$M_{2,3}$VV→VVVV cascade. The presence of this hole alters the width of the AACS spectra which makes it wider when we use the "participator valence hole" model. But in the "fixed bystander hole model" the energy of these valence holes are fixed, which reduces the width of the spectra.

6.4.2 Fixed spectator hole model of the $M_{2,3}V \rightarrow VVV$ transition

Using the same formulation as we used previously we may write eqn16 as

$$N(KE_{LMVAuger}) \propto \int_{-\infty}^{\infty}\int_{-\infty}^{\infty}\int_{-\infty}^{\infty}\int_{-\infty}^{\infty} \rho(E_1)\rho(E_2)\rho(E_3)\rho(E_4)\delta(KE_{LMVAuger} + E_4 + E_3 + E_2 - E_1 - E_M + U_1)dE_1 dE_2 dE_3 dE_4 \quad (38)$$

Using the assumption that when $E_1 = E_4$, (energy of the hole in the initial state = Energy of the final state) (i.e.) when the initial hole in the valence band is a spectator and does not participate in the subsequent Auger transition, then the above equation reduces to

$$N(KE_{LMVAuger}) \propto \int_{-\infty}^{\infty}\int_{-\infty}^{\infty}\int_{-\infty}^{\infty}\int_{-\infty}^{\infty} \rho(E_1)\rho(E_2)\rho(E_3)\rho(E_4)\delta(KE_{LMVAuger} + E_3 + E_2 - E_M + U_1)dE_1 dE_2 dE_3 dE_4 \quad (39)$$

$$N(KE_{LMVAuger}) \propto \int_{-\infty}^{\infty}\int_{-\infty}^{\infty} \rho(E_2)\rho(E_3)\delta(KE_{LMVAuger} + E_3 + E_2 - E_M + U_1)dE_2 dE_3 \int_{-\infty}^{\infty}\rho(E_1)dE_1 \int_{-\infty}^{\infty}\rho(E_4)dE_4 \quad (40)$$

Thus, the last two integrations yield a multiplicative constant α^2 where $\alpha = \int_{-\infty}^{\infty}\rho(E)dE$

$$N_{LMV}(KE) \propto \alpha^2[\rho * \rho(KE - E_M + U_1)] \quad (31)$$

The above equation is the self convolution of valence band density of states. This result is proportional to the result of eq. (15) used to model the direct $M_{2,3} \rightarrow VV$ transition.

Consequently the full width is closer 2W, (W- width of the valence band) than to 4W. Fig. 6.9 shows the $M_{2,3}V \rightarrow VVV$ AACS data compared with the spectrum obtained using the "Spectator hole" model for $L_{2,3} \rightarrow M_{2,3}V \rightarrow VVV$ Auger decay (Green curve). Clearly the "Spectator hole" model does not fit the experimental data.

6.4.3 Fixed spectator hole model of the $L_{2,3} \rightarrow VVVV$ Auger decay

The $M_{2,3}M_{2,3} \rightarrow M_{2,3}VV$ transition, as there are no initial valence holes present, the width is the same as found before in eqn. (29). In the subsequent Auger decay $M_{2,3}VV \rightarrow VVVV$. There are two valence holes in the initial state which are assumed to be fixed in energy, (i.e) when the two initial holes in the valence band are spectators and does not participate in the subsequent Auger transition, then we can write the energies of the valence hole in the initial state = energy of the valence holes in the final state which is given by

$$E_1 = E_5, E_4 = E_6$$
$$E_M + E_2 + E_3 - 5U_{dd} + 2U_{pd} - \phi - KE_{Auger} = 0$$
$$Let.....U_2 = 2U_{pd} - 5U_{dd} - \phi$$
$$\therefore E_M + E_2 + E_3 - U_2 - KE_{Auger} = 0$$

$$N_B(KE) \propto \int_{-\infty}^{\infty}\int_{-\infty}^{\infty} \rho(E_2)\rho(E_3)\delta(KE + E_3 + E_2 - E_M + U_2)dE_2 dE_3$$

$$\times \int_{-\infty}^{\infty} \rho(E_1)dE_1 \int_{-\infty}^{\infty} \rho(E_4)dE_4 \int_{-\infty}^{\infty} \rho(E_5)dE_5 \int_{-\infty}^{\infty} \rho(E_6)dE_6$$

which reduces to $N_B(KE) \propto \alpha^4[\rho * \rho(KE - E_M + U_2)]$ (32)

The above equation is also proportional to the self convolution of valence band density of states which is used to model the direct $M_{2,3}$→VV transition So the modeled width is closer to 2W, where W is the width of the valence band than to 6W as shown in Equation (12) in the model where the valence band holes participate in the decay process. We note that if the energies of the "spectator" are held fixed during the transitions or if these holes are filled or otherwise uncoupled then the model predicts that the energy distributions $N_C(KE)$ and $N_B(KE)$ reduce to narrower functions involving simple self convolutions of VBDOS. Fig. 6.10 shows the $M_{2,3}M_{2,3}$ -VVVV AACS data compared with the spectrum obtained using the "Spectator hole" model for $M_{2,3}M_{2,3}$ -VVVV transition (Green curve) which does not fit the experimental data.

The increased energy width of the transitions that follow LMX (LMM or LMV) decays strongly suggests the involvement of valence hole(s) created in the prior cascade step that have not been filled at the time of the subsequent Auger decay. This suggests that the two-step model in which it is assumed that the screening time is short compared to the core-hole life time and consequently that the Auger decay process are independent of the details of the creation of the core hole filled during the decay is not appropriate for the later stages in Auger cascades. The shifts observed in our measurements are higher than seen previously in near threshold excitation and indicate a maximal violation of the two step model of Auger emission following core hole creation through Auger cascade processes in solids.

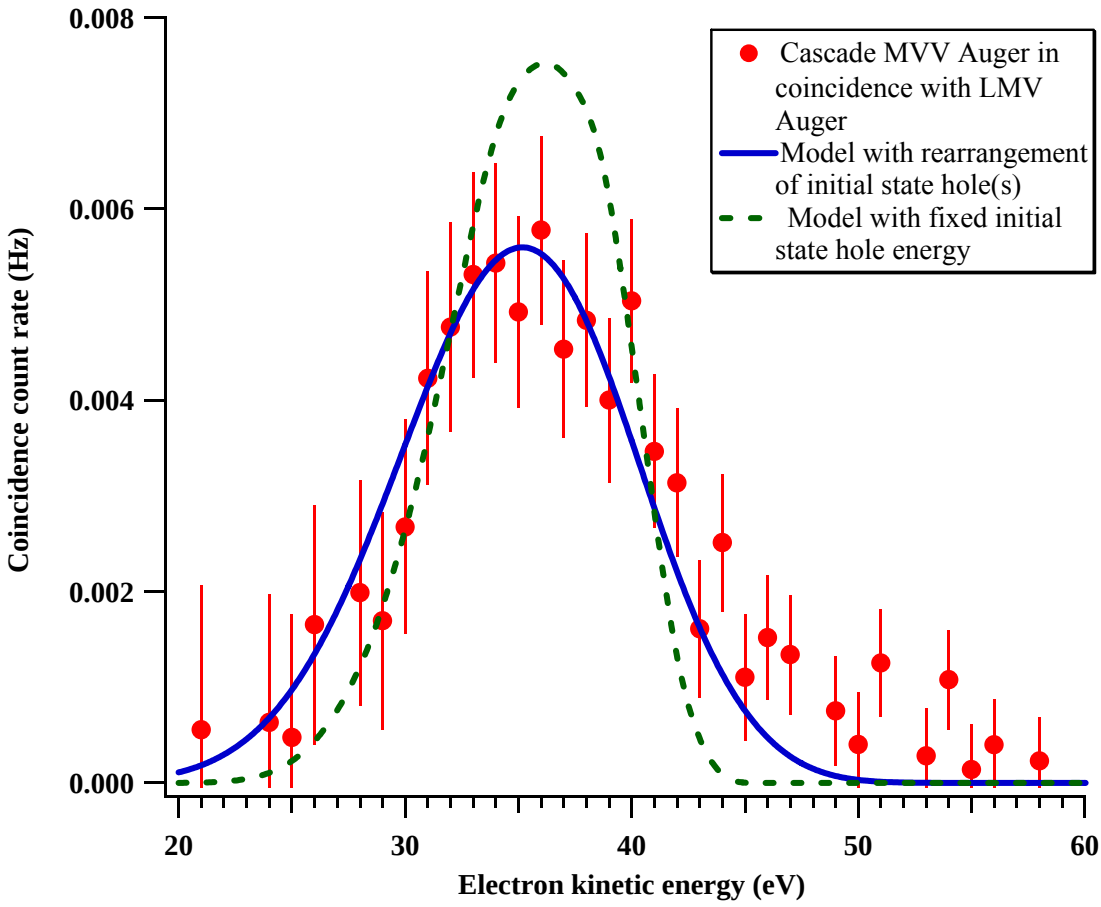

Fig. 6.9 AACS measurement of the spectra of the Mn $M_{2,3}V \rightarrow VVV$ transition compared with model spectra

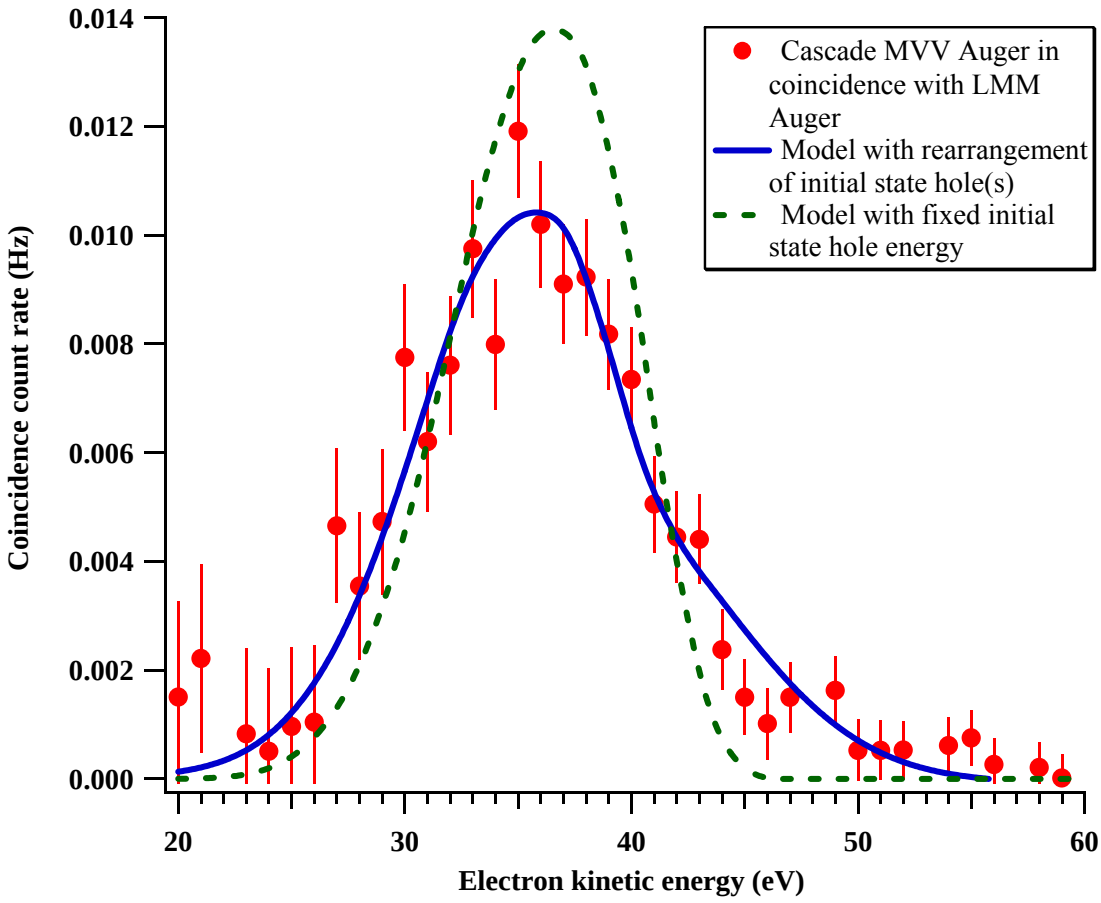

Fig. 6.10 MnO-AACS measurement of the spectra of Mn $M_{2,3}M_{2,3}$→$M_{2,3}VV$ and $M_{2,3}VV$→VVVV transitions compared with the model spectra

In summary, Fig. 6.11 compares the energy spectra of MVV Auger electrons emitted as a result of (a) the direct photo ionization of an M hole, (b) the $L_{2,3}\rightarrow M_{2,3}M_{2,3}\rightarrow M_{2,3}VV\rightarrow VVVV$ Auger cascade, and (c) the $L_{2,3}\rightarrow M_{2,3}V\rightarrow VVV$ Auger cascade. In panel (a) the data shown as solid circles was obtained by subtracting a Shirley background from the Mn 3p-MVV APECS spectrum. The solid line is a shifted self-convolution of the MnO VBDOS. The data shown as solid circles in panels (b) and (c) was obtained by subtracting a Shirley background from MVV Auger spectra taken in coincidence with $L_{2,3}\rightarrow M_{2,3}M_{2,3}$ and $L_{2,3}\rightarrow M_{2,3}V$ Auger electrons, respectively. Model calculations are shown in which the initial state hole energies were allowed to change during the transition (solid lines) or were held fixed (dotted lines).

The solid curves in Fig. 6.11(b) and 6.11(c) show model calculations for the transitions A + B (shown in Fig. 6.1 - taken to be the sum of Eqn.29 and Eqn.37) and transition C (Eqn.25), respectively, for the cases where the initial and final state valence holes are assumed to sample the entire band (solid curves) and those when the energies of the spectator holes are fixed (dashed curve). It may be seen that agreement with the AACS spectra is only obtained when the spectator holes are allowed to change energy in the decay process. Further, best agreement was obtained when the full MnO VB-DOS (determined from photo-emission) was included rather than the significantly narrower local-DOS for Mn calculated for MnO suggesting the participation of Oxygen ligand-holes in the transition.

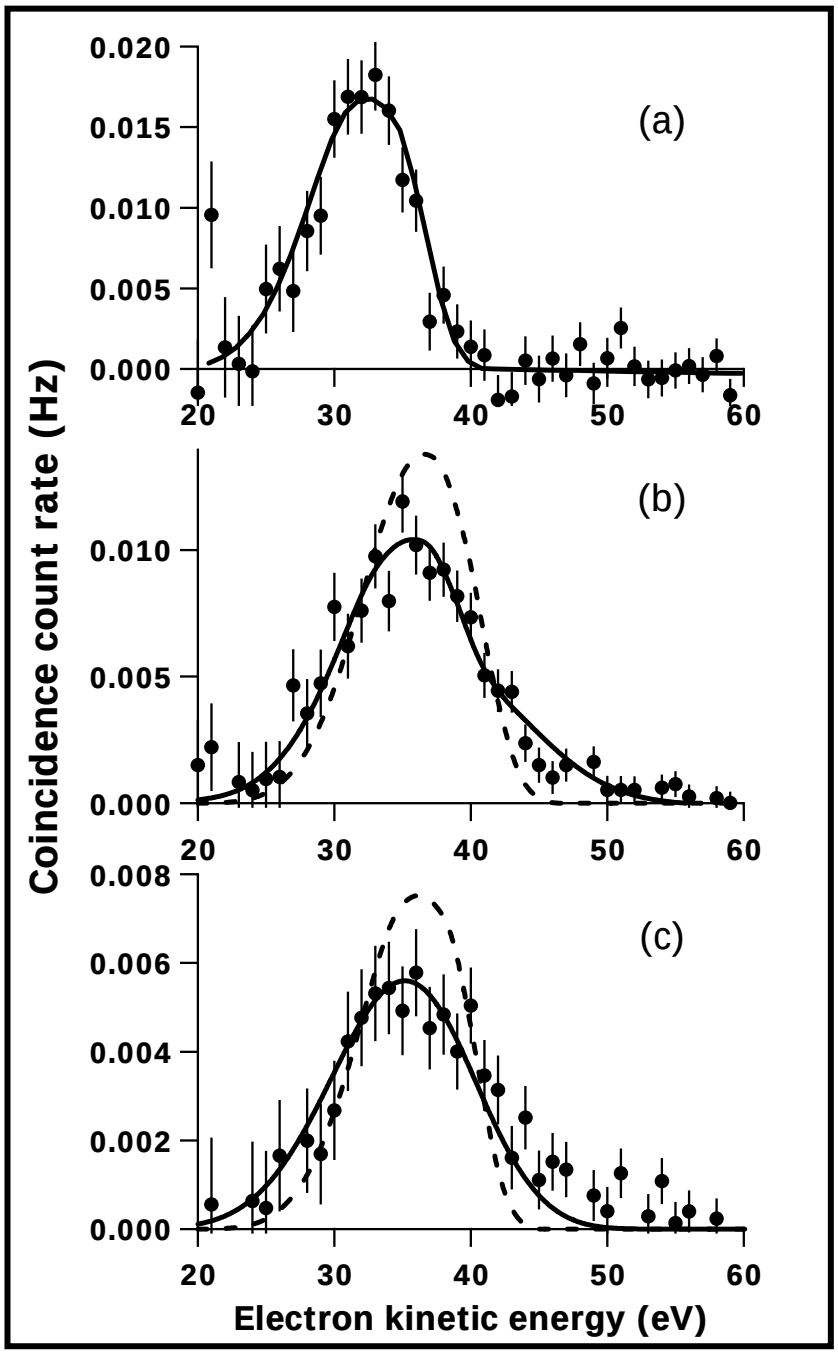

Fig. 6.11 Comparison of the energy spectra of Mn M→VV Auger electrons emitted as a result of (a) the direct photo ionization of an Mn M hole, (b) the Mn $L_{2,3}$→$M_{2,3}M_{2,3}$ →$M_{2,3}$VV→VVVV Auger cascade, and (c) the Mn $L_{2,3}$→ $M_{2,3}$V →VVV Auger cascade with model calculations described in the text

6.5 Ag Theoretical modeling

The comparison shown in Fig. 4.21 reveals that while both cascade induced decay and direct decay show a peak at ~37eV, the spectrum measured following the Auger decay is much broader than the spectrum measured following the direct decay and shows spectral contributions that extend up ~5eV higher in energy. Shirley background subtraction has been performed to remove the inelastic background representing the experimental data. We posit that the significant broadening of the Auger–Auger coincidence spectra may be accounted for in terms of the participation of valence holes remaining from previous steps in the cascade.

Fig. 6.12 compares the APECS energy spectra of the N→VV Auger electrons emitted as a result of direct ionization of the $4p_{5/2}$ core hole with a) the theoretical model where the spectator valence holes are fixed in energy (dashed green line) and b) the theoretical model in which the spectator holes are allowed to change energy in the decay process (solid blue line). Fig. 6.13 compares the AACS energy spectra of the NV→VVV Auger electrons emitted as a result of M→NV→VVV Auger cascade with a) the theoretical model where the spectator valence holes are fixed in energy (dashed green line) and b) the theoretical model in which the spectator holes are allowed to change energy in the decay process (solid blue line). AACS of Ag indicate that rearrangement of participator valence holes in the transition can lead to energy gains as large as the width of the valence band. The valence band spectrum of Ag used to obtain the convolutions and the correlations is shown in Fig. 6.14.

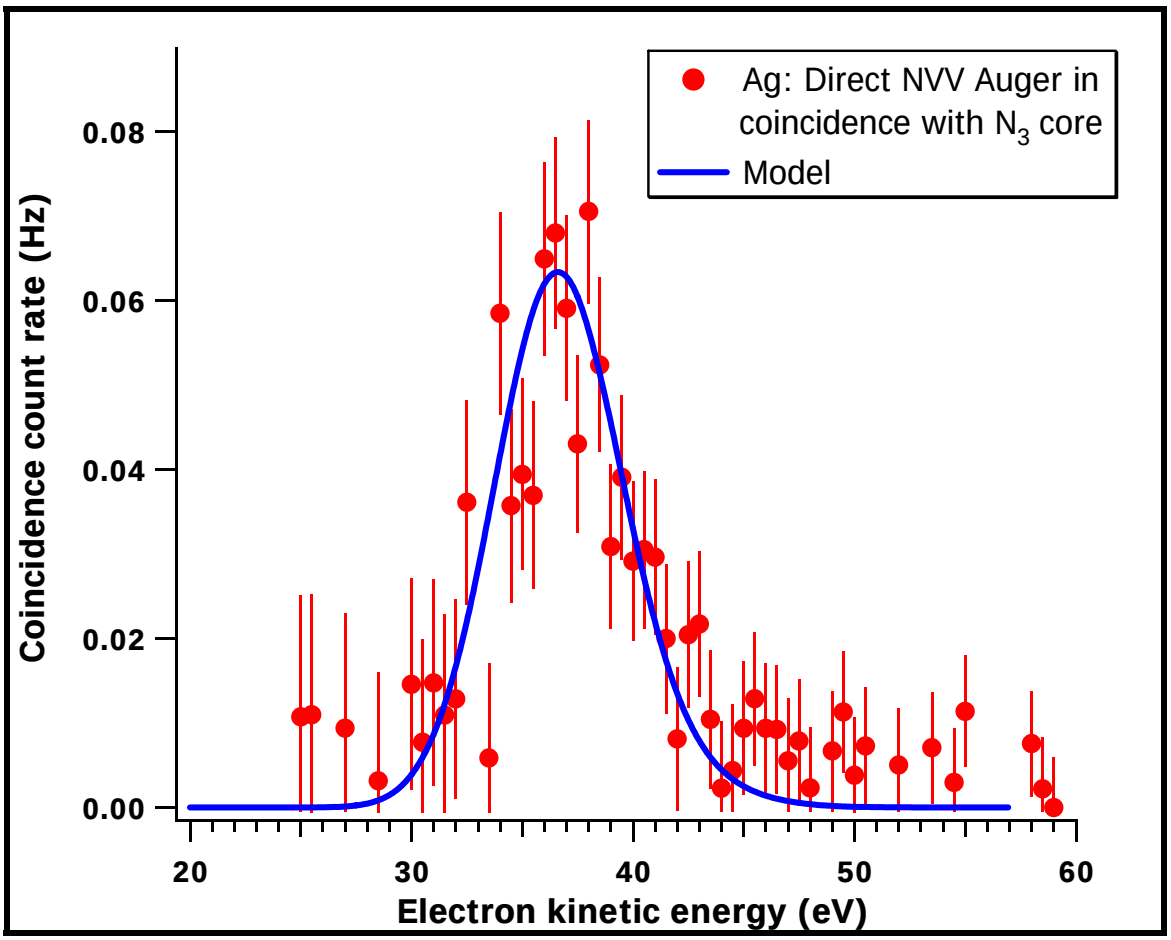

Fig. 6.12 Comparison of the background subtracted area normalized experimental APECS spectrum (Ag N→VV coincidence spectrum) with the model

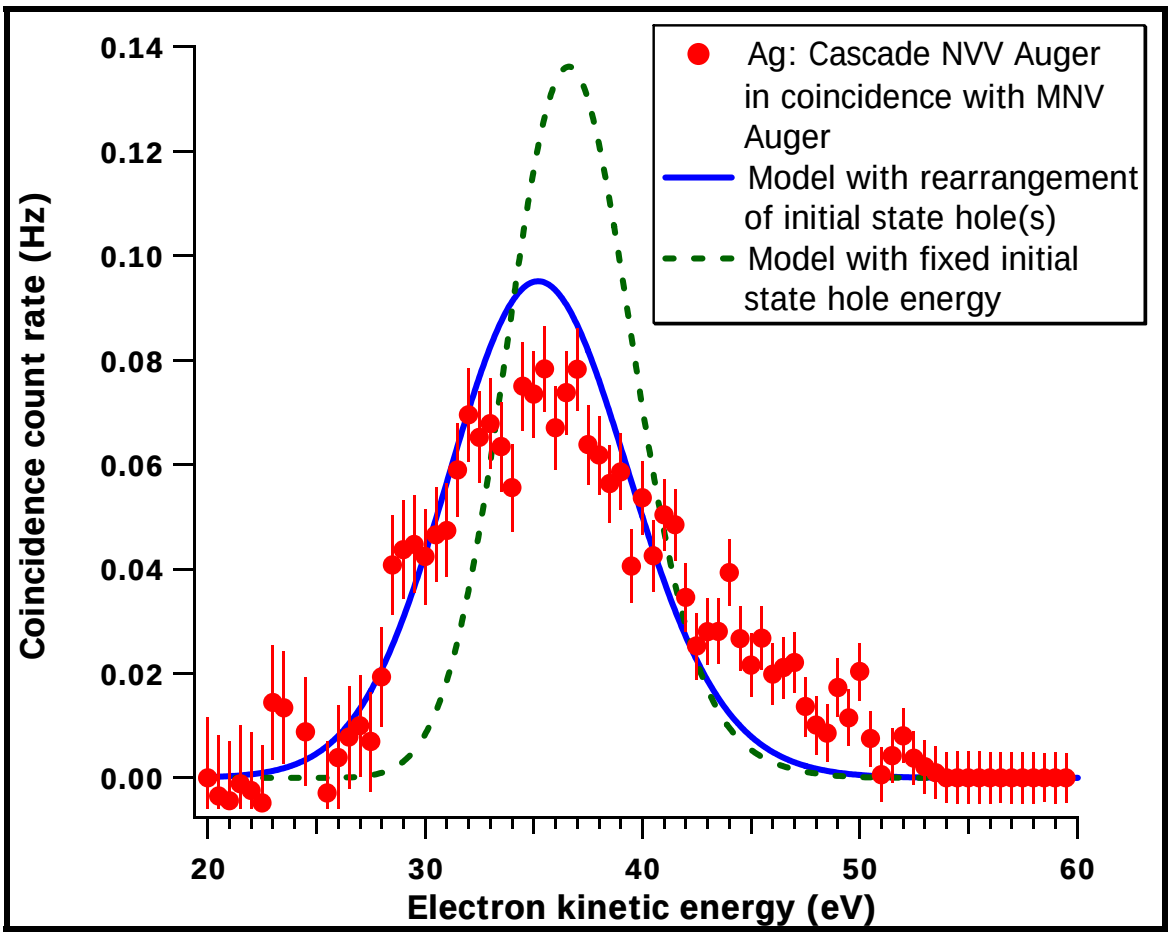

Fig. 6.13 Comparison of the background subtracted area normalized experimental AACS spectrum (Ag NV→VVV coincidence spectrum) with the model (blue-allows rearrangement of the initial state holes) with model (green-fixed initial hole state energy)

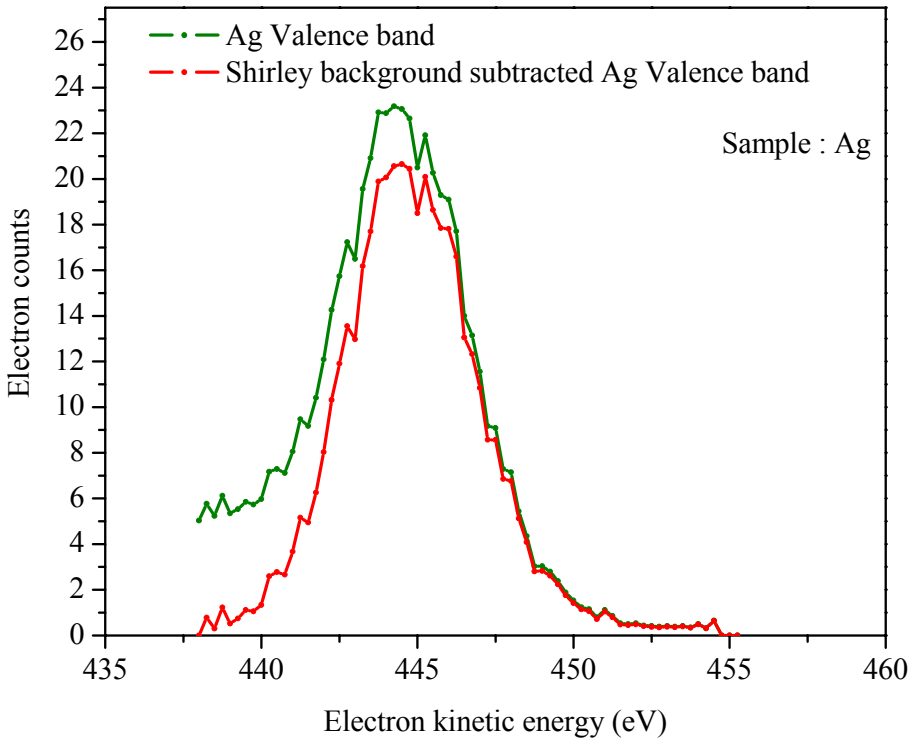

Fig. 6.14 Ag valence band spectrum (green) compared with the Shirley background subtracted valence band (in red)

The comparison of the AACS and APECS spectra shows that the AACS spectra are wider then the APECS and this is possible only if the valence holes in the initial state can move around inside the valence band during subsequent Auger decay. As there are no holes in the initial state of the direct decay process, the APECS spectrum is generally narrower than AACS. Thus our theoretical model fits the experimental data which proves that the valence band hole does not stay fixed in energy. The correlation

energies U's obtained for the Ag are as follows: Udd=4.5eV [4-13] and Upd=5.5eV and the BE of the 4p3/2 is taken to be 58.3eV.

6.6 Pd Theoretical modeling

The comparison of Fig. 5.9 and Fig. 5.11 reveals that while both cascade induced decay and direct decay show a peak at ~37eV, the spectrum measured following the Auger decay is much broader than the spectrum measured following the direct decay and shows spectral contributions that extend up ~5eV higher in energy. Again we posit that the significant broadening of the Auger–Auger coincidence spectra may be accounted for in terms of the participation of valence holes remaining from previous steps in the cascade.

Fig. 6.15 compares the APECS energy spectra of the Pd N→VV Auger electrons emitted as a result of direct ionization of the $4p_{5/2}$ core hole with a) the theoretical model where the spectator valence holes are fixed in energy (dashed green line) and b) the theoretical model in which the spectator holes are allowed to change energy in the decay process (solid blue line). Fig. 6.16 compares the AACS energy spectra of the Pd NV→VVV Auger electrons emitted as a result of Pd M→NV→VVV Auger cascade with a) the theoretical model where the spectator valence holes are fixed in energy (dashed green line) and b) the theoretical model in which the spectator holes are allowed to change energy in the decay process (solid blue line). AACS of Pd indicate that rearrangement of participator valence holes in the transition can lead to energy gains as large as the width of the valence band. The valence band spectrum of Pd used to obtain the convolutions and the correlations is shown in Fig. 6.17.

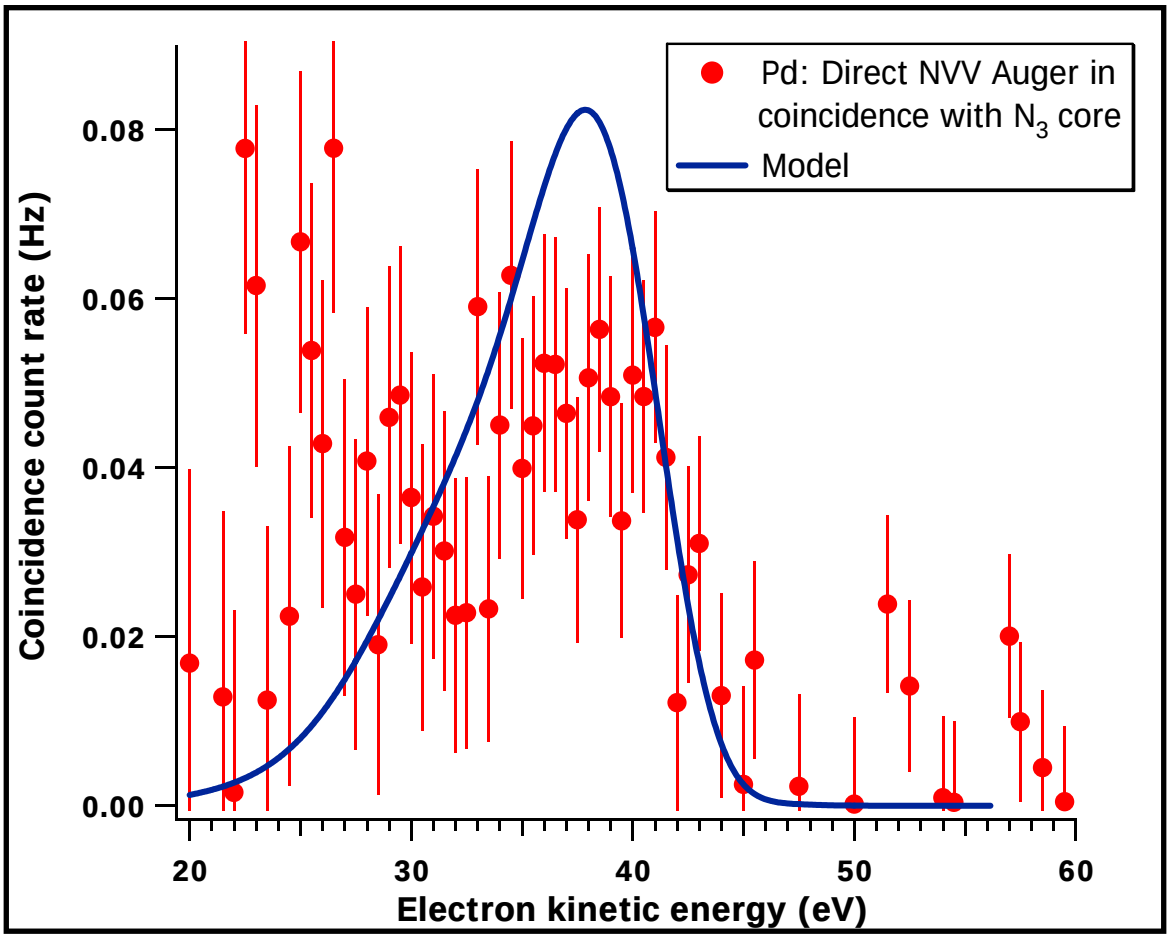

Fig. 6.15 Comparison of the background subtracted area normalized experimental APECS spectrum (Pd N→VV coincidence spectrum) with the model

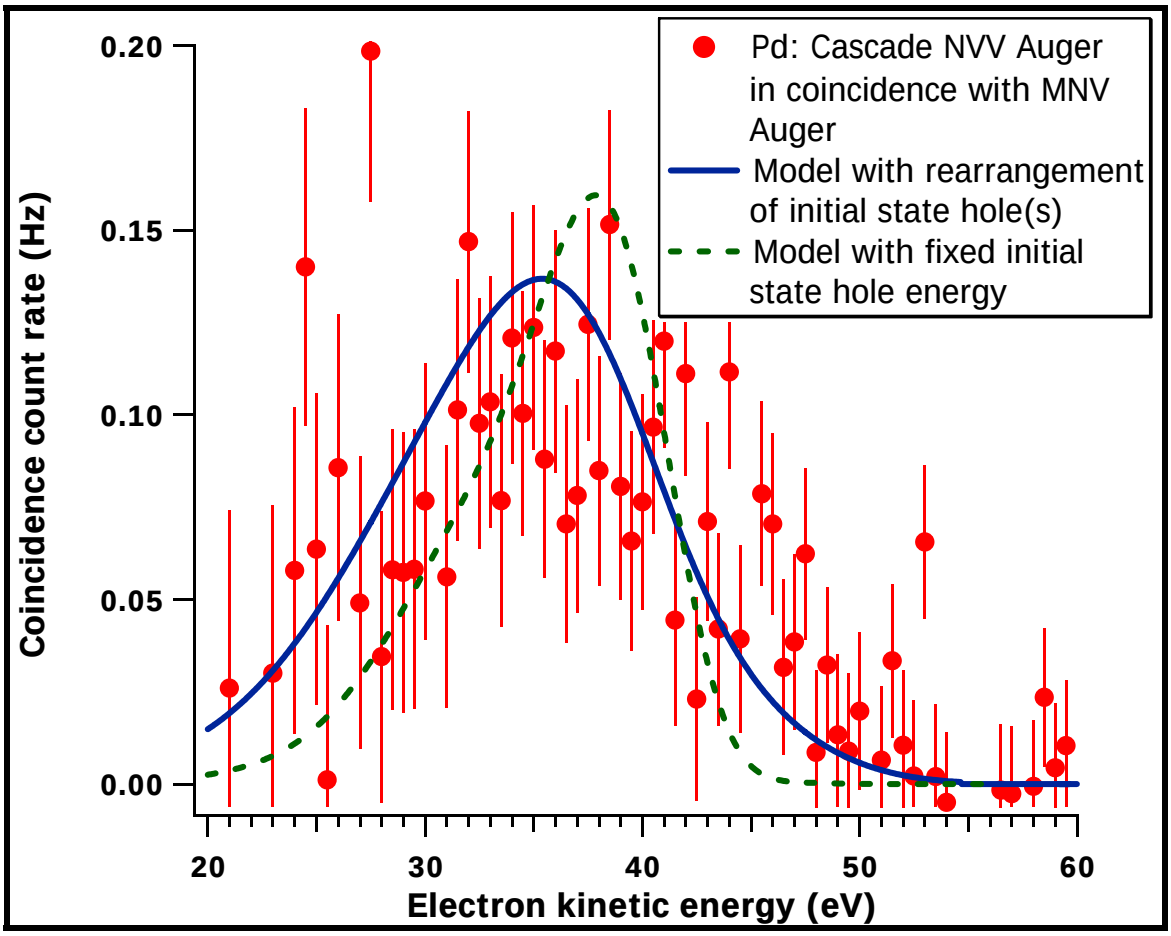

Fig. 6.16 Comparison of the background subtracted area normalized experimental AACS spectrum (Pd NV→VVV coincidence spectrum) with the model (blue-allows rearrangement of the initial state holes) with model (green- fixed initial hole state energy)

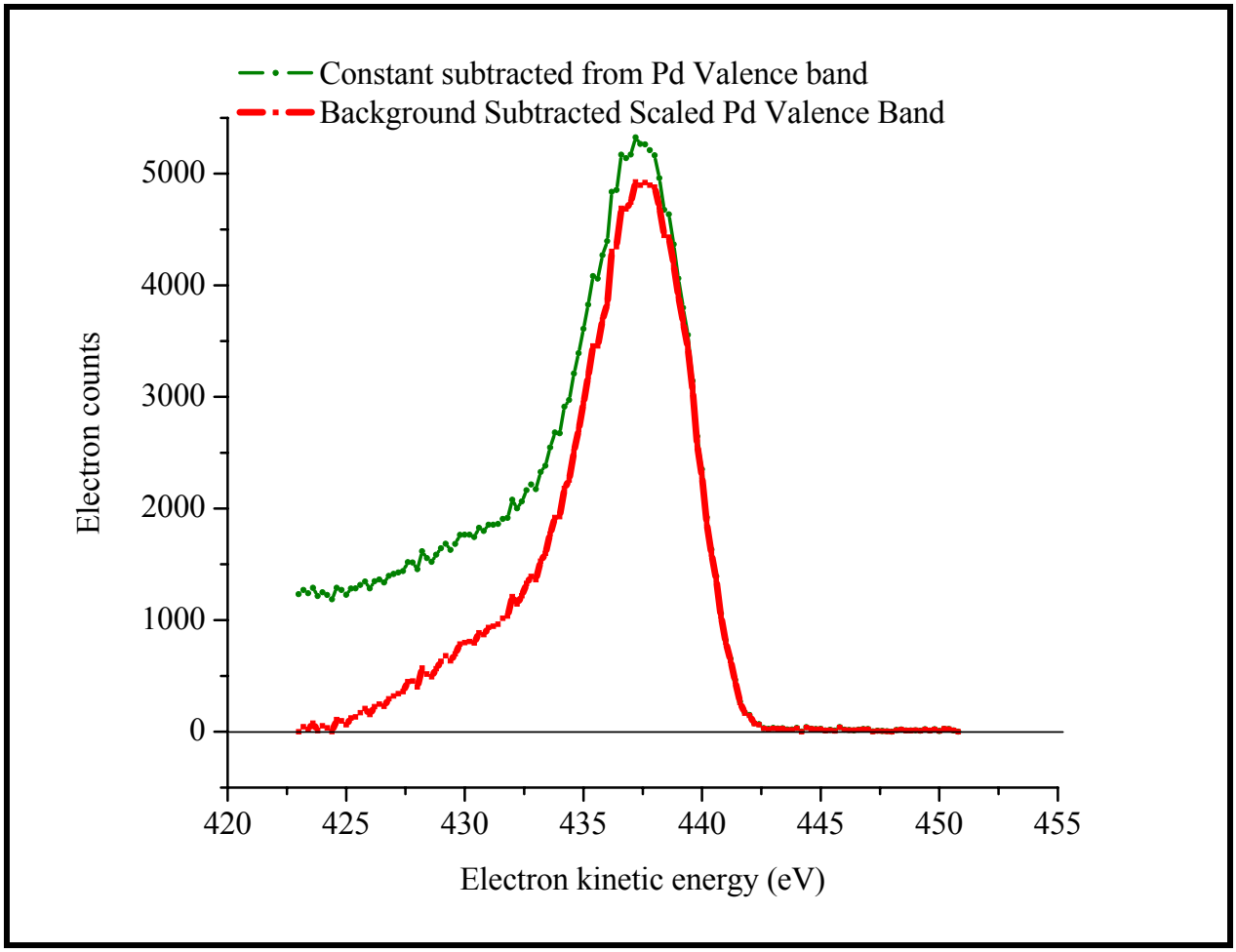

Fig. 6.17 Pd valence band spectrum (green) compared with the Shirley background subtracted valence band (red)

.

CHAPTER 7

FUTURE WORK AND CONCLUSIONS

7.1 Future work

Auger cascade processes provide a unique window into hole-lifetimes, hole-dynamics and many–hole interactions. In addition, Auger cascades are of importance in radiation damage processes in matter [137] and in the biological effects of Auger-electron emitting radionuclides and ionizing radiation [138, 139]. The high charge state of the ion created by the Auger cascade can cause Coulomb explosion [140-142] of molecules which contain atoms involved in the cascade allowing for the possibility of controlled scission of molecules via. resonant adsorption.

Auger cascade process results in the emission of multiple Auger electrons leaving the atom in a highly charged state. As a result, Coulomb explosion can occur and the energy released can be harnessed to localize biological damage from X-Rays in a very efficient manner. If nano-particles of right size and concentration are implanted in a biological tumor cell and irradiated with the laser, an Auger cascade is created in the nano-particle. If the nano-particle is assumed to be spherically symmetric, then the coulomb force created by the holes inside the nano-particle could be made large enough to exceed the yield strength of the nano-particle. If this condition is satisfied then, the X-ray irradiation could cause a Coulomb explosion releasing localized energy within the tumor cells, thereby killing the tumor.

The minimum requirment for exploding a nano particle with Coulomb force may be estimated by setting the electrostatic force per unit area equal to the yield strength of the nano-particle. The typical numbers for the yield strength for gold is found to be 250MPa.

If the isolated nano-particle is assumed to be spherically symmetric and conducting, then the force per unit area is given as [143]

$$\frac{F}{A} = \frac{\sigma^2}{2\varepsilon_0} = \frac{\left(\frac{ne}{4\pi r^2}\right)^2}{2\varepsilon_0} = \frac{n^2 e^2}{32\pi^2 \varepsilon_0 r^4} \text{ kg /(m .s}^2\text{)} \qquad (1)$$

where total charge is *ne*, n is the number of holes and "*e*" is the charge of a hole. Fig.7.1 shows a cartoon explaining Auger cascade process causing coulomb explosion.

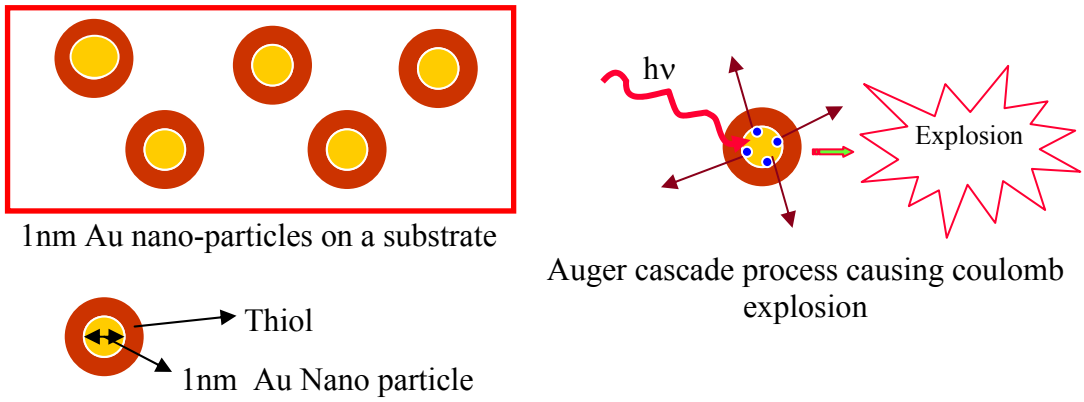

Fig. 7.1 Cartoon explaining Auger cascade causing Coulomb explosion in the nano-particle

When the nano-particles are excited by photons, then it creates a cascade of electrons which leaves the nano-particle in a highly charged state. If the internal cohesive forces

are not large enough to counter balance this electrostatic force then the nano-particle will undergo coloumb explosion.

Upon substituting the values of e =1.16*10^{-19} C; n = 4 in a L→MM cascade, and ε_0 = 8.85*10^{-12} C^2/N*m^2 and the yield strength of gold is 250MPa [144], we have

$$\frac{F}{A} = \frac{n^2 e^2}{32\pi^2 \varepsilon_0 r^4}$$

$$250 \cdot 10^6 = \frac{4^2 (1.16 \cdot 10^{-19})^2}{32 * (3.14)^2 * (8.85 * 10^{-12}) * (r^4)}$$

$$r^4 = 8.75 * 10^{-10} m$$

$$\therefore r = .875 nm$$

So if a deeper core is excited then, the Auger cascade can result in a maximum of 8 to 10 holes in a nano-particle, this makes it possible to get larger values of "n" which would in-turn make it possible to use a nano-particle with larger radius. With the 15nm Au nano-particles given by Dr.Wei Chen of Univ. of Texas at Arlington(UTA), and with collaboration with Dr. Mandal from UTA, Bio-chemistry department, we took "kidney cancerous cells" added two different concentrations (50microlitre and 150microlitre) of the Au nano-particles in the cells and also had a reference cell bath. We kept it in the incubator having 5% CO_2 for ~48hrs. Preliminary results in an optical microscope show that the higher the concentration of the nano-particles, it is difficult for the cell to grow and also since Au is not soluble, it attaches to the periphery of the cell. Future research will involve exploding nano-particles and studying their damage effects in both solids and in biological research in the treatment of cancer/ tumor cells.

7.2 Conclusions

In this concluding chapter, I summarize the results of the first direct measurements of the energy spectra due to electrons emitted in the later cascade steps in Auger Cascade Processes in solids (MnO, Ag and Pd). These results were obtained using a new type of electron coincidence spectroscopy from solids, Auger-Auger Coincidence Spectroscopy (AACS), in which the spectrum of subsequent Auger steps is measured in time coincidence with the detection of electrons from the prior Auger cascade step.

Using AACS we have measured the Mn $M_{2,3}$→VV Auger spectrum from a single crystal MnO, in time coincidence with Auger electrons emitted from prior Mn CVV Auger transitions (either Mn $L_{2,3}$ →$M_{2,3}$V or Mn $L_{2,3}$ →$M_{2,3}M_{2,3}$). Fig. 7.2 shows the comparison of the energy spectra of electrons in the range from 20 to 60eV taken in time coincidence with the $L_{2,3}$→$M_{2,3}M_{2,3}$, $L_{2,3}$→$M_{2,3}$V, $L_{2,3}$→VV Auger transitions respectively. The intensity of the AACS spectra taken in coincidence with the $L_{2,3}$→$M_{2,3}M_{2,3}$ transition is roughly twice that of the AACS spectra taken in time coincidence with the $L_{2,3}$→$M_{2,3}$V transition. This 2:1 ratio is to be expected since there are two $M_{2,3}$ →VV Auger decays ($M_{2,3}M_{2,3}$ →$M_{2,3}$VV, $M_{2,3}$VV →VVVV) in the Auger Cascade chain initiated by the $L_{2,3}$→$M_{2,3}M_{2,3}$ transition and only one decay ($M_{2,3}$V →VVV) following the $L_{2,3}$→$M_{2,3}$V transition. The spectra taken in coincidence with the $L_{2,3}$ →VV Auger transition is essentially zero, consistent with the fact that no hole is created in the M level in this transition and therefore no true coincidence is expected. This spectrum provides a measure of the effectiveness of the coincidence technique in

separating out different spectral contributions and indicates that the accidental and other backgrounds are less than ~5% of the coincidence signal for the spectra taken in coincidence with the $L_{2,3}\rightarrow M_{2,3}M_{2,3}$, $L_{2,3}\rightarrow M_{2,3}V$, $L_{2,3}\rightarrow VV$ Mn Auger transitions. We have demonstrated, using AACS, that we could unambiguously separate the individual contributions from the overlapping spectral features from various cascade processes in a solid.

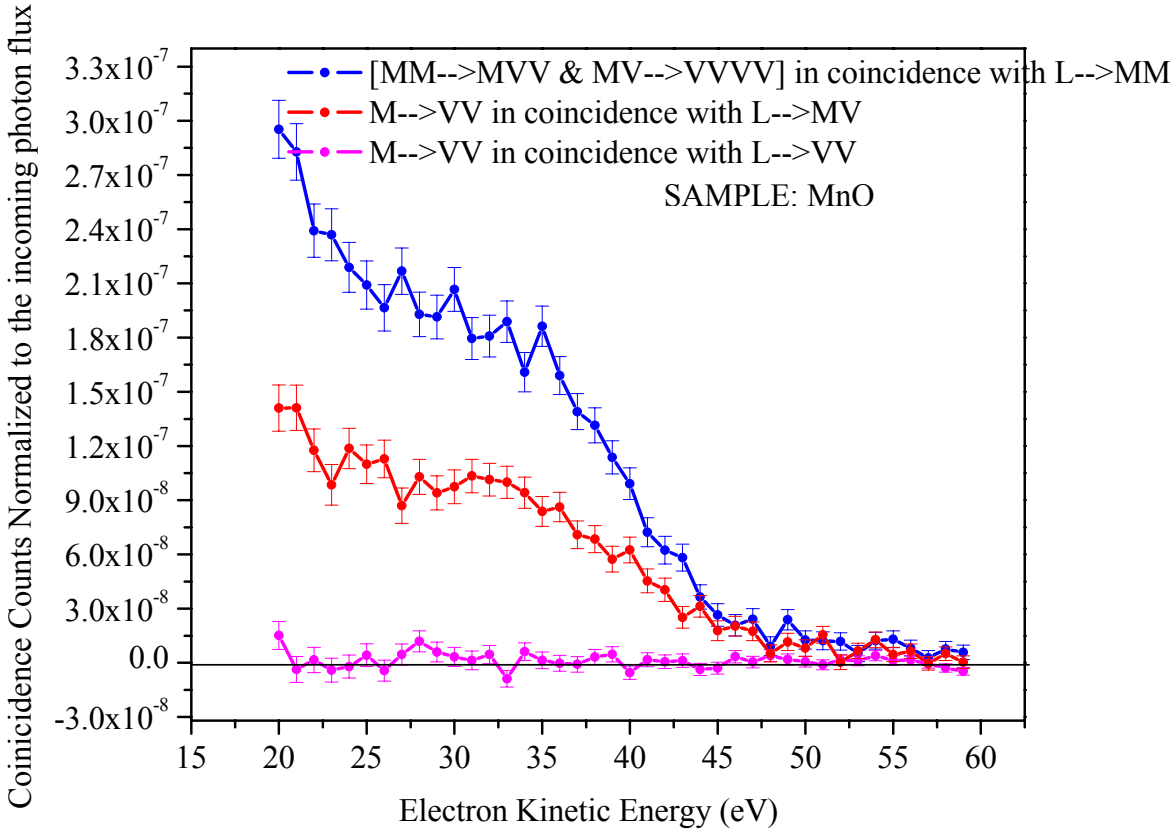

Fig. 7.2 Comparison of the spectra of Mn $M_{2,3}\rightarrow VV$ Augers from MnO measured in time coincidence with the electrons from the peak of $L_{2,3}\rightarrow M_{2,3}V$ Auger, $L_{2,3}\rightarrow M_{2,3}M_{2,3}$ Auger ,and $L_{2,3}\rightarrow VV$ Auger transitions at a photon energy of 660eV showing individual contributions of the Auger cascade steps

Fig. 7.3 shows a comparison between the AACS spectrum taken in coincidence with the Mn $L_{2,3} \rightarrow M_{2,3}M_{2,3}$ transition (corresponding to the sum of the spectra of the $M_{2,3}M_{2,3} \rightarrow M_{2,3}VV$, $M_{2,3}VV \rightarrow VVVV$ transitions) with an APECS spectrum measured in coincidence with photoelectrons from the Mn3p ($M_{2,3}$) level. This comparison reveals that while both AACS and APECS show a peak at ~32 eV, the AACS spectrum is broader than the APECS spectrum and shows spectral contributions that extend up ~5 eV higher in energy. Both the spectra exhibit significant inelastic background at the low energy side. It is important to note that the coincidence technique removes all background from the high energy side of the spectrum.

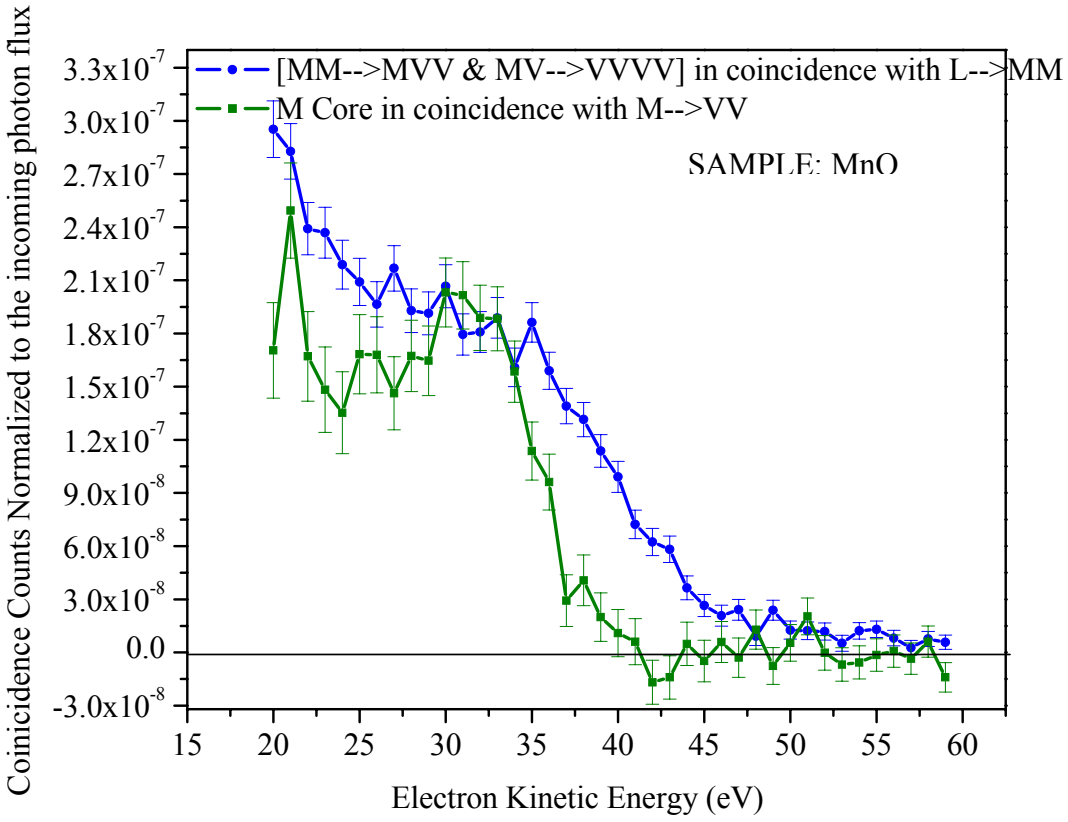

Fig. 7.3 Comparison of the spectra of Mn $M_{2,3}$→VV Augers from MnO measured in time coincidence with the electrons at 535eV (the peak of $L_{2,3}$→$M_{2,3}M_{2,3}$ transition) with the spectra of Mn $M_{2,3}$→VV Augers measured in time coincidence with the detection of electrons at 560eV (Mn $M_{2,3}$ Photoemission peak) at a photon energy of 620eV

Fig.7.2 and Fig. 7.3 reveals that Auger- Auger coincidence spectroscopy is a unique tool to separate the individual contributions to the M→VV Auger spectrum originating from unique previous steps of the cascade processes. We also performed the "reverse scans" where the M→VV spectra was held fixed while we scanned for the peak of the Auger electrons from which it originated which proved to be a stringent test for our new method.

To explain the significant broadening of the Auger–Auger coincidence spectra on the high energy side we have developed a theoretical model which strongly suggests the involvement of valence hole(s) created in the prior cascade step. This necessitates that these holes were not filled at the time of the subsequent Auger decay and it can move any where in the valence band. The Auger Photoelectron Coincidence spectra have been modeled using the self convolution density of states while the Auger-Auger coincidence spectra has been modeled using the generalization of the SCDOS which demanded that we integrate over all possible initial and final hole state combinations using a product of one-hole density of states which was used as a weighting function and the energy conserving delta function appearing in the integration picks out the right combinations which gave the particular kinetic energy of the Auger electron, released from the atom. Model calculations performed using the convolutions of the one hole density of states of the holes in the final state with the correlations of the one-hole density of states in the initial state provided a good fit to the experimental data for the low energy cascade-induced Auger spectra for the samples under study (MnO, Ag and Pd). In contrast, the model calculations in which it was assumed that the energy of the initial valence holes remained unchanged during the Auger transition did not account for the width and centroid of the individual spectra

Also a comparison of the photoelectron spectrum and the SCDOS appropriately shifted gives the correlation energies (core-core (U_{pp}), core-valence (U_{pd}) and valence-valence (U_{dd}) correlation energies) in the many-hole states. For MnO the correlation

energies are given by U_{dd} =.4eV; U_{pd} = 2.1eV and U_{pp}=5.3eV; for silver U_{dd} =4.5eV; U_{pd} =5.5eV; [145] and for Pd U_{dd} =3eV; U_{pd} = 4.5eV.

The model calculations were performed on transitions in L→MM→MVV→VVVV Auger cascade decay and found that the theory fits the experimental data only when the holes in the valence band are allowed to move anywhere in the valence band. Fig. 7.4 shows the M→VV spectra obtained using APECS- Direct Auger decay in the top panel and the MV→VVV spectra obtained using AACS- Cascade Auger decay in the bottom panel for MnO, and Fig. 7.5 and Fig. 7.6 shows the N→VV spectra obtained using APECS- Direct Auger decay in the top panel and the NV→VVV spectra obtained using AACS- Cascade Auger decay in the bottom panel for Ag and Pd. The bottom panel compares the experimental data with both the theoretical models .In one model the rearrangement of the initial valence band holes are allowed (blue spectrum) and the other one where initial state valence band holes are fixed in energy (i.e. the rearrangement of the holes are not allowed-green dashed line). The comparison strongly suggests the involvement of valence hole(s) created in the prior cascade step. The trend clearly shows that the AACS spectra are wider than the APECS spectra for all of the three samples studied. (MnO, Ag and Pd).

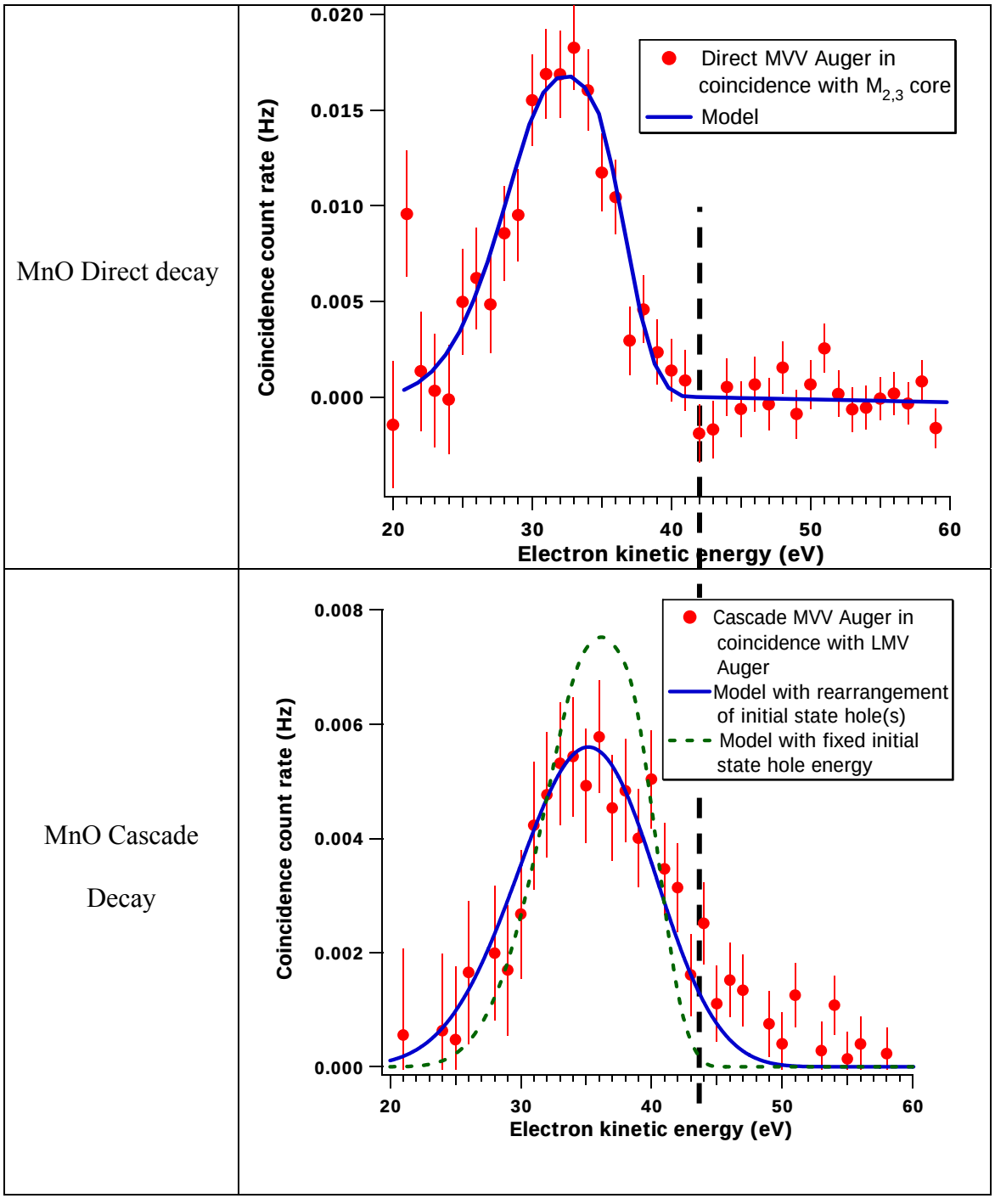

Fig. 7.4 Comparison of the APECS- Direct Auger decay with the AACS- cascade Auger decay of M→VV spectra obtained using MnO

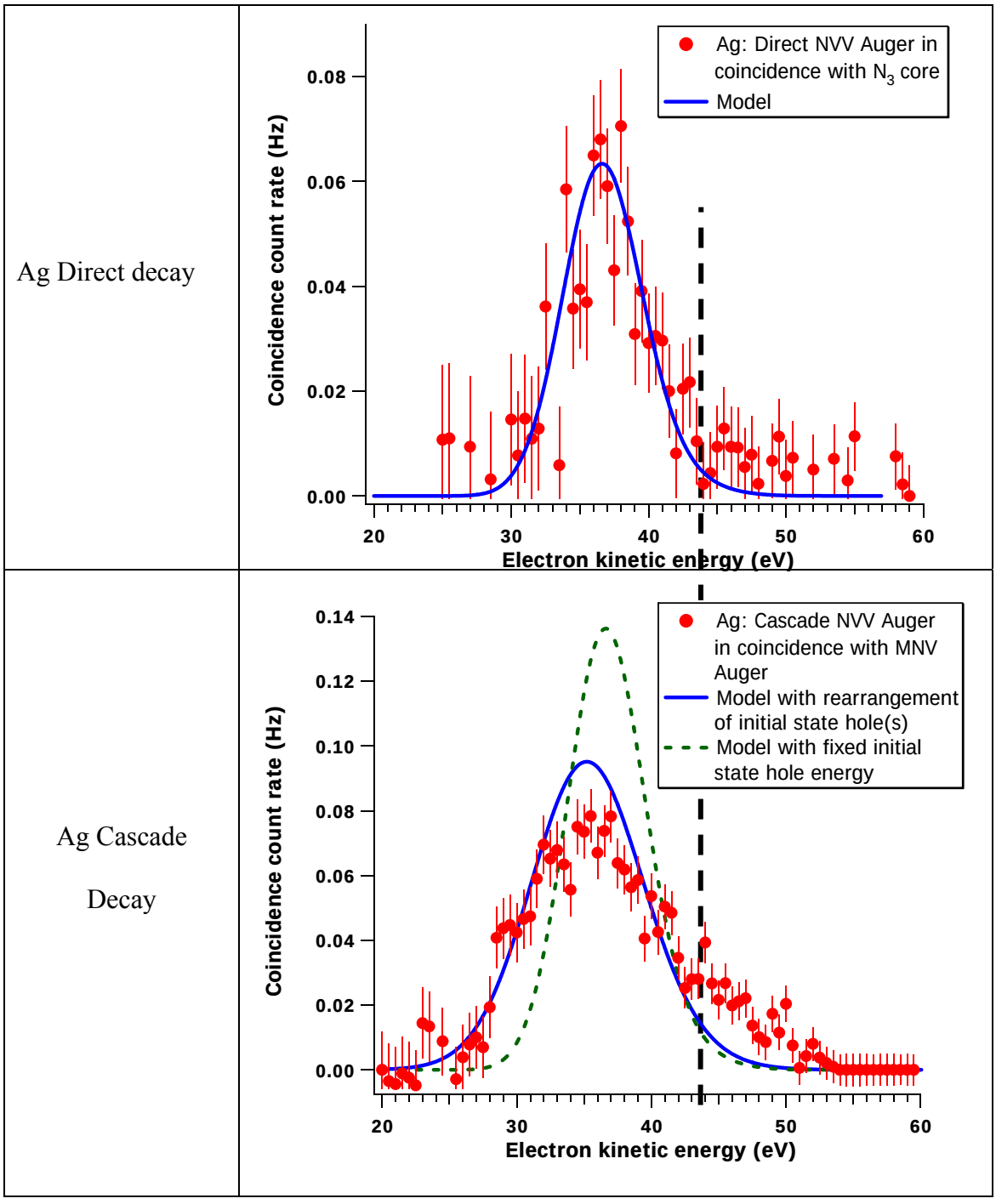

Fig. 7.5 Comparison of the APECS- Direct Auger decay with the AACS- cascade Auger decay of N→VV spectra obtained using Ag

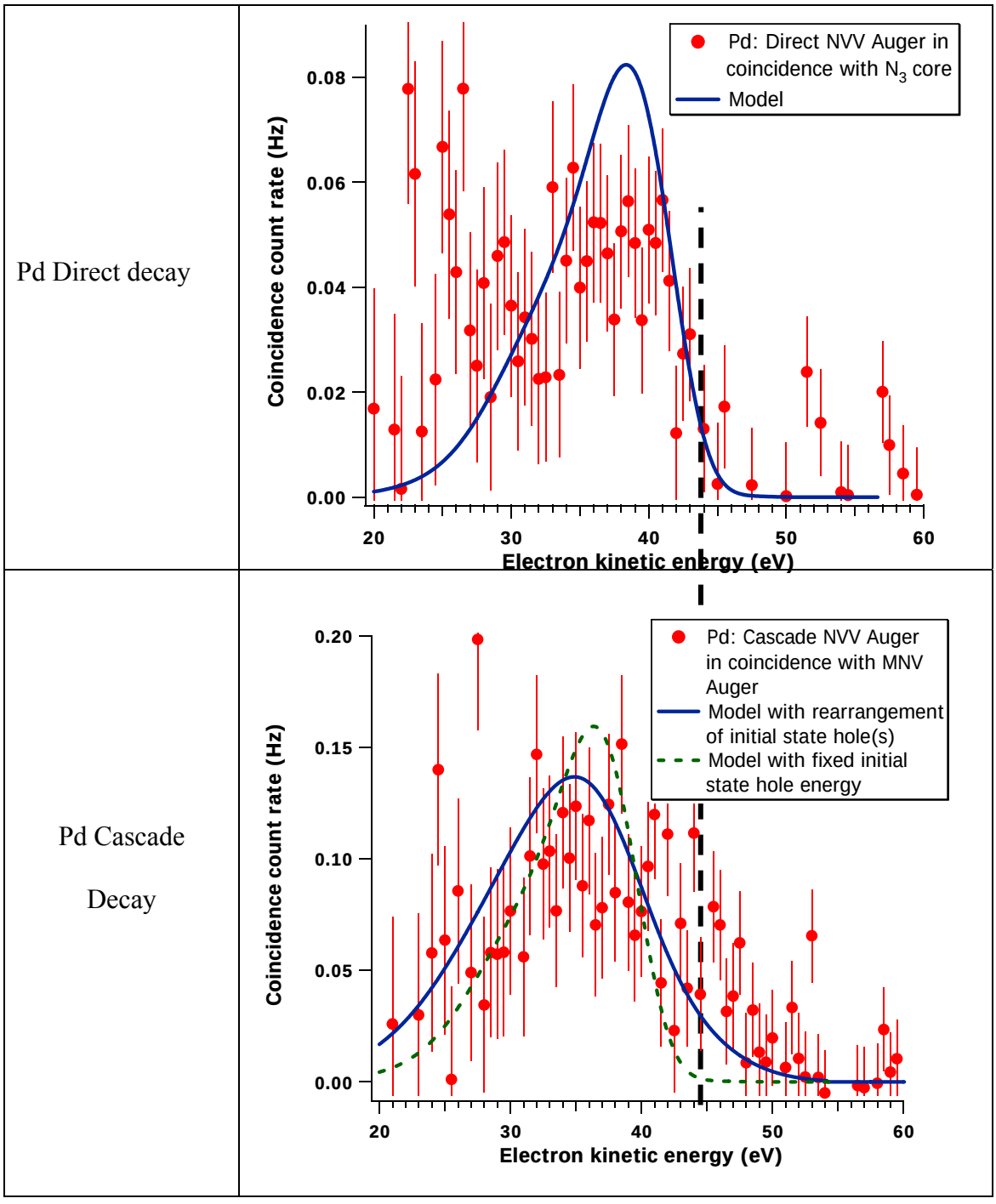

Fig. 7.6 Comparison of the APECS- Direct Auger decay with the AACS- cascade Auger decay of N→VV spectra obtained using Pd

In conclusion, the success of the model in accounting for the increased width observed in the spectra of Auger electrons emitted in the later steps of the Auger cascade provides strong evidence that valence holes left from the previous cascade step participate in the subsequent Auger transitions in the case of transitions involving the outer cores.

APPENDIX A

ACRONYMS

SR	Synchrotron Radiation
BNL	Brookhaven National Lab
NSLS	National Synchrotron Light Source
VUV	Vacuum Ultra Violet
DOE	Department Of Energy
LEBT	Low Energy Beam Transport
ERG	Extended Range Grasshopper
UHV	Ultra High Vacuum
SMT	Second Mirror Tilt
RF	Radio Frequency
MCA	Multi Channel Analyzer
AMP	Amplifier
PHA	Pulse Height Analyzer
ROI	Region Of Interest
CFD	Constant Fraction Discriminator
TAC	Time to Amplitude Converter
AACS	Auger-Auger Coincidence Spectroscopy
AES	Auger Electron Spectroscopy

APECS	Auger Photoelectron Coincidence Spectroscopy
PES	Photo Electron Spectroscopy
XPS	X-ray Photoelectron Spectroscopy
PHI	Physical Electronics
IMFP	Inelastic Mean Free Path
LINAC	Linear Accelerator
CMA	Constant Fraction Discriminator
IC	Inner Cylinder
OC	Outer Cylinder
EF	Electric Field
FWFM	Full Width Full Maximum
KE	Kinetic Energy
VB	Valence Band
TMO	Transition Metal oxides
D/A	Digital to Analog
DOS	Density Of States
DSP	Digital Signal Processing
TTL	Transistor-Transistor Logic

APPENDIX B

SHIRLEY BACKGROUND SUBTRACTION PROGRAM

```
#include<iostream>
#include <fstream>
#include <string>
#include <math.h>
#include <stdlib.h>
#include <iomanip>

#define NULLValue '\0'

using namespace std;

// Define number of elements in the array
#define NUM_OF_ELEMENTS 300
// Define arrays for storing Energy,
float Energy[NUM_OF_ELEMENTS];
float Count[NUM_OF_ELEMENTS];
float Sum[NUM_OF_ELEMENTS];
float BkGnd[NUM_OF_ELEMENTS];
float ScaledBkGnd[NUM_OF_ELEMENTS];

//Read input data; store it in two arrarys named “Energy” and “Count”
void readFromFile()
 {
  string garbage;

  cin >> garbage;
  cin >> garbage;

  for( int i = 0; i < NUM_OF_ELEMENTS; i ++)
   {
    cin >> Energy[i];
    cin >> Count[i];
   }

  return;
 }

//Print both input and out put values
void printArray()
 {
  cout << "Energy\tCount\tSum\tBkGnd\tScaledBkGnd\n";
  for( int i = 0; i < NUM_OF_ELEMENTS; i ++)
   {
    cout << Energy[i];
```

```
   cout << "\t" << Count[i];
   cout << "\t" << Sum[i];
   cout << "\t" << BkGnd[i];
   cout << "\t" << ScaledBkGnd[i];
   cout << endl;
  }
 return;
}

//Calculate cumulative sum of the counts for each energy
void calculateSum()
 {
  for( int i= 0; i < NUM_OF_ELEMENTS; i ++)
   {
    Sum[i] = 0;
    for( int j = i; j < NUM_OF_ELEMENTS; j ++)
     {
      Sum[i] += Count[j];
     }
   }
  return;
 }

// Calculate Background; define a constant which scales the cumulative sum obtained
void calculateBkGnd()
 {
  float c = Count[0]/Sum[0];
  for( int i = 0; i < NUM_OF_ELEMENTS; i ++)
   {
    BkGnd[i] = Sum[i] * c;
   }
  return;
 }

// Calculate scaled background
void calculateScaledBkGnd()
 {
  for( int i = 0 ;i < NUM_OF_ELEMENTS; i ++)
   {
    ScaledBkGnd[i] = Count[i] - BkGnd[i];
   }
  return;
 }
```

```
// Main Program
int main()
 {
  readFromFile();
  calculateSum();
  calculateBkGnd();
  calculateScaledBkGnd();
  printArray();

  return 0;
 }
```

APPENDIX C

CONVOLUTION AND CORRELATION PROGRAMS

CONVOLUTION OF TWO FUNCTIONS

```
#include<iostream>
#include <fstream>
#include <string>
#include <math.h>
#include <stdlib.h>
#include <iomanip>

#define NULLValue '\0'

using namespace std;

// Define number of elements in the array
#define NUM_OF_ELEMENTS 99999
int N = 0;
int M = 0;
float Energy1[NUM_OF_ELEMENTS] = {0.0};
float Count1[NUM_OF_ELEMENTS] = {0.0};
float Energy2[NUM_OF_ELEMENTS]= {0.0};
float Count2[NUM_OF_ELEMENTS]= {0.0};
float Sum[NUM_OF_ELEMENTS]= {0.0};
float x[NUM_OF_ELEMENTS]= {0.0};
int c, jmin, jmax;
float E11,E12,E21,shift,deltaE;

//Read input data; store it in two arrarys name “Energy” and “Count”
void readFromFile1()
{
  int i;
  float enrg1, cnt1;
  string garbage;

  cin >> garbage;
  cin >> garbage;

  for( i= 0; i < NUM_OF_ELEMENTS; i++) {
    cin >> enrg1;
    cin >> cnt1;

    if(enrg1==9999) break;
    Energy1[i] = enrg1;
    Count1[i] = cnt1;
    E11=Energy1[1];
```

```
    E12=Energy1[2];
    }

//Determine the number of rows in first array
  N = i;
  cout << "Number of elements1= ";
  cout <<  N;
  cout << endl;
  return;
}

void readFromFile2()
{
  int i=0;
  float enrg2, cnt2;
  string garbage;
  cin >> garbage;
  cin >> garbage;

  for( i= 0; i < NUM_OF_ELEMENTS; i++) {
    cin >> enrg2;
    cin >> cnt2;

    if(enrg2==9999) break;
    Energy2[i] = enrg2;
    Count2[i] = cnt2;
    E21=Energy2[1];
  }

//Determine the number of rows in second array
  M = i;
  cout << "Number of elements2= ";
  cout <<  M;
  cout << endl;
  return;
}

//Print both input and out put values
void printArray()
{
  cout << "Energy1\tCount1\n";

  for( int i = 0; i < N; i ++) {
    cout << Energy1[i];
```

```
   cout << "\t" << Count1[i];
   cout << endl;
  }
  cout << "Energy2\tCount2\n";
  for( int i = 0; i < M; i ++) {
   cout << Energy2[i];
   cout << "\t" << Count2[i];
   cout << endl;
  }

  cout << "x\tSum\n";
  for( int i = 0; i < M+N-1; i ++) {
   cout << x[i];
   cout << "\t" << Sum[i];
   cout << endl;
  }
  return;
}

// Determine the limits;  Perform Convolution
void calculateConvolutedFunction()
{
  deltaE=E12-E11;
  shift=E11+E21;
  for( int i= 0; i < M+N-1 ; i++) {
     Sum[i] = 0;
     x[i]=i+1;

//UPPERLIMIT
      if (i <= M-1)
        jmax = i;
      else
         jmax = M-1;

//LOWERLIMIT

      if (i-N+1 >= 0)

        jmin = i-N+1;
     else
        jmin = 0;

      for( int j = jmin; j <= jmax; j ++) {
        Sum[i] =Sum[i]+ (Count1[i-j]*Count2[j]);
```

```
    }
  }   /* end i */

 return;
}

// Main Program

int main()
 {
  readFromFile1();
  readFromFile2();
  calculateConvolutedFunction();
  printArray();

  return 0;
 }
```

CORRELATION OF TWO FUNCTIONS

```
#include<iostream>
#include <fstream>
#include <string>
#include <math.h>
#include <stdlib.h>
#include <iomanip>

#define NULLValue '\0'

using namespace std;

// Define number of elements in the array
#define NUM_OF_ELEMENTS 5000
int N = 0;
int M = 0;
float Energy1[NUM_OF_ELEMENTS] = {0.0};
float Count1[NUM_OF_ELEMENTS] = {0.0};
float Energy2[NUM_OF_ELEMENTS]= {0.0};
float Count2[NUM_OF_ELEMENTS]= {0.0};
float Sum[NUM_OF_ELEMENTS]= {0.0};
float x[NUM_OF_ELEMENTS]= {0.0};
int c, jmin, jmax, i2;

//Read input data; store it in two arrarys name “Energy1” and “Count1”
void readFromFile1()
{
 int i;
 float enrg1, cnt1;
 string garbage;

 cin >> garbage;
 cin >> garbage;

 for( i= 0; i < NUM_OF_ELEMENTS; i++) {
  cin >> enrg1;
  cin >> cnt1;

  if(enrg1==9999) break;
  Energy1[i] = enrg1;
  Count1[i] = cnt1;
  }
```

```
 //Determine the number of rows in first array
  N = i;
  cout << "Number of elements1= ";
  cout <<  N;
  cout << endl;
  return;
}

//Read input data; store it in two arrarys name “Energy2” and “Count2”
void readFromFile2()
{
  int i=0;
  float enrg2, cnt2;
  string garbage;
  cin >> garbage;
  cin >> garbage;

  for( i= 0; i < NUM_OF_ELEMENTS; i++) {
    cin >> enrg2;
    cin >> cnt2;

    if(enrg2==9999) break;
    Energy2[i] = enrg2;
    Count2[i] = cnt2;
    }

//Determine the number of rows in second array
  M = i;
  cout << "Number of elements2= ";
  cout <<  M;
  cout << endl;
  return;
}

//Print both input and out put values
void printArray()
{
  cout << "Energy1\tCount1\n";

  for( int i = 0; i < N; i ++) {
    cout << Energy1[i];
    cout << "\t" << Count1[i];
    cout << endl;
  }
```

```
  cout << "Energy2\tCount2\n";
  for( int i = 0; i < M; i ++) {
    cout << Energy2[i];
    cout << "\t" << Count2[i];
    cout << endl;
  }

  cout << "x\tSum\n";
  for( int i = 0; i < M+N-1; i ++) {
    cout << x[i];
    cout << "\t" << Sum[i];
    cout << endl;
  }
  return;
}

// Determine the limits; Perform Correlation
void calculateCorrelationFunction()
{

  for( int i = 0; i < M+N-1 ; i++) {
     Sum[i] = 0;
      i2=i-N+1;
      x[i]=i2+1;

//UPPERLIMIT
      if (i2 <= M-1)
        jmax = M-1;
      else
         jmax = N-1+i2;

//LOWERLIMIT

      if (i2 >= 0)

        jmin = i2;
     else
        jmin = 0;

      for( int j = jmin; j <= jmax; j ++) {
        Sum[i] =Sum[i]+ (Count1[j-i2]*Count2[j]);
      }
   }   /* end i */
```

```
 return;
}

// Main Program
int main()
 {
  readFromFile1();
  readFromFile2();
  calculateCorrelationFunction();
  printArray();

  return 0;
 }
```

APPENDIX D

ESTIMATION OF THE CORRELATION ENERGIES U_{dd}, U_{pd}, and U_{pp}

The hole-hole interaction energies were estimated by finding the set of values for U_{dd}, U_{pd} and $U_{pp,}$ which when incorporated into our theoretical model provided the best estimates of the centroids of the L→MV and L→MM Auger peaks in the measured photon induced Auger spectra and for the centroids of the M→VV, MV→VVV, MM→MVV→VVVV peaks measured using coincidence techniques.

The direct decay of the M core hole transition involves one M-hole in the initial state and two valence holes in the final state. The interaction between these two holes in the valence band (d-orbital) gives U_{dd}. In order to find the U_{dd}, the M→VV photoemission peak is compared with the SCDOS of the valence band appropriately shifted by the binding energy of the Mn M shell and the work function. We can write this in the form of an equation:

$N_{MVV-Singles}(KE) \propto \rho * \rho(KE_{MVV-Singles} - E_M + U_1)$ where $U_1 = U_{dd} + \phi$, thus we can extract the value of U_{dd}. Fig. D.1 shows the comparison and the value of $U_{dd} = 0.4$eV.

In order to find $U_{pd,}$ L→MV transition was used. In the transition L→MV the initial state hole is in the L shell and the final state has one hole in the Mn M shell and one hole in the valence band. The photoemission peak of L→MV was compared with Mn3p core convoluted with the MnO valence band shifted by the binding energy of L_3 and the work function. Thus we can extract the value of $U_{pd.}$ Fig. D.2 shows the comparison and the value of $U_{pd} = 2.1$eV. In order to find U_{pp} the L→MM photoemission peak was compared with the self convolution of the Mn3p core shifted by the binding energy of L_3 and the work function. Thus we can extract the value of U_{pp}**.** Fig. D.3 shows the comparison and the value of $U_{pp} = 5.3$eV.

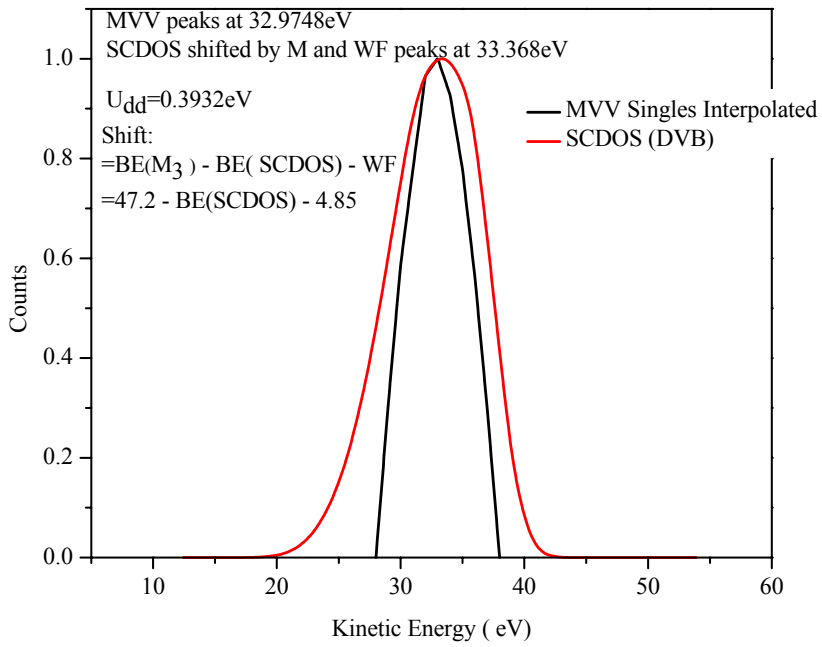

Fig. D1 M→VV singles compared with SCDOS shifted by binding energy of M and the work function

After the U's were first estimated from fitting the position of the peaks of the M→VV, L→MV, L→MM, Auger transitions, the numbers obtained were used to calculate the KE of the outgoing M→VV Auger electron for both the direct and cascade induced MVV transitions yielding four equations. The equation D1 models the centroid position of the direct Auger decay, the equation D2 the MV→VVV transition, and D3 the MM→MVV and D4 the MVV→VVVV transition.

$M - U_{dd} - wf = 41.5$ eV ……..D1
$M + U_{pd} - 3U_{dd} - wf = 45.25$ eV ……..D2
$M + U_{pp} - 2U_{pd} - U_{dd} - wf = 43.7$ eV ……..D3
$M + 2U_{pd} - 5U_{dd} - wf = 47.35$ eV ……..D4

The values of the U's determined from the direct Auger transitions were adjusted to make the four equations yield values that were consistent with the centroid positions observed in the AACS and APECS measurements of the direct and cascade induced MVV transitions assuming the binding energy (BE_M) of the M shell to be BE_M=47.2eV and the work function (wf) to be wf=4.85eV.

In summary, if U_{dd} =0.4eV then U_{pd} must range from 2.1eV to 3.5eV (determined by PES spectra) and U_{pp} must go from 5.3eV to 8.75eV (determined by PES spectra).

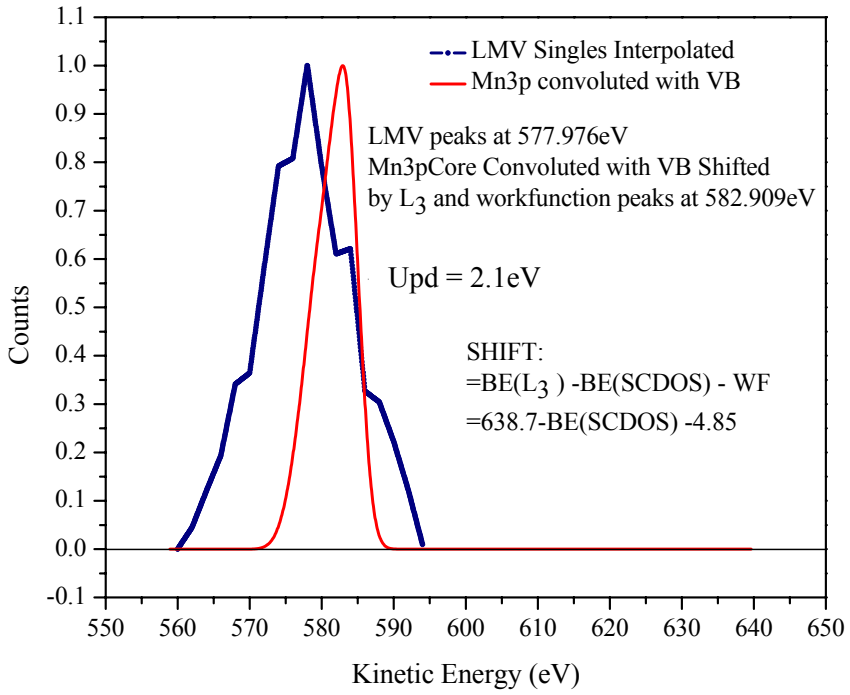

Fig. D2 L→MV singles compared with Mn3p Core convoluted with the MnO valence band shifted by binding energy of L_3 and the work function

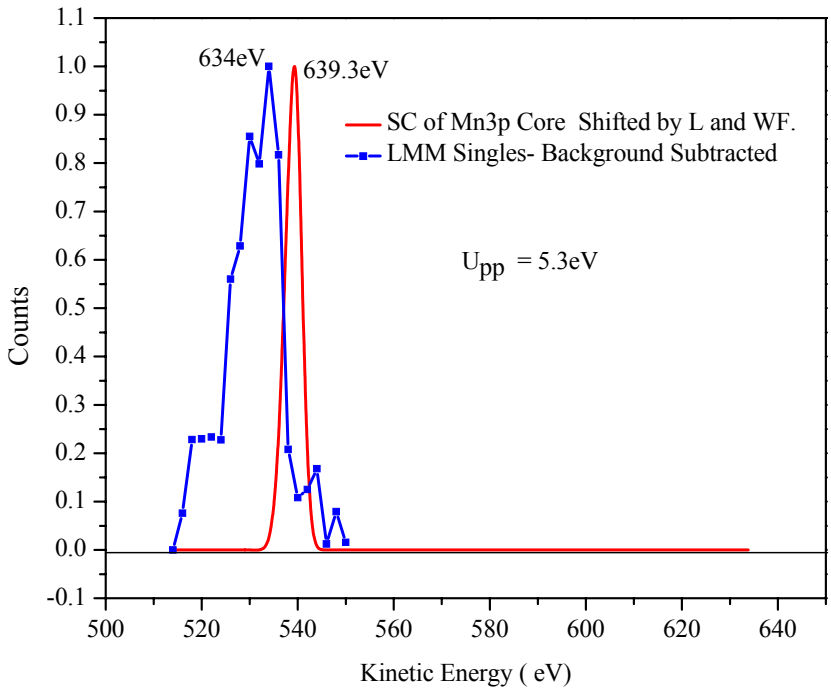

Fig. D3 L→MM Singles compared with self convolution of the Mn3p core shifted by binding energy of L_3 and work function.

REFERENCES

1 M.P.Auger, Compt. Rend.180, 65(1925)

2 M.P.Auger, J.de. Phys. Radium **6**, 205(1925)

3 M.P.Auger, Compt. Rend. 182, 773, 1215 (1926).

4 W.Bambynek, B.Creasemann, R.W.Fink, H.-U. Freund, H.Mark, C.D.Swift, R.E.Price and P.V.Rao, Rev.Mod. Phys. **44**, 716 (1972).

5 Eugene J. Mcguire Phys.Rev. A, **11**, 1889, (1975)

6 Jens Viefhaus, Markus Braune, SanjaKorica, Axel Reinkoster, Daniel Rollesand Uwe Becker, J.Phys.B: At.Mol.Opt. Phys. **38** (2005) 3885-3903

7 M.L.Knotek and Peter J. Feibelman, Phys.Rev.Lett., **40**, 964, (1978)

8 S.Ohtani, H.Nishimura, H.Suzuki,and K.Wakiya, Phys.Rev.Lett., **36**, 863(1976)

9 V.Schmidt,et.al.,Phys.Rev.Lett., **38**, 63, (1977)

10 J.A. de Gouw, J van Eck, J Vander Weg and HGM Heideman, J. Phys.B:

11 At.Mol.Opt.Phys. 28 (1995) 1761

12 H. Aksela, M. Kivilompolo, E. Nommiste, and S. Aksela, Phys. Rev. Lett., 79, 4970, (1997)

13 I.H.Suzuki, et,al, J. Phys. B:At.Mol.Opt. Phys.,37, (2004), 1433 -1441.

14 H. W. Haak and G.A. Sawatzky and T. D. Thomas, Phys.Rev.Letters, 41, 1825, (1978)

15 Wolfgang S. M. Werner,et.al. Phys Rev Letters, 94, 038302 (2005)

16 S.M. Thurgate, C.P. Lund, and A.B. Wedding, Phys. Rev. B, 50, 4810 (1994)

17 P. Lablanquie,et.al, Phys Rev Lett., **84**, 47, (2000)

18 E.Jensen,R.A.Bartynski,R.F.Garrett,S.L.Hulbert,E.D.Johnson, and C.C.Kao,Phys.Rev.B,**45**,13636(1992)

19 R.A.Bartynski and S. Yang, et. al, Phys.Rev.Letters, **68**, 2247(1992)

20 P.Lablanquie, et, al, 84, 47, (2000)

21 U. Alkemper, J. Doppelfeld, and F. Von Busch, Phys.Rev.A, **56**, 2741, (1997)

22 R.Wehlitz, L.S. Pibida, J.C. Levin, and I. A. Sellin, Review of scientific Instruments, **70**, 1978, (1999)

23 E. Von Raven, M. Meyer,M.Pahler,and B. Sonntag, Journal of Electron Spectroscopy and Related Phenomena,**52**,(1990) 677

24 E.H.S. Burhop, *The Auger Effect and other Radiationless Transitions*, (Cambridge Univ. Press, (1952)

25 W.Mehlhorn, "*The Auger Effect*" Report from the Behlen lab of Phys., Univ of Nebraska (1970).

26 E.H.S. Burhop and W.M. Asaad, Adv. Atom.Mol. Phys. **8**, 163, (1972)

27 Thomas A carlson Photoelectron and Auger spectroscopy, Plenum Press, NY (1975).

28 C. Lei *et al*. Rev. Sci. Instrum. **60**, 3656 (1989).

29 Kurt. W. Kolasinski, *Surface Science* John Wiley & sons. (2002) P.59

30 M. Cini, Solid State Communications, **20**, 605, (1976)

31. G.A. Sawatzky, Phys.Rev.Lett., **39**, 504, (1977)

32 C. J. Powell, Phys.Rev.Lett. **38**,1429 (1977)

33 J.J.Lander, Phys. Rev., **91**, 1382, (1953)

34 C.J. Powell,Phys.Rev. Letters, **30**, 1179, (1973)

35 E. Antonides,E.C.Janse, and G.A. Sawatzky, Phys.Rev. B, **15**, 1669 (1977)

36 M. Cini, Solid State Commun., **24**, 681,(1977)

37 L.D.Lang and A.R.Williams, Phys.Rev B, **16**, 2408(1977)

38 M.Cini, Phys Rev B, **17**, 2788, (1977)

39. A.R.Williams and N.D.Lang, Phys.Rev Lett., **40**, 954, (1978)

40 G.A. Sawatzky and A.Lenselink, Phys.Rev.B, **21**, 1790, (1980)

41 Claudio Verdozzi, Michele Cini, Andrea Mairini, Journal of Electron Spectroscopy and Related Phenomena 117-118(2001) 41-55.

42 S.N.El Ibyari and W.N. Asaad and Eugene J. McGuire, Phys. Rev. A, 5, 1048, (1972)

43 G. Cubiotti, A Laine and Weightman, J. Phys:Condens.Matter (1989) 7723-7732

44 Eugene J. McGuire Phys. Rev. A, **5**, 1043, (1972)

45 Eugene J. McGuire Phys. Rev. A, **5**, 1052, (1972)

46 Eugene J. McGuire Phys.Rev. A, **3**, 1801, (1971)

47.A.de.Siervo, R.Landers, G.G. Kleiman. Phys. Rev. Lett. **86**, 1362 (2001)

48 H.W.Haak, G.A.Sawatzky, and T.D. Thomas, PRL **41,**1825-7 (1978)

49 W.D.Duncan and Gwyn P.Williams, Applied Optics, **22**, 2914,(1983)

50 Herman Winick and S.Doniach, *Synchrotron radiation research* (1980)

51 Robert Z. Bachrach, *Synchrotron Radiation research* (1992)

52 C. Kunz, *Synchrotron radiation* (1979)

53. H.W. Haak and G.A. Sawatzky,L. Ungier, J.K. Gimzewski, and T.D. Thomas, Rev.Sci.Instrum.**55**, 696,(1984)

54 S. Thurgate, B. Todd, B.Lohmann, and A. Stelbovics, Rev.Sci. Instrum.61 (12), (1990)

55 P.A.Bennett, J.C.Fuggle, F.U.Hillebrecht, A.Lenselink and G.A.Sawatzky, Phys.Rev.B **27**, 2914(1983)

56 M.Vos, D.van der Marel, and G.A.Sawatzky, Phys. Rev. B **29**, 3073 (1984)

57 C. J. Powell, Phys.Rev.Lett. **38**, 1429 (1977)

58 C.O.Almbladh, A.L.Morales, and G.Grossmann. Phys. Rev. B **39**,3489 (1989)

59 NSLS Control room – LINAC, Booster and RF Notes

60 http://www.nsls.bnl.gov/facility/accelerator/vuv/vuv_parameters.pdf NSLS VUV ring parameters.

61 http://www.nsls.bnl.gov/facility/accelerator/xray/-X-ray ring

62 http://www.nsls.bnl.gov/facility/accelerator/vuv/-VUV RING

63 Frederick C. Brown, R.Z. Bahrach, Neil Lien, Nuclear Instruments and Methods **152**, 73-79 (1978)

64 S. L. Hulbert, J, P. Stott, F. C. Brown, and N, C. Lien, Nucl. Instrum. 1 208, 43 (1983).

65 K. Codling and P. Mitchell, J. Phys. h: Sci, Instrum. **3**, 685 (1970); in the ERG, N is a. 1 cm diameter gold—coated silica flat.

66 N. Salle and B. Vodar, C. R. Mad. Sci., Paris 230, 380 (1950).

67 PES Experiment Control Program Users Manual;R.F.Garrett, J.Lepeyren and S.L.Hulbert, BNL 43886 (1990)

68 V. Rehu in Workshop on X—ray Instrumentation for Synchrotron Radiation Research, SSRL Rapt._#78/04, p. VII—13, May 1978; D, A. Shirley, SSRL Rept.#78/04, p. VIf79, May 1978.

69 Applied Optics Center Corp., Burlington, MA

70 E.Jensen, R.A.Bartynski, S.L.Hulbert and E.D.Johnson, Review of Scientific Instruments **63**, (1992) 3013-26

71 R.A.Bartynski, E. Jensen, S.L. Hulbert, and C.C.Kao, Progress in Surface Science, **53**, 155-162, (1996)

72 Four channel V-F converter with independent frequency counters- Philip J Pietraski and Peter Siddons

73 Model 6485 5-1/2 digit Picoammeter with 10fA Resolution
http://www.keithley.com/products/locurrhiresist/picoammeters/?mn=6485.

74 DSP QS-450 4 - Channel Counter

76 Physical electronics Corporation model 255-G

77 T.W. Haas, J.T. Grant, and G.J.Dooley, Phys.Rev.B, **1**, 1449(1970)

78 J.Van Elp, Arata Tanaka, Phys.Rev.B, (1998)

79 F.M.F. de Groot, M. Grioni,and J.C.Fuggle, J.Ghijsen and G.A.Sawatzky, H.Petersen, Phys.Rev.B, **40**, 5715, (1989)

80 Shota Kobayashi, Tatsuya Usui, Hiromasa ikuta, Yoshiharu Uchimoto, and Masataka Wakihara, J. Am. Ceram.Soc., **87**(6), 1002, (2004)

81 Shota Kobayashi, Iresha, R.M.Kottegoda, Yoshiharu Uchimoto and Masataka Wakihara, The Royal Society of Chemistry, **14**, 1843, (2004)

82 B.Hermsmeier, J.Osterwalder, D.J.Friedman, B.Sinkovic, T.Tran and C.S.Fadley. PRB **42**, 11895 (1990)

83 Physical electronics Corporation model 255-G

84 E.Jensen, R.A.Bartynski, S.L.Hulbert, and E.D. Johnson, Rev.Sci. Instruments. **63**, 3013-3026, (1992)

85 S.Rosseland, Z.Phys., **14**,172,(1923)

86 E.H.S. Burphop, *The Auger Effect and other radiationless transitions*, Cambridge University press, Cambridge, 1952.

87 G.E McGuire and P.H.Holloway, in *Electron Spectroscopy: Theory Techniques and applications* .Vol. **4**.

88 C.R.Brundle and A.D.Baker, Eds. London: Academic press, 1981 p1-85 *Electron Spectroscopy: Theory Techniques and applications*
89 Robert J.Lad and Victor E. Henrich, Phys. Rev. B **38**, 10 860 (1988)

90 J .Van Elp, R.H.Potze, H.Eskes, R.Berger, and G.A.Sawatzky, Phys. Rev. B, **44**, 1530, (1991)

91 Shin- puu jeng, Robert J.Lad, Victor E. Henrich, Phys Rev B, **43**, 11971 (1991)
Masaoki Oku, Kazuaki Wagatsuma, Tokuzou Konishi, Journal of Electron Spectroscopy and related Phenomena, 277-285 (1998)

92 J.van Elp, R.H.Potze, H.Eskes, R.Berger, and G.A. Sawatzky. PRB **44**, 1530, (1991)

93 D.A Shirley. Phys.Rev.B **5**, 4709, (1972)

94 d-d excitations in Transition Metal Oxides, B.Fromme, Springer, 2001

95 P.S.Bagus, J.L.F.reeouf and D.E. Eastman, Phys.Rev.B.**15**, 3661,(1976)

96 C.S. Fadley and D.A. Shirley, A.J.Freeman, P.S.Bagus,and J.V.Mallow, Phys. Rev. Lett., **23**, 1397, (1969)

97 V.I Anisimov, M A Korotin and E Z Kurmaev, J.Phys.:Condens.matter **2**, 3973, (1989)

98 A.J.Nelson and John G. Reynolds, Joseph W. Roos, J.Vac.Sci. Technol.A **18** (4) 1072, (2000)

99 Eugene J. McGuire, Phys. Rev. A, **3,** 587, (1971)

100 D.A.Arena and R.A. Bartynski, R.A.Nayak and A.H. Weiss, S.L. Hulbert, Phys Rev B, **63**, 155102.-1to7

101 R.A. Bartynski, Q. Qian and S.L.Hulbert, J. Phys. IV France 9 Pr6-157-160, (1999)

102 C.J.Powell, Phys. Rev. Lett. **30**, 1179 (1973).

103 M.Cini, Solid State Commun. **24**, 681(1977).

104 G.A. Sawatzky. Phys. Rev. Lett. **39**, 504 (1977).

105 N.D.Lang and A.R. Williams, Phys. Rev. B **20**, 1369,(1979)

106 N.D.Lang and A.R.Williams, Phys. Rev. B, **16**, 2048 (1977)

107 A.R.Williams and N.D.Lang. Phys. Rev. Lett. **40**,954 (1978)

108 B.Johansson and N.Martensson, Phys.Rev. B **21**, 4427, (1980)

109 M.Matrensson, H.Hedegard, and B.Johansson, Phys. Scr., **29**, 154 (1984)

110 A.de Siervo, R. Landers, and G.G. Kleiman, Phys. Rev Lett, **86**, 1362, (2001)

111 A.de Siervo, R. Landers,and G.G. Kleiman, S.G.C.de Castro, and J. Morais, Phys Rev B, **60**, 15 790 (1999)

112 G.G. Kleiman, S.G.C.de Castro, and R. Landers, Phys.Rev.B, 49 2753, (1994); Phys Rev B, **44**, 3383, (1991)

113 R. Landers, G. Kleiman and S.G.C.de Castro, Journal of Electron Spectroscopy and Related Phenomena **72**, 211-215(1995)

114 A.de.Siervo, R.Landers, G.G. Kleiman, S.G.C. de. Castro and J.Morais Phys. Rev. B **60**, 15790 (1999)

115 G.G. Kleiman PRB, Rapid Commun. **44**, 3383 (1991)

116 W. Drube, et al, Phys.Rev.B, **60**, 15 507, (1999)

117 G.G. Kleiman, R. Landers, P.A.P.Nascente, and S.G.C. de Castro, Phys. Rev. B, **46**, 4405, (1992)

118 D.D. Sarma and Priya Mahadevan, Phys Rev Lett, **81**, 1658, (1998)

119 G.G. Kleiman, R. Landers,and S.G.C.de Castro, Journal of Electron Spectroscopy and Related Phenomena **72** ,199-203, (1995)

120 J.C.Fuggle, M. Campagna, Z. Zolnierek, and R.Lasser,and A.Platau, Phys. Rev. Lett., **45**, 1597, (1980)

121 John C. Fuggle and Rainer Lasser and Olle Gunnarsson and Kurt Schonhammer, Phys. Rev. Lett., **44**, 1090,(1980)

122 F.J. Himpsel and D.E. Eastman, and E.E.Koch, Phys. Rev. Lett., **44**, 214 (1980)

123 G.G. Kleiman and R. Landers, Journal of Electron Spectroscopy and Related Phenomena **76**, 319-323 (1995)

124 D.D. Sarma, C. Carbone, P. Sen, R.Cimino,and W.Gudat, Phys. Rev. Lett., **63**, 656, (1989)

125 J.C.Fuggle, G.A. Sawatzky, Phys. Rev. Lett., **66**, 966, (1991)

126 R. Landers, G. Kleiman and S.G.C.de Castro, Journal of Electron Spectroscopy and Related Phenomena **76**, 345-349(1995)

127 G.G.Kleiman, R. Landers, S.G.C.de Castro, and A. de Siervo, Phys. Rev. B, **58**, 16 103, (1998)

128 M.T. Butterfield, R.A. Bartynski, S.L. Hulbert --Palladium M4-Valence- Valence and M5-Valence-Valence Auger spectra determined by Auger-Photoelectron coincidence spectroscopy (NSLS Report)

129 D.A.Arena and R.A. Bartynski, R.A. Nayak and A.H. Weiss, S.L. Hulbert, M. Weinert, Phys. Rev. Lett., **91**,176403, (2003)

130 Masahide Ohno--Quantum Science Research (2005)

131 Max Wolfsberg and Morris L.Perlman, Phys. Rev., **99**, 1833, (1955)

132 E.Antonides, E.C. Janse, and G.A. Sawatzky, Phys. Rev. Lett., **15**, 1669, (1977)

133 J. Hubbard, ProcR. Soc. A 276, 238 (1963) 277, 237,(1964); 281, 401 (1964)

134 David E. Ramaker, Phys. Rev. B, **25**, 7341 (1982).

135 David E. Ramaker, Phys. Rev. B, **21**, 4608, (1980)

136 D.E. Ramaker, J.S. Murday,and N.H. Turner, G.Moore and M.G.Lagally, J.Houston, Phys. Rev. B, **19**, 5375, (1979)

137 N. Tımneanu, C. Caleman, J. Hajdu, and D. van der Spoel, Chem. Phys. **299,** 277 (2004)

138 J. L. Humm, R. W. Howell, and D. V. Rao, Med.Phys. **21,** 12 (1994)

139 K. G. Hofer, Acta Oncologica **39**, 651 (2000)

140 P. E. Sutmann, Int. J. Radiat. Biol. **80**, 855 (2004)

141 R.Stoian et.al Phys.Rev.B **62**,13167, (2000)

142 Hai-Peng Chen et.al, Phys.Rev.B, **55**, 2628 (1997)

143 Ronald Wangsness, *Electromagnetic Fields*, John Wiley& Sons.

144 http://www.goodfellow.com/csp/active/gfMaterialInfo.csp?MATID=AU00

145 Hao Tjeng, G.A. Sawatzky et.al. Phys.Rev.B **41**, 3190,(1990)

BIOGRAPHICAL INFORMATION

Rajalakshmi Sundaramoorthy did her Undergraduate studies majoring in Physics and having Mathematics and Chemistry as her ancillary subjects at Women's Christian College of Madurai Kamaraj University at Nagercoil during 1987-1990, where she was the best student of the year1988 for which she was awarded a Merit Certificate. Overall she ranked second in the Physics Department in the final year of her Graduation. She gained admission into one of the best colleges Madras University Guindy Campus for her M.Sc in Physics during the year 1990-1992.She graduated with a First Class. She then took IBM Mainframes and other computer courses and worked as a Computer programmer and Faculty member of the Krishnan Institute of Computer Technology. She joined University of Texas at Arlington in 2001. She performed her MS research at Brookhaven National Laboratory at NSLS on "Auger-Auger Coincidence Spectroscopy" under the guidance of Dr. Alex Weiss of UTA and Dr. Steve Hulbert of NSLS. She graduated in March 2003 from UTA. She continued the same research under Dr Alex Weiss for her Doctoral work. She has wide range of interests including solar cell research, Bio-physics research, and semiconductor fabrication.